Traditional Quantum Dots to Defect-Tolerant Cesium Lead Halide ($CsPbX_3$) Perovskite Nanocrystals for Optoelectronics

A thesis
submitted in partial fulfilment of the requirements
for the degree of

Doctor of Philosophy

by

ABHISHEK SWARNKAR

Indian Institute of Science Education and Research (IISER)-Pune

2018

Dedicated to

My Parents, Sisters

(Especially to Mrs. Shweta Burman)

&

My friends

भारतीय विज्ञान शिक्षा एवं अनुसंधान संस्थान, पुणे
INDIAN INSTITUTE OF SCIENCE EDUCATION AND RESEARCH (IISER) PUNE
(An Autonomous Institution of Ministry of Human Resource Development, Govt. of India)
Dr. Homi Bhabha Road, Pune - 411008.

DECLARATION

I declare that this written submission represents my ideas in my own words and wherever other's ideas have been included; I have adequately cited and referenced the original sources. I also declare that I have adhered to all principles of academic honesty and integrity and have not misrepresented or fabricated or falsified any idea / data / fact / source in my submission. I understand that violation of the above will cause for disciplinary action by the Institute and can also evoke penal action from the sources which have thus not been properly cited or from whom proper permission has not been taken when needed.

Mr. Abhishek Swarnkar

Date: 23th August 2018

(ID: 20122032)

भारतीय विज्ञान शिक्षा एवं अनुसंधान संस्थान, पुणे
INDIAN INSTITUTE OF SCIENCE EDUCATION AND RESEARCH (IISER) PUNE
(An Autonomous Institution of Ministry of Human Resource Development, Govt. of India)
Dr. Homi Bhabha Road, Pune - 411008.

Dr. Angshuman Nag
Assistant Professor
Department of Chemistry,
IISER Pune

CERTIFICATE

Certified that the work incorporated in the thesis entitled "***Traditional Quantum Dots to Defect-Tolerant Cesium Lead Halide ($CsPbX_3$) Perovskite Nanocrystals for Optoelectronics***" submitted by **Mr. Abhishek Swarnkar** was carried out by the candidate, under my supervision. The work presented here or any part of it has not been included in any other thesis submitted previously for the award of any degree or diploma from any other university or institution. For the completion of thesis, few results are taken from collaborators after their permissions and are clearly mentioned in the thesis.

Dr. Angshuman Nag

Date: 23th August 2018

(Research Supervisor)

Acknowledgements

As I reach the completion of my integrated MS-Ph.D programme, I would like to express my gratitude and thanks to all the people who helped make my Ph.D. work pleasant and successful.

First and foremost, I wish to thank my supervisor Dr. Angshuman Nag for his incredible guidance and ever-friendly nature. I am indebted to him for believing in me and providing unflinching support all through my Ph.D. duration. Without his able and erudite guidance, this work would not have been possible. His valuable suggestions and encouraging words helped greatly in shaping up this Ph.D. thesis. He trained me to work efficiently and how to handle stressful situations. His way of working motivated me a lot to be a good researcher and I learned many things from him.

I thank to my RAC members for helping me in time to time in structuring my Ph.D. work. In this regard I am lucky to have Dr. Shouvik Datta and Dr. Musthafa as my RAC member.

I specially thank G. Shiva Shanker, my special friend, for making an amicable and cheerful environment in the IISER and providing incredible contribution in my work whenever I needed.

Special thanks goes to my all other lab mates including Wasim, Jagadees, Tariq, Nila and Yogesh for their incredible friendly supports. I enjoyed my lab timing while doing funny stuffs and making jokes with you guys. Jaya and Ganesh were the best post-doctoratal lab mate and very friendly.

I am privileged to have met with a bunch of nice and talented people as my colleagues at the IISER Pune and in many science conferences, where I presented this work. We had lots of fun together as well as exciting discussions; Kiran, Avadhoot, Avinash, Hridya, Rahi, Aditi, Sneha, Shabnum, Sohini, Barun, Swati, Anjusha, Mainak, Bappa, Chetan, Chenna, Ananthraj – thanks all of you!! I always cherish those wonderful years of togetherness.

I worked in many collaborative projects and went out of my institute. I had a great experience with many collaborative lab mates, including IIT Bombay and NREL, USA. In NREL, I got the exposure to work with lab mates from different countries and shared our experiences. I remember the day I went for mountain hiking with all my lab mates at NREL and enjoyed the snow at height with sunlight. Erin, Hyekyoung and Ashley would be remembered and I thank you for being with me as a great supporter in my US visit.

Lindau Nobel Laureate Meeting, one of the most remembered events of my Ph.D. life, brought many experiences in my research life. Thanks to Lindau committee. I met great minds of the world including many nobel laureates. Many Indian friends, who are still in my touch, are a source of motivation for me and I thanks to all those friends.

Department of science and technology (DST), gov. of India has played a great role in my Ph.D. Thanks for all the fellowships which I have received for the academic/research journey of KVPY (Kishore Vaigyanik Protshahan Yajana-2009 fellowship) to the BASE (Bashkara Advanced Solar Energy fellowship), which made my Ph.D. remarkable.

I would like to thank Director, IISER Pune (past and the present one) for providing me the financial support throughout my Ph.D work and encouraging me to do good research.

I cannot imagine my Ph.D. to be successful without IISER Pune's chemistry department, chair chemistry, dean, all faculties and non-teaching staffs (including Tushar and Mayuresh sir). By providing state-of-art- research facility, research funding, Ph.D. research fellowship and world class accommodation facilities, it made my Ph.D. extraordinary. Thanks a lot to IISER Pune

I would like to thank Dr. Shouvik Datta and his Ph.D. students Arthur, Padmashri and Amit for helping me in my early struggling days of Ph.D. to learn solar cell device fabrications and semiconductor device photophysics.

I owe my parents much of what I have become. I thank them for their love, support and their confidence in me throughout my Ph.D.

I dedicate this work to my elder sister, Shweta, my role model and one who cares about me, along with her family, to honor their love, patience and support during these years.

I am very thankful to all my motivational idols in and outside of IISER Pune. Without their support my Ph.D. is unsuccessful. Prof. Hotha, Dr. Amiya Priyam, Dr. N. Nirmalya and Dr. Joey Luther are my motivational sources at different stages of my Ph.D. I can clearly remember their words which will motivate me in my life.

Finally, I thank to my friends, colleagues and faculties who gave their precious time to look for corrections in my thesis writing and made its submission successful.

Synopsis

This thesis mainly focuses on colloidal semiconductor nanocrystals (NCs) of cesium lead halide ($CsPbX_3$; X= Br and I) perovskite. Colloidal synthesis, purification of NCs, luminescence properties, crystal phase stabilization at nanoscale and deposition of electronically coupled NC film have been discussed in detail. Luminescence properties of these $CsPbX_3$ perovskite NCs has been compared with CdSe based traditional quantum dots (QDs), in which, the defect sensitiveness of CdSe QDs and the defect-tolerance nature of $CsPbX_3$ NCs has been discussed. Furthermore, optimized purification of $CsPbI_3$ NCs allows the large surface energy to stabilize the cubic perovskite black phase of $CPbI_3$ at room temperature unlike its bulk counterpart. Eventually, a layer by layer film deposition method is developed for the fabrication of optoelectronic devices. $CsPbX_3$ NCs are enough electronically coupled and these films exhibiting appreciable performance in solar cell, photodiode and light emitting diode (LED).

Chapter 1.Introduction: This chapter is a brief introduction and motivation of the work done in this thesis. Semiconductor NC or QDs are introduced, where different advantages of quantum confinement effect are discussed. Optoelectronic applications of semiconductor NCs in solar cell, LEDs and photodetector have been discussed. The fundamentals of well-adopted synthesis protocol of hot injection method are also briefly described. Different types of organic capping ligands and their nature of binding on the surface of inorganic NCs are explained. Along with advantages of colloidal QDs, the disadvantages of having high surface to volume ratio are pointed out. The nature of surface defects due to large number of surface related dangling bonds in QDs are distinguished. The concept of defect-tolerant has been introduced. For example, optoelectronic processes in traditional CdSe QDs get affected tremendously in presence of defects, but defects do not causesuch significant change to optical and optoelectronic performances of lead halide perovskites. These materials where defects are benign to the optoelectronic properties are termed as defect tolerant and $CsPbX_3$ perovskites are such a material. Looking on this property along with all-inorganic nature, NCs of $CsPbX_3$ are taken as research material in this thesis and introduced in this chapter. Reported work on the crystal structure, electronic structure and optical properties are taken as important topics for the discussion which are relevant to the whole thesis work.

Chapter 2.Role of Defects on Luminescence of CdSe Based Quantum Dots and Sensor Application: First, long-chain organic ligand capped CdSe QDs has been synthesized by following a known method. Then the organic ligands have been replaced with S^{2-} ligand. This ligand exchange increases the defect density on the surface, significantly quenching PL intensity. PL intensity go recovered in presence of Cd^{+2}. This increase in PL by addition of Cd^{2+} ions can be used as a turn-on sensor for detecting Cd^{2+} in aqueous medium. Mechanism of both, PL quenching and enhancement are discussed in details where surface defects are playing major role. The Cd^{2+}has been quantified by fluorescent based titration method and the ligand free NCs are used as sensor for Cd^{2+}. Sensitivity and selectivity of the sensor has been discussed. Similarly, the NCs are also used as nitroexplosive sensor, after looking its ligand free nature.In other words, this chapter shows the extreme sensitivity of optical properties of traditional QDs like CdSe NCs on the surface and surroundings of QDs. Therefore, the need of defect-tolerant NCs for robust and efficient optoelectronic devices has been pointed out.

Chapter 3A. Luminescence from Defect-Tolerant $CsPbBr_3$ Perovskite Nanocrystals: This chapter is focused on crystal structure and optical properties of colloidal $CsPbBr_3$NCs which has been synthesized by following a previous report. We found that the NCs crystal phase of $CsPbBr_3$ is orthorhombic unlike the previous reportthat suggest cubic phase. In our study, we have found that weak quantum confinement is sufficient enough for achieving ~90% PL quantum yield (QY)from $CsPbBr_3$ NCs without any surface passivation.As a result of slightly larger size than the Bohr's diameter the size distribution related problems do not affect the color purity resulting into narrow (~85 meV) spectral width of PL. In fact the full width at half maximum (FWHM) of PL for ensemble is similar to that of a single NC. Also, Föster resonance energy transfer (FRET) negligibly affects PL. PL dynamics show bi-excitonic decay with exhibiting 3 ns and 8 ns radiative lifetimes of nearly equal contribution. Importantly, the NCs show reduced PL blinking. These data support the defect-tolerant nature of $CsPbBr_3$ NCs.

Chapter 3B. Excellent Green but Unconvinced Blue Luminescence from $CsPbBr_3$ Perovskite Nanocrystals: In continuation of chapter 3A, this chapter discusses on smaller sized strongly quantum confined NCs of $CsPbBr_3$. On reducing the size (increasing the surface to volume ratio) of $CsPbBr_3$ NCs by reducing reaction temperature, the PLQY does not get much affected. But these blue emitting smaller size NCs have higher tendency to grow in size and also

can change their morphology. Hence, the color purity of blue PL gets affected. The growth mechanism has been discussed by using electron microscopy images. Therefore, while making blue emitting NCs of $CsPbBr_3$ by keeping high PLQY and higher color purity, it is better to adopt other strategies like change in the halide composition (alloying with Cl) instead of tuning the size of the NCs.

Chapter 4.Stabilization of α-$CsPbI_3$ Perovskite for Solar Light Harvesting: Size Effect: In this chapter, synthesis of colloidal α-$CsPbI_3$ NCs that are stable in ambient conditions are discussed. Different sized NCs in the size of 3.4 to 12.5 nm were prepared by varying the reaction temperature. The NCs were successfully purified without affecting the phase and colloidal stability. This stabilization of α-phase of $CsPbI_3$NCs at room temperature is a major development, since bulk $CsPbI_3$ crystallizes in δ-phase at room temperature. This newly developed black α-$CsPbI_3$NC is ready for use in photovoltaic cell, photodiode and LEDs. In this regard, this chapter discusses the photophysical properties of α-$CsPbI_3$ NCs to understand the effect of quantum confinement and surface defects on bandgap, excitonic transition properties and PL. All the samples show excitonic (or bandgap) emission with PLQY in the range of 21 to 51 % maintaining a narrow FWHM (83-155 meV). PL decays show average radiative lifetime in the range of 10-15 nano second for different sized NCs. The high PLQY and near absence of non-radiative component in PL decay suggest defect tolerant behaviour of these NCs and are encouraging for optoelectronic applications.

Chapter 5. Surface Ligand-Engineering of $CsPbX_3$ (X=Br, I) Nanocrystal Film for Optoelectronics: This chapter demonstrates layer-by-layer deposition of $CsPbX_3$ NC film for use in high performing optoelectronic devices such as solar cell, photodiode and LEDs.NC films are treated with MeOAc that significantly removes the long-chain organic ligands from the NC surface. This removal of ligands reduces the PL efficiency, but expected to enhance the charge transport in NC films. Thickness of the NC films was increased by layer-by-layer method, where each layer corresponds to a thickness of 50-100 nm. $CsPbX_3$ NC based optoelectronic devices, such as solar cell, photodiode and LEDs with multilayer (higher thickness) device showed outstanding performance with reasonably good stability. The solar cell employing α-$CsPbI_3$NCs shows power conversion efficiency (PCE) of >10 % with V_{OC} = 1.23 V and the photodiode using the same material exhibit remarkable detectivity value of 1.8×10^{12} Jones together with near-zero

hysteresis. In case of $CsPbBr_3$ NC based green LED, higher current density and lower turn-on operating voltages compared to that single-layer device was found. Multilayer device gets rid of pin-holes and cracks in the NC film, improving the charge-carrier-balance factor significantly to boost the efficiency number from ~1 cd/A for single-layer to ~5.2 cd/A four-layer NC film.

Appendices: There are two appendices in the thesis. Appendix-I discuss about impedance spectroscopy measurement of PbS and PbSe NCs films. Applendix-II discuss about QD sensitized solar cells fabrication with Ag_2S, $AgInS_2$and Ag_2S-$AgInS_2$heterostructured NCs. The PCE of all the solar cell are measured and compared.

Thesis Summary and Future Outlook: In this section we have summarized the major findings of the thesis work, and discussed about possible future directions.

Contents

List of Abbreviations

QDs - quantum dots

NCs – nanocrystals

CB – conduction band

CBM – conduction band minimum

VBM - valance band maximum

VB – valance band

EQE - external quantum efficiency

PLQY - photoluminescence quantum yield

TCSPC - time correlated single photon counting

QDSSC - quantum dot sensitized solar cell

NIR - near infrared

SILAR - successive ionic layer adsorption and reaction

FWHM - full width at half maximum

MPA - 3-mercaptopropionic acid

SAED – selected area electron diffraction

TEM - transmission electron microscopy

HRTEM – high resolution transmission electron microscopy

XRD - powder X-ray diffraction

FFT – fast fourier transform

TGA - thermogravimetric analysis

FTIR – fourier-transform infrared

FA – formamide

J_{sc} - short circuit current density

V_{oc} - open circuit voltage

FF - fill factor

PCE - power conversion efficiency

HDNCs - hetero dimer nanocrystals

ODE - 1-octadecene

OA- oleic acid

TOP-trioctylphosphine

TDPA-tetradecylphosphonic acid

TOPO-trioctylphosphine oxide

TNP- trinitrophenol

DNT-dinitrotoluene

DMF- dimethylformamide

OAm- oleylamine

RPM – rotation per minute

FTO - F-doped SnO_2

MEG - multiple exciton generation

FRET - Förster resonance energy transfer

LED - light emitting diode

Chapter 1
Introduction

1.1 Semiconductor Nanocrystals (NCs) or Quantum Dots (QDs)

Nanocrystals (NCs) are particles of dimension in the range of few nanometers and have atomic arrangement in a single or polycrystalline way. Quantum dots (QDs) are NCs of semiconductors in which charge carriers experiences quantum confinement effect.[1] As the size of the NC reaches near to the Bohr excitonic diameter (in 2 to 50 nm range) of the material, the properties (for example, light absorption and emission) of the NCs start to depend on the size of the crystals.[2] This effect is termed as quantum confinement effect or quantum-size effect. Quantum confinement effect results into increase in the bandgap value with decrease in the size of the QDs (Figure 1.1).[3-5] These QDs in this size range are neither molecule nor bulk solid. If illuminated/excited appropriately, QDs emit light of extremely pure color. This happens because the excitons (discussed later) created by the excitation are confined spatially in all three dimensions and recombine by emitting energy in form of light.

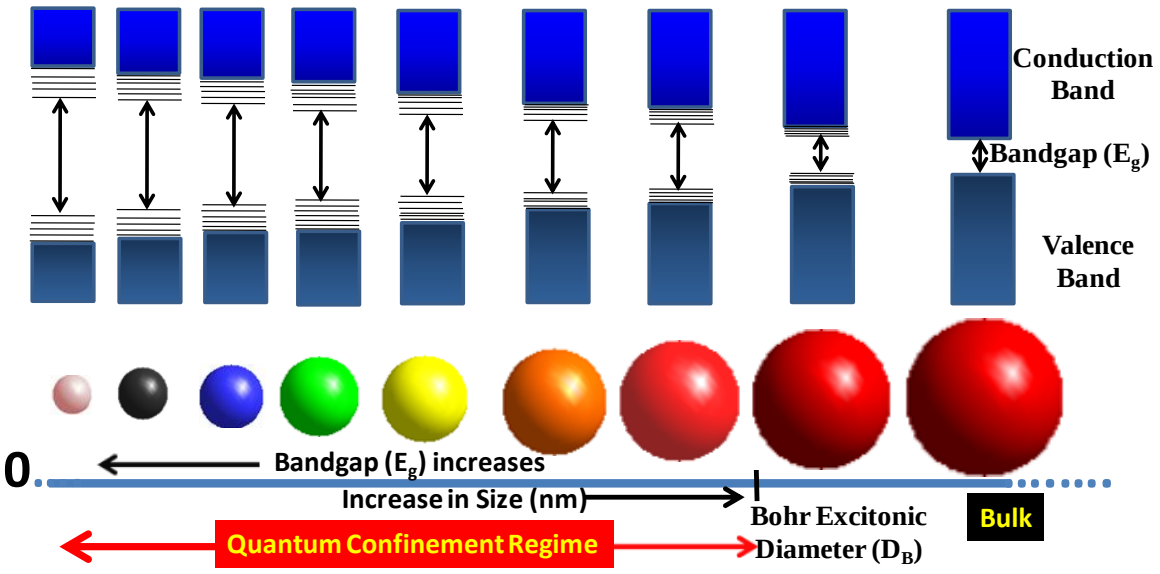

Figure 1.1 Schematic representations of the quantum confinement effect. The bandgap of the semiconductor nanocrystal increases with decreasing the size of nanocrystal below Bohr excitonic diameter. Also, discrete energy levels arise at the band-edges.

Briefly, in a semiconductor, the bandgap is the required amount of energy to create an electron and a hole in the material with zero kinetic energy and the distance between the created electron and hole should be enough so that the Coulombic attraction between them

would be negligible. These electron and hole may form exciton (bound electron-hole pair) and can reduce the optical bandgap energy by few a meV. An exciton could be treated similar to hydrogen atom where hole could be considered similar to proton. The distance between the electron and hole in the exciton is termed as exciton Bohr radius. For example, it is 2.2 nm for ZnO, 3.1 nm for CdS, 4.2 nm for Si and 6.1 nm for CdSe.[6] It could be very large for some semiconductors, such as, 20.4 nm for PbS, 46 nm for PbSe, and 67.5 nm for InSb.[6]

Although many intrinsic properties changes from bulk to QDs, for example, band dispersion, dielectric constant , a rough estimation of the optical bandgap with the size of the QDs can be obtained by following Brus and Kayanuma formula (equation1.1) which is based on effective mass approximation (particle-in-a-box) model.

$$E_{(QD)} = E_{(bulk)} + \frac{h^2}{8R^2}\left(\frac{1}{m_e^*} + \frac{1}{m_h^*}\right) - \frac{1.786e^2}{4\pi\varepsilon_o\varepsilon_r R} - 0.248\left(E * R_y\right) \qquad \text{(eq. 1.1)}$$

where h- Plank`s constant

R- Radius of the QD

m_e^*- Effective mass of excited electron

m_h^* - Effective mass of excited hole

ε_o- Permittivity of vacuum

ε_r- Relative permittivity

$E * R_y$- Rydberg energy

Often, the band gap of a QD is governed by the first two terms in the right side of equation 1.1. First, the bulk bndgap of the material and second, the extent of quantum confinement achieved by reducing the size of the QD. The third term in the equation represents the exciton binding energy in the QDs and often shows a value of a few meV range. The last term in the equation 1.1 corresponds to spatial correlation effect which is significant only in the case of low dielectric constant materials.

Apart from increase in the bandgap energy on decreasing the size of the QDs (Figure 1.1), there is an increase in absorptivity coefficient as a consequence of increase in transition probability and appearance of atomic-like discrete energy levels in the electronic band structure (as shown in Figure 1.1). Owing to the presence of discrete energy levels, these QDs are sometimes called as artificial atoms.[1] However, the properties exhibited by the QDs are in

midway of those exhibited by the bulk semiconductor material and those of the atom or molecule. Another interesting property of the QDs is the increase of the photoluminescence (PL) lifetime (for radiative recombination of electron and hole) with increasing the size of QDs. This means that the bound excitons stay in excited state for longer time in larger sized QDs in compared to smaller sized QDs before they recombine radiatively. This is because the confinement faced by the exciton in larger sized QDs is lesser than that in smaller sized QDs.

Owing to the exhibition of attractive properties such as color tunability by varying the size, high extiction coefficient, broad absorption spectrum and narrow emission line width (high color purity), scalable and solution processibilty, semiconductor QDs find their application in light emitting diodes (LEDs) for full-color displays, lasers; and in solar cells for harvesting light of broad spectrum. Furthermore, high surface-to-volume ratio of these semiconductor nanomaterials makes them suitable to be used in photocatalytic applications.

1.2 Applications of Semiconductor NCs or QDs

These QDs became popular in last three decades owing to their both fundamental properties and applications which includes energy related ones, like solar cells, LEDs, photodetector and photocatalysis.[7-8] Since semiconductor NC allows the fine tuning of electronic energy levels and other optical properties by varying the size and composition, its use in optoelectronics remains a moving area of research.

1.2.1 Light Emitting Diodes (LEDs)

As mentioned above the bandgap energy increases on decreasing the size of the semiconductor NCs or QDs, which mean more energy is required to electronically excite the smaller sized QD than that of larger one. Consequently, the emission energy due to the recombination of the electron and hole (schematic shown in Figure 1.2) can also be tuned by varying the size as shown in Figure 1.3. Owing to this property, QDs are being used in LEDs with wide color gamut.[9] Also, the color purity due to the narrow emission line width of these semiconductor NCs is an attractive property which allow the material to be used in light emission application. Furthermore, it has been found that semiconductor NCs are significantly more stable than molecular fluorescent materials.[10] Solution-processable nature of these semiconductor NCs is also making them an ideal candidate to be used in low cost printable displays.

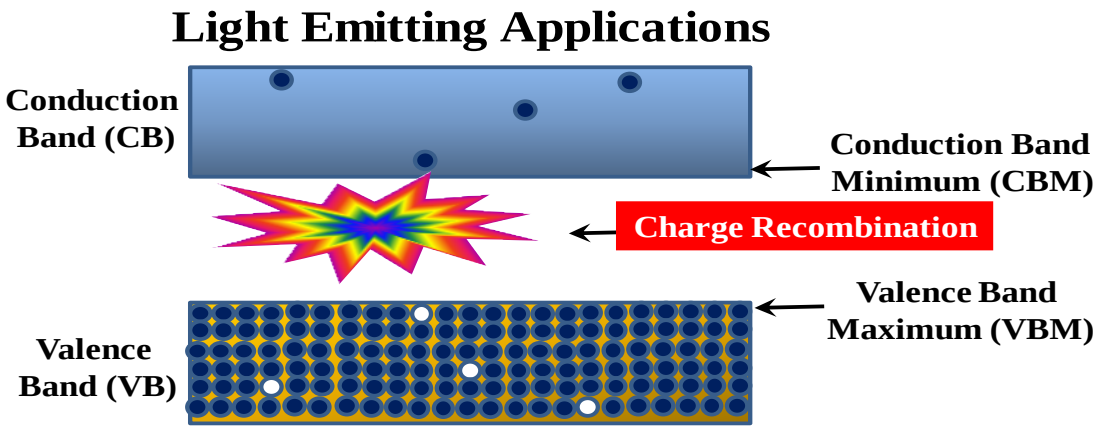

Figure 1.2: Light emission. Schematic representation of radiative charge recombination (relaxation) process (electron from conduction band and hole in valence band) in a semiconductor for light emitting application.

Figure 1.3: Color tunability. Photograph of UV-light excited colloidal solution of CdSe QDs with different sizes. PL color changes from red to blue as QD size is reduced from 6 to 2 nm. Reprinted with permission from Ref.11. Copyright 2011, Royal Society of Chemistry.

Small molecule or polymer based organic LEDs show outstanding performance and have found their use in real life applications, while the performance of the semiconductor NCs-based LEDs is lagging behind due to the grain boundary related inefficient charge transport and the deep lying defects states (discussed in later section) which traps the charge carriers. But NCs LEDs has potential to outperform the organic LED in many ways, such as i) semiconductor NCs has better emission color purity (narrow line width) in compared to those from organic luminescent materials;[10] ii) in the infrared emission range, these NCs exhibit better efficiency over organic materials, as the excitons at this low bandgap energy prefer to follow the nonradiative decay channel;[12] iii) in organic molecules the triplet state-recombination causes significant loss of efficiency which is not the case with semiconductor

NCs, as in these NCs they have a low-lying triplet state due to the high level of spin-orbit coupling. [13]

In these days QD displays, such as Samsung's QLED and Sony's Triluminos LCD displays, use a thin layer of QDs which get excited by back lying blue exciting source.[14-16] Hence green and red part comes from the charge recombination of photoexcited QDs.

1.2.2 Solar Cells

Owing to the simplicity of the synthetic procedure, broad and tunable absorption spectra, large extinction coefficient and multiple exciton generation (MEG),[17] semiconductor NCs are employed in light harvesting applications. Solar cell is one of such application, in which photons from sunlight cause exciton to form and then potential get generated after the free electron and free hole separation into the respective electrodes (schematic shown in Figure 1.4). Also, the smaller size of the NCs allow them to be used in flexible solar panel. The interest on QD solar cells started in 2001 when Professor Nozik assumed that marginal phenomena such as MEG and hot carrier collection could significantly improve the solar cell performances.[18-19] On this basis, using these QDs, the theoretical power conversion efficiency (PCE) of a solar cell can reach up to 42% which is higher in comparison to the 31% PCE of traditional single-junction semiconductor solar cells according to the Schockley-Queisser limit.[20-21] Figure 1.5 shows a detailed track of certified efficiencies of different photovoltaic technologies, in which QD solar cell research shows an exponential growth rate and the solar cell efficiency from QD solar cell crossed 10%.[22-23]

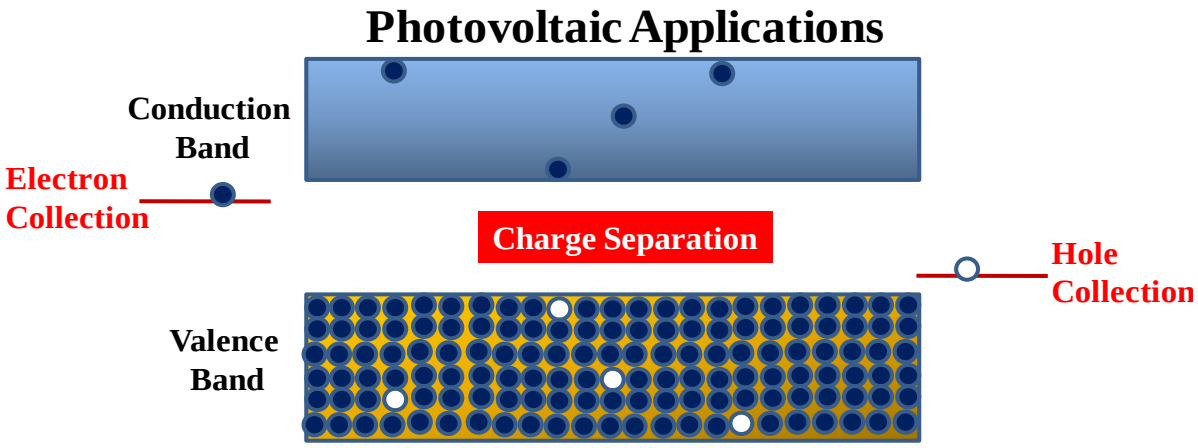

Figure 1.4: Light harvesting. Schematic representation of charge separation process (electron collection from conduction band and hole collection from valence band) in a semiconductor for photovoltaic application.

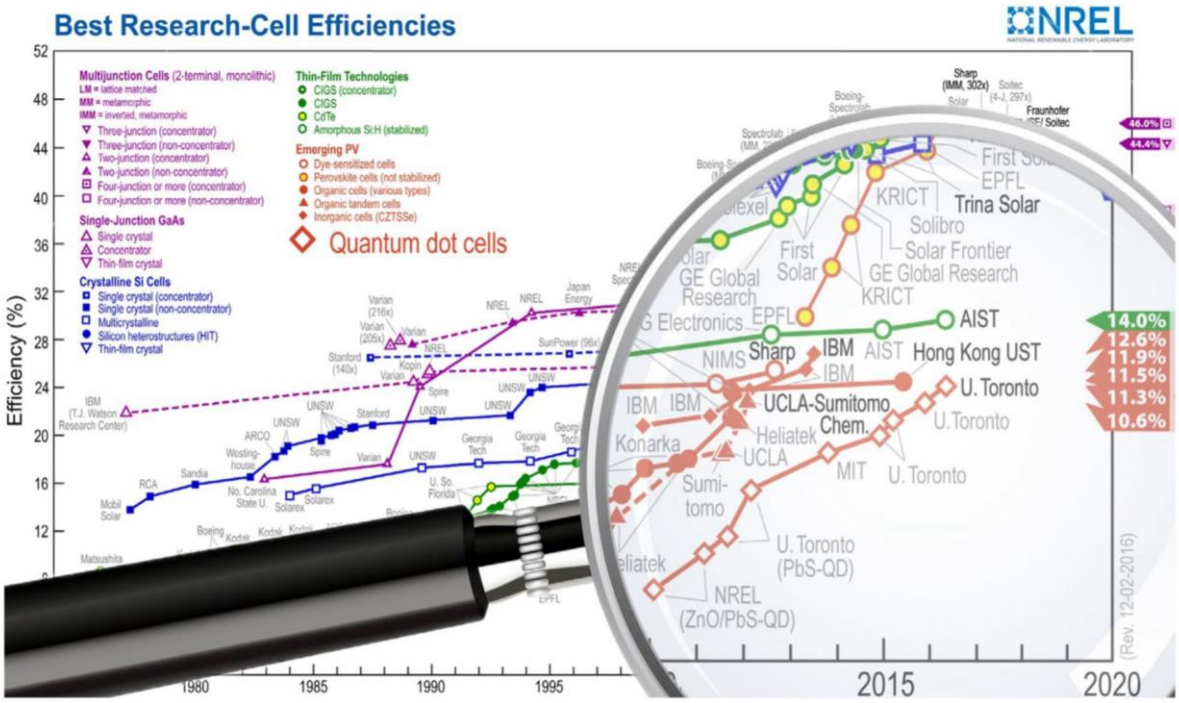

Figure 1.5: **Solar cell efficiency growth.** Best research-cell efficiencies of employing different materials, adapted with permission by the national renewable energy laboratory (NREL).[22] Reprinted with permission from ref. 22.

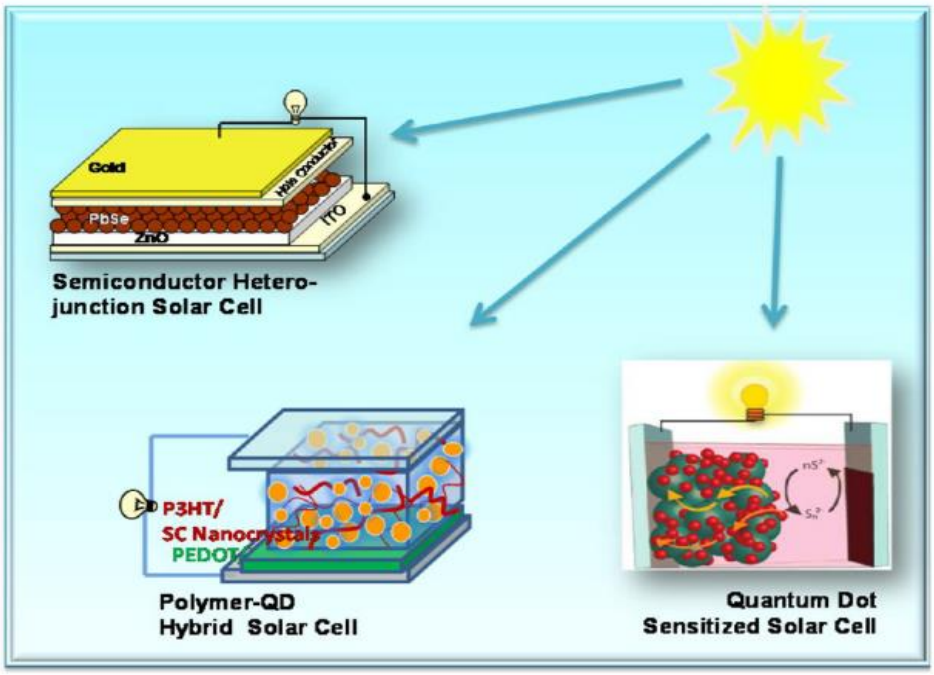

Figure 1.6. **Nanocrystal solar cells.** Schematic showing three types of semiconductor-nanocrystal-based solar cells. Reprinted with permission from ref. 24. Copyright 2012, American Chemical Society.

1.2.3 Photodetectors

As in a solar cell a power output (current along with voltage) is required from the solar light illumination, there are devices in which only current output is sufficient to detect certain frequency of light. The parameter for the efficiency of these is amount of photocurrent per unit power of incident light (Ampere/Watt). This efficiency parameter can be directly linked to the quantum efficiency i.e. collected charge carriers per incident photon. To improve the efficiency of these photodetector devices, these can be operated under a certain bias. Another important parameter is the dark current, which should be low since it dominates the noise.

Presence of trap states in PbS NCs results into photodetectors to show quantum efficiencies in excess of 100% which is called photoconductive gain and indicating that the device operation is not simply based on swiping out photogenerated electron and holes.[25] In contrast, photon absorption causes many charge carriers to be injected and transported through the device. The trap states present in the sample, in which trapping time scale is longer than the transit time scale of the charge carriers. This allows many charge carriers to pass through the device before the occurrence of charge trapping. Optimization of the performance of the NCs based photodetectors can be done by controlling the surface states and densities of trap states.[26-27] Due to the involvement of trapping states the photodetectors device can show lower response speed.

Apart from the above optoelectronic applications of the semiconductor NC, there are many other applications where these semiconductor NCs are very promising. For example, the high surface to volume ratio, along with smaller size of the semiconductor NCs plays a big role in catalysis. High PL QY of these NCs make them a challenging candidate to be used as biological tool, such as bioimaging.[28] Lasing is also another application in which semiconductor NCs are being researched heavily.[29] However, these applications are out of interest of this thesis and not discussed in details.

1.3 Synthesizing Colloidal Semiconductor NCs

Method of synthesizing colloidal nanoparticles is very old. Michael Faraday in 1857 synthesized the first colloids of gold nanoparticles. Synthesizing semiconductor NCs of good quality with less defect density is a challenging task for the research community, so that the NCs can be employed in diverse applications, including solar cells, LEDs, photodetectors, catalysis.[30] There are different methods exist to synthesize these NCs, such as electron beam lithography, molecular beam epitaxy, vapour-liquid-solid, successive ionic layer adsorption

and reaction, and the synthesis of colloidal QDs through nucleation processes. The former three are highly sophisticated ways of physical syntheses which need highly controlled atmosphere, high vacuum and also high voltage. This hinders the widespread use of these NCs. The colloidal methods which are chemical syntheses methods and solution processable in nature are relatively cost-effective, but have to be optimized significantly for better quality production of NCs. As mentioned, solution processable route of synthesizing NCs are cost effective and can be gram-scale.[31]

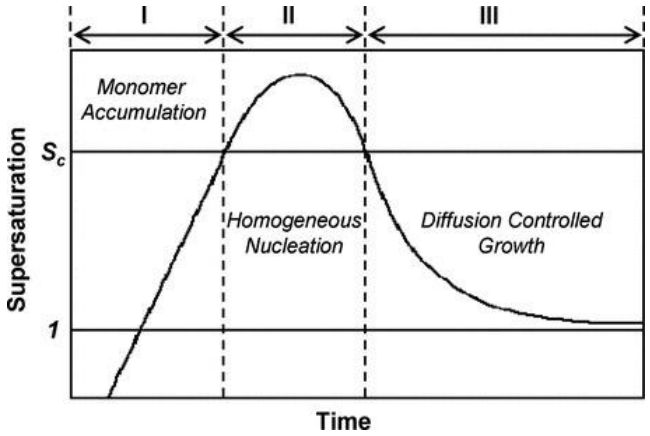

Figure 1.7: The LaMer diagram. S_c is the critical supersaturation, the minimum supersaturation level for the homogeneous nucleation. Reprinted with permission from ref.32. Copyright 2011 Wiley-VCH Verlag GmbH & Co.

Hot injection route is the most popular way to synthesize good quality semiconductor NCs. Murray et al. have first time demonstrated the synthesis of cadmium chalcogenide QDs by following hot injection route.[1] Typically, in a synthesis of semiconductor NCs, metal complexes such as, alkyl metals act as metal precusrors which are dissolved in high boiling solvents like 1-octadecene (ODE) and trioctyl phosphene oxide (TOPO). At high temperature the anion precursor such as, S, Se and/or Te dissolved in trioctyl phosphene (TOP) is injected swiftly to the reaction mixture of metal precursors. Based on La-Mer model, this event of swift injection increases the concentration of precursor to a critical value above which the nucleation and then the growth of the NCs are favored energetically (Figure 1.7).[32-33] The formed nucleus opens the NC growth and all the NCs keep growing without forming new nucleus in a condition where the feeding rate of precursor is much lower than the rate of their consumption by the pre-existing NCs. In the beginning, the distribution of NC size largely depends on the time over which the nuclei are formed and open up the growth process. Further, to reduce the total free energy of the system small-sized NCs with higher value of

surface to volume ratio re-dissolve to cause continuous growth of the larger-sized NCs. This process is called Ostwald ripening which results into further narrowing of the NC size distribution.[34] Further improvement of the resulting size distribution of as-synthesized NCs can be achieved through size selective precipitations,[1] in which slowly adding a nonsolvent to the colloidal NC dispersion causes selective precipitation of large sized NC. This happens because there is decrease in solubility of molecules or particles with increase in size. This process of size selective precipitation can be done repeatedly for several times to narrow down the size distribution of NCs to several percent of the average size.[1]

1.4 Surface Defects in Traditional (II-VI) Semiconductor NCs

Owing to the high surface to volume ratio in case of NCs, large density of surface defects trap the charge carriers (schematics shown in Figure 1.8 and 1.9) which results into decrease in their performance in term of optical, electronic and optoelectronic properties.[35] These surface related defects are inherent part of the NC. However, removal of these defect states from the bandgap region could be possible. For example, in case of CdSe/ZnS (type-I core/shell) NCs, ZnS shell removes the defect states from the bandgap region of CdSe core (as shown in Figure 1.10) resulting into achievement of near ideal photoluminescence (PL) quantum yield (QY) from the core material.[36-37] But these shells hinder the injection/extraction of charge carriers into/from the core material of the NCs and hamper their use in electronic and optoelectronic applications. By using various organic and inorganic molecular species, manipulation of defect related energy levels has also been demonstrated.[35]

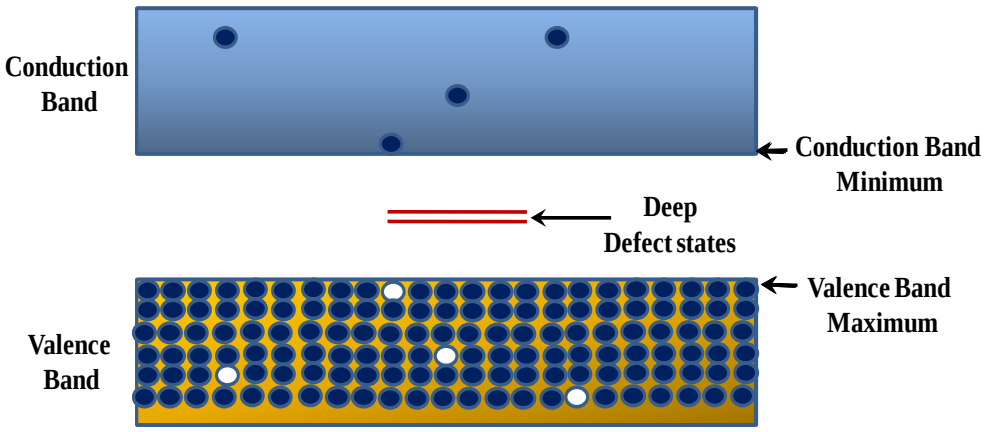

Figure 1.8: Defects acting as trap states. Schematic representation of defect states (red line) lying deep within the bandgap region of a semiconductor which trap the charge carriers (electron from conduction band and hole in valence band).

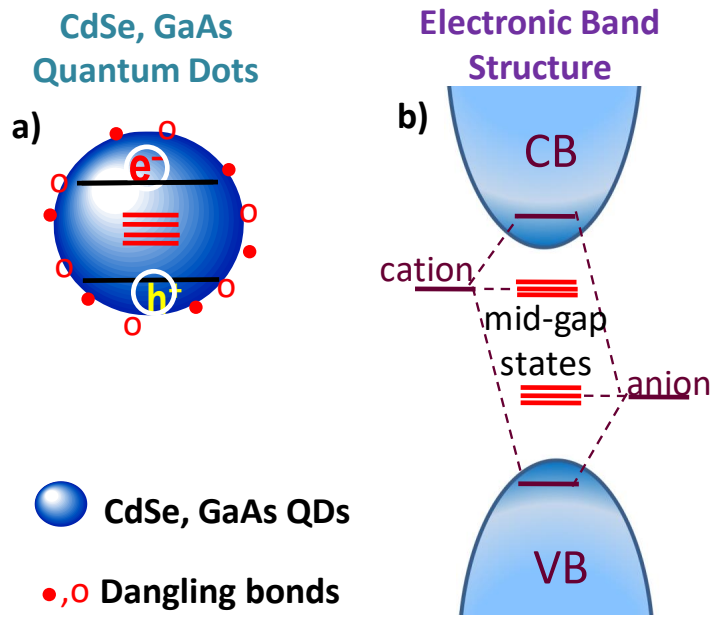

Figure 1.9: Defect intolerance in conventional semiconductors nanocrystals. a) Schematics of semiconductor nanocrystals showing surface dangling bonds and b) schematics showing electronic structures which are defect-intolerant, such as for conventional semiconductors (for example, CdSe, GaAs, and InP). [Adaped from ref. [38]]

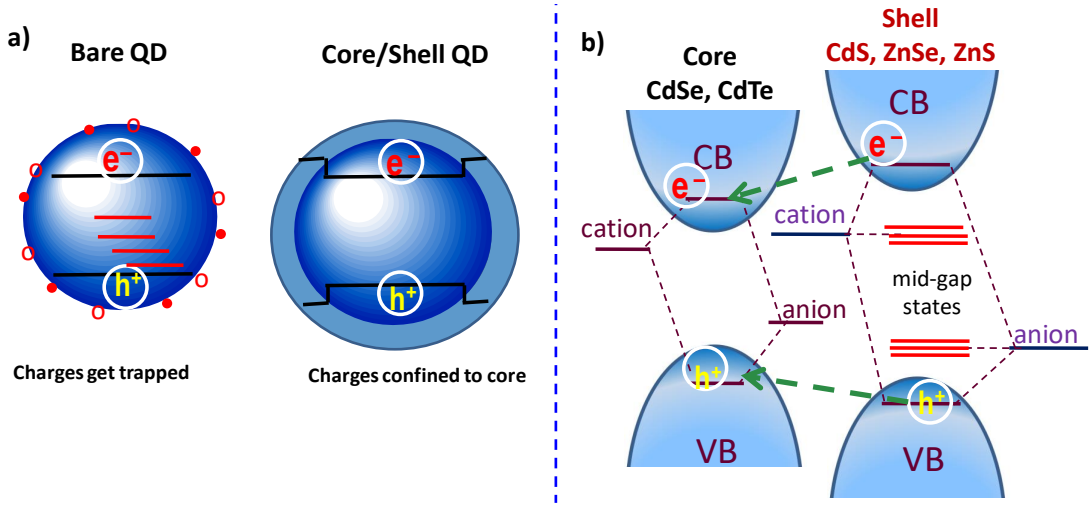

Figure 1.10: Surface passivation of a bare QD to remove the defect states from mid gap region. a) Schematic representation of surface defect passivation of semiconductor nanocrystal (bare) by growing a shell of higher bandgap (type-I core/shell band alignment). b) schematics of electronic band structure of type-I core/shell nanocrystal in which the defect states of the core particle has been passivated significantly and the defects on the surface of the shell material do not trap the charge carriers (charge carriers from the shell get confined to the core (green dashed line) due to type-I band alignment) .

1.5 Surface Ligand Chemistry of Colloidal NCs

The set of ligands attached to the surface of a NC forms a 'capping' layer. These ligands passivates the dangling bonds on the NC surface, shields the NCs from its surroundings, maintain the colloidal stability of the NC and controls nucleation and growth kinetics during NCs synthesis.[1] These ligands also help to solubilize the reaction precursors required for the synthesis of NCs. Apart from these all, surface ligands also control the optical, electrical, magnetic and catalytic properties of NCs.

As discussed above, in a semiconductor NC or QD, the valence band and the conduction band are split into discrete, quantum-confined states which results into size-tunable luminescence colors. However, under-coordinated or sub-coordinated atoms, on the surface of NCs, with dangling bonds usually contribute a set of electronic states (defect states) with energy levels lying deep within the highest occupied and lowest unoccupied quantum-confined orbitals of the NCs (Figure 1.11, red lines). These localized deep lying electronic states trap the charge carriers (electrons or holes) and consequently quenches the luminescence and hampers the performance of NC-based devices.

Bonding (hybridization) between the ligand frontier orbital and dangling bond of NC surface atom creates a new set of molecular orbitals with bonding (σ) and antibonding (σ*) character. Bonding orbitals and antibonding orbitals are formed by stabilization and destabilization, respectively, with respect to the energy level of sub-coordinated surface atom and ligands (Figure 1.11). On doing that the energy states of σ and σ*orbitals move outside the bandgap and the trap states get cleaned away which were acting as a centre for fast non-radiative recombination in absence of ligands.

Preservation of the luminescence efficiency of NCs needs removal of deep trap states (lying in the mid-gap region). However, the relationship between the surface dangling bond passivation and NC electronic structure is not yet understood clearly. For example, despite a CdSe surface atom density of ~6 nm^{-2}, a tremendous drop in CdSe luminescence occurs at modest oleate coverage of ~3 nm^{-2}.[39-40] As such, establishing the relationship between NC surface structure (which includes surface atom dangling bond and ligands) and optical properties remains a crucial open question in the field of colloidal nanomaterial research.

1.5.1 Nature of Ligand Binding to Surface of NCs

Since last five years and so, it has been reported in literature that the binding of ligands to the surface of NCs can be nicely explained by the covalent bond classification (CBC) which is

developed by Green[41-42] to categorize ligand-metal binding interactions and their complexes. In this classification, depending on the number of electrons contribution from the ligand molecule, ligands are classified. L-, X-, and Z-type ligands contribute 2, 1 and 0 electron(s) respectively. Generally, L-type ligands are neutral in charge and have two electrons with a lone electron pair which datively coordinates with metal atoms on NC surface. Examples of L-type ligands are amines (RNH_2), phosphines (R_3P) and phosphine oxides (R_3PO).

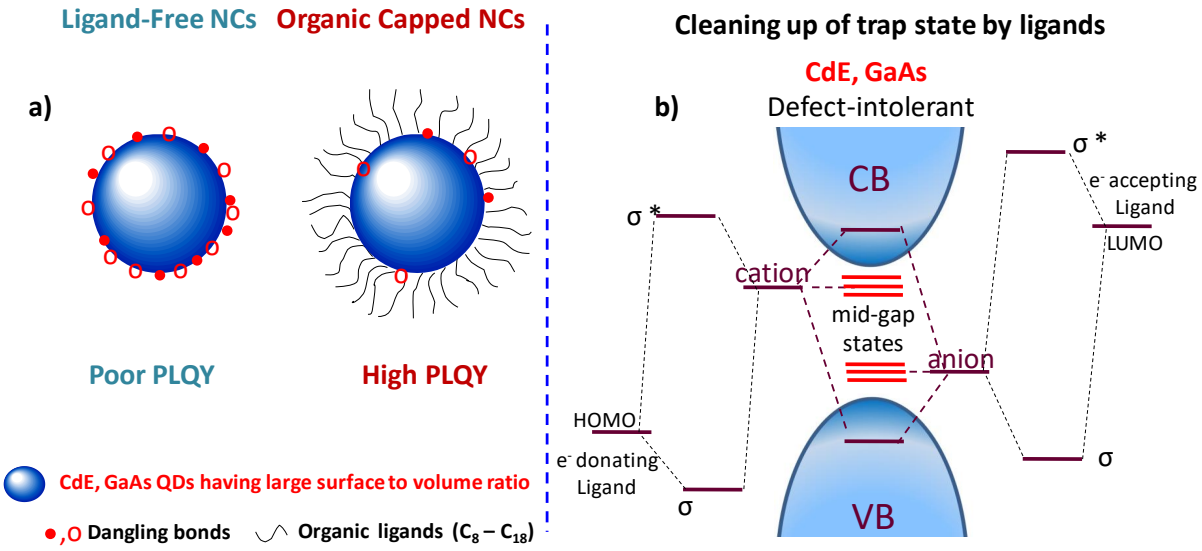

Figure 1.11: Effect of ligands on nanocrystal surface defects. a) Schematics show the adding ligand to the surface of nanocrystals causes decrease in defects states, as a result the PL efficiency increases as the charge carriers do not get trapped in deep lying defect states. b) simplified molecular orbital diagram of a CdE (E= S, Se, Te)/GaAs nanocrystals showing that the energy levels of Cd or Ga and E or As surface electronic states (red levels) are pushed outside the bandgap upon ligand binding.[40] Here, HOMO is highest occupied molecular orbital and LUMO is lowest unoccupied molecular orbital. [Adapted from ref. [40]]

X-type ligands are also neutral in nature but have an odd number of valence-shell electrons. It requires one extra electron to complete a two-electron covalent bond which could be found from the NC surface dangling bonds. Practically, the cleavage of M–X bonds is heterolytic in nature, which form ionic, closed shell fragments. Following its nature, X-type ligands can be neutral radicals (monovalent ions) and bind with the neutral surface sites of NC (each with an odd electron). Carboxylates ($RCOO^-$), thiolates (RS^-) and phosphonates ($RPO(OH)O^-$) along with inorganic ions (Cl^-, $InCl_4^-$, AsS_3^{3-}) and bound ion pairs ($NEt_4^+ I^-$) in nonpolar solvent

are the examples of X-type ligands. Briefly it can be said that the electron-rich (Nucleophilic) L- and X-type ligands bind typically to electron-deficient under-coordinated metal ions at the surface of NC with pronounced Lewis acidity. Cation rich metal chalcogenide NCs, such as PbS, PbSe, CdSe and CdTe NC are found to be capped with X-type ligands, for example $RCOO^-$ or $RPO(OH)O^-$ which bind to excess surface cations (act as lewis acid) with a binding motif of $NC(MX_n)$. In this case of ligand binding to the NC surface, charge neutrality and stoichiometry are maintained (Figure 1.12).[43]

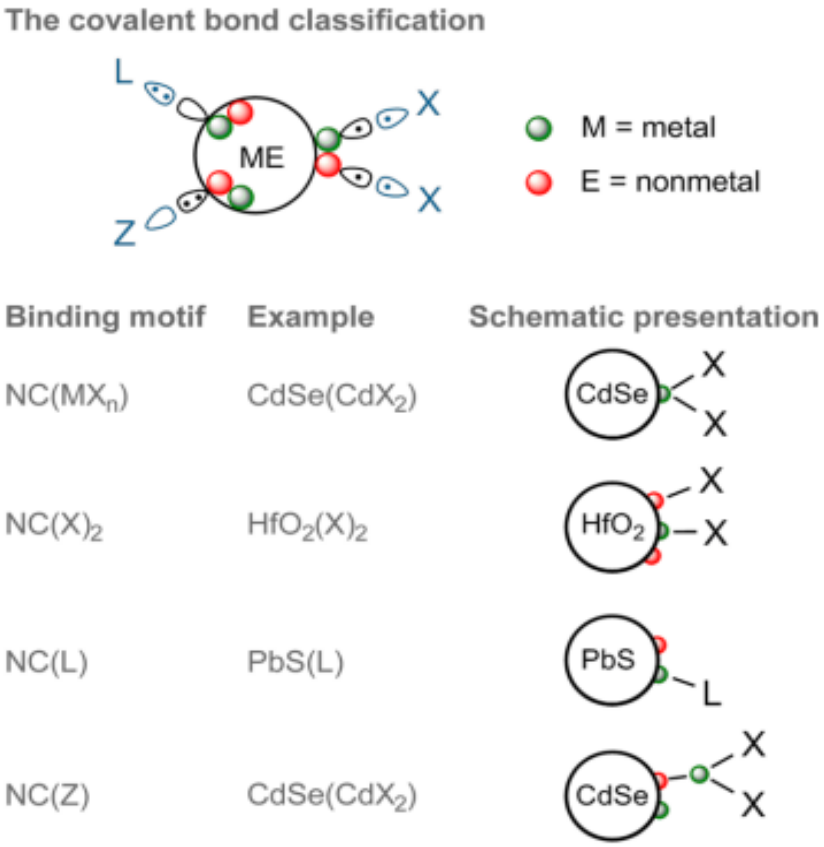

Figure 1.12: Schematic representation of different ligand catagories within the covalent bond classification scheme. L-type ligands donate 2 electrons to the NC−Ligand bond acting as Lewis base. Z-type ligands offer an empty orbital acting as lewis acid while X-type ligands donate 1 electron. The as shown schematic representations show the observable chemical reactivity of the ligand shell with the NC surface.[40] Reprinted with permission from ref.44. Copyright 2016 American Chemical Society.

In case of metal oxide NCs, for example, HfO_2, ZrO_2, an excessively involved binding motif was revealed. In some cases, electrin-rich (lewis acidic) NC surface can also be found, such as in metal oxide, chalcogenides and other compound NCs, that can interact with Z-type ligands ($CdCl_2$ or $Pb(OOCR)_2$). These Z-type ligands bind through the metal atom as lewis acid (two-electron acceptors). Additionally, oxide NCs surface can bind H^+ (electrophilic X-type positively charged ligands). Dissociated RCOOH in form of $RCOO^-$ and H^+ (2 different X-type ligands) passivate the surface of these stoichiometric NCs in a binding motif of $NC(X)_2$.[45-46] Z-type ligands and L-type ligands are Lewis acids and are Lewis bases respectively which in case of binary NCs (such as CdSe, PbS NCs) bind to anion-rich basic and cation-rich acidic surface sites, respectively. This kind of binding motifs can be abbreviated as NC(L) and NC(Z) (Figure 1.12). It should be noted that in ligand exchange reactions in case of $CdSe(CdX_2)$, involvement of either only the X-type ligand exchange or the displacement of the entire MX_2 moiety might occur, hence $CdSe(CdX_2)$ can be treated as both NC(Z) or $NC(MX_2)$.

1.6 Defect Tolerance in Semiconductors and Electronic Structure of Cesium Lead Halide Perovskite

Synthesizing a NC with defect-free (or low defect density) nature is probably not an available option. Alternatively, researchers mostly focus on controlling the energy levels of these surface defect states, in an attempt to achieve defect-tolerant system. The meaning of defect-tolerance is that the intrinsic defects do not trap the charge carriers,[47] owing to the unique electronic band structures of the material.[48] In general, electrons at conduction band minimum (CBM) and holes at valence band maximum (VBM) are responsible for optoelectronic processes in a semiconductor (as shown in Figure 1.2 and 1.4). If energy levels of defect states are close to VBM or CBM, instead of lying within the bandgap, then a defect tolerant system can be achieved.

Lead halide perovskites have been investigated as a new class of defect-tolerant system.[49-52] Intrinsic electronic band structure of lead halide perovskite mainly imparts the defect-tolerance nature,[53] in which the VBM is formed by anti-bonding (σ*) hybridization between 6s orbitals of lead and np orbitals of halogen (Figure 1.13). This nature of VBM is in stark contrast to that of II–VI metal-chalcogenides (CdS, CdSe, CdTe) in which the VBM is of bonding (σ) nature (Figure 1.9). Furthermore, the CBM in lead halide perovskite get lower

down in due to the strong spin–orbit-interaction. This causes the defect-related dangling bonds to be ineffective in generating a deep lying trap center for charge carriers.

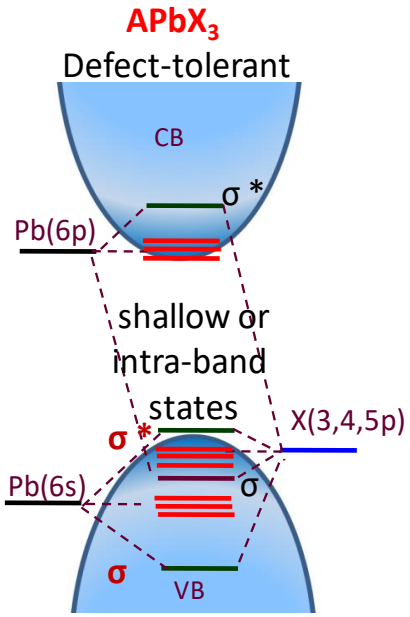

Figure 1.13: Defect tolerance in lead halide perovskite nanocrystals. Schematics showing electronic band structures that are defect-tolerant, such as for lead halide perovskites.[38]

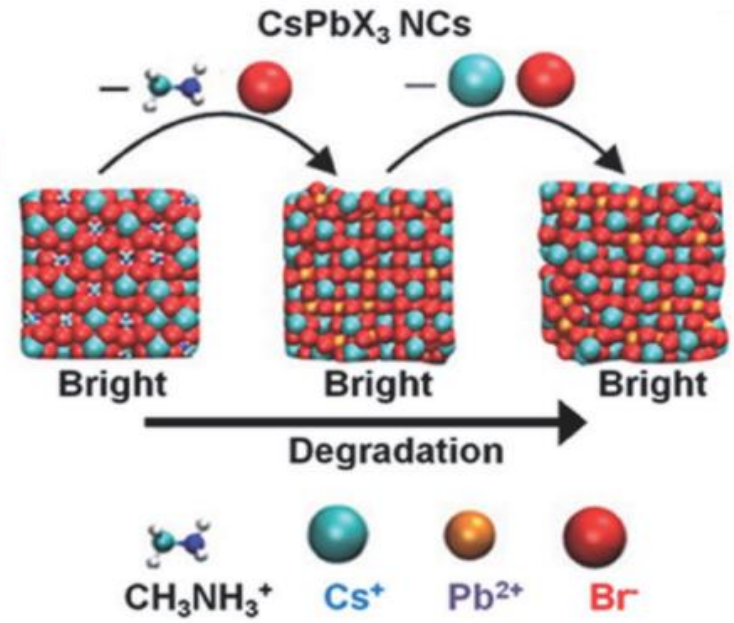

Figure 1.14: Surface defect-tolerance in $CsPbX_3$ nanocrystals. Illustration that $CsPbX_3$ nanocrystals maintaining high emission efficiency with removal of surface atoms and ligands. Reprinted with permission from ref.52. Copyright 2016 American Chemical Society.

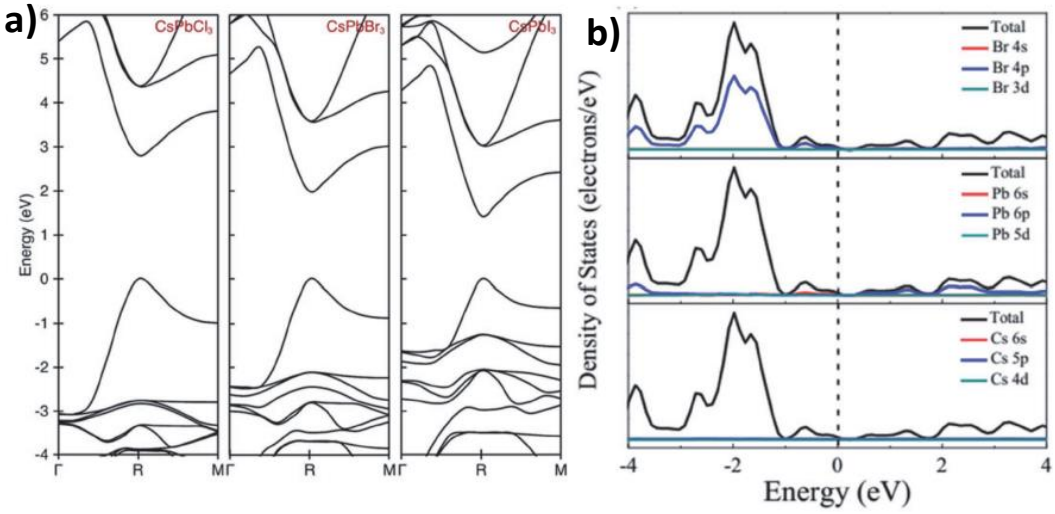

Figure 1.15: Electronic structure of $CsPbX_3$. a) Calculated electronic band structures for cubic-phase $CsPbCl_3$, $CsPbBr_3$, $CsPbI_3$, respectively. Reprinted with permission from ref.49. Copyright 2015 American Chemical Society. b) Density of states of the cubic $CsPbBr_3$ with elemental contributions to the energy band. Reprinted with permission from ref.54. Copyright 2016 Wiley-VCH Verlag GmbH & Co.

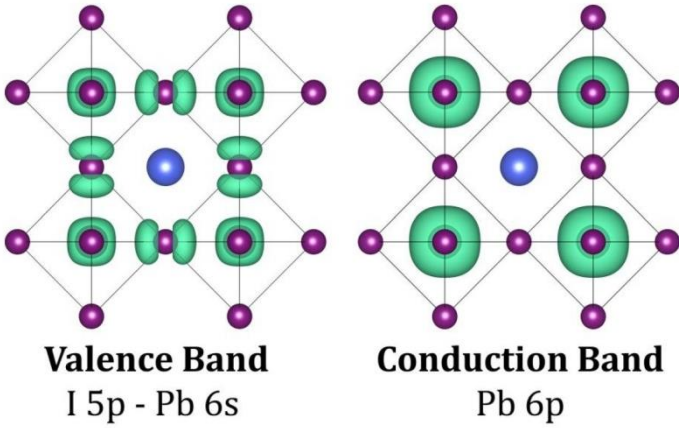

Figure 1.16: Calculated electron density associated with valence band maximum and conduction band minimum of cubic phase (α) $CsPbI_3$. Note that both the hole and electron states are associated with the PbI_3 framework formed by the $[PbI_6]^{4-}$ octahedra which support the transport of charge carrier in three dimensions framework. Similar kinds of electron distributions are found for the $CsPbBr_3$ and $CsPbCl_3$ systems. The bandgap variation is observed for different halide compositions are primarily driven by the valence orbitals of the halide ions, in which the atomic orbitals decrease in binding energy from Cl (3p) to Br (4p) to I (5p), while the Pb 6p orbitals forming conduction band remain relatively unperturbed. Reprinted with permission from ref. 49. Copyright 2015, American Chemical Society.

By doing first principles calculations, where the formation energies and charge-transition levels of intrinsic point-defects in $CsPbBr_3$ were calculated, it has been reported that most of the intrinsic defects only induce shallow transition levels.[48] This indicates that $CsPbBr_3$ virtually shows intact electronic quality, despite of having defects. Further, by DFT calculations the effect of the surface organic ligands on $CsPbBr_3$ NCs was evaluated,[52] and it has been revealed that the surface ligands do not induce additional trap states. Also, the surface dangling bonds due to removal of ligands do not quench the luminescence of $CsPbBr_3$ NCs, as shown in Figure 1.14

Calculated electronic band structures of cubic perovskite phase of $CsPbCl_3$, $CsPbBr_3$, and $CsPbI_3$ are shown in Figure 1.15, that is based on density functional theory (DFT), in which relativistic corrections and spin–orbit coupling have been considered.[55] $CsPbX_3$ with different halide compositions in perovskite structure are found to exhibit qualitatively similar electronic structure.[56-58] Figure 1.15 shows that the valence band maximum constitutes the admixture of halogen (np) orbitals (where n = 3, 4 and 5 for Cl, Br and I respectively) and Pb(6s) orbitals, whereas the conduction band is consisting admixed 6p of Pb and np of halide orbitals with major contributions from the 6p orbitals of Pb; as shown in Figure 1.16.[59-60] All compositions of $CsPbX_3$ perovskites exhibit a direct nature of bandgap and suggesting that these materials have potential to be used as light harvesters.[55, 59-61] Furthermore, the effective masses of both the electron and hole are small and similar to each other.[49] These values can be predicted from the dispersion (curvature) of electronic band near the band edges. These small values of effective masses contribute to the high carrier mobilities[49, 57] As the value of effective carrier masses change with change in symmetry of the crystals, transformation of cubic phase to tetragonal and orthorhombic perovskite crystal polymorphs leads to increase in the effective carrier masses along with increase in the bandgap.[49, 55, 62-64]

1.7 Cesium Lead Halide ($CsPbX_3$) Perovskite NCs

1.7.1 Crystal Structure

As reported in the first experimental work of Protesescu et al.[49] Pb^{2+} and X^- ions form $[PbX_6]^{4-}$ octahedral in $CsPbX_3$ NCs. These $[PbX_6]^{4-}$ octahedra are corner-shared at the X^- ion at the vertices (Figure 1.17) forming the perovskite phase. Cs^+ ions are 12-fold coordinated.

It is well known that the crystal and electronic structures significantly influence the optical properties of semiconductors.[49 62] Crystal structure of $CsPbX_3$ was first investigated in1958 by Möller.[65] It was reported that $CsPbX_3$ generally shows three types of crystal

structures; namely, cubic, tetragonal and orthorhombic phases, in which cubic phase is the most symmetric and orthorhombic phase is the least symmetric one.[65-68] The crystal phase transitions occur on varying the temperature and pressure, and the process is reversible in nature.[66, 69-70] Typically, the high symmetric cubic phase of $CsPbX_3$ crystals are stable at higher temperatures and atmospheric pressure. On cooling down, $[PbX_6]^{4-}$ octahedra tilt or rotate and the crystal structure transforms from the cubic to the lower symmetric tetragonal and to the least symmetric orthorhombic phase gradually and adopts the distorted perovskite structure. Table 1.1 list the typical phase-transition temperatures for different crystal structures.[63, 65-66, 71]

Table 1.1: Phase transition temperature at atmospheric pressure of different compositions of $CsPbX_3$ perovskite in bulk form. [65]

Material	Cubic Phase (°C)	Tetragonal Phase (°C)	Orthorhombic Phase (°C)
$CsPbI_3$	> 305		
$CsPbBr_3$	> 130	100-130	< 100
$CsPbCl_3$	> 47	42-47	< 42

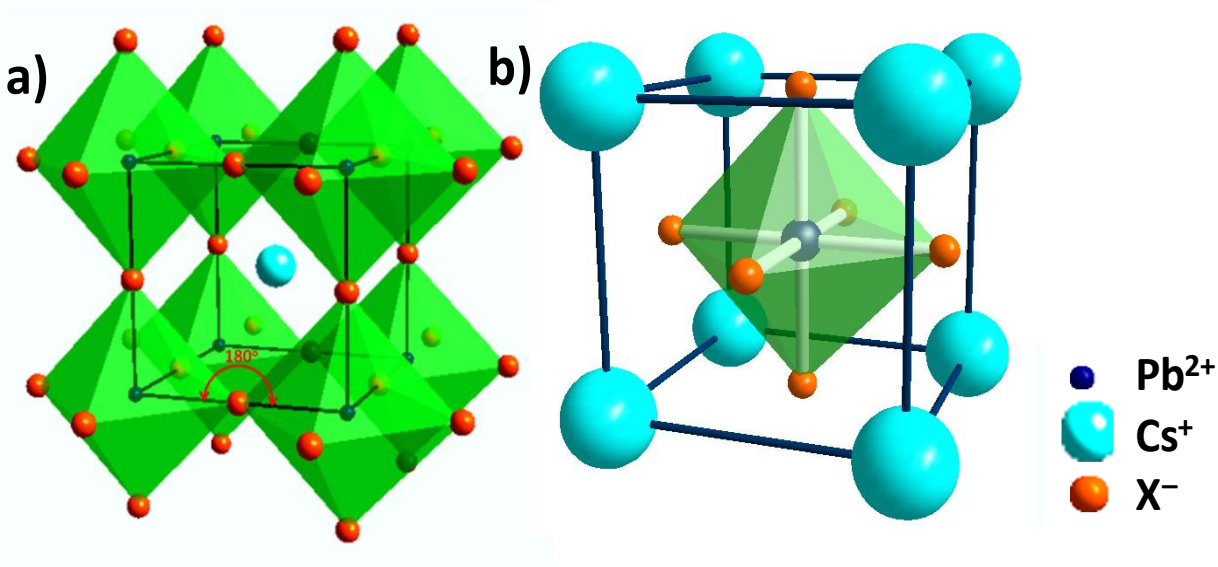

Figure 1.17: Schematic of typical cubic perovskite crystal structure. a) corner-shared $[PbX_6]^{4-}$ octahedra; and b) one representative way of forming the unit cell.

Surprisingly, Protesescu et al. reported that all compositions of $CsPbX_3$ NCs synthesized by hot injection method exhibit a stable cubic phase with the space group of Pm-3m (No. 221) at room temperature with cubic morphology, which is ascribed to the high reaction temperature and the contribution from the surface energy of the NCs (Figure 1.18).[49] In case of $CsPbI_3$ NCs, cubic crystal phase remain stable with bright luminescence after the synthesis but they convert to the non-luminescent orthorhombic phase upon extended storage (for weeks to months).[49, 55]

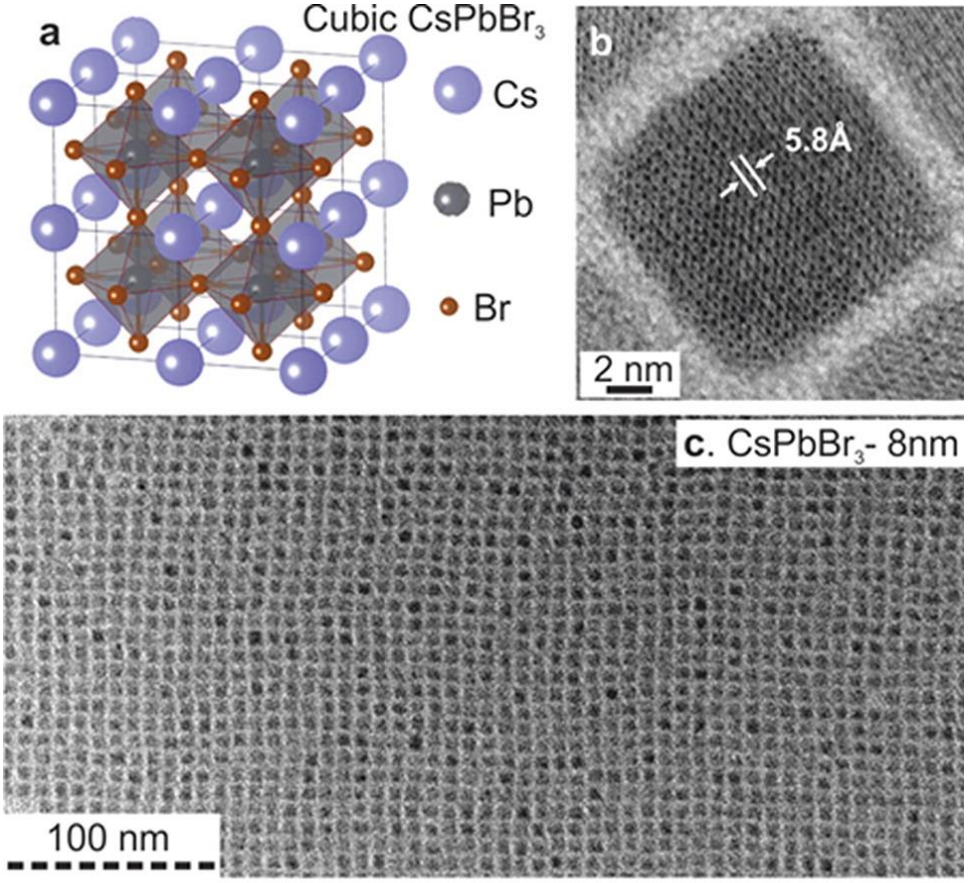

Figure 1.18 Monodisperse $CsPbX_3$ nanocrystals and their structural characterization. a) Schematic showing cubic perovskite lattice; b), high resolution transmission electron microscopy (TEM) c) TEM images showing size distribution of $CsPbBr_3$ nanocrystals. Reprinted with permission from ref. 49. Copyright 2015, American Chemical Society.

1.7.2 Thermal Stability of All-Inorganic $CsPbX_3$ Perovskite and Small Size of Cs^+

The most explored compounds in ABX_3 category are organic-inorganic hybrid perovskites such as $MAPbI_3$ and $FAPbI_3$ ($MA = CH_3NH_3^+$, $FA = [CH(NH_2)_2]^+$) forming solar cells with high (>22%) power conversion efficiency.[72] However, such hybrid systems suffer from poor

thermal stability owing to the volatile organic A-site cation.[73] A feasible solution of this problem can be substitution of organic cation with inorganic Cs^+ ion reducing the volatility of A-site cation. Figure 1.19 shows thermogravimetric data to compare the thermal stability of $MAPbBr_3$, $CsPbBr_3$ and different precursors involved.[74] But this substitution leads to a new problem, where the cubic phase of $CsPbI_3$, required for solar cell and other optoelectronic properties are not stable at room temperature.[75-76] Therefore, lots of optimizations have been reported where organic-inorganic mixed A-site cations improve the thermal stability to cubic phase of $APbI_3$ to an extent, but a compressive solution to this problem has not been achieved yet.[77-78] In an another approach, phase stable cubic $APbI_3$ was improved by partially replacing the I^- with smaller sized Br^- forming $CsPb(Br+I)_3$.[79] However, Br^- incorporation increases the bandgap which is detrimental for solar cell.[80] Making NCs reported to stabilize cubic phase of $CsPbI_3$.[49, 76, 81]

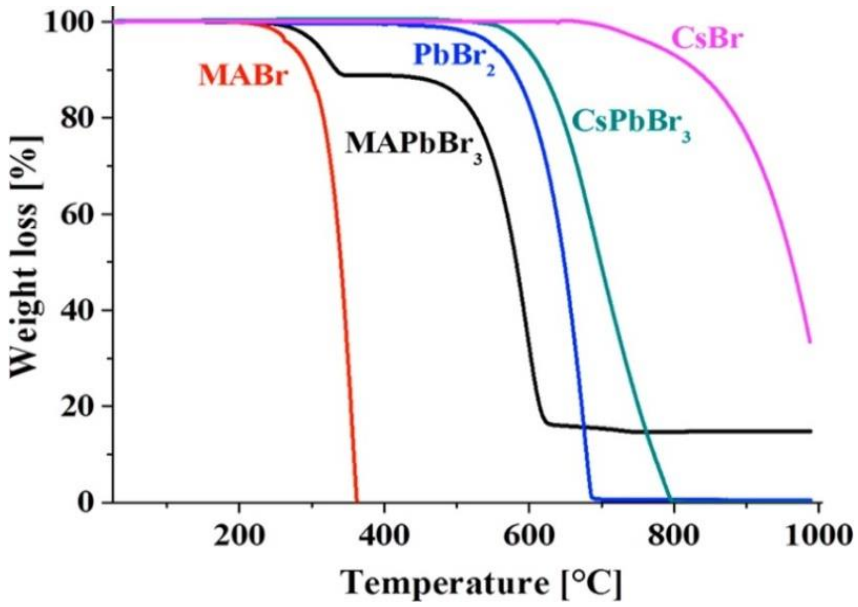

Figure 1.19: Thermal Stability. Thermogravimetric analyses (TGA) of methylammonium bromide (MABr), methylammonium lead bromide ($MAPbBr_3$), lead bromide ($PbBr_2$), cesium lead bromide ($CsPbBr_3$) and cesium bromide (CsBr), showing the higher thermal stability of the inorganic perovskite compared to the hybrid organic–inorganic perovskite. Reprinted with permission from ref.74. Copyright 2016, American Chemical Society.

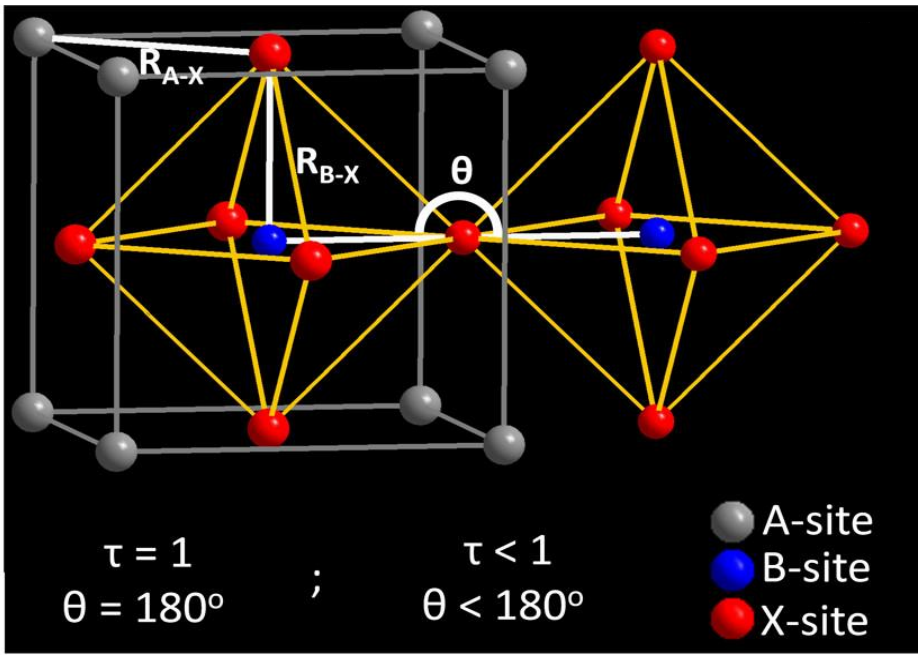

Figure 1.20: Structure stability. Relation of the tolerance factor (τ) with a B−X−B bond angle (θ) of the ABX_3 perovskite structure. Reprinted with permission from ref. 82. Copyright 2018, American Chemical Society.

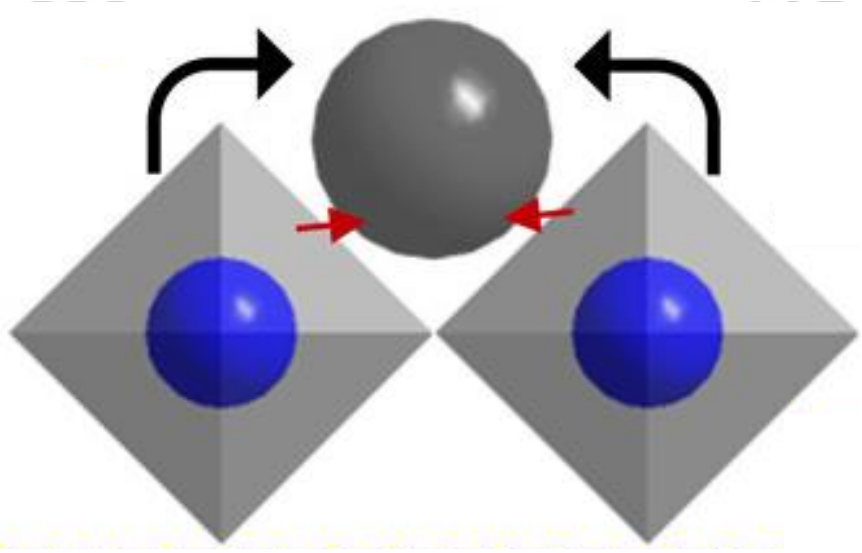

Figure 1.21: Octahedral distortion. Rotational distortion of $[BX_6]^{4-}$ ($[PbX_6]^{4-}$) octahedral in perovskite system. Reprinted with permission from ref. 82. Copyright 2018, American Chemical Society.

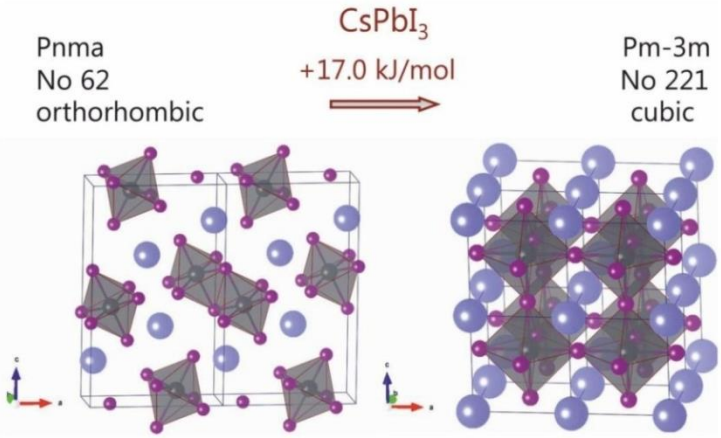

Figure 1.22: The orthorhombic (δ) and cubic (α) structures of $CsPbI_3$. The perfect corner-sharing octahedra of [PbI_6] in the cubic (α) structure becomes distorted (distortion index of 0.0176 in bond lengths) and edge-sharing in the orthorhombic (δ) structure. Representing colors: Cs (violet); Pb (grey), I (purple). Reprinted with permission from ref. 49. Copyright 2015, American Chemical Society.

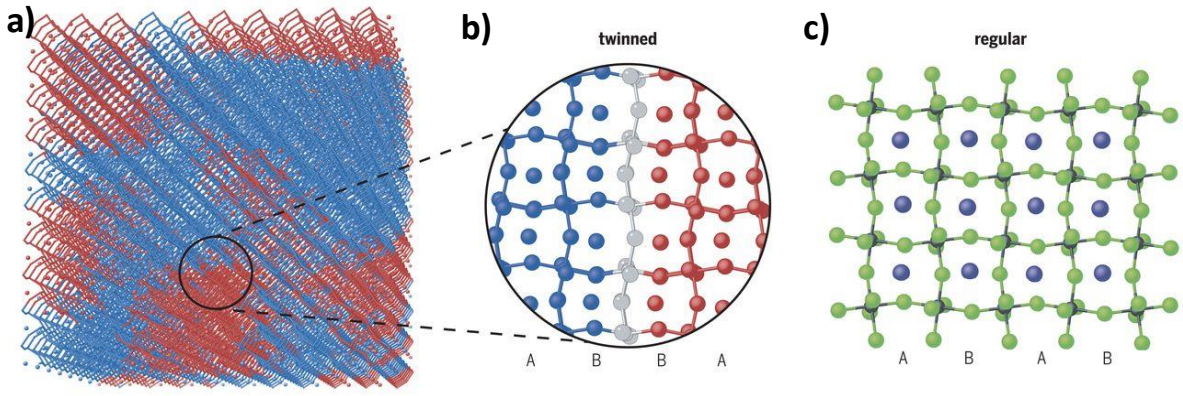

Figure 1.23: Dynamic structural disorder in LHP NCs. a) Atomistic representation of a single $CsPbBr_3$ nanocrystal with polydomain structure. b) A single twin boundary connecting domains, highlighting the discontinuity of the halide sublattice and the coherence of the Pb sublattice. c) The regular (undistorted) orthorhombic structure of a lead halide perovskite nanocrystal. The density and crystallographic and mutual orientation of these planar defects determine the observed diffraction pattern; this can cause an inherently orthorhombic lattice to appear cubic in a powder XRD experiment.[83] Reprinted with permission from ref. 83. It is to be noted that the first report on orthorhombic phase of $CsPbBr_3$ NCs was published by our group in November 2015, and the data are discussed in 3rd chapter of this thesis. For the completeness of the introduction, this figure has been added.

One major structural aspect is that the substitution at the A-site for smaller sized Cs^+ ion influences the Goldschmidt's tolerance factor, $t = \frac{R_{A-X}}{\sqrt{2}\,R_{B-X}}$, where, R_{A-X} = bond length between A-site cation and X-site anion and R_{B-X} = bond length between B-site cation and X-site anion (Figure 1.20).[84] For cubic perovskites structure, the value of t lies between 0.89 and 1.[84-85] If the value of t is larger than 1, i.e. 1.1 or more, face-sharing of $[PbX_6]^{4-}$ octahedral is preferred instead of corner-sharing octahedral. $BaNiO_3$ is one of the examples (t = 1.13).[86] On the other hand, if the value of t is smaller than 0.85, rotation/tilting of the $[PbX_6]^{-4}$ octahedra occur (schematic shown in Figure 1.21). This leads to a structure with lower symmetry, for example tetragonal (β phase) or orthorhombic (γ and δ phases) structures.[87] Bulk $CsPbI_3$ with t value of 0.81 show the orthorhombic (δ-phase) structure at room temperature in which the $[PbI_6]^{4-}$ octahedra are not corner-shared (Figure 1.22),[82] while orthorhombic $CsPbBr_3$ with larger value of t (0.824) exhibits corner-shared tilted $[PbBr_6]^{4-}$ octahedra at room temperature (Figure 1.23).[88-89]

1.7.3 Optical Properties of $CsPbX_3$ NC and its Tunability

It is surprising in a first sound that the as-synthesized bare $CsPbX_3$ perovskite NCs exhibit bright emission with a PLQY of near unity. This makes these NCs highly promising material in light-emitting applications. For traditional metal-chalcogenide NCs, such as CdSe QDs, as-synthesized NCs without any intentional surface modification typically show a PLQY of less than 20%.[1] Such advantageous optical properties of $CsPbX_3$ NCs over traditional QDs attracted the attention of material scientists around the world. So far, there are many reasonable and informative mechanisms have been reported to justify the high PLQY values of the as-prepared $CsPbX_3$ NCs.[47, 49, 52, 59] Among these all reports, defect-tolerant nature causes the material to perform exceptionally in term of optical properties.

Similar to the organic–inorganic hybrid perovskites, all-inorganic $CsPbX_3$ NCs also exhibit the property of composition-tunable bandgap and emission color.[49] By varying the halide compositions in $CsPbX_3$ (X = Cl, Br, and I), the emission color can be fine-tuned across the visible range (400 to 700 nm) while maintaining a high PL efficiency above 50% (shown in Figure 1.24).[49] As discussed above, the $CsPbX_3$ NCs show high PL color purity (narrow PL linewidth), varying from 12 nm (~75 meV) for $CsPbCl_3$ NCs to 42 nm (~ 108 meV) for $CsPbI_3$ NCs and hence a good candidate for high-quality light emitting application, and displays. Interestingly, the compositional tuning of $CsPbX_3$ NCs can be easily done

either by simply mixing required ratio of colloidal solutions of $CsPbCl_3$, $CsPbBr_3$, and $CsPbI_3$ NCs or by adding different halide sources, due to the fast anion-exchange reaction. [90-91]

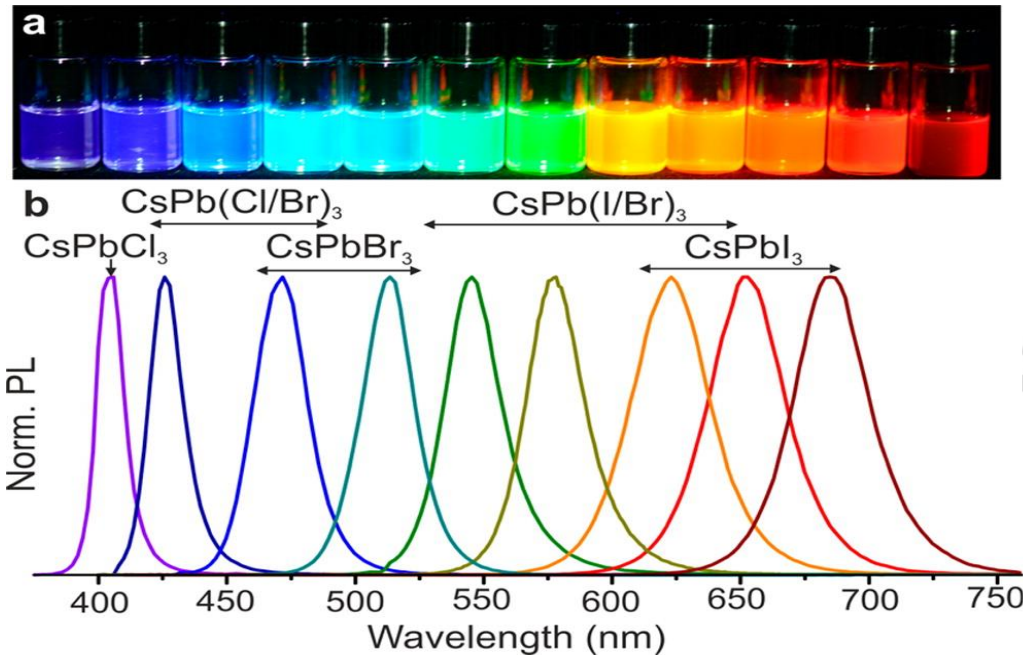

Figure 1.24: Optical properties. (a) Colloidal perovskite $CsPbX_3$ nanocrystals (X = Cl, Br, I) dispersed in toluene under UV (λ = 365 nm) excitation and; (b) representative PL spectra (λ_{exc}= 400 nm for all but 350 nm for $CsPbCl_3$ samples). Reprinted with permission from ref.49. Copyright 2015, American Chemical Society.

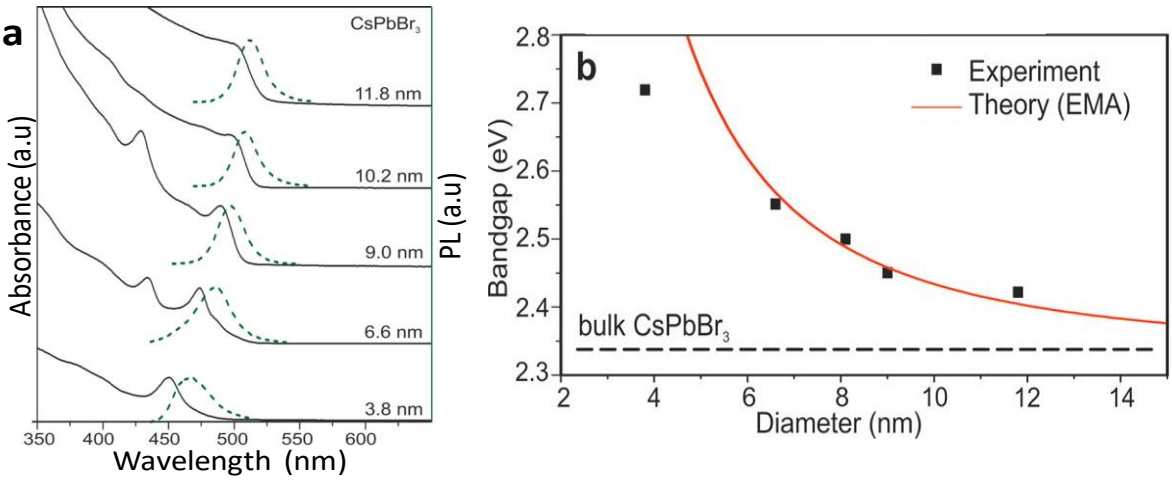

Figure 1.25: a) Quantum-size effects in the absorption and PL spectra of 5–12 nm $CsPbBr_3$ NCs. b) Experimental versus theoretical (effective mass approximation, EMA) size dependence of the band gap energy. Reprinted with permission from ref. [49]. Copyright 2015, American Chemical Society.

As the trademark of colloidal QDs, the bandgap energy is strongly dependent on size on the NCs due to the quantum-confinement effect. The absorption and emission spectra of $CsPbBr_3$ NCs also vary with different sizes of NCs from 3.8 to 11.8 nm (shown in Figure 1.25). It has been reported that both the absorption and the emission blue-shift on decreasing the size of the NC and can be explained on the basis of the effective mass approximation.[49]

1.7.4 Synthesis of $CsPbX_3$ NCs

As mentioned in previous sections, Möller in 1950s reported the bulk metal halide perovskites when he first time investigated the photoconductivity in the $CsPbX_3$ crystals.[65] Solution processed synthetic protocol of colloidal NCs of all inorganic halide three dimensional corner-shared perovskite ABX_3 (where A= methyl ammonium, formamidinium or Cs; B= Pb or Sn and X= Cl, Br, I or Cl/Br, Br/I in different compositions) are being reported since last four years.[49, 92-98] Among all of them $CsPbX_3$ NCs exhibit enhanced thermal stability (~500 ^oC) and excellent optical properties for optoelectronic applications.[49] In the year of 2015, Protesescu et al. reported an easy synthesis process for high-quality colloidal $CsPbX_3$ NCs (X = Cl, Br, and I) by following hot-injection method (schematic shown in Figure 1.26).[49] After this breakthrough, research on $CsPbX_3$ NCs exploded in a variety of directions. Schematic illustration in Figure 1.26 shows the hot-injection approach for synthesizing $CsPbX_3$ NCs. In a typical synthesis, lead halide (PbX_2) is dissolved in ODE by using oleylamine and oleic acid ligands. Then, the NCs are subsequently formed at high temperature (140-200 ^oC) by injecting the cesium oleate as cesium precursor (synthesized earlier) into the hot solvent. The chemical reaction can be written as following equation

$$2\ Cs(oleate) + 3\ PbX_2 \xrightarrow{140-200\ ^\circ C} 2\ CsPbX_3 + Pb(oleate)_2 \qquad \text{(eq. 1.2)}$$

It has been found that in combination with reaction time and precursor concentrations, reaction temperatures can be tuned to obtain various sizes and shapes of NCs. The insets of Figure 1.26 show a photograph of the as-synthesized colloidal solution of $CsPbBr_3$ NCs and the corresponding transmission electron microscopy (TEM) image of the NCs. These images indicate the ultra high brightness of the NCs even under room light and nearly monodisperse NCs of cubic morphology. Immediately after the report of the hot-injection synthesis of

$CsPbX_3$ NCs, many other synthetic methods were proposed, which are not discussed in this thesis.

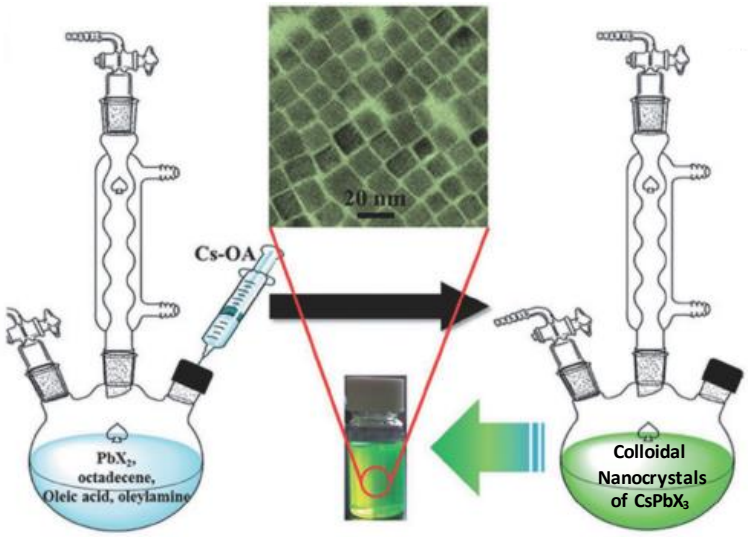

Figure 1.26: Schematic illustration of the hot-injection method for synthesizing $CsPbX_3$ nanocrystals. The inset shows colloidal solution of $CsPbBr_3$ -nanocrystal and a corresponding transmission electron microscopy (TEM) image of the nanocrystals. Reprinted with permission from ref.59. Copyright 2016 WILEY-VCH Verlag GmbH & Co.

1.8 Scope of the PhD Work

Bulk and thin films of Pb-halide perovskite have been shown to be defect-tolerant exhibiting efficient optoelectronic properties. Motivated by that, Protesescu et al.[49] reported colloidal $CsPbX_3$ perovskite NCs exhibiting ~90% PL efficiencies with narrow spectral width. As discussed in the previous sections, typical colloidal NCs often exhibit surface related defect states that trap the charge carriers. Therefore, to achieve high PL efficiencies from typical CdSe QDs, surface modifications (discussed in chapter 2), preferably in the form of core/shell structure is required. Therefore, ~90% PL efficiency from $CsPbBr_3$ NCs without any core/shell structure is a path-breaking observation. Motivated by this result, we studied the optical properties of $CsPbBr_3$ NCs in details **(**Chapter 3**)**. Origin of narrow spectral width, effect of quantum confinement, and effect of defect-tolerance on PL properties are the key feature of this study. Along with optical properties, crystal structure of $CsPbBr_3$ NCs has been studied in chapter 3.

While $CsPbBr_3$ NCs show excellent green luminescence, the bandgap is too high for solar cell and LED applications in red region. On the other hand, thin films of organic-

inorganic hybrid perovskite ($CH_3NH_3PbI_3$) are reported for their high efficiency solar cells with lower bandgap. But the organic $CH_3NH_3^+$ group makes the material thermally unstable. Substituting $CH_3NH_3^+$ group with Cs^+ ion improves thermal stability of $CsPbI_3$ till ~500 °C.[74] But the desired cubic phase of bulk $CsPbI_3$ is unstable. In chapter 4, we address this problem by successfully stabilizing the cubic phase of $CsPbI_3$ NCs in the form colloidal NCs. The effect of quantum confinement and surface energy on the structure and optical properties of cubic $CsPbI_3$ NCs have been studied.

Finally after approving potentiality of these colloidal NCs to be employed as active materials in high performing optoelectronic devices, we focused on to device fabrication. Colloidal NCs are generally coated with long-chain organic ligand**s.** These ligands are mostly insulating in nature inhibiting charge transport in a NC film. Existing ligand exchange/removal strategies developed for traditional CdSe QDs involves polar solvent and/or ligand. $CsPbX_3$ NCs are ionic compounds and degrade in polar environment. Therefore, a new method of surface modification and film deposition is required for optoelectronic applications of $CsPbX_3$ NCs. Chapter 5 deals with this aspect. We developed a surface modification and layer-by-layer method of film deposition. These films were then used for fabricating high efficiency solar cell, photodetector and LED with the help of collaborators.

References:

1. Murray, C. B.; Norris, D. J.; Bawendi, M. G., Synthesis and characterization of nearly monodisperse CdE (E = sulfur, selenium, tellurium) semiconductor nanocrystallites. *J. Am. Chem. Soc.* **1993,** *115*, 8706-8715.

2. Zhang, Q.; Uchaker, E.; Candelaria, S. L.; Cao, G., Nanomaterials for energy conversion and storage. *Chem. Soc. Rev.* **2013,** *42*, 3127-3171.

3. Baskoutas, S.; Terzis, A. F., Size-dependent band gap of colloidal quantum dots. *J. App. Phys.* **2006,** *99*, 013708.

4. Segets, D.; Lucas, J. M.; Klupp Taylor, R. N.; Scheele, M.; Zheng, H.; Alivisatos, A. P.; Peukert, W., Determination of the Quantum Dot Band Gap Dependence on Particle Size from Optical Absorbance and Transmission Electron Microscopy Measurements. *ACS Nano* **2012,** *6*, 9021-9032.

5. Moreels, I.; Lambert, K.; Smeets, D.; De Muynck, D.; Nollet, T.; Martins, J. C.; Vanhaecke, F.; Vantomme, A.; Delerue, C.; Allan, G.; Hens, Z., Size-Dependent Optical Properties of Colloidal PbS Quantum Dots. *ACS Nano* **2009,** *3*, 3023-3030.

6. Tian, J.; Cao, G., Semiconductor quantum dot-sensitized solar cells. *Nano Rev.* **2013,** *4*, 22578.

7. Pietryga, J. M.; Park, Y.-S.; Lim, J.; Fidler, A. F.; Bae, W. K.; Brovelli, S.; Klimov, V. I., Spectroscopic and Device Aspects of Nanocrystal Quantum Dots. *Chem. Rev.* **2016,** *116*, 10513-10622.

8. Kagan, C. R.; Lifshitz, E.; Sargent, E. H.; Talapin, D. V., Building devices from colloidal quantum dots. *Science* **2016,** *353*, 6302.

9. Wood, V.; Bulović, V., Colloidal quantum dot light-emitting devices. *Nano Rev.* **2010,** *1*, 5202.

10. Michalet, X.; Pinaud, F. F.; Bentolila, L. A.; Tsay, J. M.; Doose, S.; Li, J. J.; Sundaresan, G.; Wu, A. M.; Gambhir, S. S.; Weiss, S., Quantum Dots for Live Cells, in Vivo Imaging, and Diagnostics. *Science* **2005,** *307*, 538-544.

11. Donegá, C. d. M., Synthesis and properties of colloidal heteronanocrystals. *Chem. Soc. Rev.* **2011,** *40*, 1512-1546.

12. Tessler, N.; Medvedev, V.; Kazes, M.; Kan, S.; Banin, U., Efficient Near-Infrared Polymer Nanocrystal Light-Emitting Diodes. *Science* **2002,** *295*, 1506-1508.

13. Rabouw, F. T.; de Mello Donega, C., Excited-State Dynamics in Colloidal Semiconductor Nanocrystals. *Tops. in Curr. Chem.* **2016,** *374*, 58.

14. Shirasaki, Y.; Supran, G. J.; Bawendi, M. G.; Bulović, V., Emergence of colloidal quantum-dot light-emitting technologies. *Nat. Photons* **2012,** *7*, 13.

15. Kim, T.-H.; Jun, S.; Cho, K.-S.; Choi, B. L.; Jang, E., Bright and stable quantum dots and their applications in full-color displays. *MRS Bull.* **2013,** *38*, 712-720.

16. Supran, G. J.; Shirasaki, Y.; Song, K. W.; Caruge, J.-M.; Kazlas, P. T.; Coe-Sullivan, S.; Andrew, T. L.; Bawendi, M. G.; Bulović, V., QLEDs for displays and solid-state lighting. *MRS Bull.* **2013,** *38*, 703-711.

17. Ellingson, R. J.; Beard, M. C.; Johnson, J. C.; Yu, P.; Micic, O. I.; Nozik, A. J.; Shabaev, A.; Efros, A. L., Highly Efficient Multiple Exciton Generation in Colloidal PbSe and PbS Quantum Dots. *Nano Lett.* **2005,** *5*, 865-871.

18. Nozik, A. J., SPECTROSCOPY AND HOT ELECTRON RELAXATION DYNAMICS IN SEMICONDUCTOR QUANTUM WELLS AND QUANTUM DOTS. *An. Rev. Phys. Chem.* **2001,** *52*, 193-231.

19. Nozik, A. J., Quantum dot solar cells. *Physica E: Low-dimen. Sys. and Nanostruct.* **2002,** *14*, 115-120.

20. Nozik, A. J., Nanoscience and Nanostructures for Photovoltaics and Solar Fuels. *Nano Lett.* **2010,** *10*, 2735-2741.

21. Kamat, P. V., Quantum Dot Solar Cells. Semiconductor Nanocrystals as Light Harvesters. *The J.Phys. Chem. C* **2008,** *112*, 18737-18753.

22. [Internet]., N. P. R., Golden (CO):NREL; 2016 [cited 2017 Jan 5].

23. Kim, G.-H.; García de Arquer, F. P.; Yoon, Y. J.; Lan, X.; Liu, M.; Voznyy, O.; Yang, Z.; Fan, F.; Ip, A. H.; Kanjanaboos, P.; Hoogland, S.; Kim, J. Y.; Sargent, E. H., High-Efficiency Colloidal Quantum Dot Photovoltaics via Robust Self-Assembled Monolayers. *Nano Lett.* **2015,** *15*, 7691-7696.

24. Kamat, P. V., Boosting the Efficiency of Quantum Dot Sensitized Solar Cells through Modulation of Interfacial Charge Transfer. *Acc.Chem. Res.* **2012,** *45*, 1906-1915.

25. Konstantatos, G.; Howard, I.; Fischer, A.; Hoogland, S.; Clifford, J.; Klem, E.; Levina, L.; Sargent, E. H., Ultrasensitive solution-cast quantum dot photodetectors. *Nature* **2006,** *442*, 180.

26. Konstantatos, G.; Levina, L.; Fischer, A.; Sargent, E. H., Engineering the Temporal Response of Photoconductive Photodetectors via Selective Introduction of Surface Trap States. *Nano Lett.* **2008,** *8*, 1446-1450.

27. PbS colloidal quantum dot photoconductive photodetectors: Transport, traps, and gain. *Appl. Phys. Lett.* **2007,** *91*, 173505.

28. Chen, O.; Zhao, J.; Chauhan, V. P.; Cui, J.; Wong, C.; Harris, D. K.; Wei, H.; Han, H.-S.; Fukumura, D.; Jain, R. K.; Bawendi, M. G., Compact high-quality CdSe–CdS core–shell nanocrystals with narrow emission linewidths and suppressed blinking. *Nat. Mater.* **2013,** *12*, 445.

29. Sutherland, B. R.; Sargent, E. H., Perovskite photonic sources. *Nat. Photon.* **2016,** *10*, 295.

30. Gawande, M. B.; Goswami, A.; Asefa, T.; Guo, H.; Biradar, A. V.; Peng, D.-L.; Zboril, R.; Varma, R. S., Core-shell nanoparticles: synthesis and applications in catalysis and electrocatalysis. *Chem. Soc. Rev.* **2015,** *44*, 7540-7590.

31. Park, J.; An, K.; Hwang, Y.; Park, J.-G.; Noh, H.-J.; Kim, J.-Y.; Park, J.-H.; Hwang, N.-M.; Hyeon, T., Ultra-large-scale syntheses of monodisperse nanocrystals. *Nat. Mater.* **2004,** *3*, 891.

32. Kwon, S. G.; Hyeon, T., Formation Mechanisms of Uniform Nanocrystals via Hot-Injection and Heat-Up Methods. *Small* **2011,** *7*, 2685-2702.

33. R., T. A.; Susan, H.; Peidong, Y., Shape Control of Colloidal Metal Nanocrystals. *Small* **2008,** *4*, 310-325.

34. Kershaw, S. V.; Susha, A. S.; Rogach, A. L., Narrow bandgap colloidal metal chalcogenide quantum dots: synthetic methods, heterostructures, assemblies, electronic and infrared optical properties. *Chem. Soc. Rev.* **2013,** *42*, 3033-3087.

35. Talapin, D. V.; Lee, J.-S.; Kovalenko, M. V.; Shevchenko, E. V., Prospects of Colloidal Nanocrystals for Electronic and Optoelectronic Applications. *Chem. Rev.* **2010,** *110*, 389-458.

36. Hines, M. A.; Guyot-Sionnest, P., Synthesis and Characterization of Strongly Luminescing ZnS-Capped CdSe Nanocrystals. *J. Phys. Chem.* **1996,** *100*, 468-471.

37. Chen, O.; Zhao, J.; Chauhan, V. P.; Cui, J.; Wong, C.; Harris, D. K.; Wei, H.; Han, H.-S.; Fukumura, D.; Jain, R. K.; Bawendi, M. G., Compact high-quality CdSe–CdS core–shell nanocrystals with narrow emission linewidths and suppressed blinking. *Nat Mater* **2013,** *12*, 445-451.

38. Brandt, R. E.; Poindexter, J. R.; Gorai, P.; Kurchin, R. C.; Hoye, R. L. Z.; Nienhaus, L.; Wilson, M. W. B.; Polizzotti, J. A.; Sereika, R.; Žaltauskas, R.; Lee, L. C.; MacManus-Driscoll, J. L.; Bawendi, M.; Stevanović, V.; Buonassisi, T., Searching for "Defect-Tolerant"

Photovoltaic Materials: Combined Theoretical and Experimental Screening. *Chem. Mater.* **2017,** *29*, 4667-4674.

39. Anderson, N. C.; Hendricks, M. P.; Choi, J. J.; Owen, J. S., Ligand Exchange and the Stoichiometry of Metal Chalcogenide Nanocrystals: Spectroscopic Observation of Facile Metal-Carboxylate Displacement and Binding. *J. Am. Chem. Soc.* **2013,** *135*, 18536-18548.

40. Boles, M. A.; Ling, D.; Hyeon, T.; Talapin, D. V., The surface science of nanocrystals. *Nat. Mater.* **2016,** *15*, 141.

41. Green, M. L. H., A new approach to the formal classification of covalent compounds of the elements. *J. Organometal. Chem.* **1995,** *500*, 127-148.

42. Green, M. L. H.; Parkin, G., Application of the Covalent Bond Classification Method for the Teaching of Inorganic Chemistry. *J. Chem. Ed.* **2014,** *91*, 807-816.

43. Fritzinger, B.; Capek, R. K.; Lambert, K.; Martins, J. C.; Hens, Z., Utilizing Self-Exchange To Address the Binding of Carboxylic Acid Ligands to CdSe Quantum Dots. *J. Am. Chem. Soc.* **2010,** *132*, 10195-10201.

44. De Roo, J.; Ibáñez, M.; Geiregat, P.; Nedelcu, G.; Walravens, W.; Maes, J.; Martins, J. C.; Van Driessche, I.; Kovalenko, M. V.; Hens, Z., Highly Dynamic Ligand Binding and Light Absorption Coefficient of Cesium Lead Bromide Perovskite Nanocrystals. *ACS Nano* **2016,** *10*, 2071-2081.

45. Jonathan, D. R.; Yolanda, J.; Katrien, D. K.; Freya, V. d. B.; C., M. J.; Isabel, V. D.; Zeger, H., Carboxylic-Acid-Passivated Metal Oxide Nanocrystals: Ligand Exchange Characteristics of a New Binding Motif. *Angew. Chem. Intern. Ed.* **2015,** *54*, 6488-6491.

46. De Roo, J.; Van den Broeck, F.; De Keukeleere, K.; Martins, J. C.; Van Driessche, I.; Hens, Z., Unravelling the Surface Chemistry of Metal Oxide Nanocrystals, the Role of Acids and Bases. *J. Am. Chem. Soc.* **2014,** *136*, 9650-9657.

47. Dirin, D. N.; Protesescu, L.; Trummer, D.; Kochetygov, I. V.; Yakunin, S.; Krumeich, F.; Stadie, N. P.; Kovalenko, M. V., Harnessing Defect-Tolerance at the Nanoscale: Highly Luminescent Lead Halide Perovskite Nanocrystals in Mesoporous Silica Matrixes. *Nano Lett.* **2016,** *16*, 5866-5874.

48. Kang, J.; Wang, L.-W., High Defect Tolerance in Lead Halide Perovskite $CsPbBr_3$. *J. Phys. Chem. Lett.* **2017,** *8*, 489-493.

49. Protesescu, L.; Yakunin, S.; Bodnarchuk, M. I.; Krieg, F.; Caputo, R.; Hendon, C. H.; Yang, R. X.; Walsh, A.; Kovalenko, M. V., Nanocrystals of Cesium Lead Halide Perovskites

($CsPbX_3$, X = Cl, Br, and I): Novel Optoelectronic Materials Showing Bright Emission with Wide Color Gamut. *Nano Lett.* **2015,** *15*, 3692-3696.

50. Swarnkar, A.; Chulliyil, R.; Ravi, V. K.; Irfanullah, M.; Chowdhury, A.; Nag, A., Colloidal $CsPbBr_3$ Perovskite Nanocrystals: Luminescence beyond Traditional Quantum Dots. *Angew. Chem. Intern. Ed.* **2015,** *54*, 15424-15428.

51. Yettapu, G. R.; Talukdar, D.; Sarkar, S.; Swarnkar, A.; Nag, A.; Ghosh, P.; Mandal, P., Terahertz Conductivity within Colloidal $CsPbBr_3$ Perovskite Nanocrystals: Remarkably High Carrier Mobilities and Large Diffusion Lengths. *Nano Lett.* **2016,** *16*, 4838-4848.

52. ten Brinck, S.; Infante, I., Surface Termination, Morphology, and Bright Photoluminescence of Cesium Lead Halide Perovskite Nanocrystals. *ACS Energy Lett.* **2016,** *1*, 1266-1272.

53. Brandt, R. E.; Stevanović, V.; Ginley, D. S.; Buonassisi, T., Identifying defect-tolerant semiconductors with high minority-carrier lifetimes: beyond hybrid lead halide perovskites. *MRS Commun.* **2015,** *5*, 265-275.

54. Li, X.; Wu, Y.; Zhang, S.; Cai, B.; Gu, Y.; Song, J.; Zeng, H., $CsPbX_3$ Quantum Dots for Lighting and Displays: Room-Temperature Synthesis, Photoluminescence Superiorities, Underlying Origins and White Light-Emitting Diodes. *Adv. Funct. Mater.* **2016,** *26*, 2435-2445.

55. Protesescu, L.; Yakunin, S.; Kumar, S.; Bär, J.; Bertolotti, F.; Masciocchi, N.; Guagliardi, A.; Grotevent, M.; Shorubalko, I.; Bodnarchuk, M. I.; Shih, C.-J.; Kovalenko, M. V., Dismantling the "Red Wall" of Colloidal Perovskites: Highly Luminescent Formamidinium and Formamidinium–Cesium Lead Iodide Nanocrystals. *ACS Nano* **2017,** *11*, 3119-3134.

56. C., S. C.; G., K. M., Halide Perovskites: Poor Man's High-Performance Semiconductors. *Adv. Mater.* **2016,** *28* , 5778-5793.

57. Jishi, R. A.; Ta, O. B.; Sharif, A. A., Modeling of Lead Halide Perovskites for Photovoltaic Applications. *J. Phys. Chem. C* **2014,** *118*, 28344-28349.

58. Sebastian, M.; Peters, J. A.; Stoumpos, C. C.; Im, J.; Kostina, S. S.; Liu, Z.; Kanatzidis, M. G.; Freeman, A. J.; Wessels, B. W., Excitonic emissions and above-band-gap luminescence in the single-crystal perovskite semiconductors $\mathrm{$CsPbBr_3$ and $CsPbCl_3$. *Phys. Rev. B* **2015,** *92*, 235210.

59. Xiaoming, L.; Ye, W.; Shengli, Z.; Bo, C.; Yu, G.; Jizhong, S.; Haibo, Z., $CsPbX_3$ Quantum Dots for Lighting and Displays: Room-Temperature Synthesis, Photoluminescence

Superiorities, Underlying Origins and White Light-Emitting Diodes. *Adv. Funct. Mater.* **2016,** *26*, 2435-2445.

60. Xiaoming, L.; Fei, C.; Dejian, Y.; Jun, C.; Zhiguo, S.; Yalong, S.; Ying, Z.; Lin, W.; Yi, W.; Ye, W.; Haibo, Z., All Inorganic Halide Perovskites Nanosystem: Synthesis, Structural Features, Optical Properties and Optoelectronic Applications. *Small* **2017,** *13*, 1603996.

61. Heidrich, K.; Schäfer, W.; Schreiber, M.; Söchtig, J.; Trendel, G.; Treusch, J.; Grandke, T.; Stolz, H. J., Electronic structure, photoemission spectra, and vacuum-ultraviolet optical spectra of $CsPbCl_3$ and $CsPbBr_3$. *Phys. Rev. B* **1981,** *24*, 5642-5649.

62. Eperon, G. E.; Paternò, G. M.; Sutton, R. J.; Zampetti, A.; Haghighirad, A. A.; Cacialli, F.; Snaith, H. J., Inorganic caesium lead iodide perovskite solar cells. *J. Mater. Chem. A* **2015,** *3*, 19688-19695.

63. Ahmad, M.; Rehman, G.; Ali, L.; Shafiq, M.; Iqbal, R.; Ahmad, R.; Khan, T.; Jalali-Asadabadi, S.; Maqbool, M.; Ahmad, I., Structural, electronic and optical properties of $CsPbX_3$ (X=Cl, Br, I) for energy storage and hybrid solar cell applications. *J. Alloys and Comp.* **2017,** *705*, 828-839.

64. Even, J., Pedestrian Guide to Symmetry Properties of the Reference Cubic Structure of 3D All-Inorganic and Hybrid Perovskites. *J. Phys. Chem. Lett.* **2015,** *6*, 2238-2242.

65. MØLler, C. K., Crystal Structure and Photoconductivity of Cæsium Plumbohalides. *Nature* **1958,** *182*, 1436.

66. Stoumpos, C. C.; Malliakas, C. D.; Peters, J. A.; Liu, Z.; Sebastian, M.; Im, J.; Chasapis, T. C.; Wibowo, A. C.; Chung, D. Y.; Freeman, A. J.; Wessels, B. W.; Kanatzidis, M. G., Crystal Growth of the Perovskite Semiconductor $CsPbBr_3$: A New Material for High-Energy Radiation Detection. *Crys. Growth & Design.* **2013,** *13*, 2722-2727.

67. Trots, D. M.; Myagkota, S. V., High-temperature structural evolution of caesium and rubidium triiodoplumbates. *J. Phys. and Chem. Sol.* **2008,** *69*, 2520-2526.

68. Stoumpos, C. C.; Malliakas, C. D.; Kanatzidis, M. G., Semiconducting Tin and Lead Iodide Perovskites with Organic Cations: Phase Transitions, High Mobilities, and Near-Infrared Photoluminescent Properties. *Inorg. Chem.* **2013,** *52*, 9019-9038.

69. Sakata, M.; Nishiwaki, T.; Harada, J., Neutron Diffraction Study of the Structure of Cubic $CsPbBr_3$. *J. Phys. Soc. Japan* **1979,** *47*, 232-233.

70. Lai, M.; Kong, Q.; Bischak, C. G.; Yu, Y.; Dou, L.; Eaton, S. W.; Ginsberg, N. S.; Yang, P., Structural, optical, and electrical properties of phase-controlled cesium lead iodide nanowires. *Nano Res.* **2017,** *10*, 1107-1114.

71. Fu, M.; Tamarat, P.; Huang, H.; Even, J.; Rogach, A. L.; Lounis, B., Neutral and Charged Exciton Fine Structure in Single Lead Halide Perovskite Nanocrystals Revealed by Magneto-optical Spectroscopy. *Nano Lett.* **2017,** *17*, 2895-2901.

72. [Internet]., N. P. R., Golden (CO):NREL; 2016 [cited 2017 Jan 5].

73. Juarez-Perez, E. J.; Hawash, Z.; Raga, S. R.; Ono, L. K.; Qi, Y., Thermal degradation of $CH_3NH_3PbI_3$ perovskite into NH_3 and CH_3I gases observed by coupled thermogravimetry-mass spectrometry analysis. *Energy & Environ. Sc.* **2016,** *9*, 3406-3410.

74. Kulbak, M.; Gupta, S.; Kedem, N.; Levine, I.; Bendikov, T.; Hodes, G.; Cahen, D., Cesium Enhances Long-Term Stability of Lead Bromide Perovskite-Based Solar Cells. *J. Phys. Chem. Lett.* **2016,** *7*, 167-172.

75. Eperon, G. E.; Paterno, G. M.; Sutton, R. J.; Zampetti, A.; Haghighirad, A. A.; Cacialli, F.; Snaith, H. J., Inorganic caesium lead iodide perovskite solar cells. *J.Mater. Chem. A* **2015,** *3*, 19688-19695.

76. Swarnkar, A.; Marshall, A. R.; Sanehira, E. M.; Chernomordik, B. D.; Moore, D. T.; Christians, J. A.; Chakrabarti, T.; Luther, J. M., Quantum dot–induced phase stabilization of α-$CsPbI_3$ perovskite for high-efficiency photovoltaics. *Science* **2016,** *354*, 92-95.

77. Zhang, Y.; Grancini, G.; Feng, Y.; Asiri, A. M.; Nazeeruddin, M. K., Optimization of Stable Quasi-Cubic $FA_xMA_{1-x}PbI_3$ Perovskite Structure for Solar Cells with Efficiency beyond 20%. *ACS Energy Lett.* **2017,** *2*, 802-806.

78. Ghosh, D.; Walsh Atkins, P.; Islam, M. S.; Walker, A. B.; Eames, C., Good Vibrations: Locking of Octahedral Tilting in Mixed-Cation Iodide Perovskites for Solar Cells. *ACS Energy Lett.* **2017,** *2*, 2424-2429.

79. Sharma, S.; Weiden, N.; Weiss, A., Phase Diagrams of Quasibinary Systems of the Type: ABX_3 — $A'BX_3$; ABX_3 — $AB'X_3$, and ABX_3 — ABX'_3; X = Halogen. In *Zeitschrift für Phys. Chem.*, **1992,** *175*, 63.

80. Akkerman, Q. A.; Gandini, M.; Di Stasio, F.; Rastogi, P.; Palazon, F.; Bertoni, G.; Ball, J. M.; Prato, M.; Petrozza, A.; Manna, L., Strongly emissive perovskite nanocrystal inks for high-voltage solar cells. *Nat. Energy* **2016,** *2*, 16194.

81. Sim, K. M.; Swarnkar, A.; Nag, A.; Chung, D. S., Phase Stabilized α-$CsPbI_3$ Perovskite Nanocrystals for Photodiode Applications. *Laser & Photonics Rev.*, 1700209.

82. Swarnkar, A.; Mir, W. J.; Nag, A., Can B-Site Doping or Alloying Improve Thermal- and Phase-Stability of All-Inorganic $CsPbX_3$ (X = Cl, Br, I) Perovskites? *ACS Energy Lett.* **2018,** *3*, 286-289.

83. Bertolotti, F.; Protesescu, L.; Kovalenko, M. V.; Yakunin, S.; Cervellino, A.; Billinge, S. J. L.; Terban, M. W.; Pedersen, J. S.; Masciocchi, N.; Guagliardi, A., Coherent Nanotwins and Dynamic Disorder in Cesium Lead Halide Perovskite Nanocrystals. *ACS Nano* **2017,** *11*, 3819-3831.

84. Hwang, H. Y.; Cheong, S. W.; Radaelli, P. G.; Marezio, M.; Batlogg, B., Lattice Effects on the Magnetoresistance in Doped $LaMnO_3$. *Phys. Rev. Lett.* **1995,** *75*, 914-917.

85. Li, C.; Lu, X.; Ding, W.; Feng, L.; Gao, Y.; Guo, Z., Formability of ABX_3 (X = F, Cl, Br, I) halide perovskites. *Acta Crystallograph. Sect. B* **2008,** *64*, 702-707.

86. Crystallography and Chemistry of Perovskites. In *Handbook of Magnetism and Advanced Magnetic Materials*.

87. Yin, W.-J.; Yang, J.-H.; Kang, J.; Yan, Y.; Wei, S.-H., Halide perovskite materials for solar cells: a theoretical review. *J.Mater. Chem. A* **2015,** *3*, 8926-8942.

88. Stoumpos, C. C.; Kanatzidis, M. G., The Renaissance of Halide Perovskites and Their Evolution as Emerging Semiconductors. *Acc. Chem. Res.* **2015,** *48*, 2791-2802.

89. Brennan, M. C.; Herr, J. E.; Nguyen-Beck, T. S.; Zinna, J.; Draguta, S.; Rouvimov, S.; Parkhill, J.; Kuno, M., Origin of the Size-Dependent Stokes Shift in $CsPbBr_3$ Perovskite Nanocrystals. *J. Am. Chem. Soc.* **2017,** *139*, 12201-12208.

90. Nedelcu, G.; Protesescu, L.; Yakunin, S.; Bodnarchuk, M. I.; Grotevent, M. J.; Kovalenko, M. V., Fast Anion-Exchange in Highly Luminescent Nanocrystals of Cesium Lead Halide Perovskites ($CsPbX_3$, X = Cl, Br, I). *Nano Lett.* **2015,** *15*, 5635-5640.

91. Akkerman, Q. A.; D'Innocenzo, V.; Accornero, S.; Scarpellini, A.; Petrozza, A.; Prato, M.; Manna, L., Tuning the Optical Properties of Cesium Lead Halide Perovskite Nanocrystals by Anion Exchange Reactions. *J. Am. Chem. Soc.* **2015,** *137*, 10276-10281.

92. Schmidt, L. C.; Pertegas, A.; Gonzalez-Carrero, S.; Malinkiewicz, O.; Agouram, S.; Espallargas, G. M.; Bolink, H. J.; Galian, R. E.; Perez-Prieto, J., Nontemplate Synthesis of $CH_3NH_3PbBr_3$ Perovskite Nanoparticles. *J. Am. Chem. Soc.* **2014,** *136*, 850-853.

93. Zhang, F.; Zhong, H. Z.; Chen, C.; Wu, X. G.; Hu, X. M.; Huang, H. L.; Han, J. B.; Zou, B. S.; Dong, Y. P., Brightly Luminescent and Color-Tunable Colloidal $CH_3NH_3PbX_3$ (X = Br, I, Cl) Quantum Dots: Potential Alternatives for Display Technology. *Acs Nano* **2015,** *9*, 4533-4542.

94. Zhang, D. D.; Eaton, S. W.; Yu, Y.; Dou, L. T.; Yang, P. D., Solution-Phase Synthesis of Cesium Lead Halide Perovskite Nanowires. *J. Am. Chem. Soc.* **2015,** *137*, 9230-9233.

95. Huang, H.; Zhao, F.; Liu, L.; Zhang, F.; Wu, X.-g.; Shi, L.; Zou, B.; Pei, Q.; Zhong, H., Emulsion Synthesis of Size-Tunable $CH_3NH_3PbBr_3$ Quantum Dots: An Alternative Route toward Efficient Light-Emitting Diodes. *ACS Appl. Mater. & Interfaces* **2015,** *7*, 28128-28133.

96. Hassan, Y.; Song, Y.; Pensack, R. D.; Abdelrahman, A. I.; Kobayashi, Y.; Winnik, M. A.; Scholes, G. D., Structure-Tuned Lead Halide Perovskite Nanocrystals. *Adv. Mater.* **2016,** *28*, 566.

97. Sun, S.; Yuan, D.; Xu, Y.; Wang, A.; Deng, Z., Ligand-Mediated Synthesis of Shape-Controlled Cesium Lead Halide Perovskite Nanocrystals via Reprecipitation Process at Room Temperature. *ACS Nano* **2016**.

98. Jellicoe, T. C.; Richter, J. M.; Glass, H. F. J.; Tabachnyk, M.; Brady, R.; Dutton, S. E.; Rao, A.; Friend, R. H.; Credgington, D.; Greenham, N. C.; Böhm, M. L., Synthesis and Optical Properties of Lead-Free Cesium Tin Halide Perovskite Nanocrystals. *J. Am. Chem. Soc.* **2016,** *138*, 2941-2944.

Chapter 2

Role of Defects on Luminescence of CdSe Based Quantum Dots and Sensor Application

---

The following article has been published based on the work presented in this chapter.

1. Swarnkar, A.; Shanker, G. S.; Nag, A. Organic-free colloidal semiconductor nanocrystals as luminescent sensors for metal ions and nitroaromatic explosives. *Chem. Commun.* **2014**, *50*, 4743-4746.

Summary

Conventional colloidal semiconductor nanocrystals, such as CdSe and InP quantum dots exhibit excellent optical and optoelectronic properties and these properties are tunable in nature. One of the interesting properties of these nanocrystals is intense photoluminescence. However, the surface defects lying deep within the bandgap can trap the charge carriers, and consequently quench the photoluminescence efficiency. Long chain organic ligands on the surface of the colloidal nanocrystals passivate the surface traps by hybridizing with the surface dangling bonds. In this chapter, we experimentally show the role of deep-lying defects in quenching of the photoluminescence. Photoluminescence decay dynamics data shows the higher contribution from non-radiative decay channels on the removal of the long chain organic ligands. Interestingly, these surface defects could be passivated by metal ions, such as Cd^{2+} and Zn^{2+}. Hence, we explore organic-free colloidal nanocrystals as luminescent sensors, as the NCs have better accessibility to analytes and are water-soluble at physiological (pH = 7.4). Binding of a trace amount of Cd^{2+} (~110 pM) to hydrophilic S^{2-} capped quantum dot surface increases the luminescence sharply, a turn-on sensor, while, the presence of trace amount (3 μM) of 2,4,6-trinitrophenol (TNP) quenches the luminescence, a turn-off sensor. Though these organic ligand-free nanocrystals are used in solutions, a defect-tolerant material is required for optoelectronic device application.

Graphical abstract

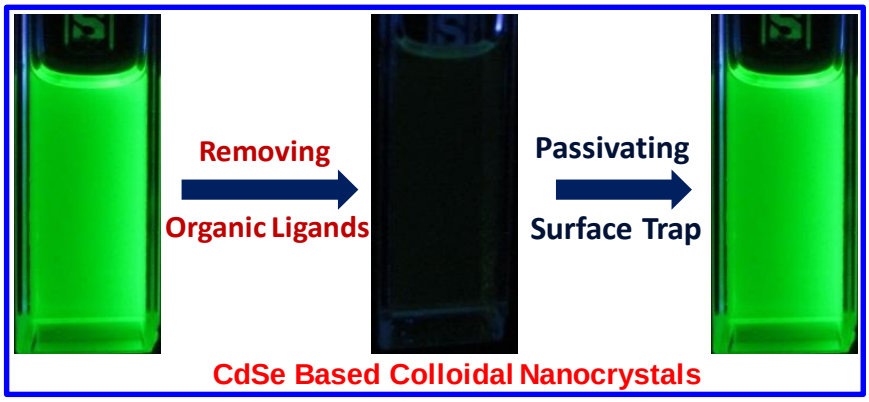

2.1 Introduction

Colloidal semiconductor nanocrystals (NCs) can exhibit nearly ideal luminescence efficiency along with some advantages over organic dyes in terms of size and composition dependent emission tunability, color purity (narrow full width at half maxima (FWHM)), broad excitation range, a high value of absorption coefficient (Ɛ) and resistance against photo-bleaching.[1-2] However, semiconductor NCs are typically capped with bulky organic ligands making them incompetent to be used in optoelectronic devices, such as solar cells, light emitting diodes (LEDs) in which, efficient charge transport is crucial. But, these ligands passivate the dangling bonds present on the surface of the NCs as discussed in the previous chapter. In CdSe based nanocrystals, these dangling bonds on the surface act as trap states which lie deep within the band gap. Consequently, removal of these ligands from the surface of the nanocrystals affects the optical and optoelectronic properties.

In this chapter, we experimentally show how the PL efficiency of the CdSe based NCs get quenched on the removal of long hydrocarbon chain ligands (oleic acid). We followed two approaches to make organic ligand-free NCs. First, S^{2-} ion, replacing the hydrophobic organic ligands resulting a negatively charged NCs surface having ζ-potential = -25 mV. Second, $(CH_3)_3OBF_4$ treatment to get ligand-free positively charged NC surface having ζ-potential = +35 mV. These organic-free NCs show good solubility in water at physiological pH~7.4. We further passivate the newly created dangling bonds on the surface of NCs by adding Cd^{2+} and Zn^{2+} to the S^{2-} capped CdSe based NCs. Good water solubility and better accessibility of these NCs make them efficient sensor for detection of metal ions and also for nitro-explosives. Trace amount of Cd^{2+} (~110 pM) bind to the surface of hydrophilic S^{2-} capped NC which results into increases the luminescence, while, a small amount (3 μM) of 2,4,6-trinitrophenol (TNP) result into quenching of PL.

2.2 Experimental Sections

2.2.1 Chemicals

Cadmium oxide (99.995%, Aldrich), zinc oxide (≥99%, Aldrich), oleic acid (OA, 90%, technical grade, Aldrich), 1-octadecene (ODE, 90%,Aldrich), sulfur (99.998%, Aldrich), selenium (99.99%, Aldrich), trioctylphosphine (TOP, 97%, Aldrich), formamide (FA, spectroscopy grade, Aldrich), hexane (AR, S D Fine chem. Ltd), ammonium sulfide (40-48 wt% solution in water, Aldrich), toluene (99.5%, Rankem), ethanol (99.9% AR, S D Fine chem. Ltd), N,N dimethyl formamide (DMF dry, S D Fine chem.),

trimethyloxonium tetrafluoroborate (95%, Aldrich), cadmium nitrate tetrahydrate (98%, Aldrich), zinc nitrate hexahydrate (98%, Aldrich), HEPES sodium salt (99.99%,Sigma), toluene (99.8%,Aldrich), acetonitrile (dry, S D Fine chem. Ltd.), 4-nitrotoluene (99%, Aldrich), 2,4- dinitrotoluene (2,4-DNT, 99%, Aldrich), 2,6-dinitrotoluene (2,6-DNT, 99%, Aldrich), 2,4,6- trinitrophenol (TNP, 99%, Aldrich). All the Chemicals were used as received without further purification.

2.2.2 Synthesis of Oleic Acid Capped CdSe/CdSeS/CdS Core/Gradient-Shell/Shell NCs

Oleic acid capped CdSe/CdSeS/CdS core/gradient-shell/shell NCs were carried out following the work of Sarma et al.[3] 0.0496 g CdO, 0.5 mL OA and 10 mL ODE was degassed (under alternate vacuum and nitrogen) at 120 °C for 30 minutes at mild stirring rate. The temperature of reaction mixture was increased up to 300 °C forming a clear solution. A clear 1 mL TOP solution containing sulfur (0.0128 g) and selenium (0.0016 g) is then quickly injected to the uniformly stirred Cd solution at 300 °C. The reaction was carried out for 20 seconds. While cooling down to room temperature, the reaction mixture was diluted with ~10 mL toluene at ~100 °C. Precipitation of NCs was carried out by addition of minimum amount of ethanol, followed by centrifugation. The wet pellet of NC obtained after centrifugation was redispersed again in toluene and precipitated using ethanol. The same process of dispersion/precipitation was repeated once more. The obtained PL quantum yields (QY) are typically in the range of 50-60%.

2.2.3 Synthesis of Oleic Acid Capped CdSe/CdS-ZnS Core/Hybrid Shell NCs

The synthesis was carried out following ref.[4] 0.0496 g CdO, 0.0496 g ZnO, 2 mL OA and 10 mL ODE was degassed (under alternate vacuum and nitrogen) at 120 °C for 30 minutes at mild stirring rate. The temperature of reaction mixture was increased up to 310 °C forming a clear solution. A clear 1 mL TOP solution containing sulfur (0.0567 g) and selenium (0.0075 g) is then quickly injected to the uniformly stirred Cd solution kept at 310 °C. The reaction was carried out for 1 min. While cooling down to room temperature, the reaction mixture was diluted with ~10 mL toluene at 100 °C. Precipitation of NCs was carried out using ethanol followed centrifugation. The NCs were redispersed in toluene and again precipitated with ethanol. The process redispersion/precipitation was repeated once more.

2.2.4 Ligand Exchange with S^{2-}

The ligand exchange reaction was carried out following ref.[5] where the native OA capping ligands were replaced by S^{2-} ligand. Organic ligand was exchanged with S^{2-} following ref.[5] where 1 mL FA was added to 1 mL OA- capped CdSeS NCs dispersed in toluene and then 10 µl aqueous solution (40-48 wt %) of ammonium sulfide was added to the FA layer. Vigorous stirring of the two phases for about 10 min led to a complete phase transfer of NCs in to FA from toluene phase. The color-less toluene phase was discarded followed by addition of fresh toluene in order to wash out any residual organic molecules from the FA phase. The washing was repeated for two more times. NCs dispersed in FA were precipitated by using minimum amount of acetonitrile (~0.8 mL) followed by centrifugation. The obtained precipitate of S^{2-} capped NCs can be redispersed in a polar solvent like FA and water. For metal ion sensing, the NC precipitate was re-dispersed in aqueous solution of HEPES buffer where pH was buffered at 7.4 (physiological pH). In some experiment the precipitate was redispersed in FA. These S^{2-} capped NCs exhibit negative charge on the NC surface with a negative ζ-potential of -25 mV and are soluble in a polar medium like water. Further, the pH of the water medium was maintained at pH 7.4 using HEPES buffer. PLQY of S^{2-} capped NCs typically decreases to ~1-5 % after the ligand exchange.

2.2.5 Ligand Removal withTriethyloxoniumTetrafluoroborate

Stripping of organic ligand was done with trimethyloxonium tetrafluoroborate following the report of Helms at al.[6] OA capped CdSe/CdS-ZnS core/hybrid-shell NCs were redispersed in 1 mL hexane (~5 mg/mL). 1 mL DMF was added to the NC dispersion in hexane, followed by addition of appropriate amount of triethyloxonium tetrafluoroborate to the DMF layer. Vigorous stirring of the two phases for about 5 minutes led to a complete phase transfer of NCs to DMF from hexane phase. The NCs dispersed in DMF was washed thrice with fresh hexane and then separated out by discarding the upper hexane phase. NCs were precipitated by adding toluene to DMF phase. The resulting precipitate was re-dispersed in DMF.

2.2.6 Preparation of Buffer Solution

10 mM HEPES buffer solution was prepared by dissolving 1.3015 g HEPES-Na salt (4-(2-Hydroxyethyl) piperazine-1-ethanesulfonic acid sodium salt,) in 500 mL water and then pH was adjusted to 7.4 by drop-wise addition of aqueous solution of 1N HCl.

2.2.7 Sensing of Metal Ions

Aqueous solutions $Zn(NO_3)_2.6H_2O$ and $Cd(NO_3)_2.4H_2O$ were added one by one to the S^{2-} capped CdSe/CdSeS/CdS NCs dispersed in the buffer solution maintained at pH 7.4. Concentration of NC was adjusted such that the optical density at the lowest energy excitonic peak is 0.1. Influence of different metal ion on the NC emission was studied by measuring PL spectra after exciting at 450 nm. After noticing that the addition of Cd^{2+} ion increases the NC PL significantly, we measured the PL of NC after adding different concentrations of Cd^{2+} ions.

2.2.8 Sensing of Nitroaromatic Compounds

Five nitroaromatic compounds- nitrobenzene, 4-nitrotoluene, 2,4-DNT, 2,6-DNT and TNP were selected to search their interaction with S^{2-} capped and ligand-free CdSe/CdS-ZnS core/hybrid-shell NCs. 0.1 mM aqueous solutions of each nitroaromatic compounds were added one by one to the aqueous solution of NCs with absorbance of lowest energy excitonic peak maintained at 0.1. PL spectra were measured subsequently corresponding to each nitroaromatic compound after excitation at 450 nm. Since TNP was found to influence NC PL, we titrated NC dispersion with different concentrations of TNP and measured PL at each concentration.

2.2.9 Characterization

UV-visible absorption and PL spectra of NCs were recorded using a Perkin Elmer, Lambda 45 UV/Vis spectrometer and FluoroMax-4 spectrofluoremeter (HORIBA scientific), respectively. PL decay dynamics were measured using time correlated single photon counting (TCSPC) technique set up from Horiba JobinYvon at excitation energy of 459 nm. Pl decays were measured for OA capped NCs dispersed in toluene and S^{2-} capped, and Cd^{2+} treated S^{2-} capped NCs were dispersed in the aqueous buffer with pH 7.4. ζ-potential were obtained employing Henry's equation in the Smoluchowski limit, using a Zetasizer Nano series, Nano-ZS90 (Malvern Instruments, U.K.). Isothermal Calorimetry (ITC) was done using MicroCal iTC200 system (GE Healthcare Life Sciences). NCs dispersed in FA were kept in the titration cell as a titer and was titrated by Cd^{2+} solution in FA. Both the titrant (Cd^{2+} ions) and the NCs were dispersed in formamide, sonicated and filtered through 0.45 m PTFE filter. Temperature of the titration cell was maintained at 298 K and ITC curve was the result of the average of nearly three successive titrations which included the subtraction of FA dilution binding energetic. Molar concentration of NCs was calculated following the report by Peng et al.[7] Fourier-transform infrared

(FTIR) spectroscopy was carried out in the transmission mode using a NICOLET 6700 FTIR spectrometer (Thermo scientific).

2.3 Results and Discussions

2.3.1 Organic (Oleic Acid) Capped CdSe Based Type-I Core/Shell Heterostructured NCs

CdSe NCs have a high density of surface-related dangling bonds which act as non-radiative recombination centers for charge carriers. To partially suppress such charge trapping, we have used type-I core/shell heterostructured nanocrystals in our study, in which most of the charge carriers will be confined to core. Furthermore, to reduce the lattice mismatch (interfacial defects at core-shell interface), and to get high PLQY CdSe/CdSeS/CdS core/gradient-shell/shell and CsSe/CdS-ZnS core/hybrid-shell NCs are synthesized.[3,4] As the post-synthesis shell growth causes degradation of size distribution, in synthesis of both types of NCs only a single step of hot injection (containing anion precursor) is involved. These OA capped CdSe/CdSeS/CdS and CdSe/CdS-ZnS NCs were synthesized by following previous reports.[3-4] NCs are synthesized at high temperature (~300 °C) to get better crystallinity and hence better optical properties. This reaction temperature is higher in comparison to the reaction temperature required to synthesize $CsPbX_3$ (X= Cl, Br, I) perovskite NCs which will be discussed later in next chapters. During the synthesis of these NCs, OA dissolves the metal precursors and control the size of the NCs. Further, it passivates the dangling bond on the surface of the NCs by its COO^- end and stabilizes the colloidal dispersion of NCs in non-polar solvent by its long hydrocarbon chain. In these NC, bonding of OA with the surface of the NCs is strong enough to purify these NCs by using high-polar solvents, such as acetone, ethanol or methanol. Consequently, the colloidal stability does not get affected on redispersing the NCs in non-polar solvents after precipitation using high-polar solvents. Figure 2.1 and Figure 2.2 show the optical data of the CdSe/CdSeS/CdS and CdSe/CdS-ZnS NCs respectively. UV-visible absorption (black line) and PL (red line) spectra (Figure 2.1) of the synthesized CdSe/CdSeS/CdS NC samples were measured in toluene and suggest an optical bandgap of ~530 nm corresponding to the energy of 2.34 eV, which is higher than the bulk band gap of CdSe (~1.74 eV)[8] and lower than bulk bandgap of CdS (~2.42).[9] Based on the reactivity difference of Se and S to Cd^{2+} ion, where Se reacts faster than sulfur, CdSe/CdSeS/CdS heterostructure is expected and thoroughly investigated in ref. 10. Hence, in this quantum confined size range the optical contribution is coming from CdSe core. Based on the previous report the size of the CdSe/CdSeS/CdS NCs is expected to be ~5

nm.[10] The sharp PL spectrum of 40 nm FWHM (164 meV) with a Stoke's shift of 20 nm (85 meV) has peak energy at 550 nm (2.25 eV). These NCs shows PLQY of 50-55 %.

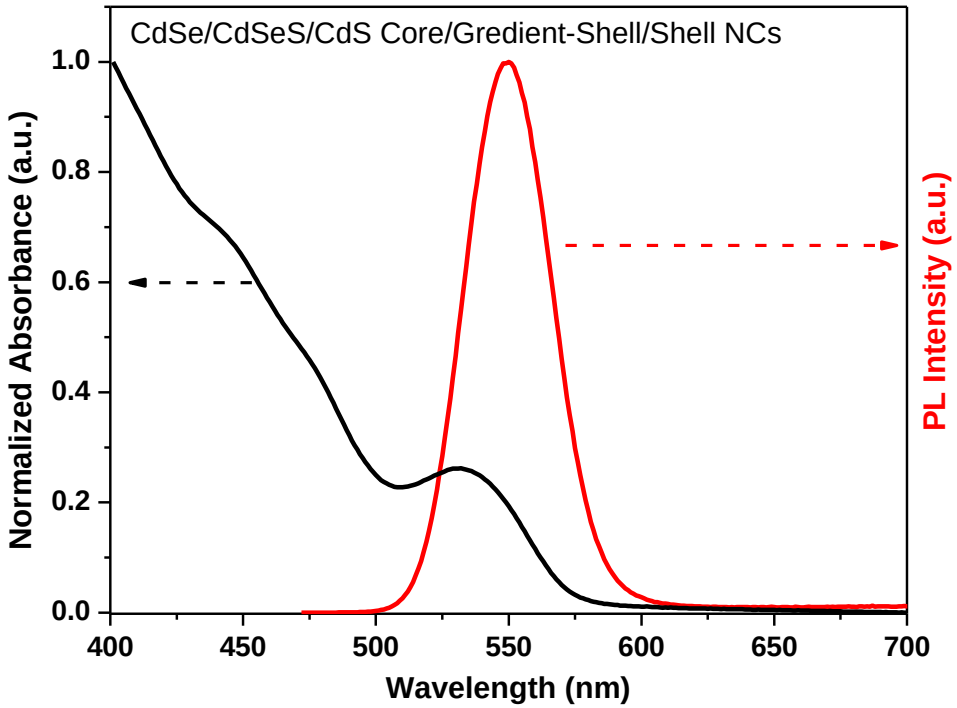

Figure 2.1: UV-visible absorption and photoluminescence spectra of oleic acid capped CdSe/CdSeS/CdS core/gradient-shell/shell nanocrystals.

Similarly, ~6.7 nm sized (from ref. 4) CdSe/CdS-ZnS core/hybrid shell NCs with higher PLQY (~65%) show optical bandgap value of ~2.2 eV corresponding to 565 nm wavelength (Figure 2.2) and emitting at ~2.14 eV (PL peak position = 580 nm). The details of formation of core/hybrid shell structure have been explained in ref. 4. Here, the optical contribution is mostly coming from CdSe, as the bulk bandgap values of CdSe, CdS, ZnSe and ZnS are 1.74, 2.42, 2.67 and 3.60 respectively.[4] Here, only CdSe shows bulk band gap value lower than the bandgap of our NCs. Also, Se exhibit more reactivity to Cd^{2+} in compared to Zn^{2+}. So alloy of CdSe and ZnSe is neglected, when Se is used as limiting reagent. Owing to the presence of extra layer of ZnS having higher bandgap value than CdS, the excitons are confined more towards core region and as a result high PLQY is obtained. The FWHM of the PL spectrum is 121 meV.

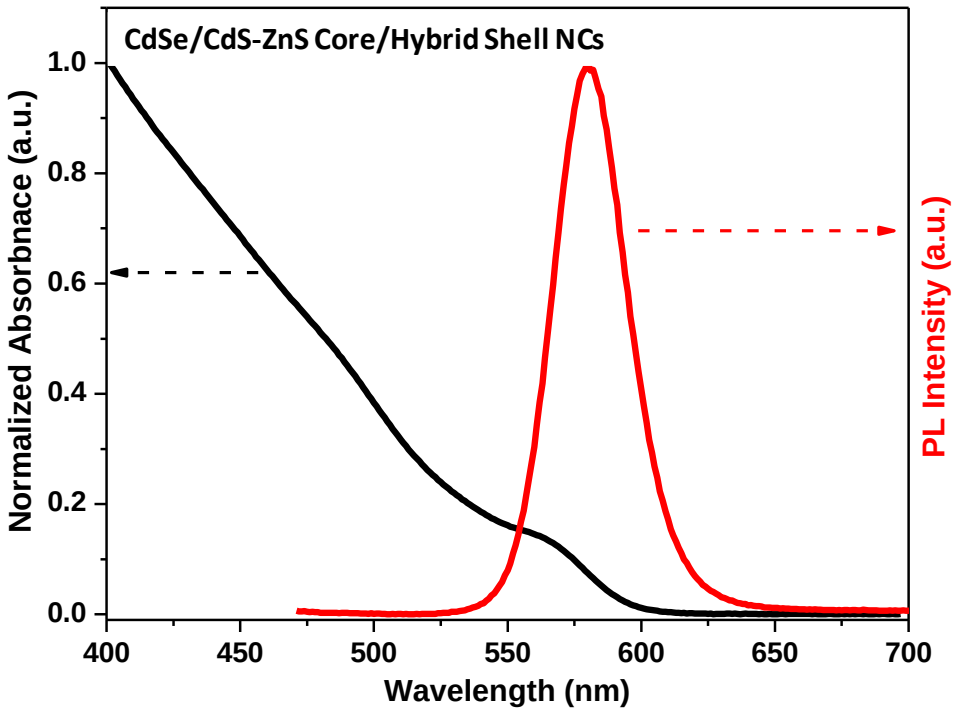

Figure 2.2: UV-visible absorption and photoluminescence spectra of oleic acid capped CdSe/CdS/ZnS core/hybrid-shell nanocrystals.

2.3.2 Removal of Organic Ligands from Surface of NCs and Stability of NCs in Polar Solvents

The ligand exchange reaction was carried out following ref.11, where, the native OA capping ligands were replaced by the S^{2-} ligand. Details of the synthesis and ligand exchange reaction are given in the experimental sections and shown schematically in Figure 2.3. This S^{2-} capped NCs exhibit negative charge on the NC surface with a ζ-potential of -25 mV and can be dispersed in polar solvents, such as, water. Figure 2.4 shows comparison of FTIR spectra of OA capped (black line) and S^{2-} capped (red line) NCs. FTIR spectra show the removal of organic ligands from the NCs on ligand treatment, given the absence of C–H modes near ~2900 cm^{-1} or below ~2000 cm^{-1} belonging to oleate, or any residual ODE. UV-visible absorption (Figure 2.5) and PL data (Figure 2.6) show that the size and size-distribution of NCs remain intact after the ligand exchange reaction, similar to a prior report.[11] PLQY of NCs decreases significantly after the ligand exchange, and the resultant S^{2-} capped NCs show 1-5% of PLQY. DLS data (Figure 2.7) show that freshly prepared S^{2-} capped NCs are not agglomerated as reported in ref. 11.

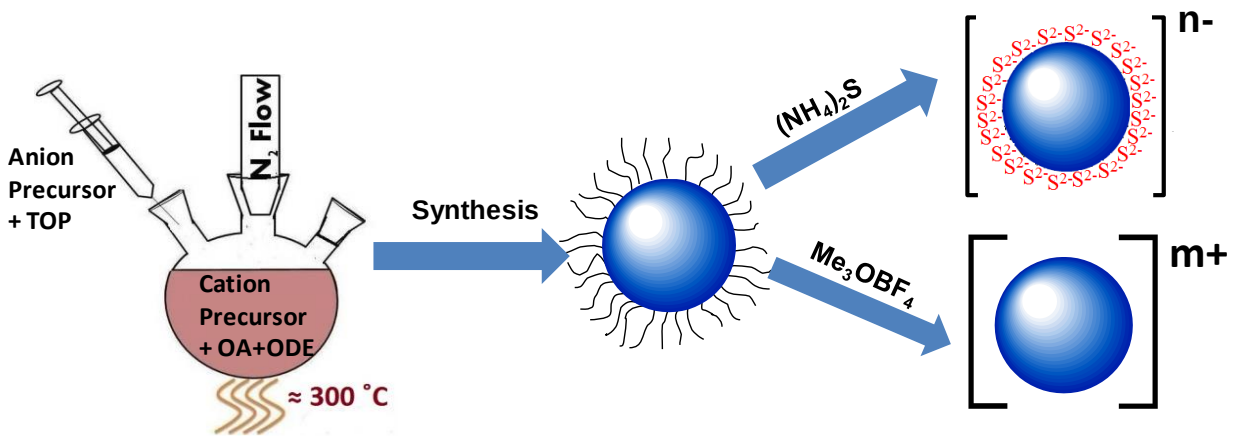

Figure 2.3: Schematics shows the synthesis and surface ligand modifications of nanocrystals.

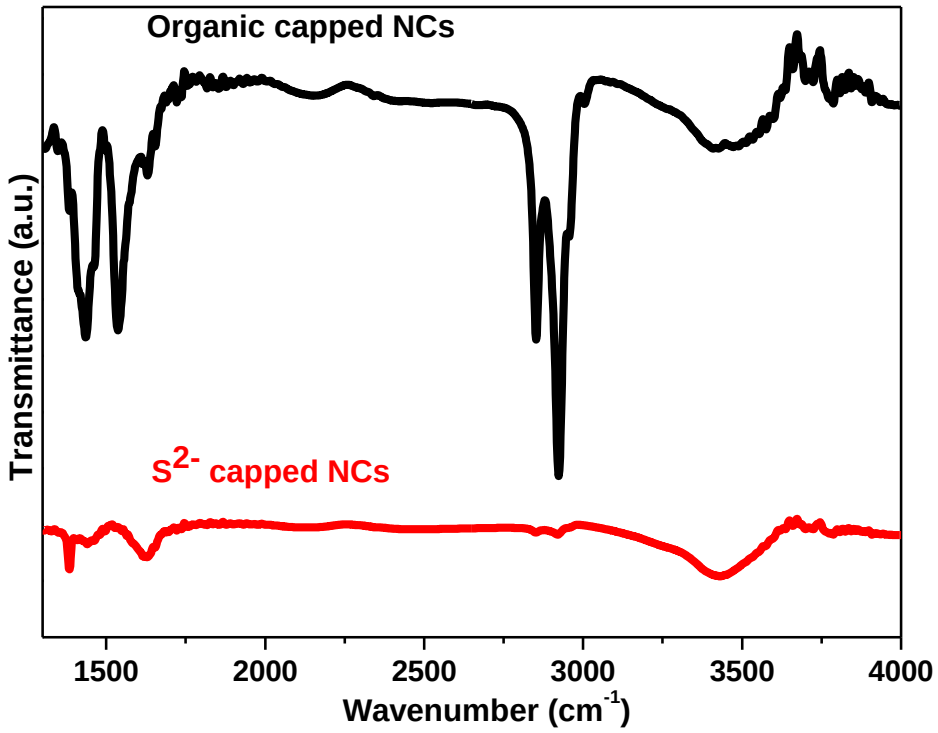

Figure 2.4: Comparison of FTIR spectra of organic and S^{2-} capped CdSe/CdSeS/CdS core/gradient-shell/shell NCs. Similar weights of both NC samples were taken for FTIR measurements. Almost absence of two bands ~2900 cm^{-1} indicates the absence organic ligands.[3]

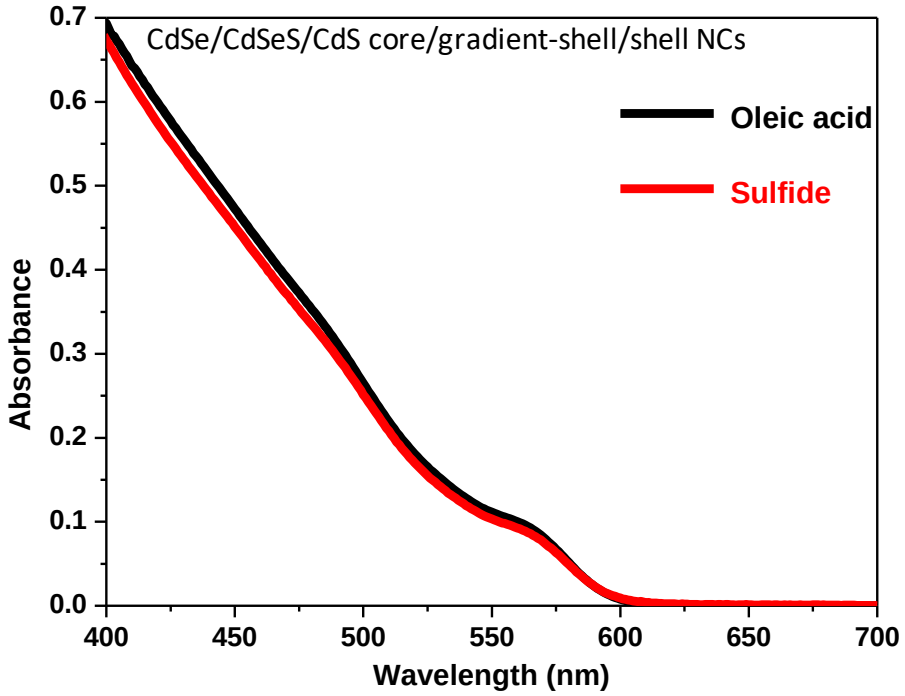

Figure 2.5: UV-visible absorption spectra of CdSe/CdSeS/CdS nanocrystals with native oleic acid capping (black line) and S^{2-} capping (red line).

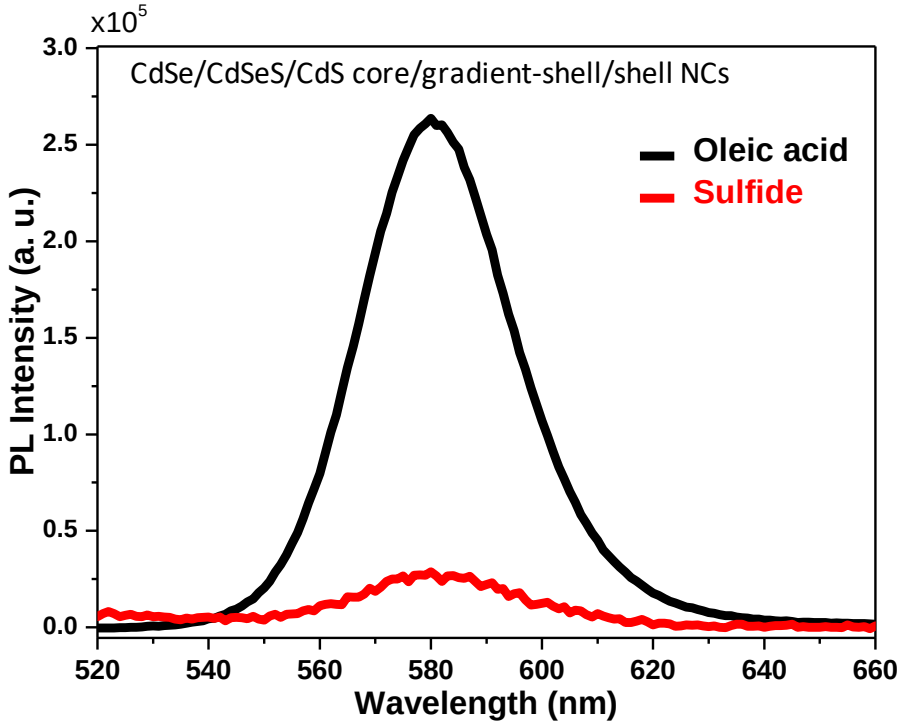

Figure 2.6: PL spectra of CdSe/CdSeS/CdS nanocrystals with native oleic acid capping (black line) and S^{2-} capping (red line).

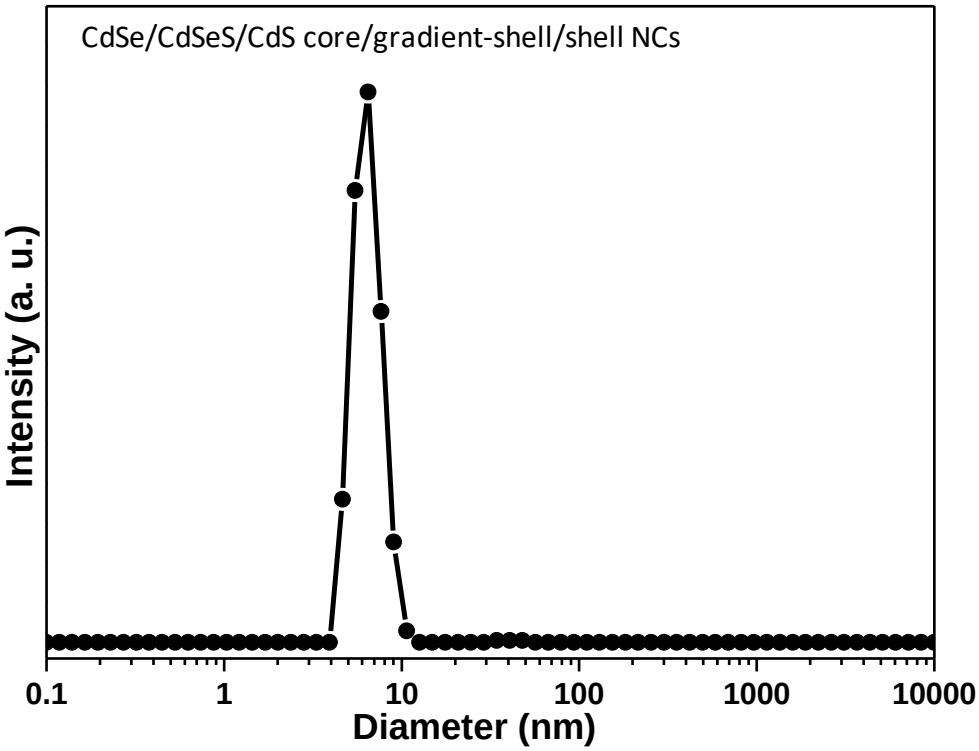

Figure 2.7: DLS data for S^{2-} capped CdSe/CdSeS/CdS NCs.

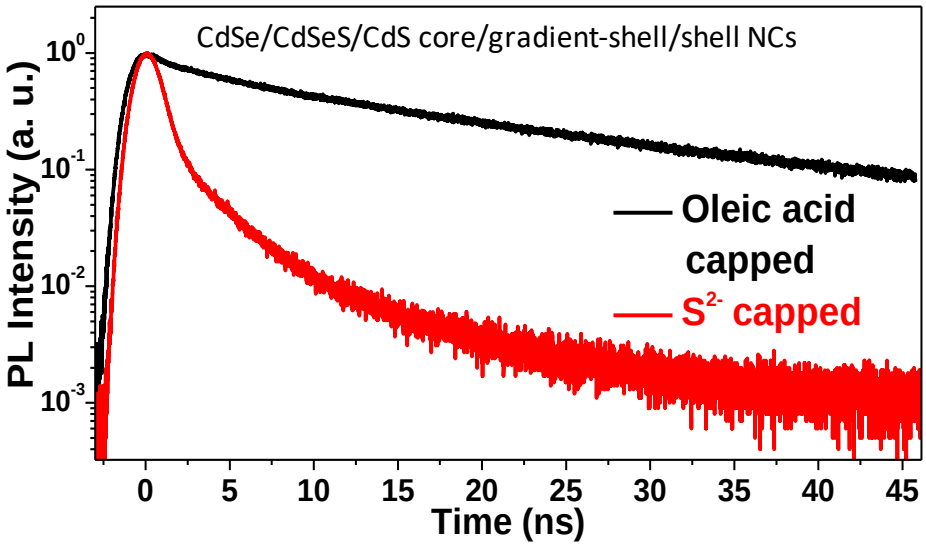

Figure 2.8: PL decay dynamics of CdSe/CdSeS/CdS nanocrystals with native oleic acid capping (black line) and S^{2-} capping (red line). Excitation at 459 nm and emission fixed at the peak maxima.

PL decay dynamics of CdSe/CdSeS/CdS NCs after surface modifications are shown in Figure 2.8. OA caped NCs show a nearly single exponential decay with little contribution from faster (< 1 ns) nonradiative decays. However, the same NCs after ligand exchange with S^{2-} shows a huge contribution from faster nonradiative decays. This was also reflected by a huge decrease in PL intensity after the ligand exchange.

2.3.3 Surface Defect Passivation by Using Cd^{2+} and Zn^{2+} Ions and Cd^{2+} Sensing

S^{2-} capped CdSe/CdSeS/CdS core/gradient shell/shell NCs in aqueous medium with pH 7.4 show enhancement of PL on treatment with Cd^{2+} and Zn^{2+} ions. Figure 2.9 shows relative PL intensity, I_{cation}/I_0, where I_0 is the PL intensity of S^{2-} capped NCs, and I_{cation} is the PL intensity of same NCs after interacting with 0.1 mM solution of respective metal ions. Shape and width of all PL spectra before and after interactions with Cd^{2+} and Zn^{2+} ions remains same and hence peak intensity is considered to obtain I_{cation}/I_0. Figure 2.9 clearly shows 6.7 and 15.0 fold increase in PL intensity of S^{2-} capped CdSe/CdSeS/CdS NCs after interacting with Zn^{2+} and Cd^{2+} ions respectively. Clearly, Cd^{2+} with 15 fold enhancement of PL intensity stands out as a strong luminescence turn-on analyte for the NC sample. Inset to Figure 2.9 shows photographs of S^{2-} capped CdSe/CdSeS/CdS NCs before and after interaction with Cd^{2+} ions upon illumination with 365 nm UV light. A large increase in the PL intensity after addition of Cd^{2+} ion is clearly visible with naked eye.

PL decay dynamics of CdSe/CdSeS/CdS NCs after Cd^{2+} treatment are shown in Figure 2.10. S^{2-} capped NCs shows a huge contribution from faster nonradiative decays. These NCs when treated with 0.1 mM Cd^{2+}, the contribution from faster nonradiative decay decreases, as shown by the slower PL decay after Cd^{2+} treatment in Figure 2.10. Clearly, addition of Cd^{2+} ion reduces defects from NC surface, therefore, enhancing (turn-on) the PL efficiency.

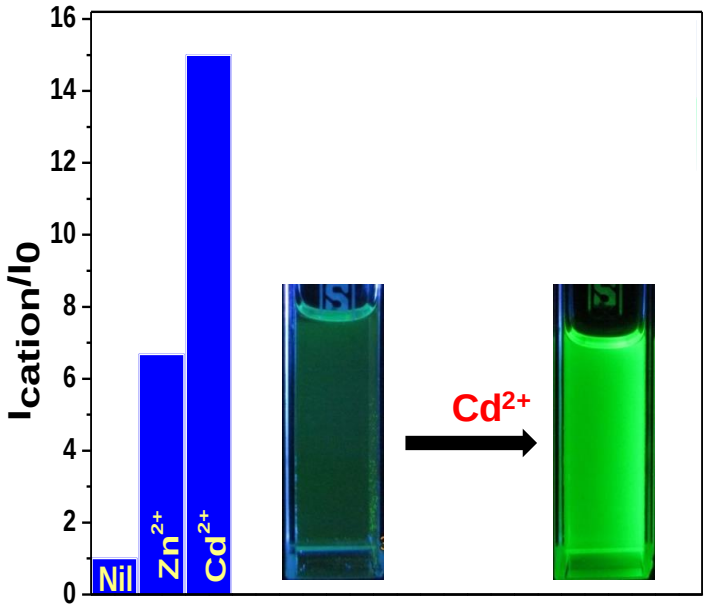

Figure 2.9: Relative PL intensity (I_{cation}/I_0) of S^{2-} capped CdSe/CdSeS/CdS NCs dispersed in aqueous buffer of pH 7.4, after addition of different cations; I_0 and I_{cation} are PL intensities of the NCs before and after addition of the respective cation (Cd^{2+} and Zn^{2+}) respectively. Inset shows photographs of the NC luminescence before and after interaction with Cd^{2+} ions, after exciting with 365 nm UV light.

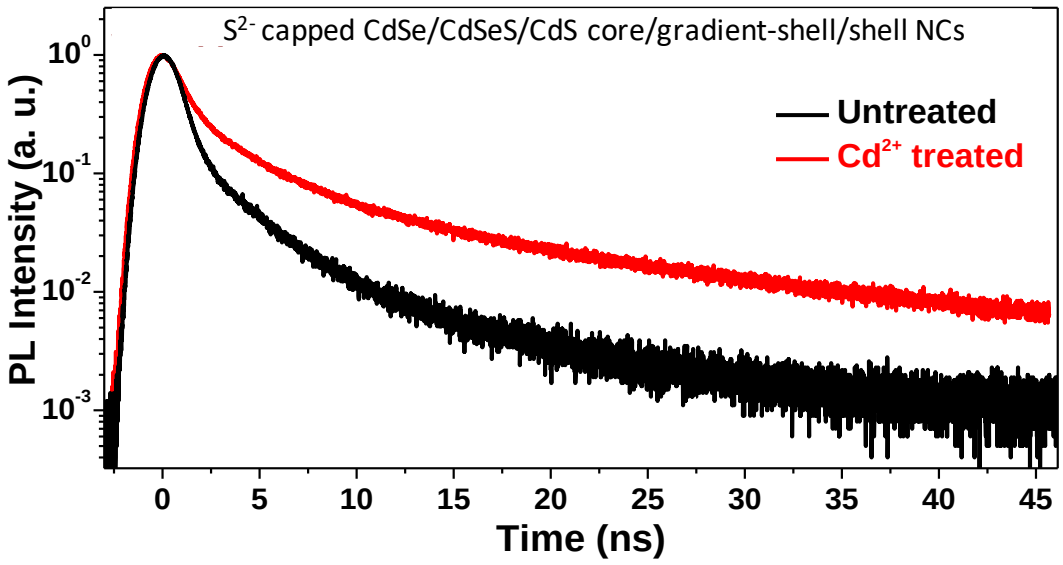

Figure 2.10: PL decay dynamics of CdSe/CdSeS/CdS NCs with different surface modifications. Excitation at 459 nm and emission fixed at the peak maxima.

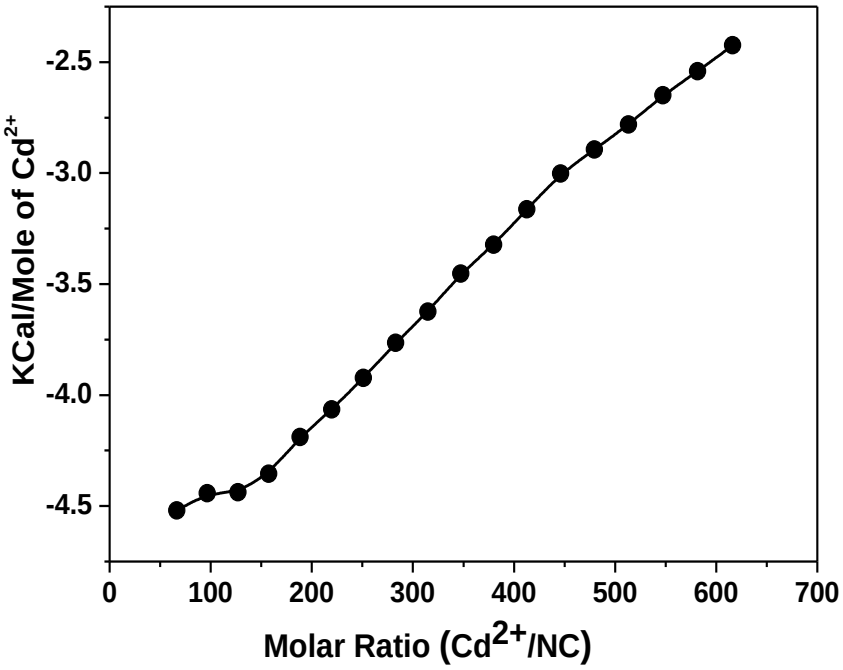

Figure 2.11: Isothermal calorimetry (ITC) data showing the integrated heat of interaction of S^{2-} capped CdSe/CdSeS/CdS NCs after injection of Cd^{2+} ions. Molar concentration of NCs were calculated using ref. 7.

ITC data in Figure 2.11 shows a clear release of heat when Cd^{2+} interact with S^{2-} capped CdSe/CdSeS/CdS NCs. Addition of larger concentration of Cd^{2+} ions would probably lead to the saturation of heat change, however, the colloidal stability of NCs get hampered with higher concentration of Cd^{2+}. This heat change suggests a significant binding interaction of Cd^{2+} ions with S^{2-} capped NC surface, thereby modifying the surface defects on the NC surface, influencing PL intensity. The strong interaction of Cd^{2+} with S^{2-} (or $S^{\delta-}$) can be explained from Pearson's hard and soft acids and bases (HSAB) principle,[12] where a soft acid Cd^{2+} interact with a soft base S^{2-}. Furthermore, the size of Cd^{2+} ion is the ideal to match the lattice parameter on the surface of S^{2-} capped CdSe/CdSeS/CdS NCs, probably forming an epitaxial adlayer of CdS on the surface.[13-14] Formation of such adlayers is expected to enhance the PL efficiency. On the other hand, it was shown previously that metal rich surface of cadmium chalcogenide NCs exhibit higher PL efficiency compared to NCs with chalcogenide rich surface.[15-17,18] We note that addition of Zn^{2+} ions to S^{2-} capped CdSe/CdSeS/CdS NCs also enhance NC PL, but to a much lower extent compared to Cd^{2+} (Figure 2.9). This lower efficacy of Zn^{2+} can be because of both Zn^{2+} is a harder base compared Cd^{2+} therefore having weaker affinity towards soft S^{2-} and smaller size of Zn^{2+} ions compared to lattice parameters of NC surface.

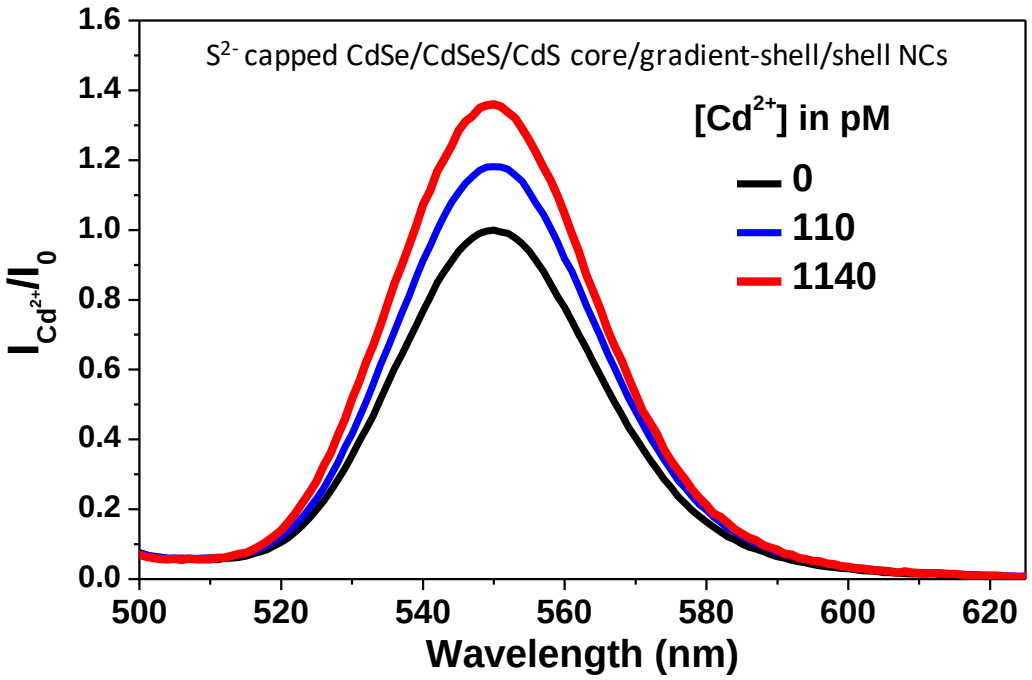

Figure 2.12: Variation of PL intensity of S^{2-} capped CdSe/CdSeS/CdS nanocrystals after interacting with different concentrations of Cd^{2+} in aqueous buffer. I_0 and I_{cd2+} are PL intensities of the NCs before and after addition of the Cd^{2+} ion.

PL spectra in Figure 2.12 show a systematic enhancement of relative intensity (I_{Cd}^{2+}/ I_0) with increasing the concentration of Cd^{2+} ion. The PL intensity changes just by addition of 110 pM Cd^{2+} ion. 110 pM Cd^{2+} is equal to 1.24×10^{-5} ppm, which is ~4 orders of magnitude lower than the typical detection limit of techniques like atomic absorption spectroscopy (AAS). To the best of our knowledge, 110 pM range detection of Cd^{2+} is by far the best for any luminescence based NC sensor.[19] Our NC sensor relies on direct interaction between the metal ion analyte and the NC surface. 3-mercaptopropionic acid-capped CdTe NCs sensors for Cd^{2+} ion with similar direct interaction approach showed a sensing in the micromolar (μM) region,[20] however, this 4 orders of magnitude improvement in the sensitivity of our organic-free NCs can be attributed to the bare NC surface which facilitate the interaction of NCs with Cd^{2+} ions. It is to be noted that, according to the standards by United States Environmental Protection Agency (EPA),[21] the maximum contaminant level of Cd^{2+} in drinking water is 44 nM, so the sensitivity of our organic-free NCs is well within the prescribed range.

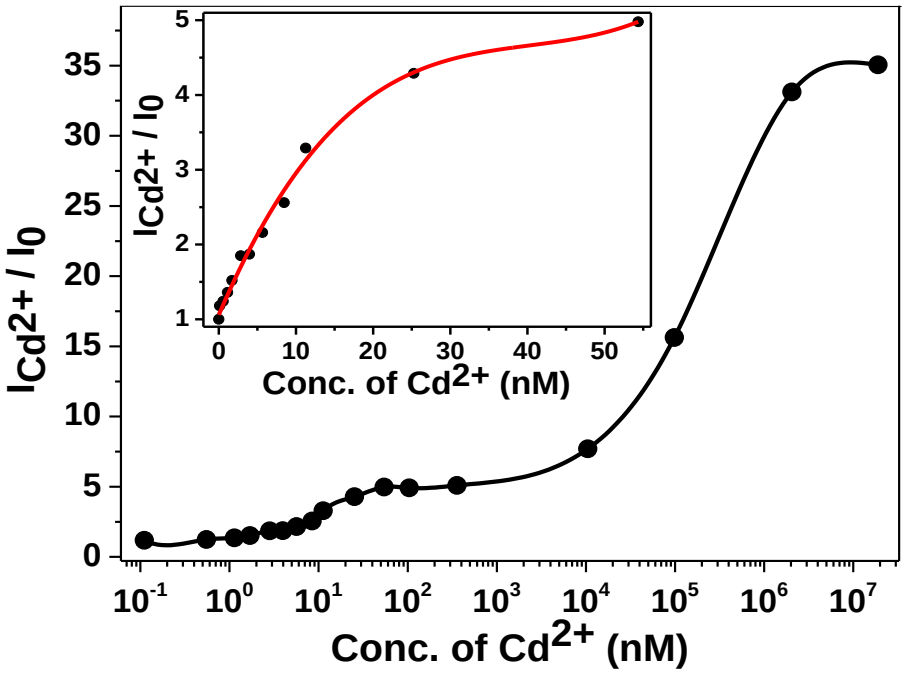

Figure 2.13: Plot of relative intensity (I_{Cd2+}/I_0) of S^{2-} capped CdSe/CdSeS/CdS NCs against concentration of added Cd^{2+} ion. Closed circles are experimental data and the line is just a guide to eye. Inset shows same plot of I_{Cd2+}/I_0 against lower concentration range of Cd^{2+} ions. The red line is a polynomial fit to the experimental data shown by closed circle. Excitation wavelength for all the spectra was fixed at 450 nm.

Figure 2.13 shows the variation of I_{Cd2+}/ I_0 with concentration of Cd^{2+} ion where the symbols are data and the line is just a guide to eye. Inset to Figure 2.13 shows a systematic increase in the I_{Cd}^{2+}/ I_0 with increasing Cd^{2+} content from 110 pM up to 55 nM region, encompassing the EPA suggested 44 nM upper limit in drinking water. The data (symbols) can be fitted by the empirical equation, $I_{Cd}^{2+}/ I_0 = 1.03968 + 0.24133 \times [Cd] - 0.00565 \times [Cd]^2 + 4.67067 \times 10^{-5} \times [Cd]^3$, where [Cd] is the concentration of Cd^{2+} ion in nM. When [Cd] < 100 nM, NCs (with optical density ~0.1 for the lowest energy excitonic peak) form a stable solution exhibiting ζ-potential < -20 mV. However, further increase in [Cd] in the region of 10^2 to 5×10^3 nM, the NC dispersion get destabilized with measured ζ-potential in between -10 mV to +10 mV. Figure 2.13 shows a nearly constant I_{Cd2+}/ I_0 in this [Cd] region, where NCs tends to agglomerate. Further increase in the [Cd] > 10^4 nM, provides positively charged NC surface with ζ-potential >15mV, and consequently colloidal stability and sharp increase in the I_{Cd2+}/ I_0 (Figure 2.13). This set of observations suggest that surface of our S^{2-} capped NCs were negatively charged and the

added Cd^{2+} ions bind to negatively charged surface, which also passivate the nonradiative decay channels on NC surface, enhancing the PL intensity. Initially, for [Cd] < 100 nM, surface of the NC still remains enough negatively charged to maintain colloidal stability, so surface passivation enhanced the PL intensity. For [Cd] in between 10^2 to 5×10^3 nM, NC surface get passivated to enhance the PL intensity, however, the agglomeration of NCs has an opposing effect on the PL intensity. Consequently, PL intensity does not change much in this [Cd] range. However, at very high concentration, [Cd] > 10^4, charge inversion takes place where a negatively charged NC converts to a positively charged NC similar to ref.[16] along with enhancement in PL intensity.

2.3.4 Organic Ligand-Free CdSe Based NCs As Nitroexplosive Sensor

After establishing the good sensitivity for Cd^{2+} ions, we explored sensitivity of organic-free NCs for different nitroaromatic compounds. Aqueous solution of S^{2-} capped CdSe/CdSeS/CdS NCs did not exhibit a significant PL enhancement after interacting with different nitroaromatic molecules, instead, turn-off behavior, i.e., PL quenching is observed for TNP. To test the turn-off sensing ability, we choose a different NC system S^{2-} capped CdSe/CdS-ZnS core/hybrid-shell NCs, which is brighter compared to S^{2-} capped CdSe/CdSeS/CdS NCs. The CdS-ZnS hybrid shell imposes larger band offsets for electron and hole in the CdSe core, and therefore the PL is less sensitive to surface modification. Therefore, CdSe/CdS-ZnS core/hybrid-shell NCs exhibit stronger luminescence to act as a turn-off sensor even after exchanging the OA ligand with S^{2-} ion and dispersing the NCs in water. The organic ligand was replaces with S^{2-} ligand by following the same protocol discussed above. Figure 2.14 shows I_{nitro}/I_0, where I_{nitro} is the PL intensity of NCs after interacting with different nitroaromatic compounds. Clearly, addition of TNP shows a sharp decrease in PL of NCs, whereas, other nitroaromatic compounds do not change the PL intensity significantly. In fact, the selective sensing of TNP is conserved even in the mixture of all these different nitroaromatic compounds.

Figure 2.15 compares the change in PL intensity with concentration of TNP. A clear decrease in PL intensity has been observed for TNP at 3.31 μM concentration, and the PL intensity decreases systematically with increasing TNP concentrations. The sensitivity in the range of few μM or sub-μM is poor compared to that achieved for Cd^{2+} sensing, however, can be comparable with some of the prior reports of luminescence sensing of TNP.[22-23] The quenching of NC PL after interaction with TNP can be caused by various mechanisms, namely, charge transfer,[24] energy transfer,[25] modification of surface

defects, or combination of multiple processes. Figure 2.16 shows that there is no overlap between NC emission spectrum and absorption spectrum of TNP, ruling out the energy transfer mechanism as a cause of PL quenching.

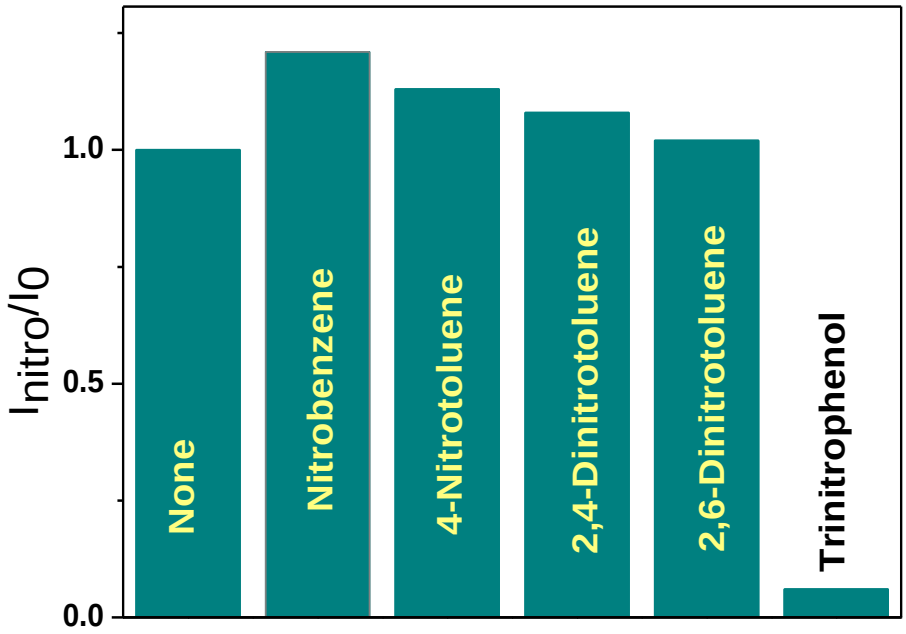

Figure 2.14: Change in PL intensity (I_{nitro}/I_0) of S^{2-} capped CdSe/CdS-ZnS core/hybrid-shell NCs dispersed in aqueous solution, after addition of different nitromatic compounds. I_0 and I_{nitro} are PL intensity of the NC before and after addition of the respective nitroaromatic compounds, namely, nitrobenzene (NB), 4-nitrotoluene (4-NT), 2,4-dinitrotoluene (2,4-DNT), 2,6-dinitrotoluene (2,6-DNT) and 2,4,6-trinitrophenol (TNP).

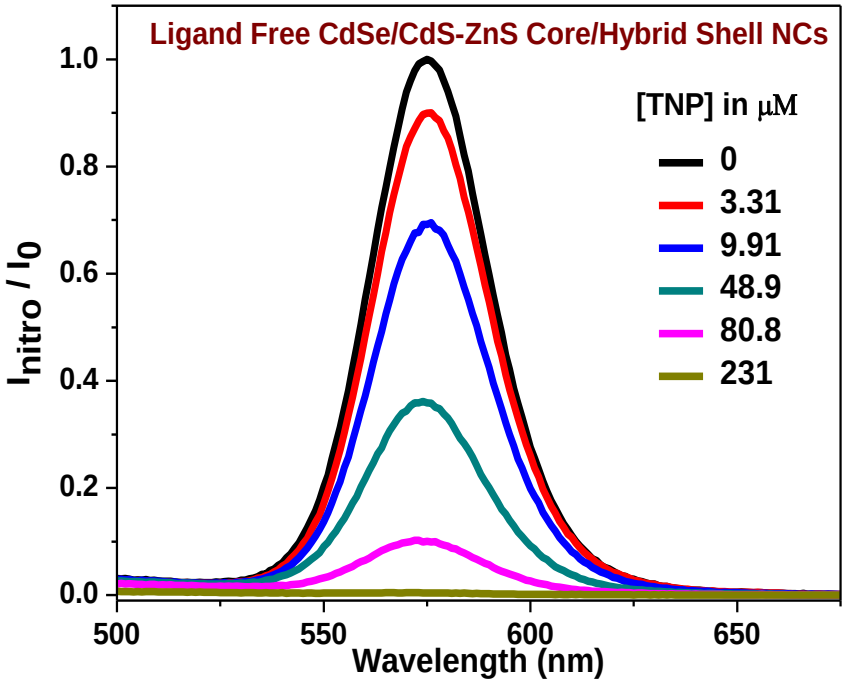

Figure 2.15: Variation of PL intensity of S^{2-} capped CdSe/CdS-ZnS NCs after interacting with varying concentrations of TNP. I_0 and I_{nitro} are PL intensities of the NCs before and after addition of the nitroexplosive (TNP).

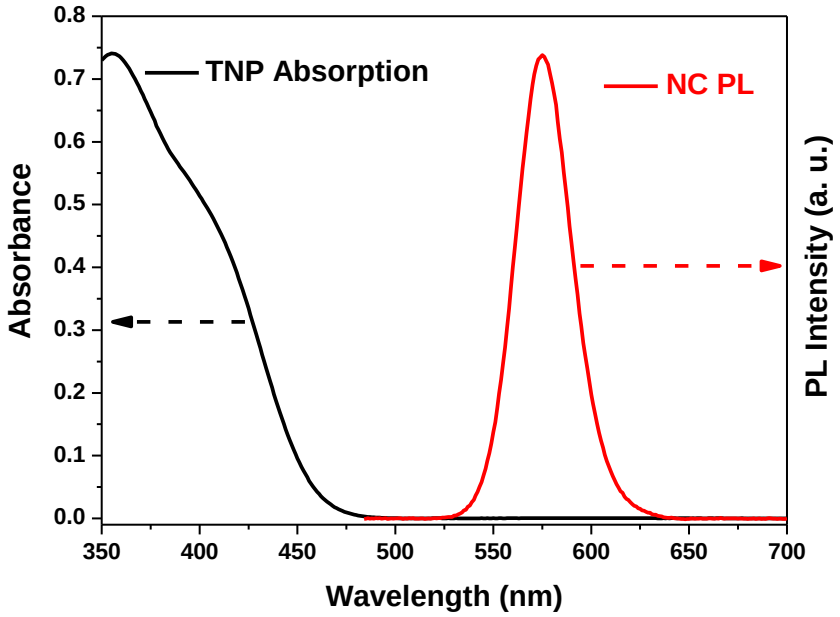

Figure 2.16: UV-visible absorption spectrum of TNP, and PL spectrum of S^{2-} CdSe/CdS-ZnS core/hybrid-shell nanocrystals. There is no spectral overlap between NC emission and TNP absorption.

In order to investigate any role of S^{2-} ligand, we employed the same CdSe/CdS-ZnS NCs but with different surface modification. Oleic acid capped CdSe/CdS-ZnS NCs were transformed to ligand-free NCs, employing trimethyloxonium tetrafluoroborate following ref[6] (Figure 2.3). These ligand-free NCs were also employed for the sensing of nitroaromatic compounds and results were similar to those of S^{2-} capped NCs. This observation suggest that the sensing capability of our NCs towards nitroaromatic compounds does not entirely depend on surface modification, and the fact the NC surface is accessible to nitroaromatic compounds was sufficient enough to quench the NC PL. Since the binding probability of TNP towards negatively charged S^{2-} capped NC and positively charged ligand-free NCs are expected to be different, the observed similarity in PL quenching for both kinds of NC surface suggests poor binding of TNP on NC surface, instead, PL quenching probably happens through collision between NC and TNP owing to their Brownian motion in solution. Such poor binding of TNP to the NC surface can hinder to achieve ultra high sensitivity for TNP detection.

After negating out the energy transfer and surface modification of NCs as a possible cause for quenching the NC PL, we explore the possibility of charge transfer. Prior literature[23, 26] suggests that, electron transfer from the conduction band minimum of CdSe to the lowest unoccupied molecular orbital (LUMO) of TNP is energetically favorable. On the other hand, LUMO levels of all other nitroaromatic compounds are significantly higher compared to the conduction band minimum of CdSe. Therefore, electron transfer from NC to TNP upon collision could be a plausible mechanism for PL quenching, which also explain the selectivity of nanosensor towards TNP compared to other nitroaromatic compounds.

2.4 Conclusions and Need of Defect Tolerant NCs for Optoelectronics

We synthesized colloidal CdSe based type-I core/shell heterostructured NCs of high PL efficiency (50-65%). These NCs are OA capped and soluble in non-polar solvents. PLQY of these NCs decreases to 1-5% on replacing OA cappings with S^{2-} ions or removing them completely. PL decay data suggest PL quenching is due to the trapping of charge carriers in defects states lying deep within the band gap of these compound semiconductor NCs. These organic free NCs have charge on their surface and can be dispersed in polar solvent such as water. Further, the surface defects are passivated by using Cd^{2+} and Zn^{2+} ions which result into enhancement of PL. This property makes these organic-free NCs a luminescent sensor to detect trace amounts of chemical species. Another interesting fact is removal of

bulky organic ligands from the surface of NCs facilitates easy interaction of different analytes with the NC surface. S^{2-} capped CdSe/CdSeS/CdS core/gradient-shell/shell NCs acts as turn-on sensors for the toxic Cd^{2+} ions. To the best of our knowledge, the detection 110 pM Cd^{2+} ions by our nanosensor is the highest sensitivity for any NC based sensor at the time of this work. PL decay dynamics and ITC data show that the Cd^{2+} ions bind to the NC surface reducing surface defects, thereby, enhancing the PL efficiency. The turn-on sensing of the NC is towards Cd^{2+} ion, because of (i) preferred binding between soft Cd^{2+} acid and soft S^{2-} base, and (ii) ionic size of Cd^{2+} is a perfect match for the lattice parameter of CdSe/CdSeS/CdS NC surface, forming CdS adlayer on the NC surface. On the other hand, different nitroaromatic compounds were also employed as analytes. Explosive TNP molecules quench NC PL, a turn-off behavior. The mechanism of PL quenching appears to the charge transfer from NC to TNP. However, even after having organic free nature of these NCs to fabricate electronically coupled NC film, these NCs are not ideal to be used in optoelectronic applications. The charge carriers would be trapped in the deep lying defects and would hamper the performance of NC device. Hence, there is a need of defect tolerant materials in which the defects do not trap the charge carriers. Lead halide perovskite are one of those defect tolerant materials and would be studied in rest of the thesis.

References:

1. Srivastava, B. B.; Jana, S.; Karan, N. S.; Paria, S.; Jana, N. R.; Sarma, D. D.; Pradhan, N., Highly Luminescent Mn-Doped ZnS Nanocrystals: Gram-Scale Synthesis. *J. Phys. Chem. Lett.* **2010,** *1*, 1454-1458.

2. Saha, A.; Chellappan, K. V.; Narayan, K. S.; Ghatak, J.; Datta, R.; Viswanatha, R., Near-Unity Quantum Yield in Semiconducting Nanostructures: Structural Understanding Leading to Energy Efficient Applications. *J. Phys. Chem. Lett.* **2013,** *4*, 3544-3549.

3. Sarma, D. D.; Nag, A.; Santra, P. K.; Kumar, A.; Sapra, S.; Mahadevan, P., Origin of the Enhanced Photoluminescence from Semiconductor CdSeS Nanocrystals. *J. Phys. Chem. Lett.* **2010,** *1*, 2149-2153.

4. Nag, A.; Kumar, A.; Kiran, P. P.; Chakraborty, S.; Kumar, G. R.; Sarma, D. D., Optically bifunctional heterostructured nanocrystals. *J. Phys. Chem. C* **2008,** *112*, 8229-8233.

5. Nag, A.; Kovalenko, M. V.; Lee, J. S.; Liu, W. Y.; Spokoyny, B.; Talapin, D. V., Metal-free Inorganic Ligands for Colloidal Nanocrystals: S^{2-}, HS^{-}, Se^{2-}, HSe^{-}, Te^{2-}, HTe^{-}, TeS_3^{2-}, OH^{-}, and NH_2^{-} as Surface Ligands. *J. Am. Chem. Soc.* **2011,** *133* , 10612-10620.

6. Rosen, E. L.; Buonsanti, R.; Llordes, A.; Sawvel, A. M.; Milliron, D. J.; Helms, B. A., Exceptionally Mild Reactive Stripping of Native Ligands from Nanocrystal Surfaces by Using Meerwein's Salt. *Angew. Chem.-Int. Edit.* **2012,** *51*, 684-689.

7. Yu, W. W.; Qu, L.; Guo, W.; Peng, X., Experimental Determination of the Extinction Coefficient of CdTe, CdSe, and CdS Nanocrystals. *Chem. Mater.* **2003,** *15*, 2854-2860.

8. Ninomiya, S.; Adachi, S., Optical properties of cubic and hexagonal CdSe. *J. Appl. Phys.* **1995,** *78*, 4681-4689.

9. Boakye, F.; Nusenu, D., The energy band gap of cadmium sulphide. *Solid State Commun.* **1997,** *102*, 323-326.

10. Jang, E.; Jun, S.; Pu, L., High quality CdSeS nanocrystals synthesized by facile single injection process and their electroluminescence. *Chem. Commun.* **2003,** 24, 2964-2965.

11. Nag, A.; Kovalenko, M. V.; Lee, J.-S.; Liu, W.; Spokoyny, B.; Talapin, D. V., Metal-free Inorganic Ligands for Colloidal Nanocrystals: S^{2-}, HS^{-}, Se^{2-}, HSe^{-}, Te^{2-}, HTe^{-}, TeS_3^{2-}, OH^{-}, and NH_2^{-} as Surface Ligands. *J. Am. Chem. Soc.* **2011,** *133*, 10612-10620.

12. Pearson, R. G., HARD AND SOFT ACIDS AND BASES. *J. Am. Chem. Soc.* **1963,** *85*, 3533-3539.

13. Verwey, E. J. W., The electrical double layer and the stability of lyophobic colloids. *Chem. Rev.* **1935,** *16*, 363-415.

14. Ithurria, S.; Talapin, D. V., Colloidal Atomic Layer Deposition (c-ALD) using Self-Limiting Reactions at Nanocrystal Surface Coupled to Phase Transfer between Polar and Nonpolar Media. *J. Am. Chem. Soc.* **2012,** *134*, 18585-18590.

15. Jasieniak, J.; Mulvaney, P., From Cd-rich to Se-rich - The manipulation of CdSe nanocrystal surface stoichiometry. *J. Am. Chem. Soc.* **2007,** *129*, 2841-2848.

16. Nag, A.; Chung, D. S.; Dolzhnikov, D. S.; Dimitrijevic, N. M.; Chattopadhyay, S.; Shibata, T.; Talapin, D. V., Effect of Metal Ions on Photoluminescence, Charge Transport, Magnetic and Catalytic Properties of All-Inorganic Colloidal Nanocrystals and Nanocrystal Solids. *J. Am. Chem. Soc.* **2012,** *134*, 13604-13615.

17. Ip, A. H.; Thon, S. M.; Hoogland, S.; Voznyy, O.; Zhitomirsky, D.; Debnath, R.; Levina, L.; Rollny, L. R.; Carey, G. H.; Fischer, A.; Kemp, K. W.; Kramer, I. J.; Ning, Z. J.; Labelle, A. J.; Chou, K. W.; Amassian, A.; Sargent, E. H., Hybrid passivated colloidal quantum dot solids. *Nat. Nanotechnol.* **2012,** *7*, 577-582.

18. Nicholas C. Anderson, Mark P. Hendricks, Joshua J. Choi, and Jonathan S. Owen *J. Am. Chem. Soc*. **2013**, 135, 18536−18548

19. Li, Y. L.; Zhou, J.; Liu, C. L.; Li, H. B., Composite quantum dots detect Cd(II) in living cells in a fluorescence "turning on" mode. *J. Mater. Chem.* **2012,** *22*, 2507-2511.

20. Xu, H.; Miao, R.; Fang, Z.; Zhong, X. H., Quantum dot-based "turn-on" fluorescent probe for detection of zinc and cadmium ions in aqueous media. *Anal. Chim. Acta* **2011,** *687*, 82-88.

21. http://water.epa.gov/drink/contaminants/basicinformation/cadmium.cfm

22. Freeman, R.; Finder, T.; Bahshi, L.; Gill, R.; Willner, I., Functionalized CdSe/ZnS QDs for the Detection of Nitroaromatic or RDX Explosives. *Adv. Mater.* **2012,** *24*, 6416-6421.

23. Nagarkar, S. S.; Joarder, B.; Chaudhari, A. K.; Mukherjee, S.; Ghosh, S. K., Highly Selective Detection of Nitro Explosives by a Luminescent Metal-Organic Framework. *Angew. Chem.-Int. Edit.* **2013,** *52*, 2881-2885.

24. Kamat, P. V., Manipulation of Charge Transfer Across Semiconductor Interface. A Criterion That Cannot Be Ignored in Photocatalyst Design. *J. Phys. Chem. Lett.* **2012,** *3*, 663-672.

25. Dey, S.; Das, B.; Voggu, R.; Nag, A.; Sarma, D. D.; Rao, C. N. R., Interaction of CdSe and ZnO nanocrystals with electron-donor and -acceptor molecules. *Chem. Phys. Lett.* **2013,** *556*, 200-206.

26. Wei, S. H.; Zunger, A., Calculated natural band offsets of all II-VI and Ill-V semiconductors: Chemical trends and the role of cation d orbitals. *Appl. Phys. Lett.* **1998,** *72,* 2011-2013.

Chapter 3

(PART-A)

Luminescence from Defect-Tolerant $CsPbBr_3$ Perovskite Nanocrystals

---

The following article has been published based on the work presented in this chapter.

1. Swarnkar, A.; Chulliyil, R.; Ravi, V. K.; Irfanullah, M.; Chowdhury, A.; Nag, A. Colloidal $CsPbBr_3$ Perovskite Nanocrystals: Luminescence beyond Traditional Quantum Dots. *Angew. Chem., Int. Ed.* **2015,** *54*, 15424. Copy right permission has been taken from Wiley-VCH Verlag GmbH & Co. for the entire article.

Summary

As discussed in previous chapters that defects lying deep within the bandgap in a semiconductor trap the charge carriers and hamper the performance of optoelectronic devices. This problem becomes more severe in case of nanocrystals, in which, surface related defects dominate. Cesium lead halide ($CsPbX_3$; X = Cl, Br, I) perovskite shows defect tolerance nature because of its unique electronic band structure. Hence, nanocrystals of these materials exhibits high photoluminescence quantum yield (50-90%) without any core/shell type electronic passivation of surface. Suppression of blinking-off time is another interesting result, which arises due to the defect-tolerance nature of $CsPbBr_3$ nanocrystals. While the solution processed bulk organic-inorganic hybrid perovskite is an excellent material for solar cell applications, here we show the colloidal $CsPbBr_3$ nanocrystals have great potentials for light emitting applications. Also, all-inorganic $CsPbBr_3$ is thermally more stable than their hybrid counterpart. Colloidal $CsPbBr_3$ nanocrystals have many advantages over the traditional CdSe based colloidal quantum dot light emitters. Particularly, 11 ± 0.7 nm $CsPbBr_3$ nanocrystals exhibit intense light emission in the weak quantum confinement regime, and hence do not get affected by size-distribution issues. Consequently, spectral width of photoluminescence from ensemble of nanocrystals is similar to that from single-nanocrystal (78-86 meV). The fact that all the nanocrystals in the ensemble has almost identical band gap, results into negligible influence of Förster resonance energy transfer (FRET) and self-absorption on photoluminescence.

Graphical abstract

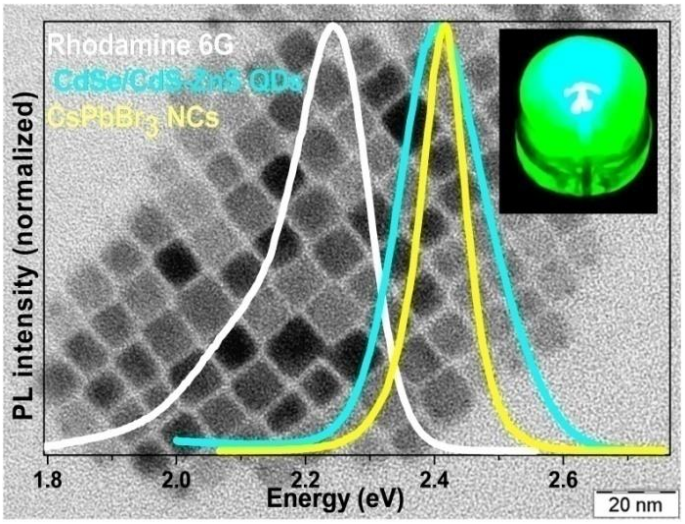

3A.1 Introduction

As discussed in chapter 1 that $CsPbX_3$ (X = Cl, Br or I) perovskite was reported by Møller in 1958.[1] Mitzi and coworkers showed interesting optoelectronic properties of organic-inorganic perovskite materials about twenty years back.[2] In about last ten years, solution processed organic-inorganic hybrid perovskite such as $CH_3NH_3PbI_3$ became one of the most celebrated material because of exhibiting >22% solar cell efficiency.[3-7] Defect tolerant nature of these lead halide perovskite, also prompted a few reports (at the time of this present work) on colloidal nanocrystals (NCs) of $APbX_3$ (A = CH_3NH_3 and Cs; X = Cl, Br and I), where intense photoluminescence (PL) has been the main property in spite of having surface defects.[8-11] At present time, there are a good number of reports coming on these colloidal nanostructures.

State of the art, highly luminescent CdSe based colloidal quantum dots (QDs), particularly, core/shell NCs found applications in ultra high definition displays because of narrower full width at half maxima (FWHM) of emission spectrum compared to that of organic dyes.[12-18] Additionally, such CdSe based core/shell QDs exhibit better photo-stability and size-dependent tunability of emission color. Kovalenko et al.[9] reported in year 2015 that $CsPbX_3$ (X = Cl, Br and I) NCs exhibit all the above mentioned benefits of traditional QDs. In fact, ~90% PL efficiency with narrow FWHM from $CsPbBr_3$ NCs is superior to most CdSe based NCs obtained even after surface modifications.

Intense luminescence from traditional CdSe based QDs can be observed only when the size of NC is smaller (<5 nm) than natural delocalization length of exciton (Bohr excitonic diameter), where strong quantum confinement of charge carriers enhances the transition probability. This requirement of quantum confinement, however, results into spectral broadening because of the size-distribution problem, and high density of trap states because of large surface to volume ratio (as discussed in chapter 1).[19] Owing to this size-distribution problem where smaller sized NCs exhibit higher optical gap compared to larger sized ones, chromaticity and PL quantum yield (QY) changes with concentration of NCs because of self-absorption and Förster resonance energy transfer (FRET).[20] For example, closed packed film of traditional QDs exhibit red-shifted PL with reduced intensity compared to the dilute solution of same NCs. Also, since the optical bandgap of such luminescent QD is strongly dependent on size of NCs, reproduction of NC synthesis resulting PL peak position within an error bar of ±5 nm is difficult. Another disadvantages of CdSe based QDs for light emitting diode (LED) applications is, decrease in optical gap with increasing temperature that can change the chromaticity of an LED with operation temperature.

In this work, we experimentally establish the defect tolerance in $CsPbBr_3$ perovskite NCs of size 11 ± 0.7 nm and show that these NCs are intrinsically different kind of highly luminescent NCs where size-distribution is not an issue, unlike traditional QDs. Our results show that emission from ensemble of $CsPbBr_3$ NCs does not suffer from any of these above mentioned demerits of traditional QDs, while maintaining nearly ideal (90%) PLQY. In order to understand luminescence from $CsPbBr_3$ NCs, we studied single-NC PL of such colloidal perovskite NCs. Surprisingly, FWHM (85 meV) of single NC is almost identical with that of ensemble measurement. Fluorescence intermittency, also known as blinking,[21-25] shows suppression of off-time.

3A.2 Experimental Sections

3A.2.1 Chemicals

Cesium carbonate ($CsCO_3$, Aldrich, 99.9%), lead (II) bromide ($PbBr_2$, 99.999%, Aldrich), cadmium oxide (CdO, 99.995%, Aldrich), zinc oxide (ZnO, ≥99%, Aldrich), oleic acid (OA, 90%, Aldrich), oleylamine (OAm, technical grade 70%, Aldrich), 1-Octadecene (ODE, technical grade 90%,Aldrich), sulfur (99.998%, Aldrich), selenium (99.99%, Aldrich), trioctylphosphine (TOP, 97%, Aldrich), trioctylphosphine oxide (TOPO, 99%, Aldrich), toluene (99.5%, Rankem), ethanol (99.9% AR, S D Fine chem. Ltd) formamide (FA, spectroscopy grade, Aldrich), *tert*-butanol (AR 99.5%, Rankem), Rhodamine-6G (99%, Aldrich), ethyl cellulose (48% ethoxyl , Aldrich), tetradecylphosphonic acid (TDPA, 97%, Aldrich). All the solvents and liquid reagents used in this work were made moisture free by applying vacuum for 1 hour at 120 ^oC and referred as "dried" in remaining sections.

3A.2.2 Synthesis of Cs-oleate as Cesium Precursor

0.407 g (1.25 mmol) Cs_2CO_3, 1.25 mL OA and 20 mL ODE were taken in a 50 mL 3-necked round bottom flask and the mixture was kept under vacuum for 30 min at 120 ^oC followed by purging with N_2 for 10 min along with mild magnetic stirring. This process of alternate application of vacuum and N_2 was repeated for 3 times to achieve the removal of moisture and O_2 from the reaction mixture. The temperature was increased to 150 ^oC. The reaction was continued until the Cs_2CO_3 got dissolved to give a clear solution after reacting with OA. The as-synthesized Cs-oleate solution in ODE was kept as cesium precursor for synthesis of $CsPbBr_3$ NCs.

3A.2.3 Synthesis of Colloidal $CsPbBr_3$ Perovskite NCs

In our present work, colloidal NCs of $CsPbBr_3$ of two different sizes were synthesized following a previous report.[9] 5 ml dried ODE and 69 mg (0.188 mmol) $PbBr_2$ were taken in a 25 mL 3-necked round bottom flask. The mixture was degassed (under alternate vacuum and nitrogen) at 120 °C for 60 minutes along with magnetic stirring. Dried OA and OAm, each 0.5 mL, was added to the mixture at 120 °C. After 30 min, $PbBr_2$ get dissolved in ODE and then the temperature was increased to 190 °C. As synthesized Cs-oleate (0.1M, 0.4 mL) solution in ODE, pre-heated at 100 °C, was swiftly injected to the reaction mixture. The reaction mixture became greenish and the reaction was stopped by dipping the reaction flask into an ice bath. The synthesized $CsPbBr_3$ NCs were precipitated by adding 5 ml *tert*-butanol at room temperature and then centrifuged at 7000 rpm. In this work, we have used epprndorf centrifuge machine of model number 4530 for the NCs purification. The radius of rotor is 100 mm. Finally, the wet pellet of the NCs was redispersed in 5 ml toluene for characterization. The obtained NCs were cubic in shape with edge length of 11±0.7 nm. To achieve smaller sized NCs (cube with 8±1 nm length), the reaction temperature was kept at 165 °C.

3A.2.4 Synthesis of Colloidal CdSe NCs

Colloidal CdSe NCs were synthesised after modifying the recipe given in ref. 26. 0.082 g (0.64 mmol) CdO, 0.356 g (1.28 mmol) TDPA, 1.62 g (4.2 mmol) TOPO and 5 mL OAm were taken in a 3-necked round bottom flask. The reaction mixture was degassed (under alternate vacuum and nitrogen) at 120 °C for 60 minutes. The temperature was then raised to 320 °C forming a clear solution. 4 mL of 0.2 M Se solution in TOP was swiftly injected causing a decrease in temperature to 270 °C. The reaction was stopped after 10 min, followed by addition of 10 ml toluene at 90 °C. NCs were precipitated by adding ethanol and centrifuged at 7000 rpm for 10 min. Obtained wet precipitate was redispersed in toluene, and the washing (precipitation-centrifugation-redispersion) of NCs was repeated thrice to remove any unreacted precursors. Final CdSe NC precipitate was redispersed in toluene for further measurements.

3A.2.5 Synthesis of Colloidal CdSe/CdS-ZnS Core/Hybrid-Shell NCs

The synthesis was carried out following ref.27. 0.0496 g CdO, 0.0496 g ZnO, 2 mL OA and 10 mL ODE was degassed (under alternate vacuum and nitrogen) at 120 °C for 60 minutes. The temperature of reaction mixture was increased to 310 °C forming a clear solution. 1 mL TOP solution containing sulfur (0.0567 g) and selenium (0.0075 g) is then quickly injected to the uniformly stirred Cd and Zn oleate

solution kept at 310 °C. The reaction was carried out for 30 sec. While cooling down to room temperature, the reaction mixture was diluted with ~10 mL toluene at 90 °C. Precipitation of NCs was carried out using ethanol followed by centrifugation. The NCs were redispersed in toluene and again precipitated with ethanol. The process of redispersion/precipitation was repeated once more. The final NCs were redispersed in toluene.

3A.2.6 Characterization

UV-visible absorption spectra were recorded using a Perkin Elmer, Lambda-45 UV/Vis spectrometer. Steady state PL and PL decay dynamics (time correlated single photon counting (TCSPC)) of NCs were measured using FLS 980 (Edinburgh Instruments). UV-visible absorption and PL experiments were done in solution as well as on thin film prepared by spin-coating of the colloidal NCs solution (~5 mg/ml, dispersed in toluene) on quartz substrate and then dried in ambient condition. UV-visible absorption spectra for both solution and film were taken in transmittance mode. Powder x-ray diffraction (XRD) data were recorded using a Bruker D8 Advance x-ray diffractometer using Cu Kα radiation (1.54 Å). Transmission electron microscopy (TEM) studies were carried out using a JEOL JEM 2100 F field emission transmission electron microscope at 200 kV. The sample preparation for TEM was done by putting a drop of the colloidal solution of NCs in hexane on the carbon coated copper grids. Differential Scanning Calorimeter (DSC) measurements were carried out on $CsPbBr_3$ NC powder using TA Q20 DSC. The data were recorded at heating and cooling rate of 10 °C/min.

3A.2.7 Effect of UV-light and Temperature on PL

PL spectra at varying temperatures were recorded by increasing the temperature by a step width of 10 °C of cuvette holder enabled with a digital temperature controller. In the experiment of photostability, the sample was exposed to 365 nm UV light and PL spectra were recorded at varying interval of UV exposure time. All the measurements were done under inert atmosphere and using anhydrous solvents. NC dispersions were prepared and filled in a cuvette inside a N_2 filled glove box. The cap of the cuvette was sealed before taking it out of glove box.

3A.2.8 Measurement of PLQY

PLQY of colloidal solution of $CsPbBr_3$ NCs has been measured at room temperature by taking rhodamine 6G dissolved in ethanol as a reference dye. $CsPbBr_3$ NCs were dispersed in toluene. For NC

films, UV-visible absorption and PL spectra were measured at 10 different points in the film and then averaged out to calculate approximate QY.

3A.2.9 Coating of $CsPbBr_3$ NCs on UV Light Emitting Diodes (LEDs)

A gel of colloidal solution of $CsPbBr_3$ NCs was prepared by mixing 1 g ethyl-cellulose in 5 mL of toluene and 1 mL of as-synthesized colloidal solution of $CsPbBr_3$ (~5 mg/mL) dispersed in toluene. The mixture was sonicated for ~ 60 min to get a homogeneous gel. Then the UV (λ_{max} = 365 nm) LEDs were dip coated in the gel of NCs and dried for 60 min before lighting. $CsPbBr_3$ coated LED emits intense green light (as shown in Figure 3A.8 in this chapter) by applying a voltage 3.0 V and passing a current of 60 μA across the terminals of the LED.

3A.3 Results and Discussion

3A.3.1 Crystallographic Phase and Morphology of $CsPbBr_3$ NCs

Colloidal $CsPbBr_3$ NCs were prepared following ref.9. Details of synthesis are given in the experimental sections. Characterization of $CsPbBr_3$ NCs using TEM, powder XRD, DSC and high resolution TEM are shown in Figure 3A.1 to 3A.5. Figure 3A.1 shows that the size of the NCs can be controlled by varying the reaction temperature, in which, 8±1 nm (Figure 3A.1a) and 11±0.7 nm (Figure 3A.1b) sized (edge length of cube shaped NCs) $CsPbBr_3$ NCs are synthesized at reaction temperature of 165 and 190 ^oC respectively. These reaction temperatures are much lower than those of the traditional II-VI[26-27] and III-V[28] colloidal QDs. It is to be noted that the perovskite NCs can be synthesized even at room temperature because of their more ionic nature than the traditional QDs.[10]

Powder XRD pattern in Figure 3A.2 shows orthorhombic phase of $CsPbBr_3$ NCs. This observation agrees with bulk $CsPbBr_3$ that are known to exhibit thermodynamically stable orthorhombic phase at room temperature. But first report of $CsPbBr_3$ NCs in ref. 9 suggested cubic phase though their XRD pattern appear similar to our NCs powder XRD pattern. To clarify this further, we measure DSC data, which also suggested orthorhombic phase of our $CsPbBr_3$ NCs. DSC data in Figure 3A.3 agrees with that reported[29] for bulk $CsPbBr_3$, where orthorhombic to tetragonal transition at 91 ^oC, and tetragonal to cubic transition at 132 ^oC are observed. Orthorhombic $CsPbBr_3$ exhibits corner-shared $[PbBr_6]^{4-}$ octahedra in 3-D fashion (see Figure 3A.4) and is an optoelectronically active perovskite phase, unlike the orthorhombic $CsPbI_3$, in which the octahedra are not corner-shared.[9]

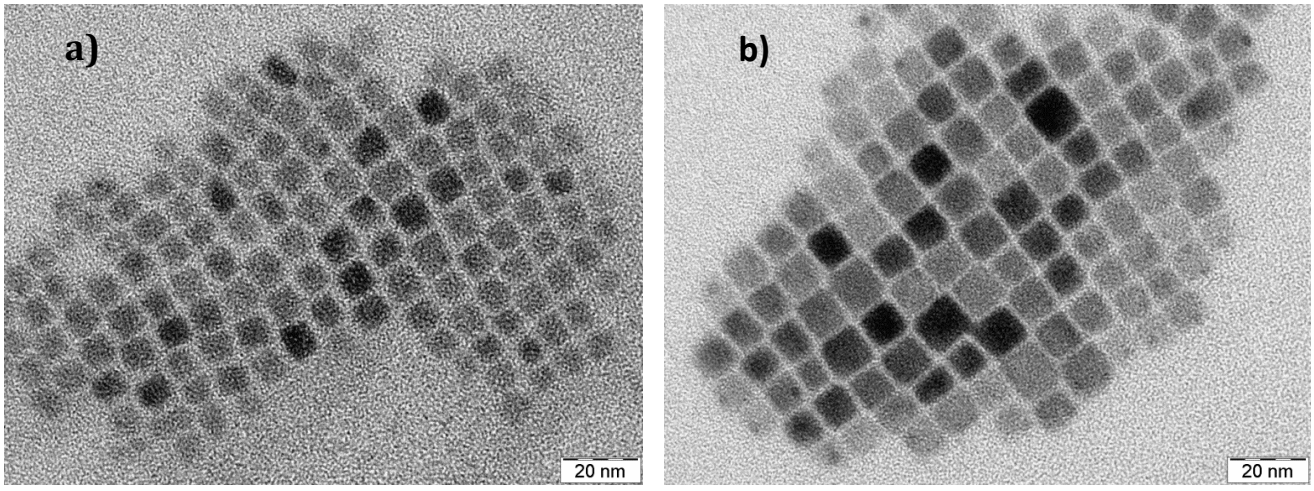

Figure 3A.1: Controlling the size of $CsPbBr_3$ nanocrystals. Transmission electron microscopy (TEM) image of a) 8±1 nm and b) 11±0.7 nm $CsPbBr_3$ nanocrystals synthesized by hot injection synthesis.

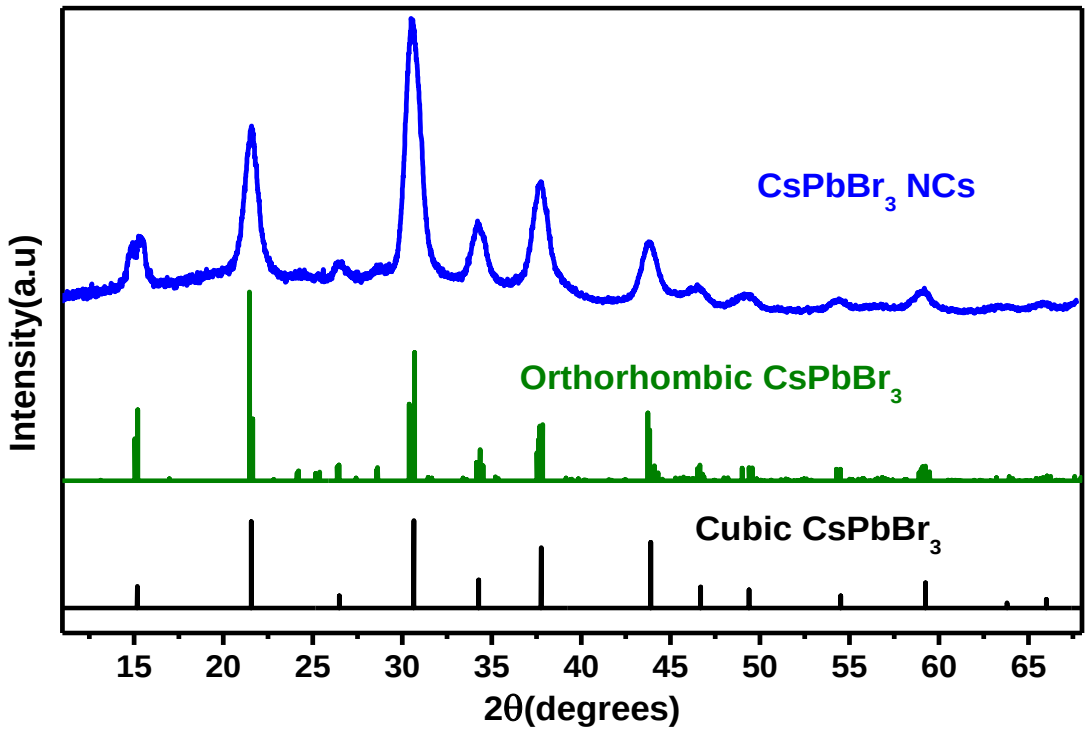

Figure 3A.2: Crystal structure of $CsPbB_3$ nanocrystals. Powder XRD pattern of 11±0.7 nm $CsPbBr_3$ nanocrystals showing orthorhombic phase.

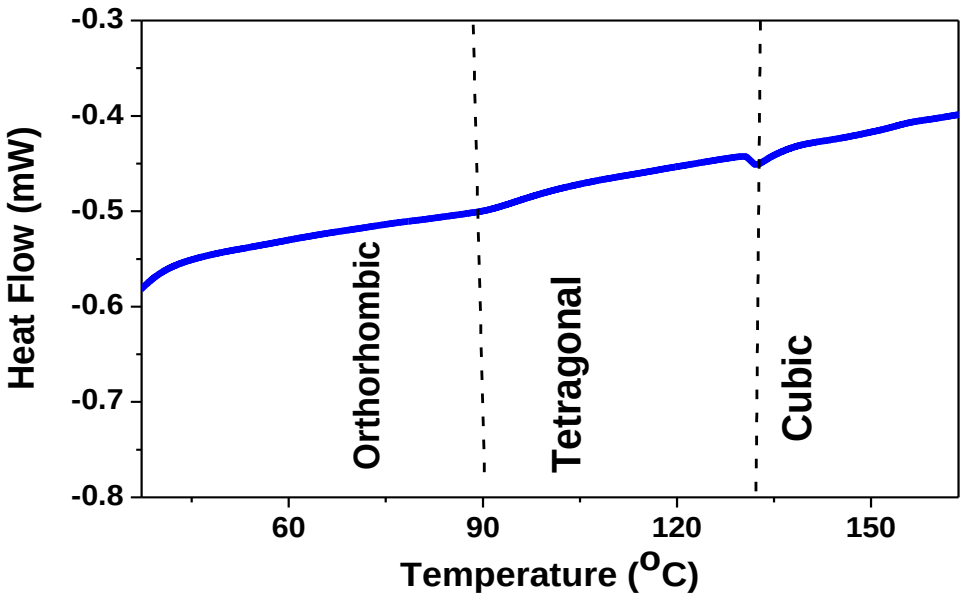

Figure 3A.3: Phase transition of $CsPbB_3$ nanocrystals. Differential scanning calorimetric (DSC) data of 11±0.7 nm $CsPbBr_3$ nanocrystals.

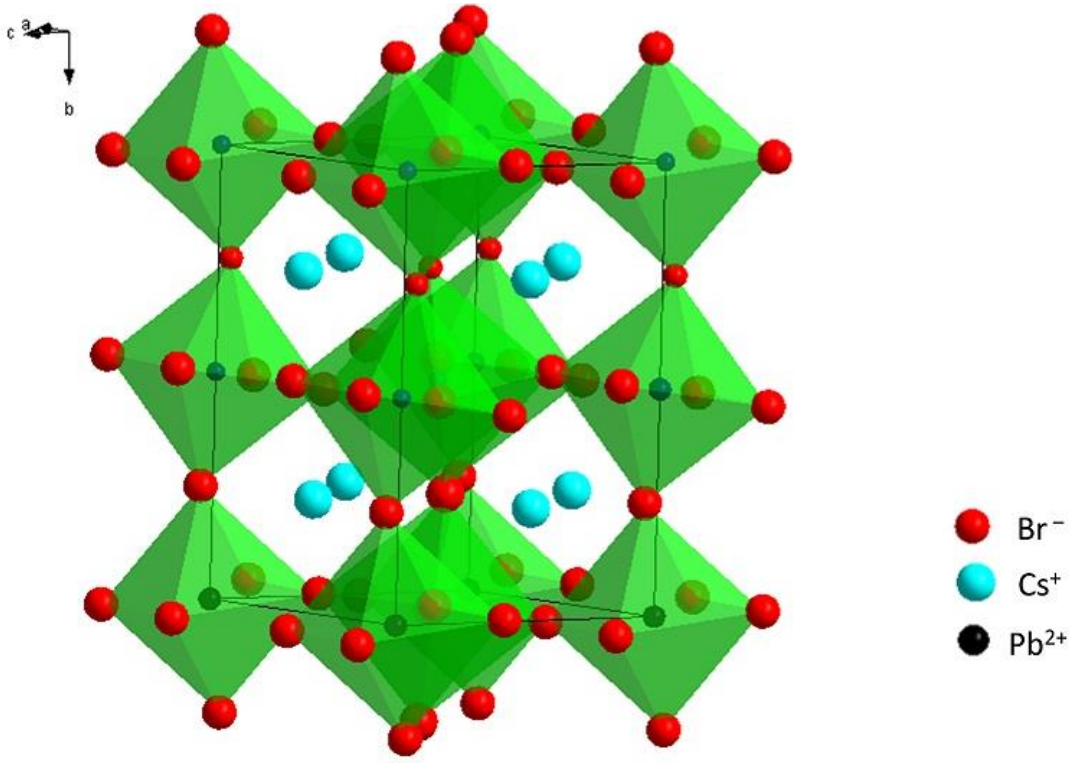

Figure 3A.4: Orthorhombic crystal structure of $CsPbBr_3$. Orthorhombic phase of $CsPbBr_3$ showing tilted and corner-shared $[PbBr_6]^{4-}$ octahedra.[30]

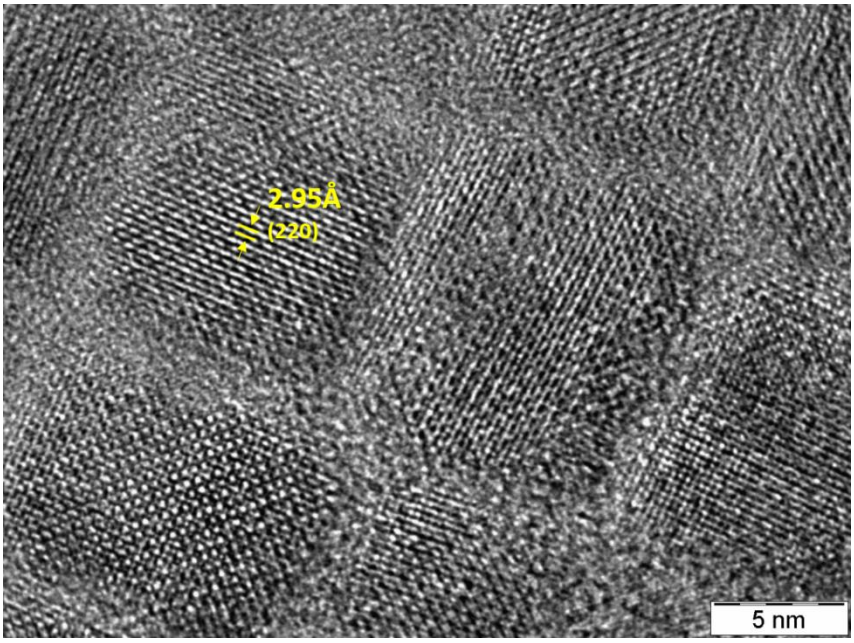

Figure 3A.5: Crystal planes of $CsPbBr_3$ nanocrystals. High resolution TEM (HRTEM) image of $CsPbBr_3$ nanocubes, synthesized at 190 ^oC showing lattice fringes.

This first report of similarity of crystal phase behavior of $CsPbBr_3$ NCs with its bulk counterpart is important in order to understand the origin of difference in PL behavior between bulk and NC samples. In support of all these above data, high resolution TEM (HRTEM) image (in Figure 3A.5) shows interplanner distance of 2.95 Å corresponding to (220) plane of orthorhombic $CsPbBr_3$.

3A.3.2 Luminescence Properties of $CsPbBr_3$ NCs

Figure 3A.6 a (UV-visible absorption spectra) and Figure 3A.6 b (PL data) shows very small (0.02 eV) blue shift in the absorption edge and emission maxima by reducing the edge length of $CsPbBr_3$ cubes from 11 to 8 nm. This observation suggest week quantum confinement of charge carriers in this size regime, which agrees with the reported[9] ~7 nm excitonic Bohr diameter of $CsPbBr_3$. In spite of having weakly confined charge carriers, our 11 nm $CsPbBr_3$ NCs exhibit the best PLQY of 90%, and has been studied more extensively in this chapter. Figure 3A.7 compares spectral shapes of PL originating from organic dye rhodamine 6G, CdSe/CdS-ZnS core/hybrid shell NCs, and $CsPbBr_3$ NCs. Clearly, $CsPbBr_3$ NCs exhibit the best color purity of emitted light with narrowest FWHM (85 meV). Such a narrow FWHM, along with 90% PL QY, makes these $CsPbBr_3$ NCs suitable for application in ultra-high

definition displays. Figure 3A.8 shows photograph of an LED prepared by coating $CsPbBr_3$ NCs on UV (λ_{max}= 365 nm) LED. The LED continues to emit intense light after 3 months from the date of fabrication, even when stored under ambient condition suggesting high stability of $CsPbBr_3$ NCs. This low sensitivity to moisture might arise from the coating of hydrophobic capping ligands on the NC surface, but needs to be studied further. Also, Figure 3A.9 shows that the PL from colloidal $CsPbBr_3$ NCs is stable under prolonged exposure to 365 nm UV light.

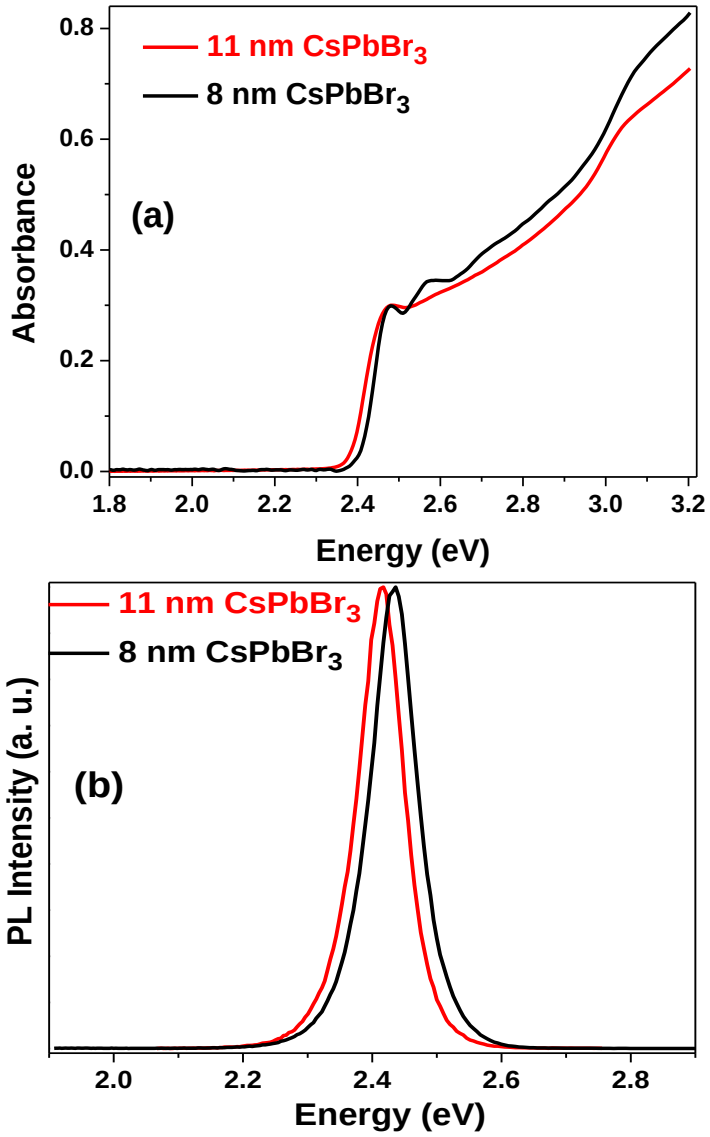

Figure 3A.6: Optical properties of different sized $CsPbBr_3$ nanocrystals. (a) UV-visible absorption and (b) PL spectra for 8±1 nm (black line) and 11±0.7 nm (red line) $CsPbBr_3$ nanocrystals dispersed in toluene.

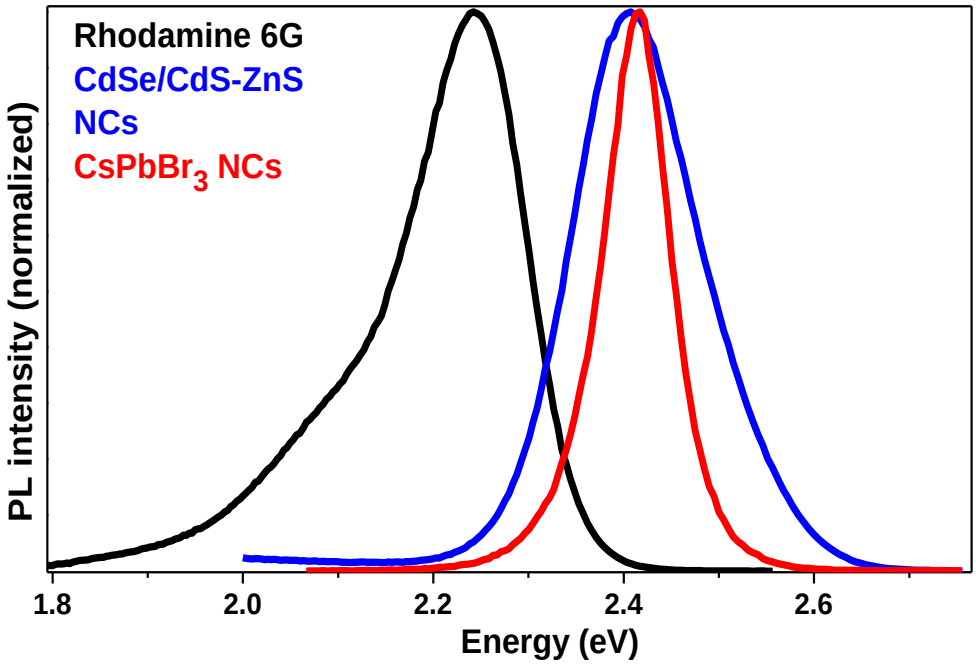

Figure 3A.7: Emission color purity of different fluorescent materials. PL spectral line widths obtained from a representative organic dye Rhodamine 6G (black line), CdSe/CdS-ZnS core/hybrid-shell nanocrystals (blue line), and $CsPbBr_3$ nanocrystals (red line).

Figure 3A.8: $CsPbBr_3$ nanocrystals as emitter. Photograph of a green LED obtained after coating an UV-LED with $CsPbBr_3$ nanocrystals.

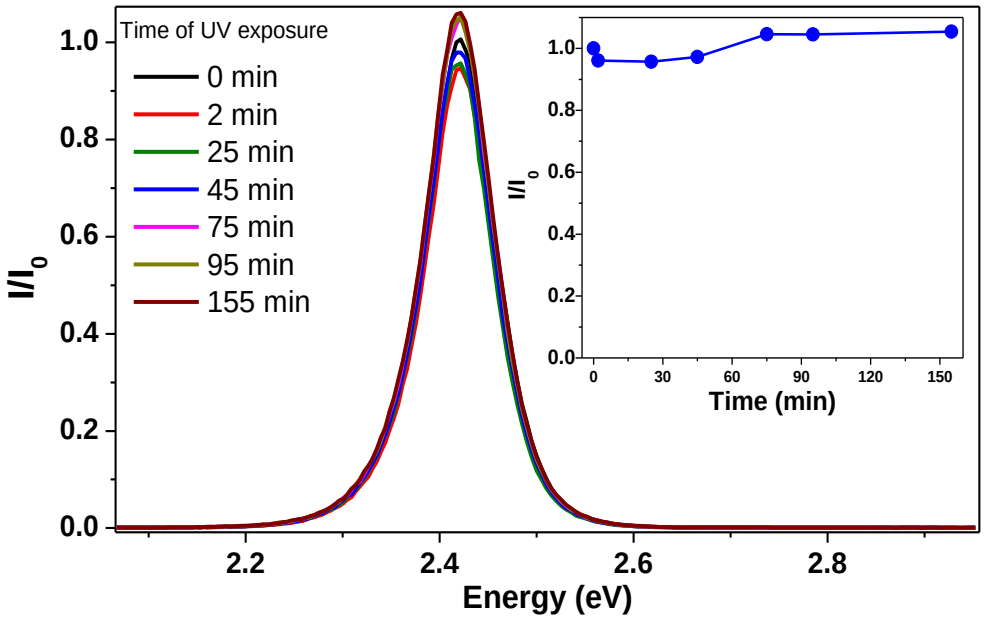

Figure 3A.9: Photostability of $CsPbBr_3$ nanocrystals. PL spectra, and relative PL intensity (inset) of 11±0.7 nm $CsPbBr_3$ nanocrystals with exposure to 365 nm UV light. I is the PL intensities measured at a given time during UV exposure, and I_0 corresponds to PL intensity before UV exposure. Note that PL energy and FWHM also does not change with exposure to UV light.

Optical bandgap of a semiconductor usually decreases with increasing temperature mainly because of electron-phonon interaction.[31] PL spectra of colloidal CdSe NCs (Figure 3A.10) and CdSe/CdS-ZnS core/hybrid-shell NCs (Figure 3A.11) systematically red-shifted by 0.03 eV (8 nm), and 0.04 eV (9 nm), upon increasing the measurement temperature from 25 ^{o}C to 100 °C. Such temperature-dependent change in emission energy can change the chromaticity of an LED, since the device often gets heated up during prolonged operation. To our surprise, $CsPbBr_3$ NCs get rid of this problem, and do not exhibit any change in PL peak position in the temperature range of 25 to 100 ^{o}C as shown in Figure 3A.12. This unusual behavior can be attributed to the electronic band structure of $CsPbBr_3$, where the optical bandgap predominantly arises from anti-bonding (Pb 6s and Br 4p) valence band maximum and non-bonding (Pb 6p) conduction band minimum. Therefore, thermal expansion of the lattice which would decrease the cation–anion interaction, does not decrease the optical gap.[31-33] Further theoretical and experimental studies over a wider temperature range are required for a better understanding of this behavior.

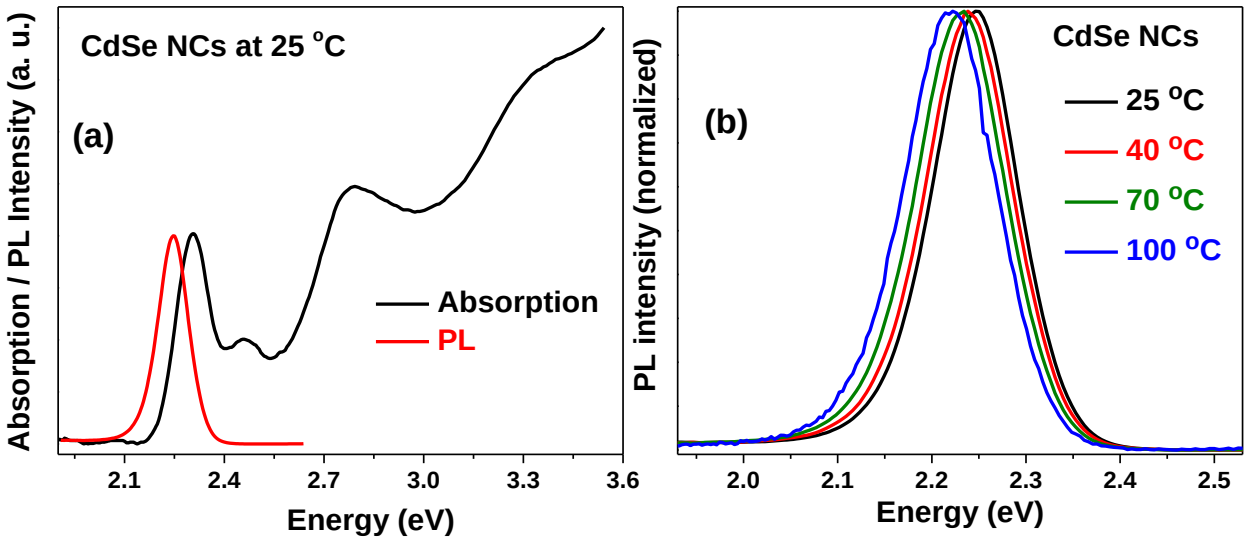

Figure 3A.10: CdSe nanocrystals and its temperature dependent chromaticity. (a) UV-visible absorption and PL spectra of ~2.6 nm CdSe nanocrystals at room temperature. Size of the nanocrystals is calculated by using the relation of size of nanocrystals and the lowest energy absorption peak by following ref [34]. (b) Change in PL spectra of the same CdSe nanocrystals with temperature of PL measurement. This temperature dependent change is reversible suggesting the nanocrystal size does not change during these experiments.

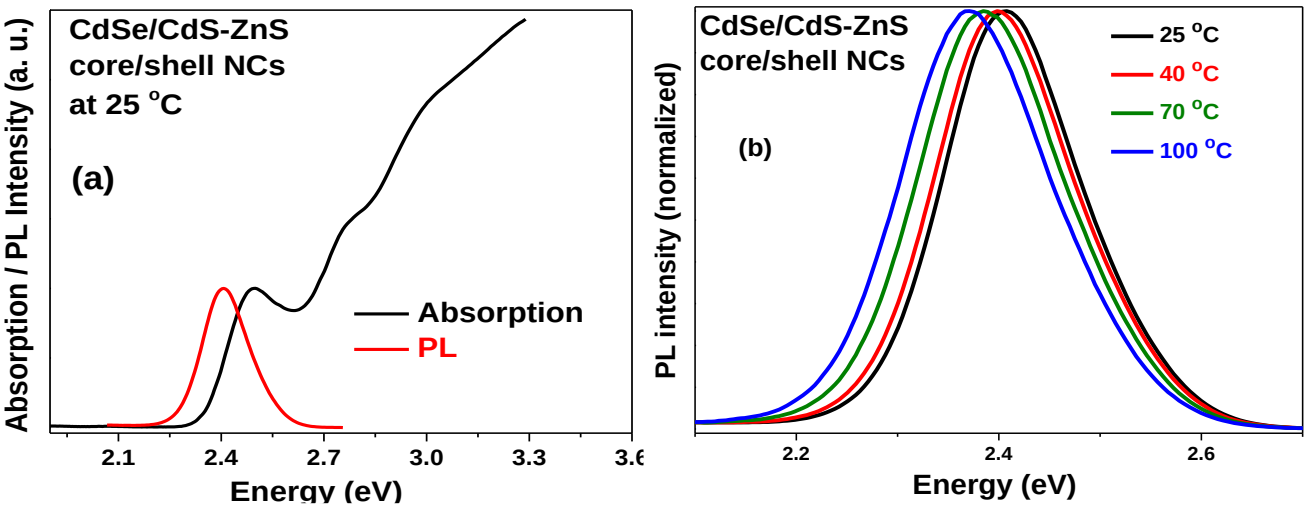

Figure 3A.11: CdSe/CdS-ZnS core/hybrid shell nanocrystals and its temperature dependent chromaticity. (a) UV-visible absorption and PL spectra at room temperature, and (b) PL spectra at different temperatures for CdSe/CdS-ZnS core/hybrid-shell nanocrystals.

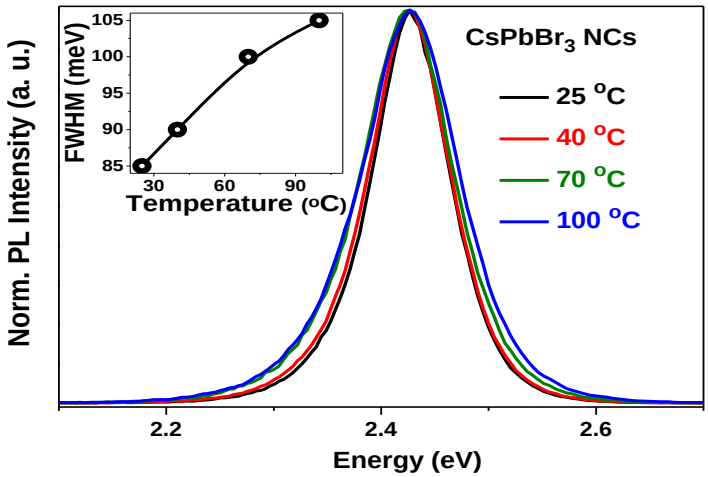

Figure 3A.12: Temperature independent chromaticity of $CsPbBr_3$ nanocrystals at high temperature. Variation in PL spectra of colloidal $CsPbBr_3$ nanocrystals with measurement temperature. Inset shows the variation in the value of FWHM on varying the temperature.

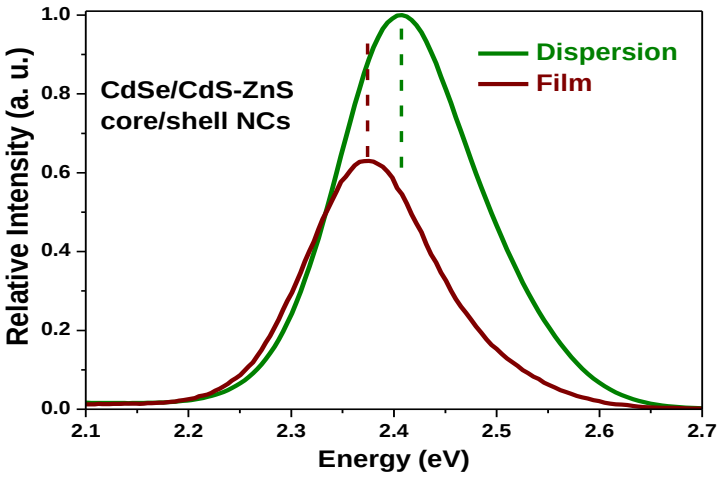

Figure 3A.13: Change in chromaticity of PL from CdSe based nanocrystals. PL spectra for CdSe/CdS-ZnS core/hybrid-shell nanocrystals dispersed in toluene and a film of the same nanocrystals on a quartz substrate. PL intensities were compared after normalizing with absorbance at the excitation wavelength 3.1 eV (400 nm). For films, absorption and PL data were collected at 10 different locations of the film, averaged spectra are plotted to minimize the error that can arise because of inhomogeneity in film thickness.

Another aspect of luminescent semiconductor NCs is red-shift in PL spectrum at very high concentration compared to their dilute dispersion, because of self-absorption and/or FRET.[20, 35] For

example, Figure 3A.13 shows the red-shift in the PL spectrum of CdSe/CdS-ZnS core/hybrid-shell NC film, compared to the corresponding dilute dispersion in toluene. Such red-shifts in close-packed films happens either because of light emitted by a smaller NC is re-absorbed (self-absorption) by a larger NC in the ensemble, and/or the excited smaller NC non-radiatively (FRET) transfers its energy to a larger NC. Both phenomena can take place because larger NC has a smaller optical gap compared to that of smaller NC. Such processes result into more contribution to PL from the fraction of larger NCs within the ensemble, therefore, red-shifting the spectrum with increasing the concentration (closer proximity) of NCs. Figure 3A.13 also exhibits a decrease in the relative PL intensity for CdSe/CdS-ZnS core/hybrid-shell NC film compared to the corresponding dilute dispersion. This decrease is because of the fact that some of the lager NCs that got excited at the cost of emission from the smaller NCs, might be non-emitting (or poorly emitting) NCs. To our surprise, (Figure 3A.14) both peak position and relative intensity of $CsPbBr_3$ NCs remained almost identical for both close-packed film and dilute dispersion. This unique observation suggests that both self-absorption and FRET negligibly influence the PL spectrum of the $CsPbBr_3$ NC film.

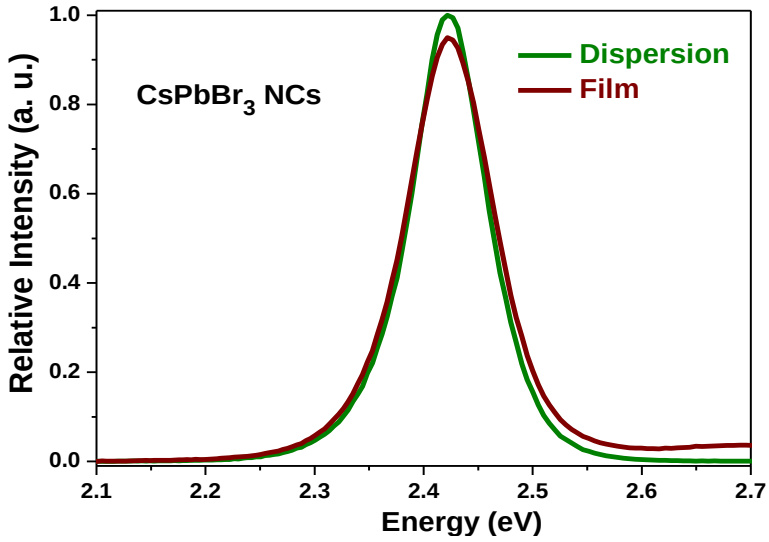

Figure 3A.14: No change in chromaticity of PL from $CsPbBr_3$ nanocrstals. PL spectra for $CsPbBr_3$ nanocrystals dispersed in toluene and a film of the same nanocrystals on a quartz substrate. PL intensities were compared after normalizing with absorbance at the excitation wavelength 3.1 eV (400 nm). For films, absorption and PL data were collected at 10 different locations of the film, averaged spectrum is plotted to minimize the error that can arise because of inhomogeneity in film thickness.

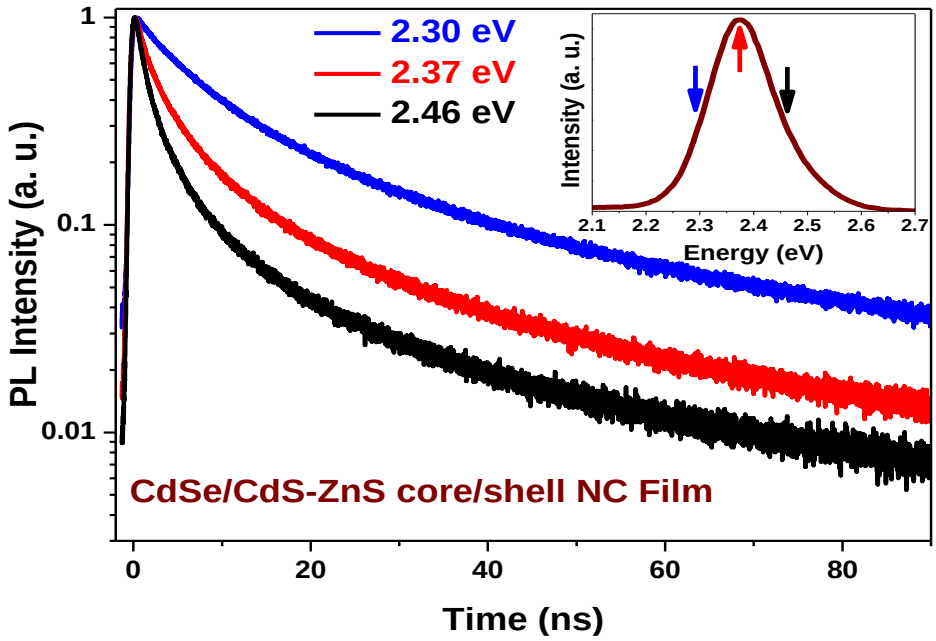

Figure 3A.15: Energy transfer in CdSe based nanocrystal film. PL decay profiles obtained from film of CdSe/CdS-ZnS core/hybrid-shell nanocrystals at different emission wavelengths as mentioned in each panel. Insets: corresponding PL spectrum indicating the emission wavelengths for PL decay by color coded arrows. NCs were excited 400 nm.

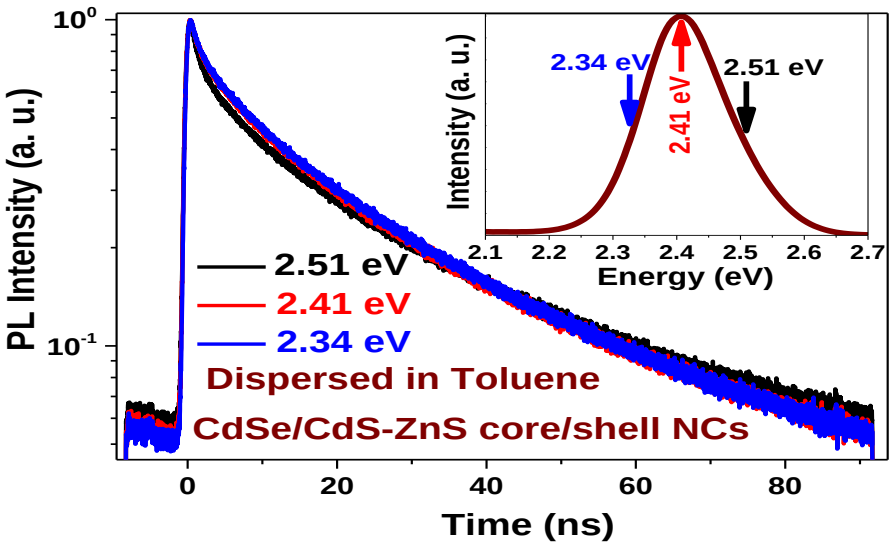

Figure 3A.16: Suppression of influence of energy transfer in dispersion of nanocrystals. PL decay profiles obtained from dispersion of CdSe/CdS-ZnS core/hybrid-shell nanocrystals in toluene at different emission wavelengths as mentioned in each panel. Insets: corresponding PL spectrum indicating the emission wavelengths by color coded arrows.

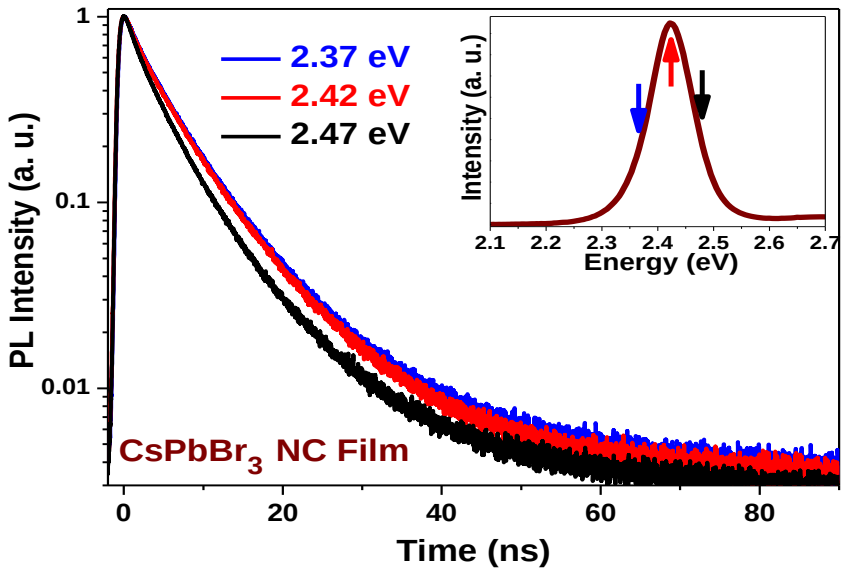

Figure 3A.17: Suppression of influence of energy transfer in $CsPbBr_3$ nanocrystal film. PL decay profiles obtained from film of $CsPbBr_3$ nanocrystals at different emission wavelengths as mentioned in each panel. Insets: corresponding PL spectrum indicating the emission wavelengths by color coded arrows.

PL decay dynamics in Figure 3A.15 show that the film of CdSe/CdS-ZnS core/hybrid-shell NCs systematically exhibit faster decay at higher emission energies. This is because smaller NCs that emit at higher energies exhibit an additional FRET related decay channels compared to larger NCs emitting at lower energies. On the other hand the dilute dispersion of the same sample (Figure 3A.16) does not show such differences in PL decay at different emission energies because of larger inter-NC distance disfavoring FRET. In contrast, Figure 3A.17, does not show any significant difference in the PL decay from the film of $CsPbBr_3$ NCs when measured at different emission energies. Such similarities suggest that contribution from FRET is less in the case of $CsPbBr_3$ NC film. Also, Figure 3A.18 shows that absorption tail at energies lower than the peak corresponding to lowest energy excitonic absorption of $CsPbBr_3$ NC is significantly less compared to that for CdSe/CdS-ZnS core/hybrid-shell NCs. This sharp rise in the excitonic absorption of $CsPbBr_3$ NCs can explain the suppression of FRET, and agrees with both absence of size-distribution related broadening of optical gap, and small Urbach energy reported[7] for bulk lead-halide perovskites.

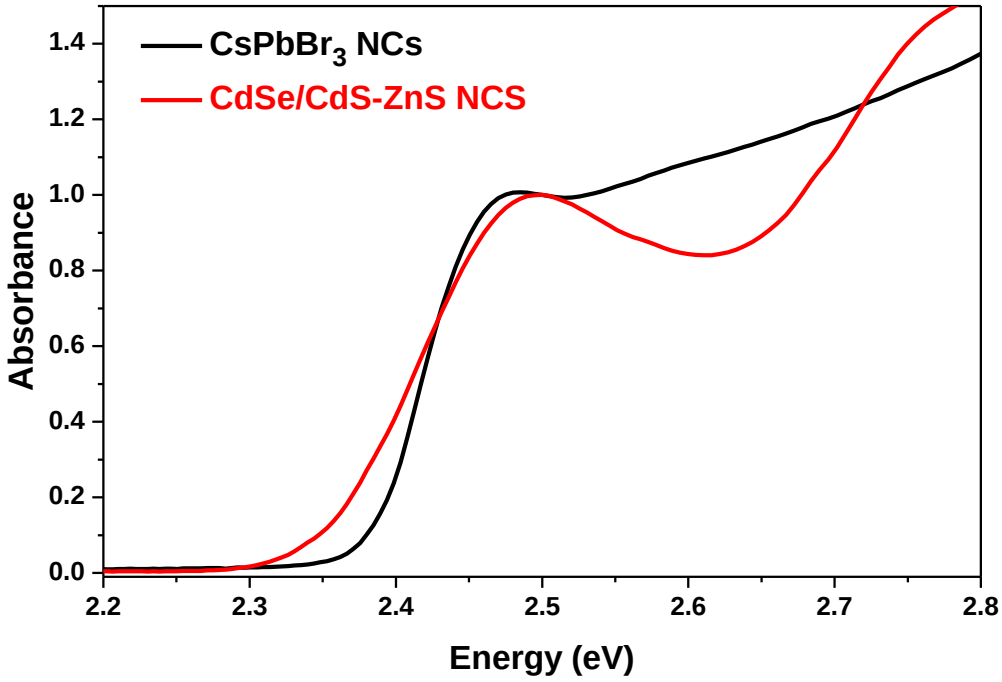

Figure 3A.18: Urbach tail. Comparison of absorption tail at energies below the peak for lowest energy excitonic absorption.

PL decays from $CsPbBr_3$ NC film at different emission energies were fitted with a bi-exponential decay, and results are shown in Figure 3A.19 and Table 1. Two lifetimes obtained from the fittings are around 3 ns and 8 ns, with nearly equal contributions. Interesting to note that (i) there is no sub-ns non-radiative decay channels agreeing with the nearly ideal PLQY, and (ii) radiative lifetimes are significantly shorter compared to typical lifetimes (~100 ns) observed for bulk perovskites such as $CH_3NH_3PbBr_3$.[10] The decrease in the radiative lifetime, along with the observed excitonic features in absorption spectrum (Figure 3A.6a) suggest that the PL of $CsPbBr_3$ NCs arises from excitonic recombination, unlike the recent reports[36-37] of bulk $CH_3NH_3PbI_3$, where recombination of free electron and hole has been proposed to give rise PL. Our excitonic emission from $CsPbBr_3$ NCs can be explained by higher excitonic binding energy for bulk $CsPbBr_3$ (40 meV) compared to that of bulk $CsPbI_3$ (20 meV).[5] Furthermore, nanocrystalline dimension also promotes Columbic interaction between electron and hole.

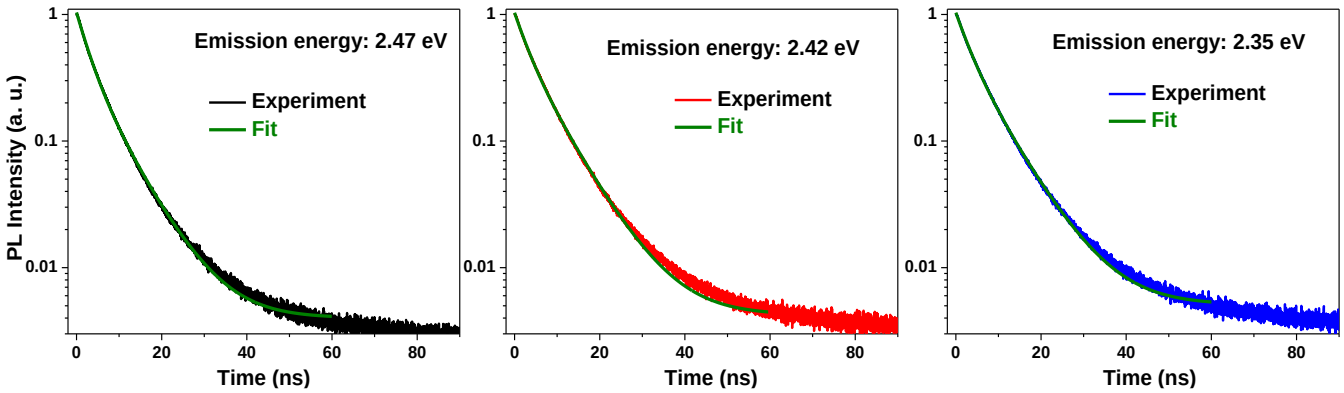

Figure 3A.19: PL lifetime of $CsPbBr_3$ nanocrystals. PL decay profiles obtained for $CsPbBr_3$ nanocrystals (11±0.7 nm) film at different emission energies as mentioned in each panels. Experimental data are same as those shown in Figure 3A.16 of chapter. Experimental data were fitted in the range of 0 to 60 ns, using bi-exponential decay.

Table 3A.1: The best fit parameters of photoluminescence decay profiles of $CsPbBr_3$ NC film at different emission energies shown in Figure 3A.19, using bi-exponential decay: $I(t) = a_1\exp(-t/\tau_1) + a_2\exp(-t/\tau_2)$.

Emission Energy (eV)	a_1 (%)	τ_1 (ns)	a_2 (%)	τ_2 (ns)
2.37	49	3.1	51	7.8
2.42	48	3.0	52	7.7
2.47	60	2.9	40	7.3

Another major problem of traditional CdSe based QDs is the poor reproducibility of emission wavelength for NCs synthesized in different batches. This problem of reproducibility is absent in the case of $CsPbBr_3$ NCs (Figure 3A.20) with batch to batch reproducibility of optical gap within ± 1 nm. Not only is the peak position, PLQYs of $CsPbBr_3$ NCs are also reproducible. Such unique reproducibility of PL from $CsPbBr_3$ is probably because larger size (~11 nm) of NCs, where, size-dependent change in bandgap is less prominent, and also surface defects do not trap the charge carriers. It is to be noted that the synthesis of $CsPbBr_3$ NCs is rather simple compared to complex synthesis of a typical core/shell NCs.

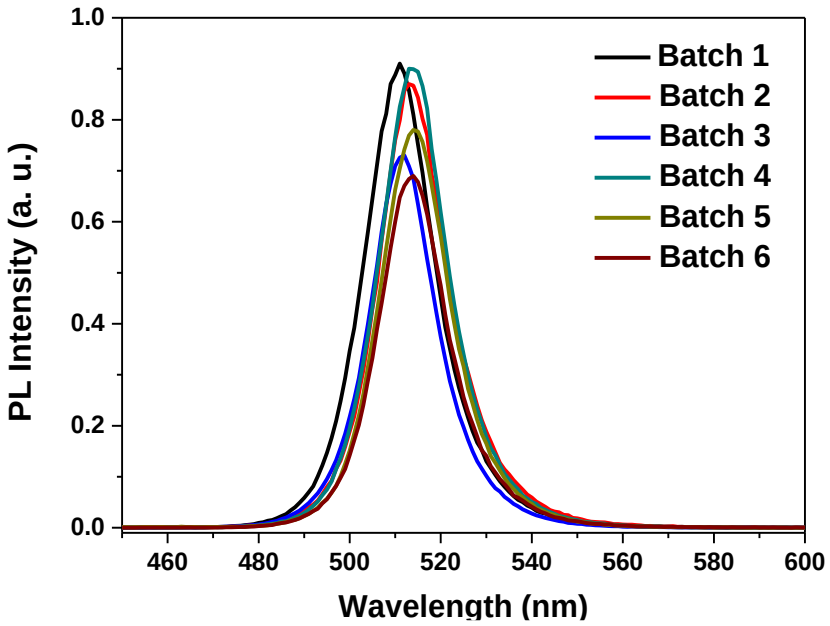

Figure 3A.20: Reproduction of PL properties. Reproducibility of emission wavelength of 11±0.7 nm $CsPbBr_3$ nanocrystals synthesized in different batches keeping all the reaction parameter same.

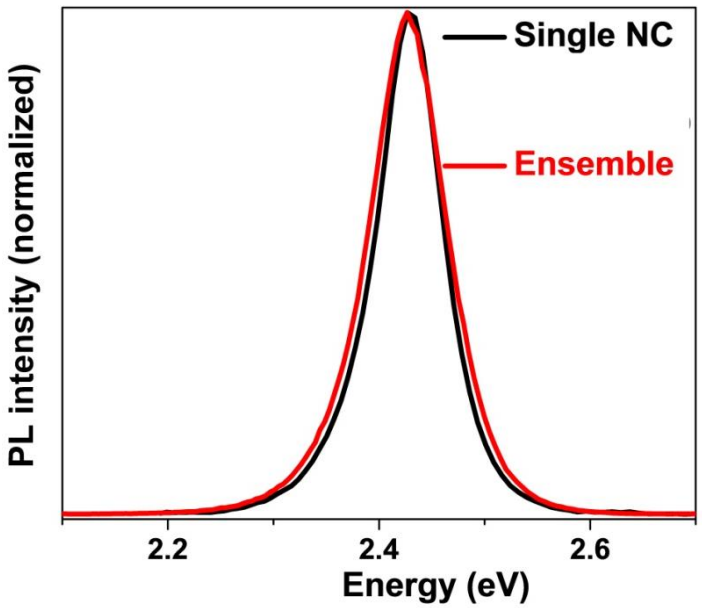

Figure 3A.21: Single nanocrystal versus ensemble PL. Normalized PL emission spectra of an ensemble of nanocrystals in solution (red line) and a representative single-nanocrystal (black line) spectra. Single-nanocrystal photoluminescence measurements were done in collaboration with Prof. Arindam Chowdhury at Indian Institute of Technology (IIT), Bombay, India.

3A.3.3 Single-NC PL of $CsPbBr_3$ NCs and PL Blinking

In order to understand the unique features from PL of $CsPbBr_3$ NCs, we studied single-NC PL in collaboration with Prof. Arindam Chowdhury group at Indian Institute of Technology (IIT), Bombay, India. Remarkably, FWHM of single-NC PL is almost identical with that of ensemble (Figure 3A.21), showing that the detrimental effect of size-distribution in broadening PL spectrum is absent for ensemble of $CsPbBr_3$ NCs. The absence of size-distribution related broadening of PL spectrum of ensemble of highly luminescent $CsPbBr_3$ NCs is rather unique, compared to traditional CdSe based QDs. Our ~11 nm $CsPbBr_3$ NCs is slightly larger than the corresponding Bohr excitonic diameter of 7 nm, exhibiting weak quantum confinement effect on charge carriers. This weak nature of confinement, along with obtained narrow size-distribution, ensures that the individual $CsPbBr_3$ NCs within an ensemble exhibit almost identical optical bandgap. On the other hand, traditional QDs require a stronger confinement of charge carriers in order to exhibit high PL QY,[19] where a larger inhomogeneity in optical bandgap of NCs within an ensemble arises even after achieving a narrow size distribution. In the case of $CsPbBr_3$ NCs, weak confinement of charge carrier is sufficient enough exhibiting high transition probability for luminescence unlike their bulk counterpart. In addition to the extraordinary semiconducting properties explored for such bulk perovskite structure.[2-7, 38] nearly identical effective mass of electron (m_e = 0.15 electron mass) and hole (m_h = 0.14 electron mass),[9] will lead to equal extent of confinement for both charge carriers, which in turn is expected to increase the QY of excitonic PL. Detailed theoretical studies on the quantum confinement effect of such perovskite NCs are required for a better understanding. The fact that PL is not much influenced by size-distribution of ~11 nm $CsPbBr_3$ NCs, explains our observations such as (i) narrow FWHM of ensemble, (ii) batch to batch reproducibility, and (iii) negligible influence of self-absoprion and FRET on emission energy. This weak confinement on the other hand will inhibit significant size-dependent tuning of emission color, which can be overcome by controlling the composition of $CsPbX_3$, where X can be a combination of Cl, Br, and I as shown in ref. 9.

Figure 3A.22 shows the blinking characteristics along with the fraction of single $CsPbBr_3$ NCs that exhibit similar nature of PL intermittency. Importantly, the vast majority (ca. 90%) of several hundred individual NCs studied display substantial blinking suppression, that is, remain mostly emissive (on-time > 85%), and the nature of blinking is not severely affected over a wide range of excitation powers. Details of the single-NC PL could be found in our published article.

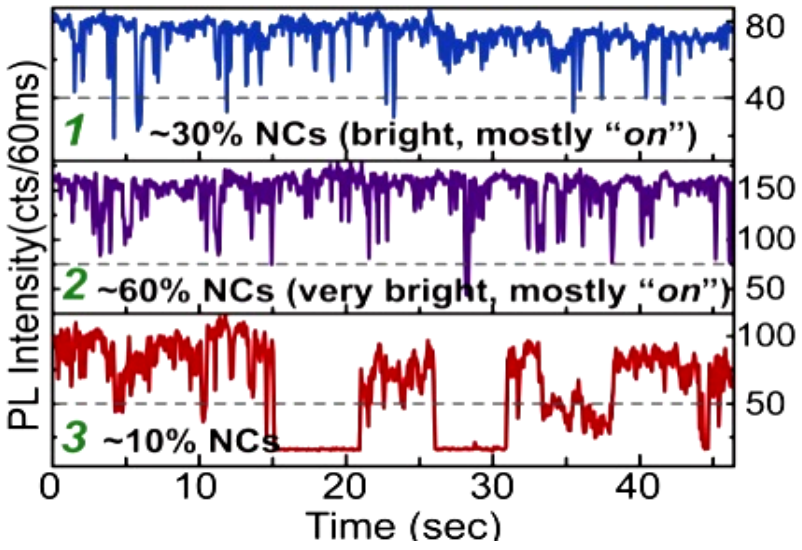

Figure 3A.22: PL blinking. Characteristic temporal fluctuation of PL intensity for three typical single nanocrystals marked (1-3), along with proportion of nanocrystals (for several hundred single NCs studied) which exhibit corresponding intensity/blinking behaviors; Dashed lines mark approximately 50% intensity compared to the "bright" level. Measurements were done in collaboration with Prof. Arindam Chowdhury at Indian Institute of Technology (IIT), Bombay, India.

3A.4 Conclusions

We have highlighted advantageous PL behavior of orthorhombic $CsPbBr_3$ NCs compared to traditional QDs. 90% PLQY with narrow (86 meV) FWHM, negligible influence of FRET and self-absorption, temperature-independent chromaticity, and batch to batch reproducibility suggest that our $CsPbBr_3$ NCs can be a better candidate for high-definition displays than traditional QDs. The key aspect that leads to improved PL behavior of $CsPbBr_3$ NCs is that such NCs exhibit strong excitonic PL when the charge carriers are just weakly confined, and excitonic transition energy is less sensitive to NC size. The FWHM of single-NC PL (78 meV) is almost same as that of ensemble of $CsPbBr_3$ NCs, signifying that size-distribution does not broaden the PL spectrum of the ensemble. Temporal PL behavior shows suppression of blinking-off states. In fact, approximately 90% of the individual $CsPbBr_3$ NCs remain emissive (on-time > 85%) without much influence of excitation power. Such suppression of blinking will be useful for single-NC-based super-resolution PL imaging.

References:

1. MØLler, C. K., Crystal Structure and Photoconductivity of Cæsium Plumbohalides. *Nature* **1958,** *182*, 1436.

2. Kagan, C. R.; Mitzi, D. B.; Dimitrakopoulos, C. D., Organic-Inorganic Hybrid Materials as Semiconducting Channels in Thin-Film Field-Effect Transistors. *Science* **1999,** *286*, 945-947.

3. Kojima, A.; Teshima, K.; Shirai, Y.; Miyasaka, T., Organometal Halide Perovskites as Visible-Light Sensitizers for Photovoltaic Cells. *J. Am. Chem. Soc.* **2009,** *131*, 6050-6051.

4. Etgar, L.; Gao, P.; Xue, Z.; Peng, Q.; Chandiran, A. K.; Liu, B.; Nazeeruddin, M. K.; Grätzel, M., Mesoscopic $CH_3NH_3PbI_3/TiO_2$ Heterojunction Solar Cells. *J. Am. Chem. Soc.* **2012,** *134*, 17396-17399.

5. Lee, M. M.; Teuscher, J.; Miyasaka, T.; Murakami, T. N.; Snaith, H. J., Efficient Hybrid Solar Cells Based on Meso-Superstructured Organometal Halide Perovskites. *Science* **2012,** *338*, 643-647.

6. Christians, J. A.; Fung, R. C. M.; Kamat, P. V., An Inorganic Hole Conductor for Organo-Lead Halide Perovskite Solar Cells. Improved Hole Conductivity with Copper Iodide. *J. Am. Chem. Soc.* **2014,** *136*, 758-764.

7. Stranks, S. D.; Snaith, H. J., Metal-halide perovskites for photovoltaic and light-emitting devices. *Nat. Nanotechnol.* **2015,** *10*, 391.

8. Schmidt, L. C.; Pertegás, A.; González-Carrero, S.; Malinkiewicz, O.; Agouram, S.; Mínguez Espallargas, G.; Bolink, H. J.; Galian, R. E.; Pérez-Prieto, J., Nontemplate Synthesis of $CH_3NH_3PbBr_3$ Perovskite Nanoparticles. *J. Am. Chem. Soc.* **2014,** *136*, 850-853.

9. Protesescu, L.; Yakunin, S.; Bodnarchuk, M. I.; Krieg, F.; Caputo, R.; Hendon, C. H.; Yang, R. X.; Walsh, A.; Kovalenko, M. V., Nanocrystals of Cesium Lead Halide Perovskites ($CsPbX_3$, X = Cl, Br, and I): Novel Optoelectronic Materials Showing Bright Emission with Wide Color Gamut. *Nano Lett.* **2015,** *15*, 3692-3696.

10. Zhang, F.; Zhong, H.; Chen, C.; Wu, X.-g.; Hu, X.; Huang, H.; Han, J.; Zou, B.; Dong, Y., Brightly Luminescent and Color-Tunable Colloidal $CH_3NH_3PbX_3$ (X = Br, I, Cl) Quantum Dots: Potential Alternatives for Display Technology. *ACS Nano* **2015,** *9*, 4533-4542.

11. He, H.; S., S. A.; V., K. S.; Fu, H. T.; L., R. A., Control of Emission Color of High Quantum Yield $CH_3NH_3PbBr_3$ Perovskite Quantum Dots by Precipitation Temperature. *Adv. Sci.* **2015,** *2*, 1500194.

12. Hines, M. A.; Guyot-Sionnest, P., Synthesis and Characterization of Strongly Luminescing ZnS-Capped CdSe Nanocrystals. *J. Phys. Chem.* **1996,** *100*, 468-471.

13. Peng, X.; Schlamp, M. C.; Kadavanich, A. V.; Alivisatos, A. P., Epitaxial Growth of Highly Luminescent CdSe/CdS Core/Shell Nanocrystals with Photostability and Electronic Accessibility. *J. Am. Chem. Soc.* **1997,** *119*, 7019-7029.

14. Dabbousi, B. O.; Rodriguez-Viejo, J.; Mikulec, F. V.; Heine, J. R.; Mattoussi, H.; Ober, R.; Jensen, K. F.; Bawendi, M. G., (CdSe)ZnS Core−Shell Quantum Dots: Synthesis and Characterization of a Size Series of Highly Luminescent Nanocrystallites. *J. Phys. Chem. B* **1997,** *101*, 9463-9475.

15. L., R. A.; Nikolai, G.; M., L. J.; Cristina, B.; E., G. D.; Steve, D.; Nello, L. P.; Marzia, P.; Piermario, R.; G., R. S.; Colm, O. D.; M., S. T. C.; Alexander, E., Light-Emitting Diodes with Semiconductor Nanocrystals. *Angew. Chem. Intern. Ed.* **2008,** *47*, 6538-6549.

16. Bourzac, K., Quantum dots go on display. *Nature.* **2013,** *493*, 283.

17. Talapin, D. V.; Steckel, J., Quantum dot light-emitting devices. *MRS Bull.* **2013,** *38*, 685-691.

18. Hossain, K. A.; Amit, D.; Soham, M.; U., S. C.; D., S. D.; Somobrata, A., Efficient Solid-State Light-Emitting CuCdS Nanocrystals Synthesized in Air. *Angew. Chem. In. Ed.* **2015,** *54*, 2643-2648.

19. Qu, L.; Peng, X., Control of Photoluminescence Properties of CdSe Nanocrystals in Growth. *J. Am. Chem. Soc.* **2002,** *124*, 2049-2055.

20. Kagan, C. R.; Murray, C. B.; Nirmal, M.; Bawendi, M. G., Electronic Energy Transfer in CdSe Quantum Dot Solids. *Phys. Rev. Lett.* **1996,** *76*, 1517-1520.

21. Blanton, S. A.; Hines, M. A.; Guyot-Sionnest, P., Photoluminescence wandering in single CdSe nanocrystals. *Appl. Phys. Lett.* **1996,** *69*, 3905-3907.

22. A., E. S.; R., N.; K., S.; G., B. M., Photoluminescence from Single Semiconductor Nanostructures. *Adv. Mater.* **1999,** *11*, 1243-1256.

23. Chen, Y.; Vela, J.; Htoon, H.; Casson, J. L.; Werder, D. J.; Bussian, D. A.; Klimov, V. I.; Hollingsworth, J. A., "Giant" Multishell CdSe Nanocrystal Quantum Dots with Suppressed Blinking. *J. Am. Chem. Soc.* **2008,** *130*, 5026-5027.

24. Tyagi, P.; Kambhampati, P., Independent Control of Electron and Hole Localization in Core/Barrier/Shell Nanostructures. *J. Phys. Chem. C* **2012,** *116*, 8154-8160.

25. Hazarika, A.; Layek, A.; De, S.; Nag, A.; Debnath, S.; Mahadevan, P.; Chowdhury, A.; Sarma, D. D., Ultranarrow and Widely Tunable Mn^{2+} Induced Photoluminescence from Single Mn-Doped Nanocrystals of ZnS-CdS Alloys. *Phys. Rev. Lett.* **2013,** *110*, 267401.

26. Sahu, A.; Kang, M. S.; Kompch, A.; Notthoff, C.; Wills, A. W.; Deng, D.; Winterer, M.; Frisbie, C. D.; Norris, D. J., Electronic Impurity Doping in CdSe Nanocrystals. *Nano Lett.* **2012,** *12*, 2587-2594.

27. Nag, A.; Kumar, A.; Kiran, P. P.; Chakraborty, S.; Kumar, G. R.; Sarma, D. D., Optically Bifunctional Heterostructured Nanocrystals. *J.Phys. Chem. C* **2008,** *112*, 8229-8233.

28. Cossairt, B. M., Shining Light on Indium Phosphide Quantum Dots: Understanding the Interplay among Precursor Conversion, Nucleation, and Growth. *Chem. Mater.* **2016,** *28*, 7181-7189.

29. Rodová, M.; Brožek, J.; Knížek, K.; Nitsch, K., Phase transitions in ternary caesium lead bromide. *J. Therm. Anal. and Calorim.* **2003,** *71*, 667-673.

30. Kumawat, N. K.; Swarnkar, A.; Nag, A.; Kabra, D., Ligand Engineering to Improve the Luminance Efficiency of $CsPbBr_3$ Nanocrystal Based Light-Emitting Diodes. *J. Phys. Chem. C* **2018,** *122*, 13767.

31. Yu, C.; Chen, Z.; Wang, J. J.; Pfenninger, W.; Vockic, N.; Kenney, J. T.; Shum, K., Temperature dependence of the band gap of perovskite semiconductor compound $CsSnI_3$. *J. Appl. Phys.* **2011,** *110*, 063526.

32. Huang, L.-y.; Lambrecht, W. R. L., Electronic band structure, phonons, and exciton binding energies of halide perovskites $CsSnCl_3$, $CsSnBr_3$, and $CsSnI_3$. *Phys. Rev. B* **2013,** *88*, 165203.

33. Jishi, R. A.; Ta, O. B.; Sharif, A. A., Modeling of Lead Halide Perovskites for Photovoltaic Applications. *J.Phys. Chem. C* **2014,** *118*, 28344-28349.

34. Yu, W. W.; Qu, L.; Guo, W.; Peng, X., Experimental Determination of the Extinction Coefficient of CdTe, CdSe, and CdS Nanocrystals. *Chem.Mater* **2003,** *15*, 2854-2860.

35. Achermann, M.; Petruska, M. A.; Crooker, S. A.; Klimov, V. I., Picosecond Energy Transfer in Quantum Dot Langmuir−Blodgett Nanoassemblies. *The J. Phys. Chem. B* **2003,** *107*, 13782-13787.

36. Deschler, F.; Price, M.; Pathak, S.; Klintberg, L. E.; Jarausch, D.-D.; Higler, R.; Hüttner, S.; Leijtens, T.; Stranks, S. D.; Snaith, H. J.; Atatüre, M.; Phillips, R. T.; Friend, R. H., High Photoluminescence Efficiency and Optically Pumped Lasing in Solution-Processed Mixed Halide Perovskite Semiconductors. *J. Phys. Chem. Lett.* **2014,** *5*, 1421-1426.

37. Manser, J. S.; Kamat, P. V., Band filling with free charge carriers in organometal halide perovskites. *Nat. Photonics.* **2014,** *8*, 737.

38. Mitzi, D. B.; Feild, C. A.; Schlesinger, Z.; Laibowitz, R. B., Transport, Optical, and Magnetic Properties of the Conducting Halide Perovskite $CH_3NH_3SnI_3$. *J. Solid State Chem.* **1995,** *114*, 159-163.

Chapter 3

(PART-B)

Excellent Green but Unconvinced Blue Luminescence from $CsPbBr_3$ Perovskite Nanocrystals

---

The following article has been published based on the work presented in this chapter.

1. Ravi, V. K.[†]; Swarnkar, A.[†]; Chakraborty, R.; Nag, A. Excellent Green but Less Impressive Blue Luminescence from $CsPbBr_3$ Perovskite Nanocubes and Nanoplatelets. *Nanotechnology* **2016,** *27*, 325708. Copyright permission has been taken from IOP publishing for the entire paper.

[†] Authors contributed equally.

Summary

It has been reported in literature that getting blue emission in defect tolerant $CsPbX_3$ perovskite system is possible by replacing required amount of Br with Cl in $CsPbBr_3$ nanocrystals. In part-A of this chapter we found that green photoluminescence from $CsPbBr_3$ nanocubes (~11 nm edge-length) exhibit high quantum yield (up to 90 %), narrow spectral width (~85 meV), and high reproducibility. But in order to extend these properties towards blue (photoluminescence peak maximum, λ_{max} < 500 nm) by halide substitution decreases the photoluminescence quantum yield. Tuning the emission color towards blue region can also be done by employing quantum size effect in $CsPbBr_3$ nanocrystals. So in this work smaller sized $CsPbBr_3$ nancubes (comparable to the size of Bohr excitonic diameter) were prepared, in which the charge carriers are strongly quantum confined. High quantum yield (> 50%) was achieved for such blue emission, but the spectral width increases and become asymmetric. Photoluminescence is unstable and irreproducible for samples with λ_{max} ~ 460 nm, exhibiting multiple peaks. These problems arise because of smaller (< 7 nm) $CsPbBr_3$ cubes/spheres have tendency to form nanoplatelets and nanorods, eventually yielding inhomogeneity in shape and size in the final blue emitting nanocrystals. Photoluminescence decay dynamics show a systematic decrease in average radiative lifetime with decreasing λ_{max} (increasing quantum confinement) because of better overlap of electron and hole wavefunctions.

Graphical abstract

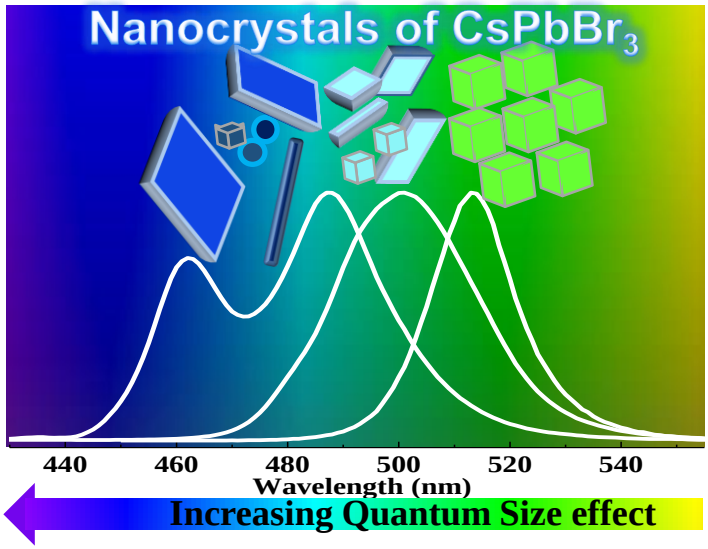

3B.1 Introduction

In part-A of this chapter, we discussed on PL spectral widths of single nanocrystal (NC) and ensemble are almost identical for ~11 nm $CsPbBr_3$ nanocubes overcoming the vexing problems of size-distribution. While all the exciting new properties of $CsPbBr_3$ nanocubes (with edge-length ~11 nm) were mainly achieved for samples emitting green light (λ_{max} > 500 nm), photophysics of smaller nanocubes with blue emission (λ_{max} < 500 nm) remained less explored. Since the excitonic Bohr diameter of $CsPbBr_3$ is ~7 nm,[1] photophysics of smaller (< 7 nm) NCs will provide information about the influence of quantum confinement of charge carriers on physical properties. Such tuning of luminescence color of $CsPbBr_3$ NCs by employing quantum confinement effect has been partially successful but remained complicated. The main problem arises from the fact that attempts to prepare smaller nanocubes, often lead to the formation of nanocrystals (NCs) with different shapes including quasi 2D nanoplatelets, which in turn can assemble/stack providing complex higher order nanostructures.[2-6] Therefore explaining blue-shift in optical bandgap just by considering smaller size of $CsPbBr_3$ nanocubes can be misleading. In fact, the blue emission from $CsPbBr_3$ NCs often results from shape-induced quantum confinement forming nanoplatelet, instead of simple size-dependent quantum confinement of smaller $CsPbBr_3$ nanocubes.[3, 5, 7]

On the other hand, color of emitted light can be controlled over the visible region by controlling the composition of $CsPbX_3$ NCs, where X = Cl, Br, I and their mixture in different ratios.[1, 8-10] Such compositional tuning has its own demerits such as PL quantum yield (QY) decreases drastically as the composition changes on either side from the ideal $CsPbBr_3$ NCs. However, this part of the chapter is not on composition tuning, instead we focus on size-controlled luminescence of colloidal $CsPbBr_3$ NCs. The merits and demerits of blue emission (along with that of green emission) from $CsPbBr_3$ nanocubes have been studied explicitly. $CsPbBr_3$ nanocubes (~11 nm edge-length) expectedly exhibit excellent green (514 nm) PL with 80-85% QY, narrow (85 meV) full width at half maxima (FWHM), and are stable in a non-polar medium. The effect of quantum confinement on increasing the optical bandgap was observed for smaller $CsPbBr_3$ nanocubes. But the uncontrolled growth of the smaller sized NCs affects the color purity. The average radiative PL lifetime decreases with increasing quantum confinement that enhances transition probability. PL from the smallest 5.5 nm cubes are not stable, often forming nanorodss, and therefore, PL spectra changes with time.

3B.2 Experimental Sections

3B.2.1 Synthesis of Smaller $CsPbBr_3$ Nanocubes Involving Size Selective Precipitation

In order to achieve smaller (7.5 and 5.5 nm edge length) nanocubes, the reaction temperature was reduced to 140 °C. Remaining part of the reaction is similar to that discussed in Part-A of this chapter for 11 nm $CsPbBr_3$ nanocubes. However, here we employ the technique of size selective precipitation, in order to separate out larger and smaller NCs obtained after carrying out reaction at 140 °C. The obtained final mixture after the reaction was first precipitated by adding 6 mL of *n*-butanol and centrifuged for 5 min at 7000 rpm precipitating out 7.5 nm nanocubes. This first precipitation has been termed as first fraction in the manuscript. The obtained supernatant (after precipitating out the first fraction) was then centrifuged again for 30 min at 17 °C and at 14000 rpm yielding some NC precipitate. In this work, we have used epprndorf centrifuge machine of model number 4530 for the NCs purification. The radius of rotor is 100 mm and based on this the rcf value for 8000 rpm is 7200.This precipitate was again redispersed in toluene, followed by centrifugation (30 min, 14000 rpm) at 4 °C. This final precipitate obtained at this stage has been termed as second fraction.TEM images show that second fraction consists of 5.5 nm $CsPbBr_3$ nanocubes along with nanorods and also NCs with other shapes as impurities.

3B.2.2 Characterization

UV-visible absorption spectra were recorded using a Perkin Elmer, Lambda-45 UV/Vis spectrometer. Steady state PL and PL decay dynamics (time correlated single photon counting (TCSPC) of NCs were measured using FLS 980 (Edinburgh Instruments). UV-visible absorption and PL experiments were done in solution. UV-visible absorption spectra were taken in transmittance mode. Powder x-ray diffraction (XRD) data were recorded using a Bruker D8 Advance x-ray diffractometer using Cu Kα radiation (1.54 Å). Transmission electron microscopy (TEM) studies were carried out using a JEOL JEM 2100 F field emission transmission electron microscope at 200 kV. The sample preparation for TEM was done by putting a drop of the colloidal solution of NCs in hexane on the carbon coated copper grids.

3B.3 Results and Discussion

3B.3.1 Tuning of Optical Bandap and Synthesis Challenges for Smaller $CsPbBr_3$ Nanocubes

$CsPbBr_3$ NCs are expected to have an excitonic Bohr diameter of ~7 nm.[1] Therefore, controlled

synthesis of smaller (< 7 nm) $CsPbBr_3$ NCs with narrow size distribution is desirable in order to realize size-dependent optoelectronic properties. We prepared different sized colloidal $CsPbBr_3$ nanocubes after modifying the recipe reported by Protesescu et al.[1]

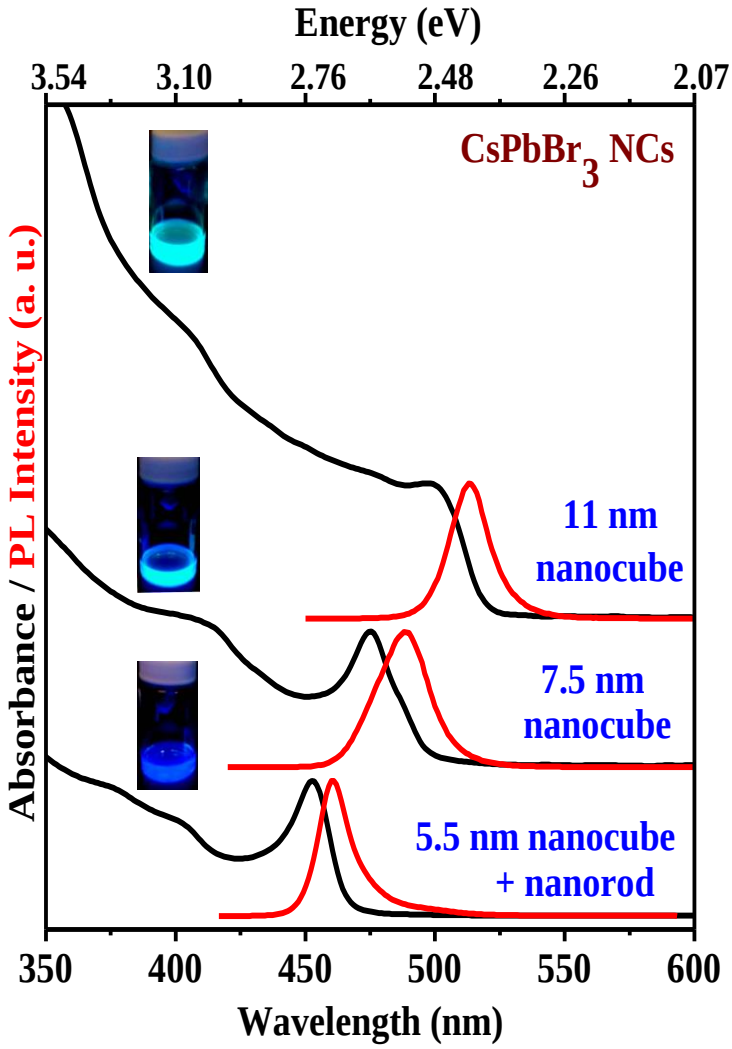

Figure 3B.1: Quantum confinement effect. UV-visible absorption and PL spectra of $CsPbBr_3$ nanocrystals prepared at 190 ˚C (11 ± 0.7 nm nanocube), 140 ˚C, first fraction of size selective precipitation (7.5 ± 1.5 nm nanocube,) and 140 ˚C second fraction of size selective precipitation (5.5 ± 2 nm nanocube + nanorod).

Figure 3B.1 shows UV-visible absorption and PL spectra of different sized NCs. The NCs prepared at 190 °C show band-edge emission (green) with a narrow spectral width (FWHM = 18 nm or

85 meV). To achieve smaller nanocubes, we used an intermediate reaction temperature of 140 °C, above which larger (8–11 nm) nanocubes are formed, and below which nanoplatelets are formed.[1,5] Furthermore, we employed size selective precipitation in order to separate smaller and larger sized NCs from a given batch of synthesis. The first fraction obtained after size selective precipitation is expected to consist of larger NCs and the second fraction is supposed to have smaller NCs. Indeed, UV-visible absorption and PL spectra in Figure 3B.1 show that the optical bandgap for the second (smaller size) fraction blue shifts compared to that of the first (larger size) fraction. These observations appear to be in the expected line where smaller sized nanocubes exhibit a stronger quantum confinement effect increasing the optical bandgap. However, we need to be cautious here and the shape effect needs to be investigated before making a final interpretation.

TEM images in Figure 3B.2a shows the formation of nanocubes when the reaction was carried out at 190 °C. Importantly, the shape and size of the nanocubes are homogenous, without forming impurity in terms of nanoplatelets or nanorods. The edge-length of these nanocubes is 11 ± 0.7 nm. While the TEM image in Figure 3B.2b shows that the first fraction obtained for NCs synthesized at 140 °C after the size selective precipitation contains nanocubes with 7.5 ± 1 nm edge length. The TEM image over a larger area of the same sample shown in Figure 3B.2c ensures the formation of nanocubes, but few nanorods are also observed. TEM image (Figure 3B.3a) of the second fraction exhibits 5.5 ± 2 nm sized distorted nanocubes, but an image over a larger area (Figure 3B.3b) of the same sample (second fraction) shows a mixture of nanorods, nanocubes, and even a small fraction of rectangular (probably 2D) shaped NCs. Figure 3B.3b also suggests the possibility of an intermediate state where nanocubes assemble to form nanorods. Such assemblies can form post-synthesis as well, for example, during drying of samples on a TEM grid.

As a result of instability in NC morphology, the PL spectra in Figure 3B.4 suggest that the emission from the smaller sized NCs is not stable even in colloidal form. Within a few hours, a new PL peak appears at lower energies (490 nm) signifying the formation of larger crystallite dimensions, because of self-assembly/fusion of the smaller sized NCs;[2-5] however, further study is required to understand the mechanism of such transformation. These results suggest that achieving smaller nanocubes of $CsPbBr_3$ with an edge length of < 7 nm is difficult, and the usual tendency of assigning the tuning of the optical gap by size variation can be misleading if we do not consider the effect of shape.

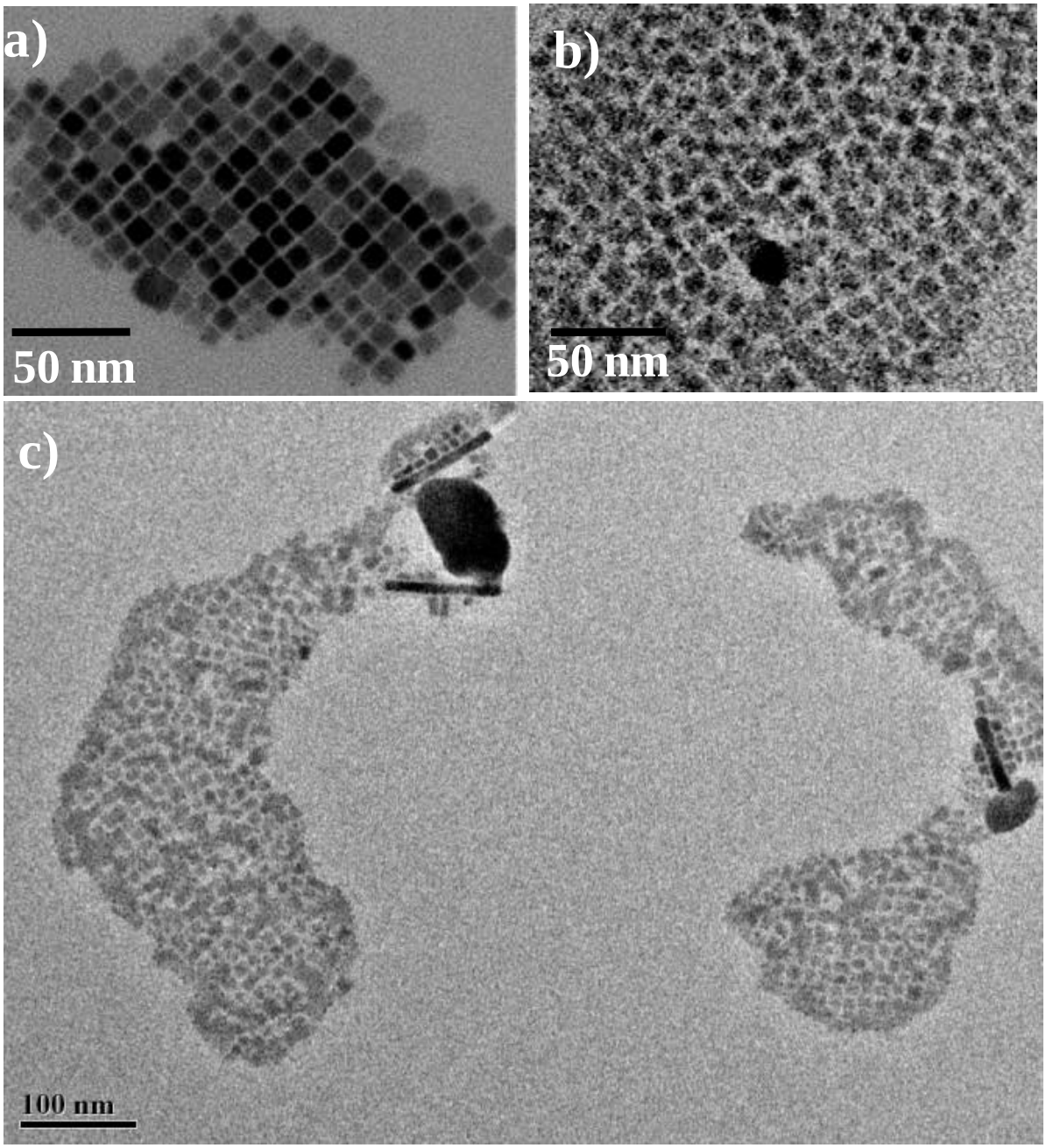

Figure 3B.2: Controlling the size of $CsPbBr_3$ nanocrystals. TEM image of $CsPbBr_3$ nanocrystals prepared at a) 190 °C, forming 11 ± 0.7 nm nanocube, b) 140 °C, first fraction of size selective precipitation forming 7.5 ± 1 nm nanocubes, and c) larger area of the 7.5 nm nanocube sample shown in b). Formations of a few nanorods are also observed along with 7.5 nm nanocubes.

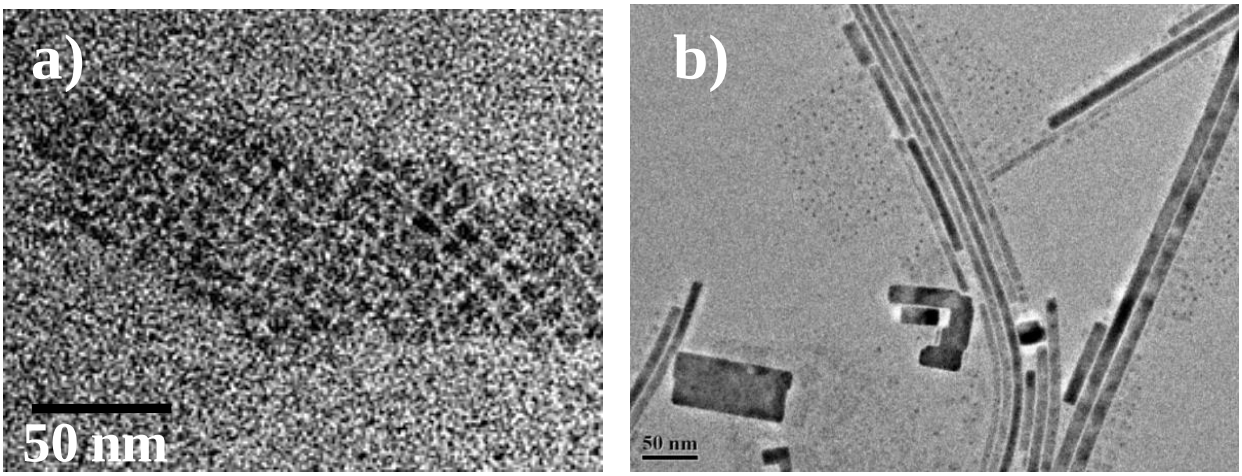

Figure 3B.3: **Instability of smaller sized nanocubes.** TEM images of $CsPbBr_3$ nanocrystals prepared at 140 °C, second fraction of size selective precipitation forming a) 5.5 ± 2 nm nanocube along with b) mixture of nanorod and a few rectangular shape crystals as impurity.

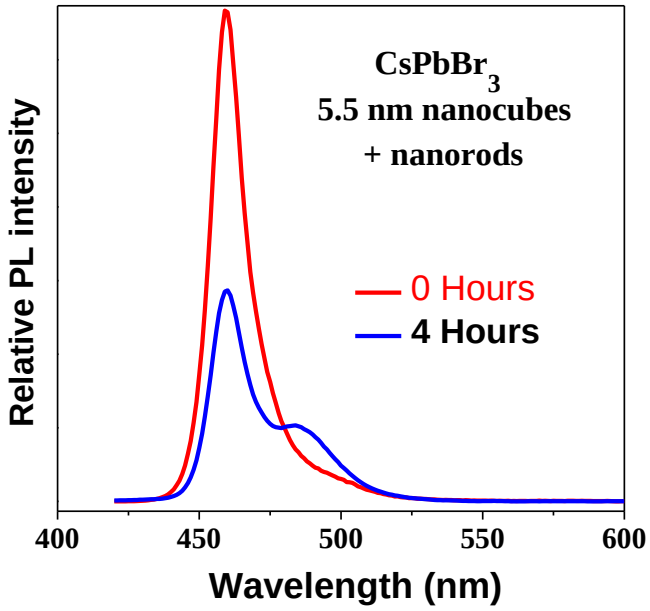

Figure 3B.4: Instability of PL from smaller sized $CsPbBr_3$ nanocrystals. PL spectra of nanocrystals obtained after 0 and 4 hours from completion of reaction for smaller size $CsPbBr_3$ NCs prepared at 140 °C and obtained in the second fraction of size selective precipitation.

3B.3.2 Crystal Phase and Compositional Purity of Different Sized NCs

To understand the materials compositional purity, powder XRD patterns were measured. As discussed in part-A of this chapter and Figure 3B.5 show all the major peaks for both the cubic and orthorhombic phase of bulk $CsPbBr_3$ are at similar Bragg's angles (2θ). However, the orthorhombic phase has some additional low-intensity peaks, particularly at 2θ ~ 22 to 30°. Such low-intensity orthorhombic peaks sometimes might not appear distinctly in the XRD pattern of small NCs because of both the broadening of the XRD peaks along with decreased diffraction intensity. But our ~11 nm $CsPbBr_3$ NCs show the additional peaks in the range of 2θ = 22 to 30° clearly signifying the orthorhombic crystal structure of $CsPbBr_3$.

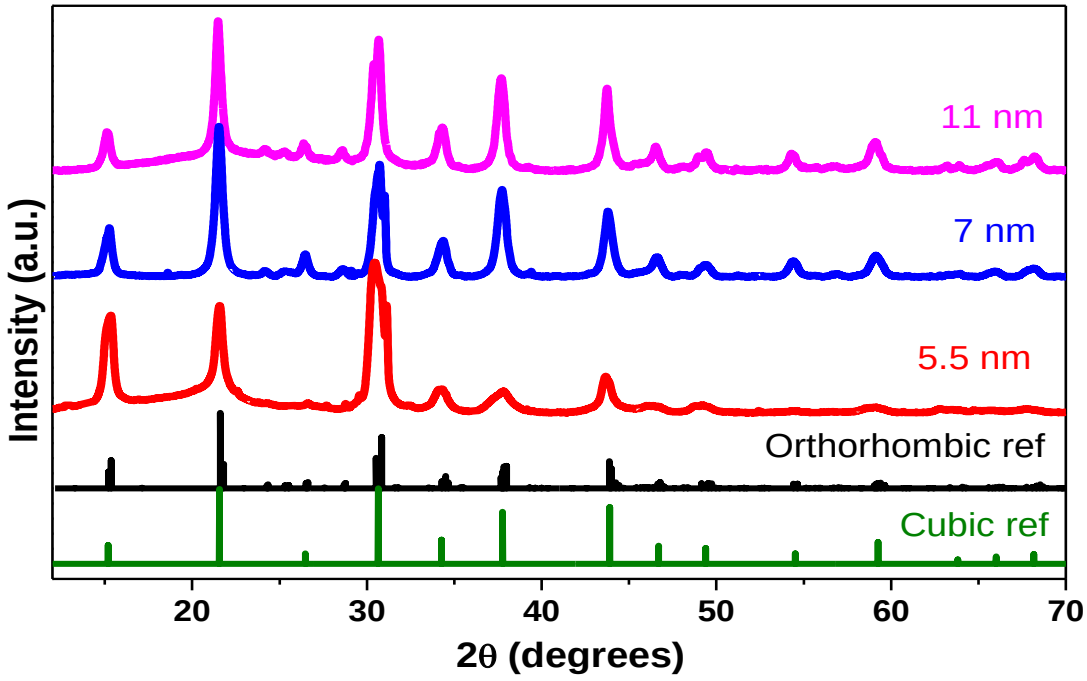

Figure 3B.5: Crystal phase purity of different sized nanocrystals. Powder XRD data of $CsPbBr_3$ nanocrystals prepared at 190 ^oC (11 ± 0.7 nm nanocube), 140 ^oC, first fraction of size selective precipitation (7.5 ± 1.5) nm nanocube,) and 140 ^oC second fraction of size selective precipitation (5.5 ± 2 nm nanocube + nanorod). XRD patterns are vertically shifted for clarity.

3B.3.3 Effect of Quantum Confinement on PL Decay of $CsPbBr_3$ Nanocubes

PL decay profiles (Figure 3B.6) of $CsPbBr_3$ NCs with different sizes were fitted with bi-exponential decay, and the best fit parameters are given in Table 3B.1. None of these samples show measurable contribution from lifetime below 1 ns, suggesting no significant nonradiative decay channels in these NCs. This observation of negligible nonradiative decay channels agrees with near ideal (80-85%) PLQY of these $CsPbBr_3$ NCs. Two radiative lifetimes, ~3 ns and ~7 ns, are observed for all samples similar to part-A of this chapter. However, Table 3A.1 shows that the contribution from a shorter lifetime increases with decreasing nanocube size, probably as a consequence of the quantum confinement effect. Both electrons and holes in $CsPbBr_3$ NCs have similar effective masses (~0.15 me),[1] and therefore, both charge carriers are expected to experience a nearly equal extent of confinement when the size of NCs decreases compared to the excitonic Bohr diameter (also discussed in part-A of this chapter). Such confinement increases the overlap between the electron and hole wavefunctions, which in turn can increase the optical transition probability, thereby decreasing the radiative lifetime. This size-dependent reduction in radiative lifetime suggests that the PL is due to excitonic transitions, instead of the recombination of free electrons and free holes.

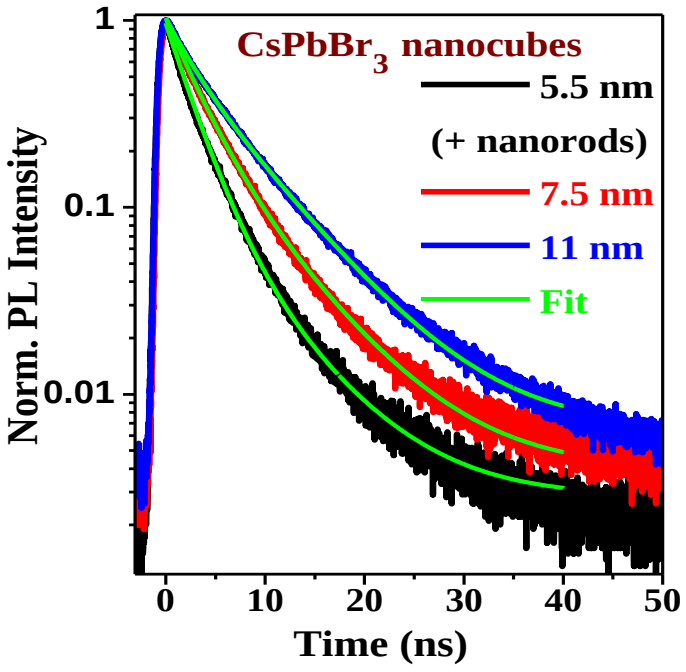

Figure 3B.6: PL decay dynamics. PL decay profiles of $CsPbBr_3$ nanocubes with different sizes.

Table 3B.1 The best fit parameters of PL decay profiles of $CsPbBr_3$ nanocube dispersions measured at corresponding emission peak energy shown in Figure 1, using bi-exponential decay. a_1 and a_2 are percent contributions of lifetimes from τ_1 and τ_2 respectively. Average decay time (av. τ) was calculated as av. $\tau_{avg} = \sum A_i\tau_i^2 / \sum A_i\tau_i$

Edge-length (nm)	a_1 (%)	τ_1 (ns)	a_2 (%)	τ_2 (ns)	av τ (ns)
5.5 + nanorods	84	2.5	16	6.7	3.2
7.5	73	2.8	27	6.9	3.9
11	37	2.5	63	6.9	5.3

3B.3.4 Strongly quantum confined $CsPbBr_3$ nanoplatelets

To get homogeneity in NCs shape, we reduced the reaction temperature below 140 ^oC (threshold temperature point for nanocubes to nanoplatelets). When a synthesis similar to that of $CsPbBr_3$ nanocubes are carried out at lower temperatures (130 and 90 °C), nanoplatelets (rectangular shaped NCs with varying dimensions (~3 to 70 nm)) are observed. The NCs show homogeneity in the shape but the optical data show inhomgeneity in term of color purity in the blue region. The detailed result of these nanoplatelets will be part of Ph.D. thesis of Mr. Vikash Kumar Ravi. However, the details can be also found in our published article (Nanotechnology **2016,** *27*, 325708).

3B.4 Conclusions

$CsPbBr_3$ nanocubes (~11 nm edge-length) prepared at 190 °C exhibit excellent green (514 nm) luminescence with 85-90% PLQY and very narrow (18 nm or 85 meV) FWHM. The decrease in synthesis temperature to 140 °C, along with size-selective precipitation, yields smaller nanocubes with edge-lengths of 7.5 and 5.5 nm with PL peaks at 488 and 460 nm respectively, exhibiting a size-dependent quantum confinement effect. Expectedly, the radiative lifetime of nanocubes decreases with the decreasing size of nanocubes because of a better overlap of electron and hole wavefunctions arising from the confinement effect. However, ~5.5 nm cubes are not very stable, and a mixture of nanorods and platelets are also observed along with nanocubes. Consequently, obtaining high quality blue emission (<500 nm) from $CsPbBr_3$ NCs is challenging. In recent times, other research groups has shown

narrow and stable blue emission with very high PL QY (75-96%) from few monolayer thick $CsPbBr_3$ nanoplatelets.[11-12] But to the best of our knowledge controlled blue emission in $CsPbBr_3$ nanocubes has not been achieved by any group, till date.

References:

1. Protesescu, L.; Yakunin, S.; Bodnarchuk, M. I.; Krieg, F.; Caputo, R.; Hendon, C. H.; Yang, R. X.; Walsh, A.; Kovalenko, M. V., Nanocrystals of Cesium Lead Halide Perovskites ($CsPbX_3$, X = Cl, Br, and I): Novel Optoelectronic Materials Showing Bright Emission with Wide Color Gamut. *Nano Lett.* **2015,** *15*, 3692-3696.

2. Zhang, D.; Eaton, S. W.; Yu, Y.; Dou, L.; Yang, P., Solution-Phase Synthesis of Cesium Lead Halide Perovskite Nanowires. *J. Am. Chem. Soc.* **2015,** *137*, 9230-9233.

3. Sichert, J. A.; Tong, Y.; Mutz, N.; Vollmer, M.; Fischer, S.; Milowska, K. Z.; García Cortadella, R.; Nickel, B.; Cardenas-Daw, C.; Stolarczyk, J. K.; Urban, A. S.; Feldmann, J., Quantum Size Effect in Organometal Halide Perovskite Nanoplatelets. *Nano Lett.* **2015,** *15*, 6521-6527.

4. Dou, L.; Wong, A. B.; Yu, Y.; Lai, M.; Kornienko, N.; Eaton, S. W.; Fu, A.; Bischak, C. G.; Ma, J.; Ding, T.; Ginsberg, N. S.; Wang, L.-W.; Alivisatos, A. P.; Yang, P., Atomically thin two-dimensional organic-inorganic hybrid perovskites. *Science* **2015,** *349*, 1518-1521.

5. Bekenstein, Y.; Koscher, B. A.; Eaton, S. W.; Yang, P.; Alivisatos, A. P., Highly Luminescent Colloidal Nanoplates of Perovskite Cesium Lead Halide and Their Oriented Assemblies. *J. Am. Chem. Soc.* **2015,** *137*, 16008-16011.

6. Akkerman, Q. A.; Motti, S. G.; Srimath Kandada, A. R.; Mosconi, E.; D'Innocenzo, V.; Bertoni, G.; Marras, S.; Kamino, B. A.; Miranda, L.; De Angelis, F.; Petrozza, A.; Prato, M.; Manna, L., Solution Synthesis Approach to Colloidal Cesium Lead Halide Perovskite Nanoplatelets with Monolayer-Level Thickness Control. *J. Am. Chem. Soc.* **2016,** *138*, 1010-1016.

7. Tyagi, P.; Kambhampati, P., Independent Control of Electron and Hole Localization in Core/Barrier/Shell Nanostructures. *J.Phys. Chem. C* **2012,** *116*, 8154-8160.

8. Nedelcu, G.; Protesescu, L.; Yakunin, S.; Bodnarchuk, M. I.; Grotevent, M. J.; Kovalenko, M. V., Fast Anion-Exchange in Highly Luminescent Nanocrystals of Cesium Lead Halide Perovskites ($CsPbX_3$, X = Cl, Br, I). *Nano Lett.* **2015,** *15*, 5635-5640.

9. Akkerman, Q. A.; D'Innocenzo, V.; Accornero, S.; Scarpellini, A.; Petrozza, A.; Prato, M.; Manna, L., Tuning the Optical Properties of Cesium Lead Halide Perovskite Nanocrystals by Anion Exchange Reactions. *J. Am. Chem. Soc.* **2015,** *137*, 10276-10281.

10. Ramasamy, P.; Lim, D.-H.; Kim, B.; Lee, S.-H.; Lee, M.-S.; Lee, J.-S., All-inorganic cesium lead halide perovskite nanocrystals for photodetector applications. *Chem. Commun.* **2016,** *52*, 2067-2070.

11. Wu, Y.; Wei, C.; Li, X.; Li, Y.; Qiu, S.; Shen, W.; Cai, B.; Sun, Z.; Yang, D.; Deng, Z.; Zeng, H., In Situ Passivation of $PbBr_6^{4-}$ Octahedra toward Blue Luminescent $CsPbBr_3$ Nanoplatelets with Near 100% Absolute Quantum Yield. *ACS Energy Lett.* **2018**, 2030-2037.

12. Bohn, B. J.; Tong, Y.; Gramlich, M.; Lai, M. L.; Döblinger, M.; Wang, K.; Hoye, R. L. Z.; Müller-Buschbaum, P.; Stranks, S. D.; Urban, A. S.; Polavarapu, L.; Feldmann, J., Boosting Tunable Blue Luminescence of Halide Perovskite Nanoplatelets through Postsynthetic Surface Trap Repair. *Nano Lett.* **2018,** *18*, 5231-5238.

Chapter 4

Stabilization of α-$CsPbI_3$ Perovskite for Solar Light Harvesting: Size Effect

---

The following article has been published based on the work presented in this chapter.

1. Swarnkar, A.; Marshall, A. R.; Sanehira, E. M.; Chernomordik, B. D.; Moore, D. T.; Christians, J. A.; Chakrabarti, T.; Luther, J. M. Quantum Dot–Induced Phase Stabilization of α-$CsPbI_3$ Perovskite for High-Efficiency Photovoltaics. *Science* **2016,** *354*, 92. Copyright permission has been taken from American Association for the Advancement of Science (AAAS) for the entire article.

Summary

Organic-inorganic hybrid perovskite, $CH_3NH_3PbI_3$, exhibit solar cell efficiency of >22 %, but the volatile nature of $CH_3NH_3^+$ makes the device thermally unstable above 80 °C. On the other hand, cubic (α-) phase all-inorganic $CsPbI_3$ have high melting point till ~500 °C, and exhibit electronic properties similar to $CH_3NH_3PbI_3$. But the α-phase of $CsPbI_3$ is thermodynamically stable only at > 320 °C, so optoelectronic application of α-$CsPbI_3$ at room temperature is not possible. In this chapter, we show that, stable α-$CsPbI_3$ can be obtained at room temperature by reducing the crystallite size to a few nanometers. Colloidal α-$CsPbI_3$ nanocrystals (NCs) of size 3 to 12.5 nm were prepared, which are stable for months after employing our novel method of NC purification. Size tunable bandgap in the range of 1.8 to 2.1 eV were obtained with high photoluminescence quantum yield of 21-55 %. These results along with high absorption coefficient for visible light absorption suggest that α-$CsPbI_3$ NCs can be a good harvester of light in photovoltaics and other applications.

Graphical abstract

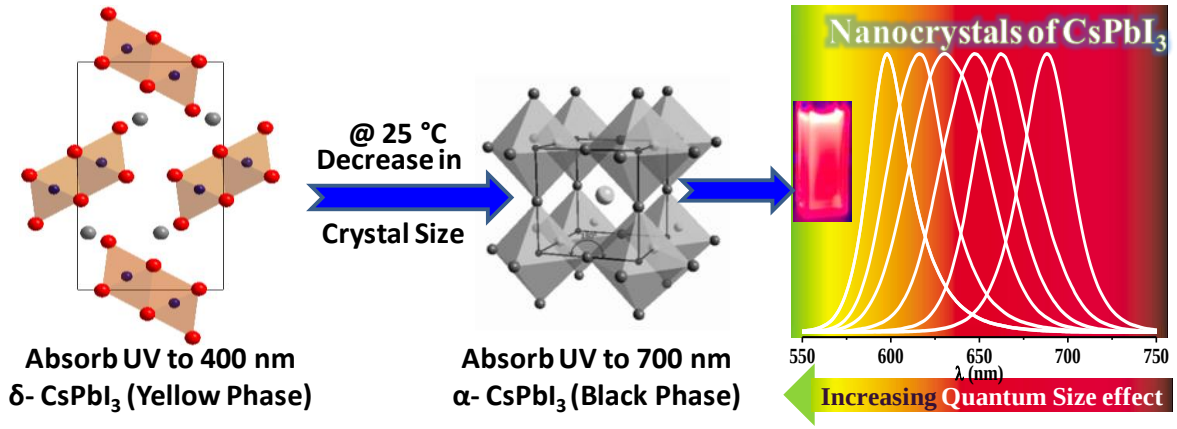

4.1 Introduction

Green emitting $CsPbBr_3$ nanocrystals (NCs) exhibit outstanding optical properties among all the halide compositions of $CsPbX_3$ (where X= Cl, Br, I). For example, low-threshold lasing,[1-2] reduced photoluminescence (PL) blinking,[3-4] light emitting diodes (LEDs)[5-6] and single-photon emission[4, 7] have been reported for $CsPbBr_3$ NCs. In chapter 3, the advantageous PL properties of 11±0.7 nm size $CsPbBr_3$ NCs over CdSe based quantum dots (QDs) have been discussed.[3] Also, the experimental works on size dependent optical properties,[8] surface chemistry[9] and other photophysics are being reported for the $CsPbBr_3$ NCs. These reports suggest that $CsPbBr_3$ NCs is a promising candidate for light emitting applications. But the larger band gap energy (~2.4 eV) of $CsPbBr_3$ does not allow the material to absorb or emit red part of the visible light. As a result, it cannot be employed for efficient light harvesting applications such as solar cell. However, replacing Br with I in the $CsPbX_3$ perovskite structure reduces the band gap energy to 1.73 eV and the resultant material can be useful for solar cell and other light harvesting applications.[10] Further for emission from orange to red region, it has been found that PL quantum yield (PLQY) decreases on tuning the PL color by varying halide composition in $CsPb(Br+I)_3$ NCs.[11] It suggests approach of color tuning by employing the quantum size effect in $CsPbI_3$ system, instead of varying halide composition, can be efficient way to get better PLQY towards orange/red region.[8, 11-12]

This black (α-) phase of $CsPbI_3$ has $[PbI_6]^{4-}$ octahedra arranged in corner-shared 3D fashion. α-$CsPbI_3$ is the all-inorganic counterpart of $CH_3NH_3PbI_3$ hybrid organic-inorganic perovskite with significantly improved thermal stability (decomposition temperature ~500 ^oC).[13] But at room temperature, thermodynamically stable crystal phase of $CsPbI_3$ is non-perovskite yellow (δ-) phase, in which, $[PbI_6]^{4-}$ octahedra are not corner shared.[10] The δ-phase absorbing at high energy (~3 eV), along with poor charge transport properties, is non-desirable for solar cell application.[10] Interestingly, it has been reported that reducing the crystal/grain size of $CsPbI_3$ to few nanometers stabilizes the α-phase at room temperature.[8, 14] The high surface energy and crystal strain introduced on reducing the size are the key factors behind the crystal phase stability of α-$CsPbI_3$ NCs.[8, 14]

Hot injection synthesis is one of the favored solution processable ways for NC synthesis.[15] Following this synthetic route, colloidal α-$CsPbI_3$ NCs can be easily synthesized.[8] Unlike the traditional colloidal NCs, such as CdE (where E = S, Se, Te) and PbE (where E = S, Se) QDs, purification of these α-$CsPbI_3$ NCs[1,14,17] from its reaction solution is challenging by using even low polar extracting solvents.[16] It has been reported that

crystal phase of α-$CsPbI_3$ NCs transforms to δ-phase within two days after synthesis,[11, 17] following their bulk counterpart,[18] on handling the colloidal NCs in ambient condition. For larger sized (>11 nm) $CsPbI_3$ NCs, purification by employing high speed centrifugation partially helps but the NCs remain poorly stable.[19] The purification becomes even more difficult for small sized NCs (smaller than Bohr exciton diameter of 12 nm).[16] The reason behind this problem of purification is that these NCs are comparatively more ionic than the traditional QDs.[9] Also, the NCs surface ligands are more dynamic than those present on the surface of CdSe based QDs.[9] It is to be noted that owing to the optimized purification, traditional QDs[15, 20-28] along with $CsPbBr_3$[1-4, 29] are being well studied for different applications. Consequently, their exciting new properties and synthetic methodologies have governed the literature.

In this chapter, we report the controlled synthesis of stable colloidal α-$CsPbI_3$ NCs. Purification of NCs from reaction mixture after synthesis holds the key for stabilizing the α-$CsPbI_3$ NCs. After synthesizing and successful purification of different sized α-$CsPbI_3$ NCs, we have studied the effect of quantum confinement on bandgap, PL and excitonic transition probabilities. Detailed photophysics suggest α-$CsPbI_3$ NCs are potential material for optoelectronics including solar cell, photodiode and LEDs.

4.2 Experimental Sections

4.2.1 Chemicals

All chemicals were purchased from Sigma Aldrich and used without purification, unless otherwise noted. Cesium carbonate (Cs_2CO_3, 99.9%), lead (II) iodide (PbI_2, 99.9985%, Alfa Aesar), oleic acid (OA, technical grade 90%), oleylamine (OAm, technical grade 70%), 1-octadecene (ODE, technical grade 90%), toluene (anhydrous 99.8%), hexane (reagent grade ≥95%), octane (anhydrous, ≥99%), 1-butanol (anhydrous 99.8%), methyl acetate (MeOAc, anhydrous 99.5%), rhodamine-6G (99%), ethanol (EtOH, 200 proof, ≥99.5%).

4.2.2 Synthesis of Cs-Oleate As A Cesium Precursor

0.5 g of Cs_2CO_3, 2 mL OA and 50 mL ODE were added to a 100 mL 3-necked round bottom flask and stirred under vacuum for 30 min at 120 °C. The flask was purged with N_2 for 10 min and then placed back under vacuum. This process of alternately applying vacuum and N_2 was repeated for a total of 3 times to remove moisture and oxygen. The reaction was considered complete when the solution was clear, indicating that the Cs_2CO_3 had reacted with

the OA. The Cs-oleate solution in ODE was stored in N_2 until it was needed for the NC synthesis.

4.2.3 Synthesis of Colloidal $CsPbI_3$ NCs

Colloidal $CsPbI_3$ NCs were synthesized following ref 8 after few modifications. In this work we have done the synthesis in large scale. A mixture of PbI_2 (1 g) with 50 mL ODE was degassed (under alternate vacuum of ~0.1 Torr and N_2) at 120 °C for ~1 hour along with magnetic stirring. Hot OA and OAm, each 5 mL, was added to the mixture at 120 °C. After ~30 min, PbI_2 get dissolved in ODE and then the temperature was varied to reaction temperature for synthesizing different size NCs (60 °C for 3.4 nm, 100 °C for 4.5 nm, 130 °C for 5 nm, 150 °C for 6.8 nm, 170 °C for 8 nm, 180 °C for 9 nm, and 185 °C for 12.5 nm NCs). Since the NCs are in cubical shape, we present the size of these NCs using the edge length of the NCs and in whole chapter NC size indicates the edge length. Cs-oleate (0.0625 M, 8 mL) solution in 1-octadecene, pre-heated at 70 °C, was swiftly injected to the reaction mixture. The temperature range of the synthesis is determined by the solubility of the precursors; Cs-oleate is insoluble in ODE below 60 °C and PbI_2 begins to precipitate out of the reaction solution above 185 °C. Compared to previous work, here Cs-oleate was diluted two times and used double volume to quench the reaction faster. The reaction mixture became reddish (orange in case of smaller NCs) and the reaction was stopped by dipping the reaction flask into an ice bath (~5 sec after injection).

4.2.4 Purification of Colloidal $CsPbI_3$ NCs

The synthesized $CsPbI_3$ NCs were precipitated by adding 200 mL anhydrous MeOAc (ratio of NC reaction solution:MeOAc is 1:3) and then centrifuged at 8000 RPM for 5 min. In this work, we have used epprndorf centrifuge machine of model number 4530 for the NCs purification. The radius of rotor is 100 mm and based on this the rcf value for 8000 rpm is 7200. The wet pellet of NCs in each centrifuge tube was redispersed in 3 mL hexane, precipitated again with an equal volume MeOAc and centrifuged at 8000 RPM for 2 min. It is to be noted that adding excess MeOAc removes the surface ligands, causing the NCs to agglomerate and revert to the yellow δ-phase. The NCs were dispersed in 20 mL of hexane and centrifuged again at 4000 RPM for 5 min to remove excess PbI_2 and Cs-oleate. The solution of colloidal $CsPbI_3$ NCs was kept in the dark at 4 °C for 48 hours to precipitate

excess Cs-oleate and Pb-oleate, which solidify at low temperatures. The NC solution was decanted and centrifuged again at 4000 RPM for 5 min before use.

4.2.5 Characterization

Ultraviolet-visible (UV-vis) absorption spectra were recorded using a Shimadzu UV-3600 UV-vis-NIR spectrophotometer. Steady-state PL and room temperature PLQY were measured using a Horiba Jobin Yvon fluoromax-4 spectrophotometer. For PLQY measurements, the NCs were dispersed in toluene using rhodamine 6G in EtOH as a reference. UV-vis absorption and PL experiments were done in solution and on thin films (prepared as described below). Powder X-ray diffraction (XRD) data were recorded using a Bruker D8 Discover X-ray diffractometer with a Hi-Star 2D area detector using Cu Kα radiation (1.54 Å). Reference markers for XRD are calculated with Crystal Diffract software using the crystallographic information file #250744 (orthorhombic (δ-) $CsPbI_3$), #161481 (cubic (α-) $CsPbI_3$), and #908790 (CsI) from the Inorganic Crystal Structure Database. Transmission electron microscopy (TEM) studies were carried out using FEI T30 at 300 kV. TEM grids were prepared by dropping a dilute colloidal solution of NCs in a (9:1) hexane-octane mixture onto the carbon coated copper grids. Time-resolved PL measurements were taken of the NCs in solution. The excitation source was a pulsed Fianium, SC-450-PP, laser with a wavelength of 500 nm and a repetition rate of 1 MHz. A 590 nm long pass filter was used to remove scatter from the excitation source. The emission was detected using a Hamamatsu streak camera model number c10910 with a wavelength range of 200-900 nm and response of <20 ps.

Determination of concentration of properly cleaned NCs solution of known absorbance was performed by ICP-MS (inductively coupled plasma-mass spectroscopy) analysis. For ICP-MS, equal amount of different sized once washed NCs sowing absence of PbI_2 in XRD and similar absorbance value was again cleaned twice with MeOAc to get rid of any possible presence of precursors. The NCs was then digested with 5% of HNO_3 for the measurement. Since in case $CsPbX_3$ NCs, it is reported[9] that byproduct PbBr(oleate) may remain on the surface of the NCs[9] and hence the Pb concentration vary with size as a consequence of varying surface to volume ratio. To get rid of this non crystalline Pb contribution, we used Cs content (Cs remains in crystalline part of the NCs and also used as limiting reaction reagent)[9] as a key parameter to calculate the concentration of NCs.

4.3 Results and Discussion

4.3.1 Colloidal and α-Phase Stability of $CsPbI_3$ NCs

NCs of $CsPbI_3$ are prepared by following the reported protocol[8] after a few modifications. In contrast to previous reports, in our application oriented work, we scaled up the synthesis 10 times. Details of synthetic procedure are provided in experimental sections (section 4.2). Typically polar non-solvents are used to precipitate organic capped NCs from non-polar solvent that is also mixed with unreacted impurities. As shown in Figure 4.1, in a non-polar media $CsPbX_3$ NCs get colloidal stability from dynamic ligands (mostly oleylammonium and iodide)[9] which are bound ionically to the surface of NCs unlike the oleate and phosphonate capped traditional CdE, PbE based QDs where oleate ligand binds covalently. Also, the dynamic nature of the oleylammonium ligand can increase on moving from $CsPbBr_3$ NCs to $CsPbI_3$ NCs because of relatively poor hard acid-soft base interaction[30] between positively charged oleylammonium (hard acid) and surface I^- (softer base than Br^-). This makes the purification of α-$CsPbI_3$ NCs difficult and the polar non-solvents instead cause a reversion to the δ-phase due to agglomeration or simply re-dissolution of the $CsPbI_3$ NCs.

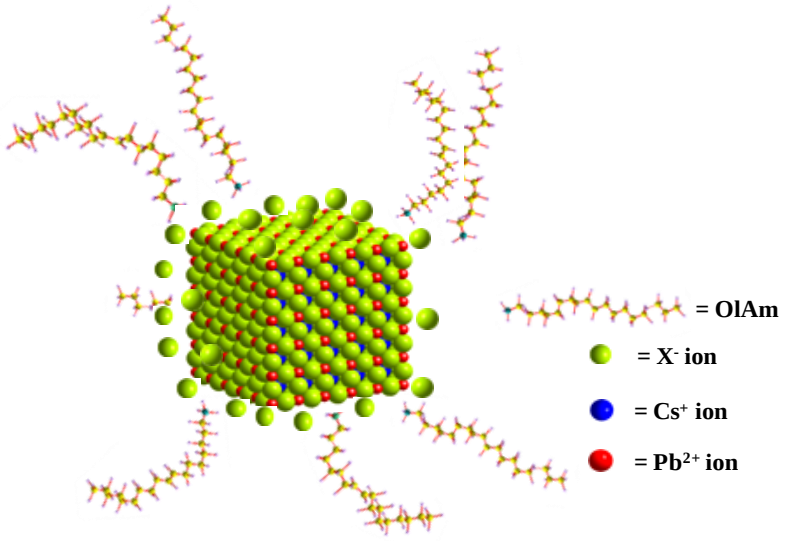

Figure 4.1: Organic capped colloidal $CsPbX_3$ perovskite nanocrystals. Schematic showing dynamic nature of the ligands present on the surface of colloidal $CsPbX_3$ perovskite nanocrystals.

A variety of low polarity non-solvents were tested: 1-butanol,[8] acetone,[31] and ethyl acetate[32] destabilized the α-$CsPbI_3$ NCs and resulted in a pale yellow suspension constituting δ-$CsPbI_3$ and probably a small amount of dissociated product (see the XRD data shown in Figure 4.2),

while MeOAc successfully isolated α-$CsPbI_3$ NCs (gives colorless supernatant with precipitate of easily dispersible colloidal NCs). Cleaned NCs powder synthesized at different reaction temperatures shown in Figure 4.3 exhibits strong luminescence under 365 nm UV light. Due to the dynamic nature of ligands, it has been also found that on using excess MeOAc, the α-$CsPbI_3$ NCs grow in size (red shift of absorption and PL) in multiple wash and become polydispersed (disappearance of the excitonic features of absorption spectrum). Figure 4.4 shows the effect of using excess MeOAc on UV-visible absorption and PL spectra of α-$CsPbI_3$ NCs.

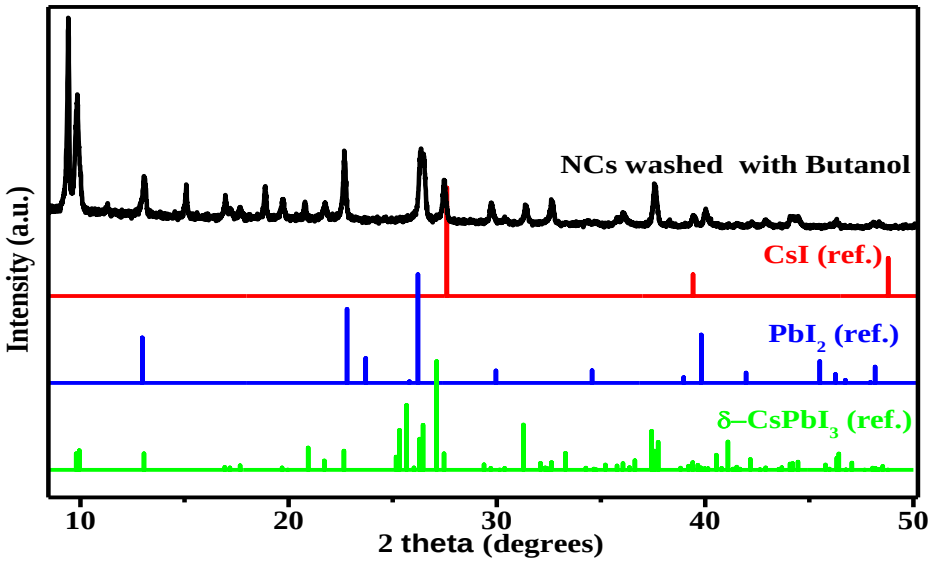

Figure 4.2: Stability of $CsPbI_3$ NCs washed with polar solvent. XRD pattern of the $CsPbI_3$ nanocrystal sample washed with n-butanol showing Brag's peak from δ-$CsPbI_3$ and dissociated precursors CsI and PbI_2. Data are vertically shifted for clarity.

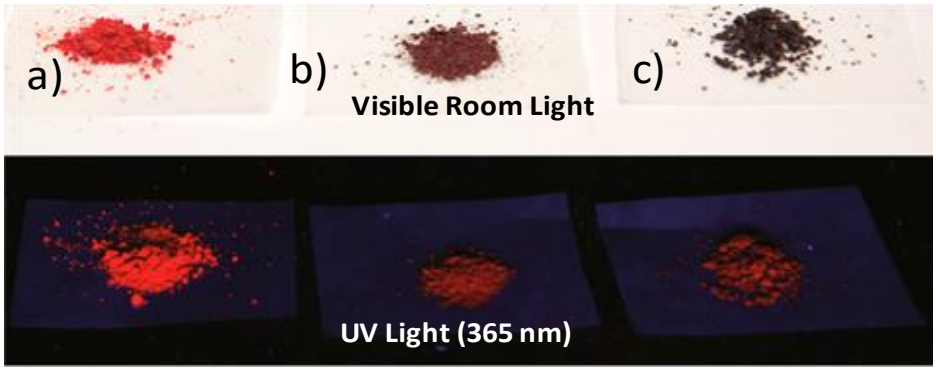

Figure 4.3: Luminescent α-$CsPbI_3$ NC powders. Photographs under visible room light (top) and UV (365 nm) illumination (bottom) of α-$CsPbI_3$ NC powders, synthesized at (a) 130, (b) 150 and (c) 180 °C.

In contrast to most of the reports mentioning the instability of α-$CsPbI_3$ at room temperature, our α-$CsPbI_3$ NCs are remaining stable and show strong luminescence for months even after storing the NC colloidal solution in ambient condition. In support of our observation, recent reports also suggest that at lower temperature thermodynamically unstable α-phase may remain stable because of the contribution from surface energy of small NCs/grain sizes.[8, 14] Hence, maintaining the surface energy while purification of α-$CsPbI_3$ NCs by preserving the required amount of ligands on the surface of the NCs may result helpful to make the α-$CsPbI_3$ NCs stable.

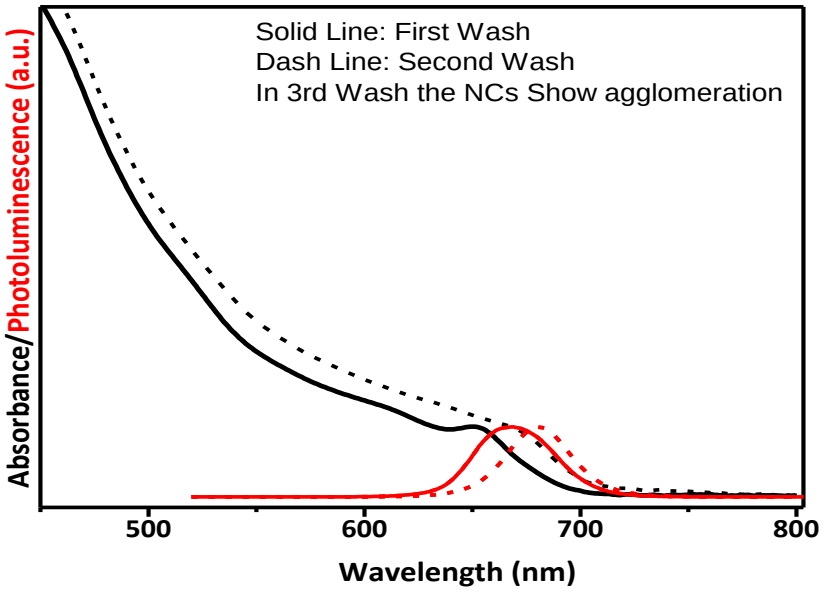

Figure 4.4: Stability of $CsPbI_3$ nanocrystals in excess MeOAc. Ultraviolet-visible spectra of low energy absorbing α-$CsPbI_3$ nanocrystals show effect of multiple washing of nanocrystals with excess MeOAc.

We study the crystal phase purity of synthesized $CsPbI_3$ NCs, particularly, when there is chance of transformation to high energy absorbing δ-phase due to agglomeration of NCs while washing with non-solvents. Figure 4.5 shows XRD data of $CsPbI_3$ NCs, synthesized at different temperatures, having same peak positions with broadening of diffraction peak with decreasing the reaction temperature. This broadening of XRD peak with decreasing the reaction temperature suggests that at lower temperature smaller size $CsPbI_3$ NCs are formed and vice-versa.[8] The diffraction peaks shows the presence of α-$CsPbI_3$ and no peak from δ-$CsPbI_3$ and from PbI_2 precursor. However, we observe that unwashed α-$CsPbI_3$ NCs transform to wide bandgap δ-phase (UV-visible spectra shown in Figure 4.6) within two days

similar to previous reports.[11, 17] Interestingly, MeOAc washed NCs remained in α- phase for months on keeping the NC sample in ambient storage, as the UV-visible spectra of these α-$CsPbI_3$ NCs recorded in varying storage time (Figure 4.7) confirms the absence of high energy (~3 eV) peak from δ-phase.[14] However, we found blue shift of lowest energy absorption peak (as shown in inset of Figure 4.7) which is probably because of the photooxidation of the NCs surface with time. Also, the XRD patterns, shown in Figure 4.8, do not show any appearance of diffraction peaks corresponding to δ-phase of $CsPbI_3$ on keeping the sample for 60 days, which further support the α-phase stability of NCs at room temperature. All the results (Figure 4.7 to 4.8) conclude that MeOAc, which isolates the NCs without full removal of the surface ligands, is critical to the stability of α-phase.

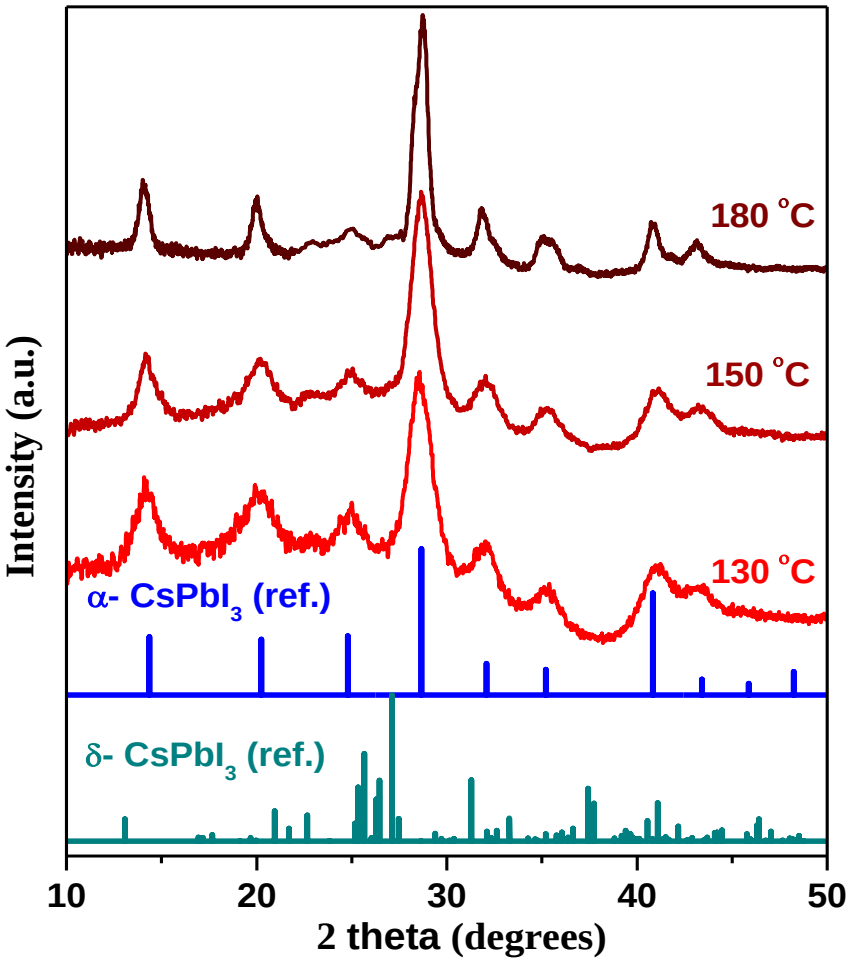

Figure 4.5: Phase stability of α-$CsPbI_3$ nanocrystals after MeOAc wash. XRD patterns of nanocrystals synthesized at (from bottom to top) 130, 150 and 180 °C confirming that they crystallize in the cubic (α-) crystallographic phase of $CsPbI_3$. Data are vertically shifted for clarity.

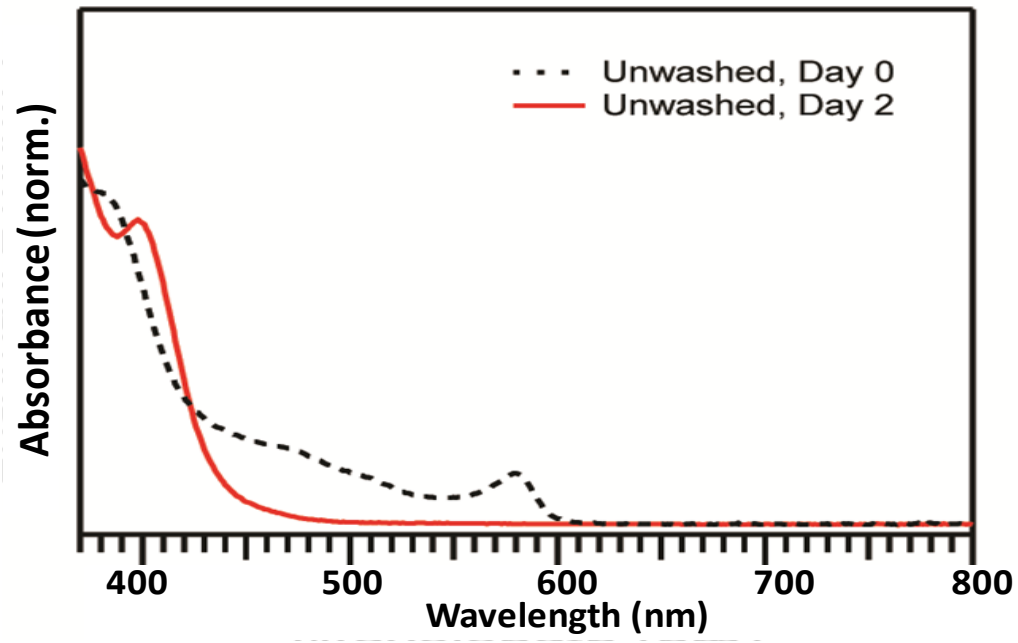

Figure 4.6: Poor stability of unwashed $CsPbI_3$ nanocrystals. UV-visible absorption spectra of nanocrystals stored in ambient conditions without washing (separating nanocrystals from unreacted precursors) for 2 days.

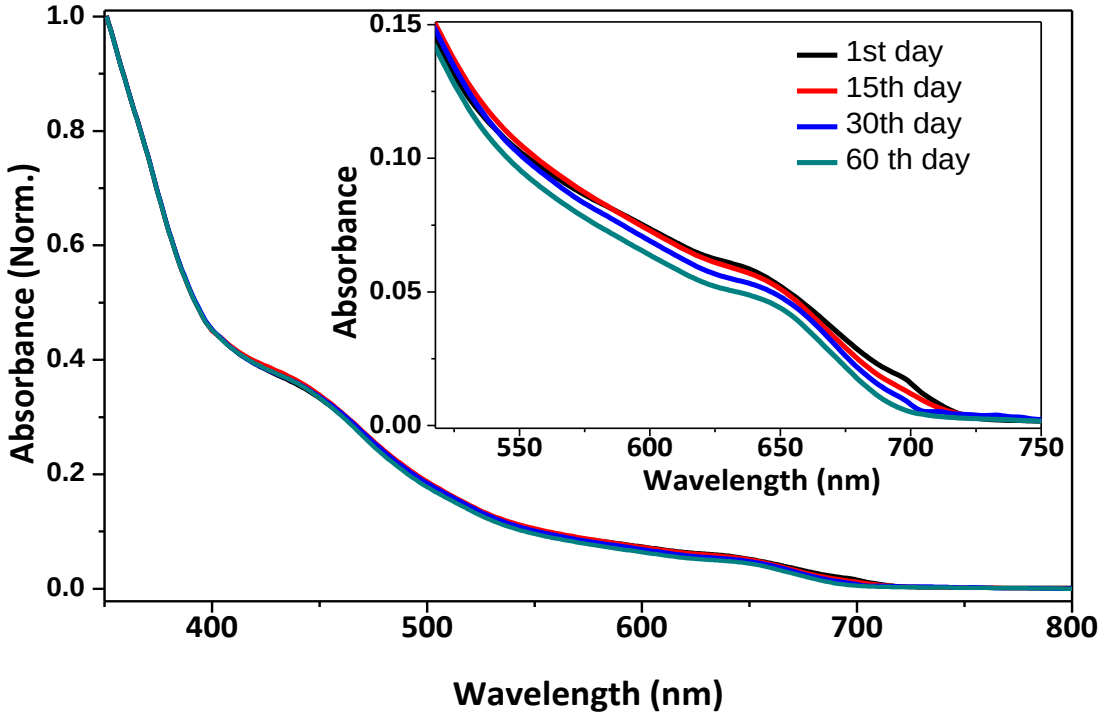

Figure 4.7: Phase stability of α-$CsPbI_3$ nanocrystals with time. UV-visible absorption (normalized at 350 nm) spectra of α-$CsPbI_3$ nanocrystals with varying storage time. Inset: enlarged view of absorption spectra showing blue shift of lower energy absorption feature on storing the sample in ambient condition.

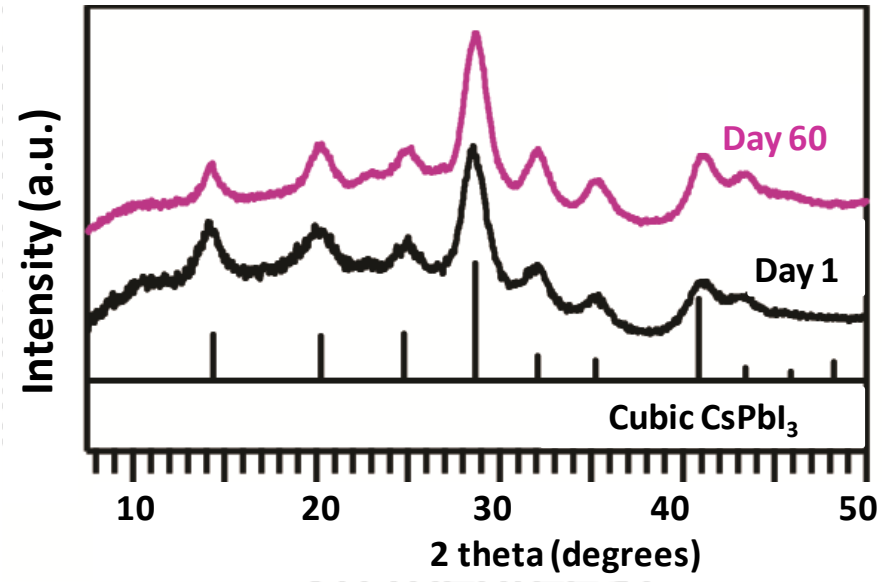

Figure 4.8: Phase stability of α-$CsPbI_3$ nanocrystals with time. Powder XRD patterns shows phase stability of α-$CsPbI_3$ nanocrystals after keeping the nanocrystal solution in ambient storage for 60 days. Data are vertically shifted for clarity.

4.3.2 Tuning of Energy Bandgap by Quantum Size Effect

Kovalenko et al[16] mentioned that it is nearly impossible to measure the size dependent emission and absorption spectra of $CsPbI_3$ NCs for batch reactions due to phase transition to orthorhombic (δ-) phase, occurring quickly for small sizes during NC isolation. Hence, they could only get in-situ evolution of absorption spectra with time where size distribution dominates and excitonic peak remain invisible in UV-visible absorption spectra. Looking at α-phase stability of our $CsPbI_3$ NCs after optimized purification, we have synthesized different sized α-$CsPbi_3$ NCs (Figure 4.9) in different batches of synthesis by varying the reaction temperature in the range of 60-185 °C.

Owing to the fast reaction kinetics and ionic nature of metathesis reaction, synthesis of smaller sized $CsPbI_3$ NCs with narrow size distribution is challenging. Smaller size NCs, capped with dynamic ligands, have higher contribution of surface energy tends to grow faster. Moreover, growth of heavier halide (iodide) containing $CsPbX_3$ NCs grow faster than those of having lighter halide[8]. Therefore, for synthesizing smaller sized α-$CsPbI_3$ NCs, lower reaction temperature (<140 °C) and fast quenching approach were employed to suppress the NC growth.

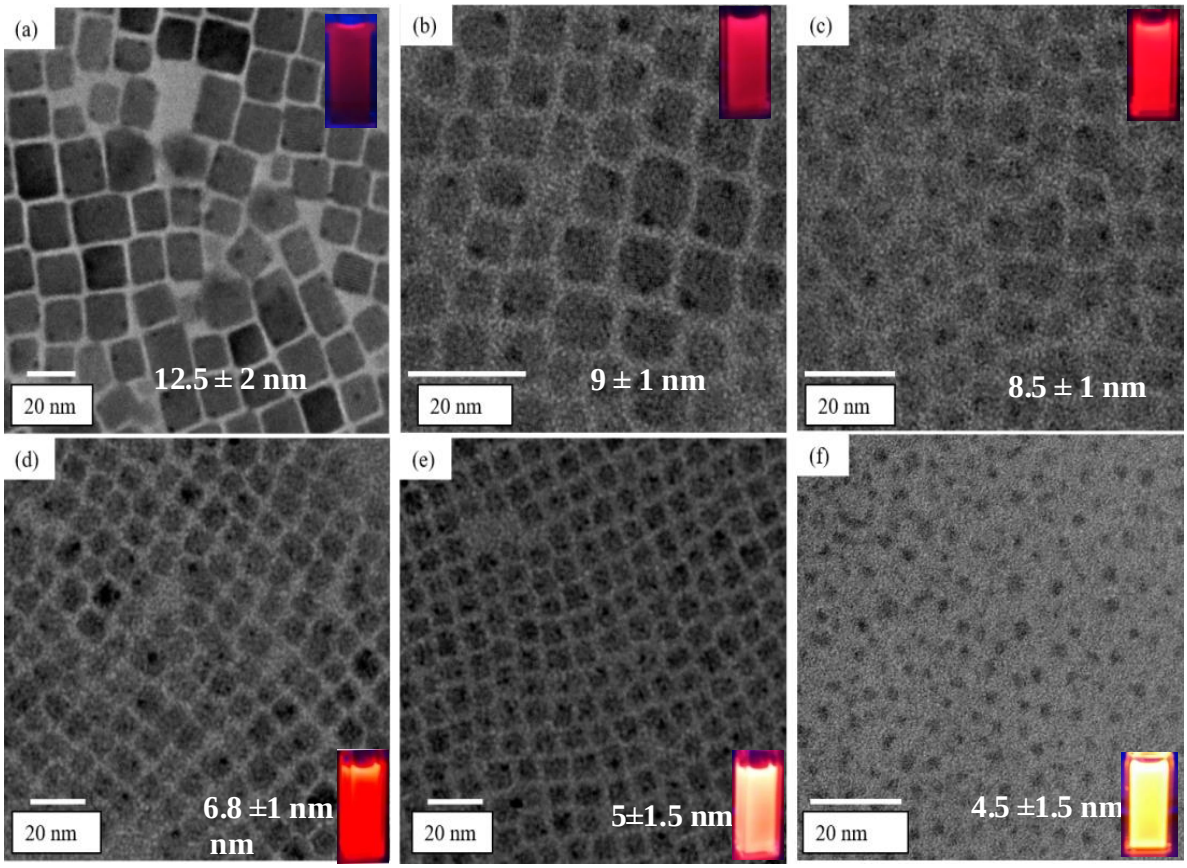

Figure 4.9: Controlling the size of α-$CsPbI_3$ nanocrystals. TEM images of α-$CsPbI_3$ nanocrystals synthesized at a) 185 °C, b) 180 °C, c) 170 °C, d) 150 °C, e) 130 °C and f) 100 °C. Their sizes and the photograph of the luminescent solutions are shown in the respective TEM images.

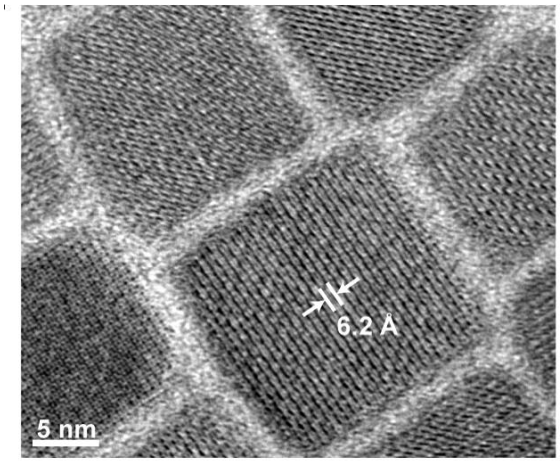

Figure 4.10: Lattice planes of α-$CsPbI_3$. High-resolution TEM image of α-$CsPbI_3$ nanocrystals synthesized at 180 °C.

TEM image in Figure 4.9 shows the edge lengths of α-$CsPbI_3$ cubes are 4.5±1.5, 5±1.5, 6.8±1, 8.5±1, 9±1 and 12.5±1 nm when the synthesis was carried out at 100, 130, 150, 170, 180 and 185 °C respectively. These edge lengths will be used to represent the size of the corresponding NCs in the remaining part of the chapter. The high resolution TEM (HRTEM) image of sample synthesized at 180 °C (Figure 4.10) shows an interplanar distance of 6.2 Å which is consistent with the (100) plan of α-$CsPbI_3$.[23- 14, 18]

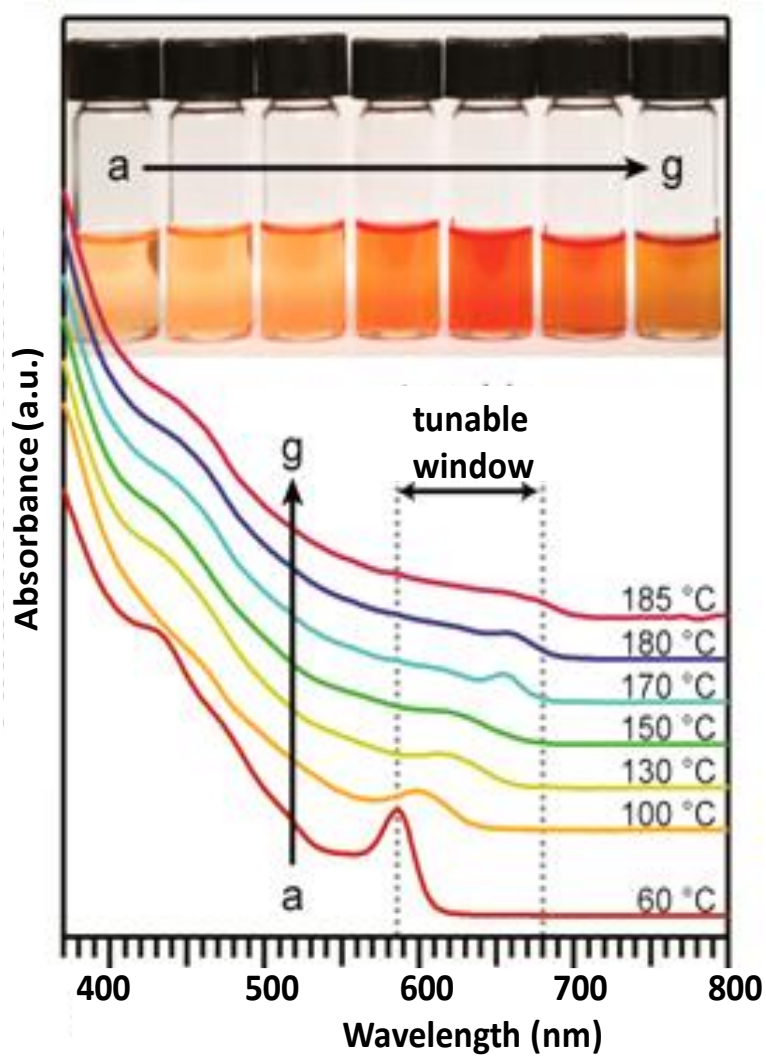

Figure 4.11: Controlling optical properties by tuning the size of α-$CsPbI_3$ nanocrystals. UV-visible absorption spectra and photographs of colloidal α-$CsPbI_3$ nanocrystals synthesized at (a) 60 °C (3.4 nm), (b) 100°C (4.5 nm), (c) 130 °C (5 nm), (d) 150 °C (6.8 nm), (e) 170 °C (8 nm), (f) 180 °C (9 nm), and (g) 185 °C (12.5 nm). The numbers in parentheses are the average edge length from TEM. Data are vertically shifted for clarity.

The optical bandgap tunability with varying the size of NCs is shown in Figure 4.11. The bandgap shifted from 680 nm (1.82 eV) to 585 nm (2.12 eV) by reducing the size of the NCs from 12.5 nm to 3.4 nm. UV-visible absorption shows that the optical gaps of all sized NCs are larger than the bandgap value of bulk α-$CsPbI_3$ (1.73 eV)[24] and increases with decreasing size of NCs. This suggests the quantum confinement effect on charge carriers.[12] Interestingly, UV-visible absorption spectra of smaller size NCs show sharp excitonic feature suggesting for better size distribution. In previous reports and in Figure 4.12, the sharp excitonic feature at the similar range of energy has not been achieved by tuning the halide composition of $CsPbX_3$ nanocubes.[29,32] Hence, the sharp excitonic feature make the smaller sized NCs suitable for investigation of intrinsic photophysics of α-$CsPbI_3$ NCs arising from quantum confinement effect. Furthermore, the Bohr excitonic diameter for α-$CsPbI_3$ system (~12 nm)[8] is larger than the $CsPbBr_3$ (~7 nm)[8] hence for a similar size range the quantum size effect will be more for $CsPbI_3$ system in comparison to that of $CsPbBr_3$ system. As a result on studying $CsPbI_3$ NCs, it will be easier to study the intrinsic phototophysics of $CsPbX_3$ system as a function of quantum size effect without going to too small size range, where surface to volume ratio dominates and makes the study complicated together with error sources from imaging of too small NC.

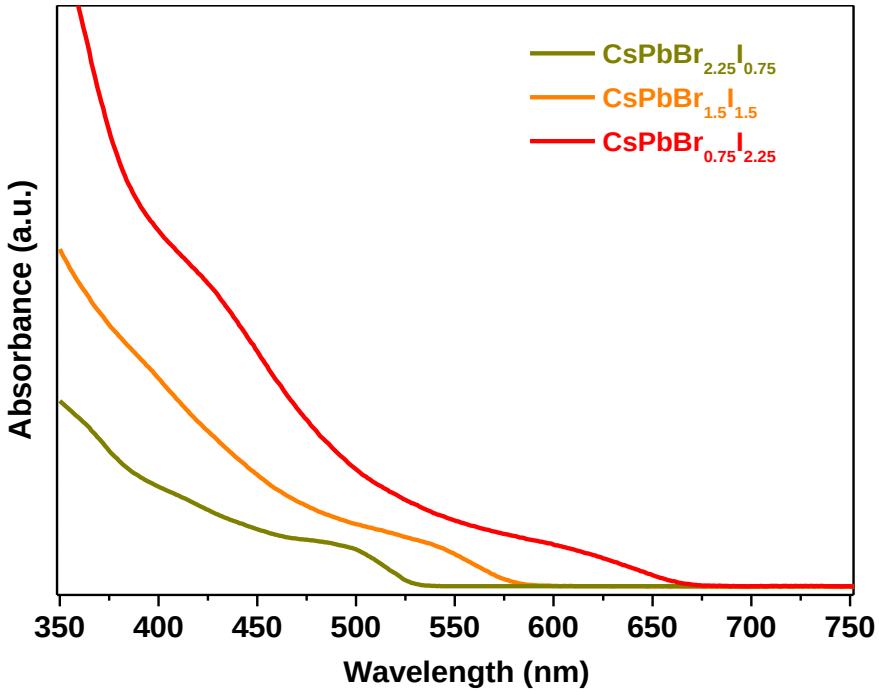

Figure 4.12: Tuning the energy band gap by varying the halide composition. UV-visible absorption spectra of $CsPb(Br/I)_3$ of varying halide composition showing very less excitonic feature in comparison to those of smaller sized α-$CsPbI_3$ NCs, as shown in Figure 4.11.

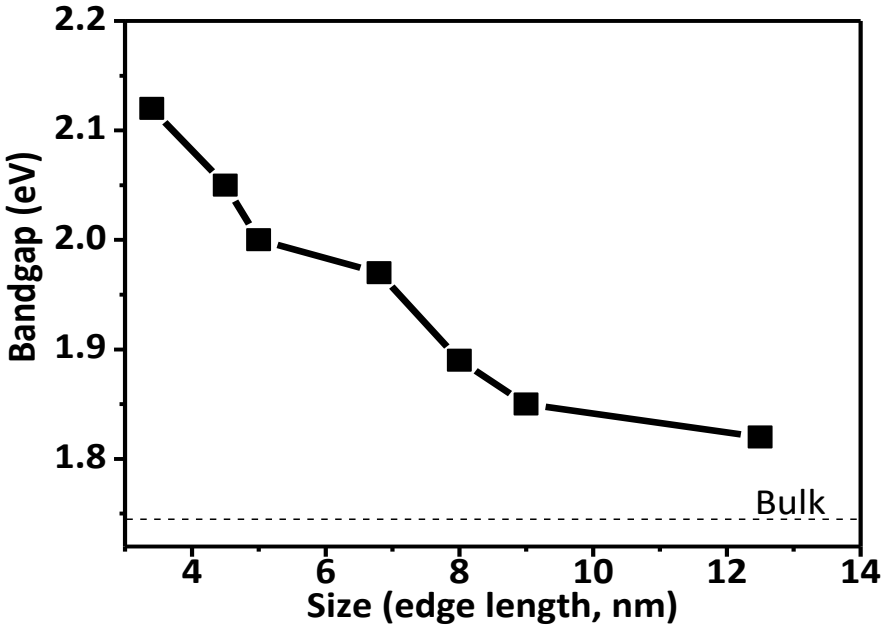

Figure 4.13: Quantum size effect. Size dependence of optical bandgap energy of α-$CsPbI_3$ nanocrystals. Filled square symbols are experimental data, solid line is guide to eye, and dashed-line indicates energy bandgap of bulk α-$CsPbI_3$.

Figure 4.13 shows the size versus optical bandgap for α-$CsPbI_3$ NCs. Using the size versus bandgap plot, it will be easier to determine the size of the synthesized $CsPbI_3$ NCs just by putting the bandgap value (in eV) from the UV-visible absorption spectrum of those NCs.

4.3.3 Luminescence

Size-dependent tuning of PL emission is shown in Figure 4.14 along with photograph of UV excited NCs dispersed in hexane. Upon UV excitation, emission was in the orange (600 nm) to red (685 nm) color range, corresponding to a bandgap between 2.07 and 1.81 eV. The full width at half maximum (FWHM) of the PL for the smallest NCs was 83 meV and increased slightly for the larger sizes (Figure 4.15), whereas the PLQY varied from 21 to 55% for different sizes of NCs (Figure 4.16). PLQY remains high and shows a trend of increase on decreasing the size of $CsPbI_3$ NCs as a consequence of increase of PL transition probability on decreasing the NC size. The smaller sized NCs (3.4 nm), having peak energy at 2.07 eV, show deviation from the trend and the PLQY of these NCs is low, probably, because of the poor crystallinity, as these NCs are synthesized at very low temperature (60 ^{o}C).

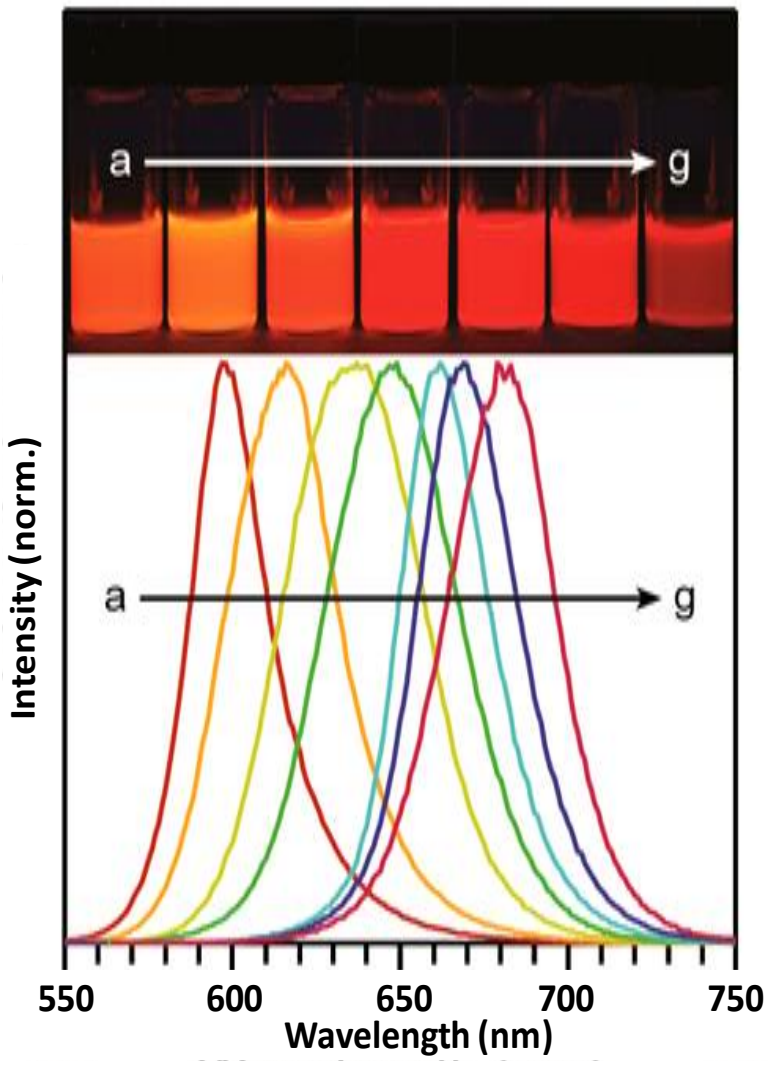

Figure 4.14: Controlling photoluminescence by tuning the size of α-$CsPbI_3$ nanocrystals. Normalized photoluminescence spectra and photographs under UV (365 nm) illumination of the nanocrystals synthesized at (a) 60 °C (3.4 nm), (b) 100 °C (4.5 nm), (c) 130 °C (5 nm), (d) 150 °C (6.8 nm), (e) 170 °C (8 nm), (f) 180 °C (9 nm), and (g) 185 °C (12.5 nm).The numbers in parentheses are the average size from TEM. The sample were excited at 500 nm to measure the PL.

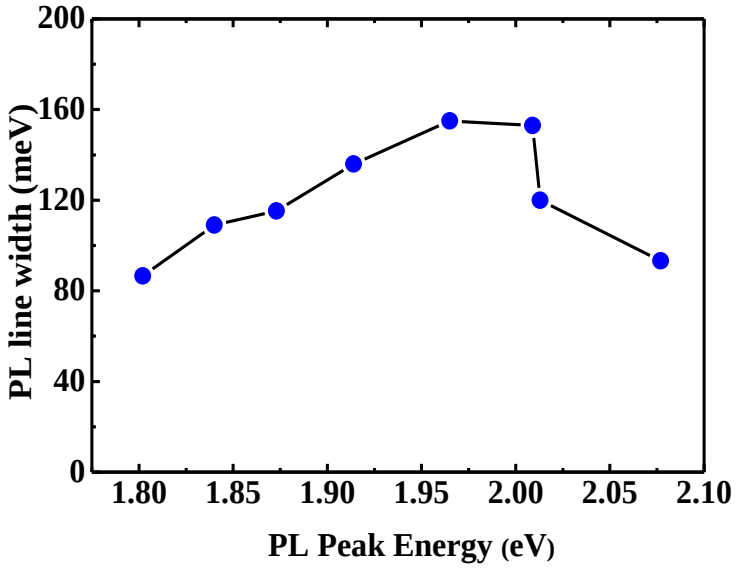

Figure 4.15: Emission color purity. Full width at half maximum (FWHM) of photoluminescence of different sized nanocrystals in term of their photoluminescence peak energy. Filled circles are experimental data and the solid line is just a guide to eye.

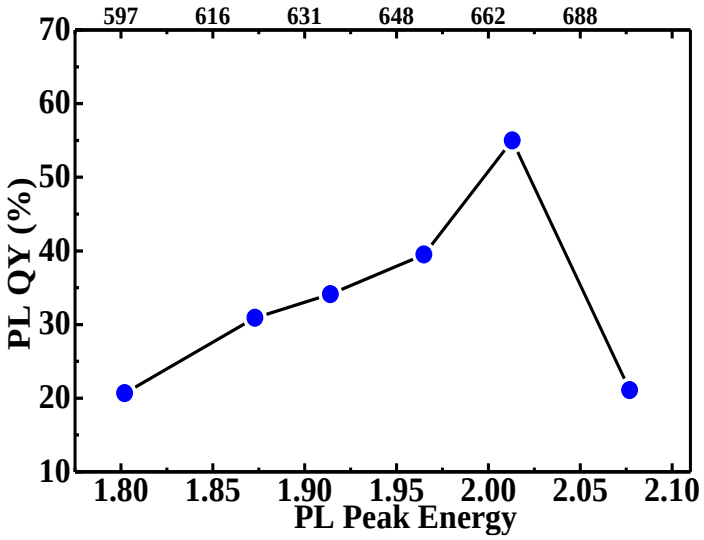

Figure 4.16: Emission color efficiency. Photoluminescence quqntum yield (PLQY) of different size nanocrystals in term of their photoluminescence (PL) peak energy. Filled circles are experimental data and the solid line is just a guide to eye.

PL decay profiles (shown in Figure 4.17) of different sizes α-$CsPbI_3$ NCs, were fitted with bi-exponential decay, and the best fit parameters are shown in Table.1. None of these samples show lifetime ≤ 1 ns, suggesting no significant nonradiative recombination related decay

channels in these NCs. This observation of negligible non-radiative recombination agrees with high PLQY of α-$CsPbI_3$ NCs without having any surface modifications. The average lifetime varies from 15 to 9 ns on varying the size from 12.5 nm to 4.5 nm. Two radiative lifetimes of nearly equal contribution, first in the range of 5-8 nm and second in the range of 11-19 ns, were observed for all samples. Table 1 shows that both the lifetimes decreases with decreasing the NC size, as a consequence of quantum confinement effect. Since, both electron and hole in $CsPbI_3$ NCs have similar effective masses (m_e = 11 and m_h = 13),[8] hence, both charge carriers are expected to experience nearly equal extent of confinement when size of NCs decreases compared to excitonic Bohr diameter. Such a confinement increases the overlap between electron and hole wave functions, which in turn can increases the optical transition probability, thereby decreasing the radiative lifetime. When compare to traditional QDs, radiative life times of α-$CsPbI_3$ NCs are similar to those of CdSe NC system.[33]

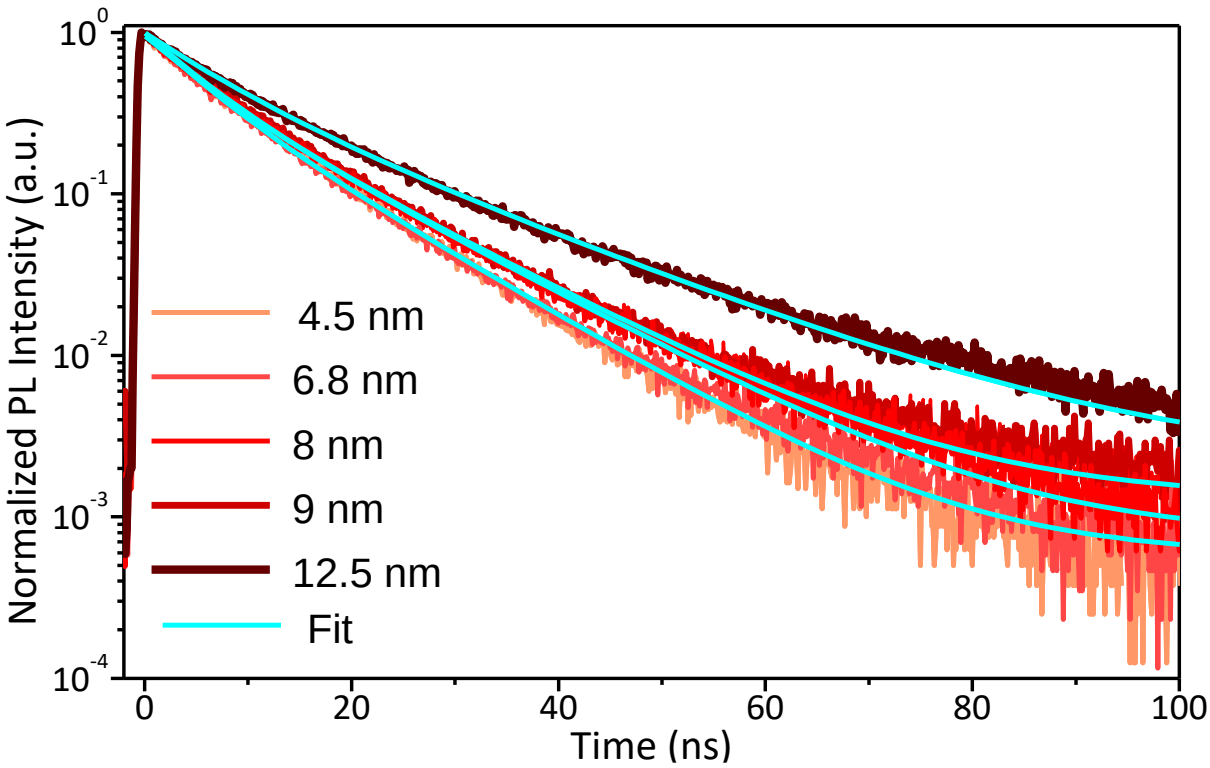

Figure 4.17: PL decay dynamics. PL decay dynamics of colloidal α-$CsPbI_3$ nanocrystal of different sizes dispersed in hexane. Excitation wavelength is kept at 500 nm for all the samples and emissions were collected at the PL peak position of the respective samples, as shown in Figure 4.14.

Table 4.1: The best fit parameters (with 95% confidence limit) of photoluminescence decay profiles of different sized α-$CsPbI_3$ NCs solution measured at different emission peak energies shown in Figure 4.17 using bi-exponential decay: A_1 and A_2 are percent contributions of lifetimes from $\tau_1$and τ_2 respectively.The average lifetimes (τ_{avg}) were calculated as $\tau_{avg} = \sum A_i\tau_i^2 / \sum A_i\tau_i$

Size (nm)	A_1 (%)	τ_1 (ns)	A_2 (%)	τ_2 (ns)	τ_{avg} (ns)
4.5	46	5.1	54	11.6	9.9
6.8	50	5.3	50	11.9	9.9
8	49	5.6	51	12.9	10.7
9	48	6.4	52	13.3	11.1
12.5	52	7.8	48	18.3	15.0

4.3.4 Absorption or Extinction Coefficient of α-$CsPbI_3$ NCs

High PL QY along with narrow PL line width for $CsPbI_3$ NCs are important for various efficient light emitting applications, including single-NC-based super-resolution PL imaging. Furthermore, α-$CsPbI_3$ is a low band gap (1.73 eV) all-inorganic halide perovskite and thermally more stable in comparison to $CH_3NH_3PbI_3$. Hence, these α-$CsPbI_3$ NCs are suitable candidate for light harvesters in solar cell application. To make these devices and for their optimization, one has to know the concentration (*C*) of the NCs solution and also the absorption coefficient of the NCs. A common analytical method for determining *C* is the Beer-Lambert's law by employing absorption coefficient, often expressed in terms of molar extinction coefficient ε with unit $M^{-1}\,cm^{-1}$ ($1\ mol^{-1}\,cm^{-1}$).

$$\varepsilon = \frac{A}{CL}$$

Where,

A = Absorbance (it depend on ratio of transmitted (*I*) and incident (I_o) light intensity on neglecting reflection of the light from the cuvette surfaces). Its value is a measure of probability of electronic transition of the material and could be recorded in UV-visible absorption spectroscopy measurement. To get rid of scattering phenomenon, very dilute NC solution were taken for the measurement.

L = optical pathlength (from dimension of used cuvette).

C = Concentration of the NC solution expressed in term of mol L^{-1}. Calculation of the value of *C* was done by following elemental analysis (ICP-MS) of Cs ion concentration of digested $CsPbI_3$ NCs as discussed in the experimental section.

Further. the molar extinction coefficient at wavelength, λ (ε_λ) is related to the absorption coefficient at that value of λ, (μ_λ) as

$$\mu_\lambda = \frac{\ln(10)\,\epsilon_\lambda}{V N_A}$$

Where.

V = volume of NC (here $(size)^3$) and N_A = Avogadro's number

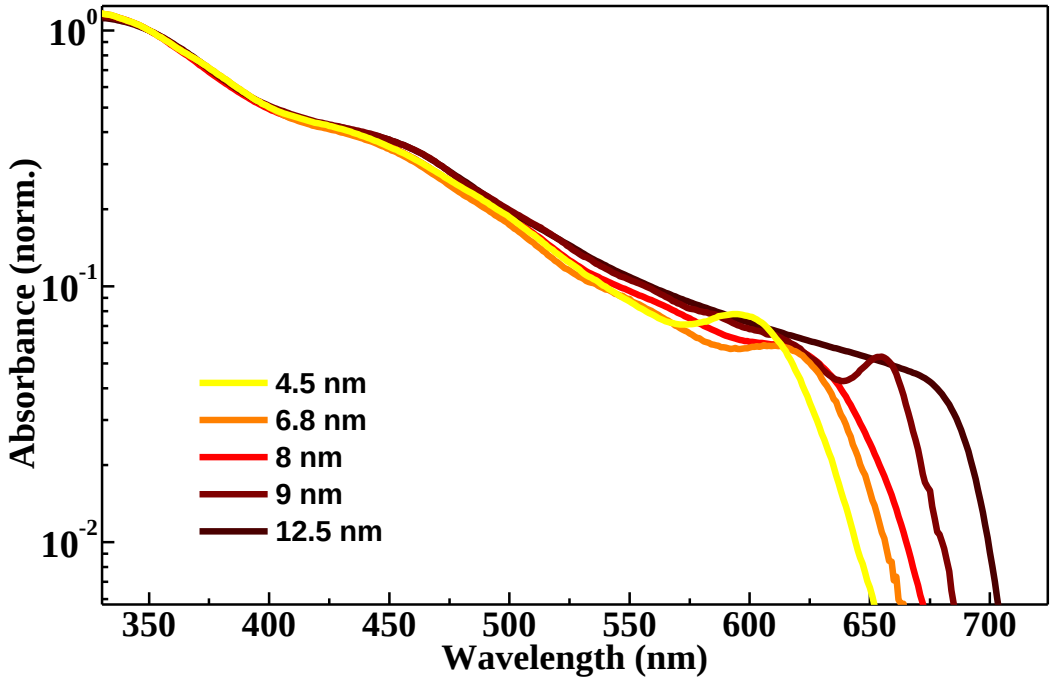

Figure 4.18: **Different sized nanocrystals absorb similar amount of light at high energies.** Series of absorbance spectra of α-$CsPbI_3$ nanocrystals suspended in hexane, normalized at ~3.5 eV (350 nm).

Figure 4.18 shows UV-visible absorption spectra of different sized α-$CsPbI_3$ NCs normalized at 350 nm (~3.5 eV). At higher energy (>3 eV or <400 nm) the absorption spectra show size independency which is similar to that of CdSe,[21] InAs[34] and PbSe[27] QDs systems and following the Maxwell-Garnett (MG) effective medium model.[35] It suggests exhibition of

bulk like optical properties and no influence of quantum confinement on μ at high energy regime (> 3 eV) for a specified shape.

In our elemental analysis, it has been found that the cation ratio, Pb^{2+}/Cs^{+} (R), value increases on decreasing the size of the NC as shown in Table 2. This suggest that on increasing the surface to volume ratio while decreasing the size of the NCs, content of Pb^{2+} increases as some amount of Pb^{2+} ions contribute to the surface on remaing as non-crystalline lead-oleate. This data support the previous literature.[9] Looking at the inconsistency of Pb^{2+} concentration value, we took concentration of Cs^{+} as a key parameter to calculate the concentration of α-$CsPbI_3$ NCs, as Cs^{+} contribute more to crystalline part of α-$CsPbI_3$ NCs in compared to Pb^{2+} and I^{-}.

Following the absorption spectra, our calculations show similar value of μ at high energy region (at 335 and 400 nm) for different sized NCs (Table 2). These result show analogy with PbE system.[25] α-$CsPbI_3$ NCs exhibits μ value of $1.1\pm0.05 \times 10^5$ cm^{-1} at wavelength 400 nm (as shown in Figure 4.19), which is similar to that of CdE based QDs[15, 20-28] and also to that of $CsPbBr_3$ NCs[9] in term of order of magnitude. This high value of μ value is another advantage exhibited by α-$CsPbI_3$ NCs, for applications involving absorption or harvesting of light.

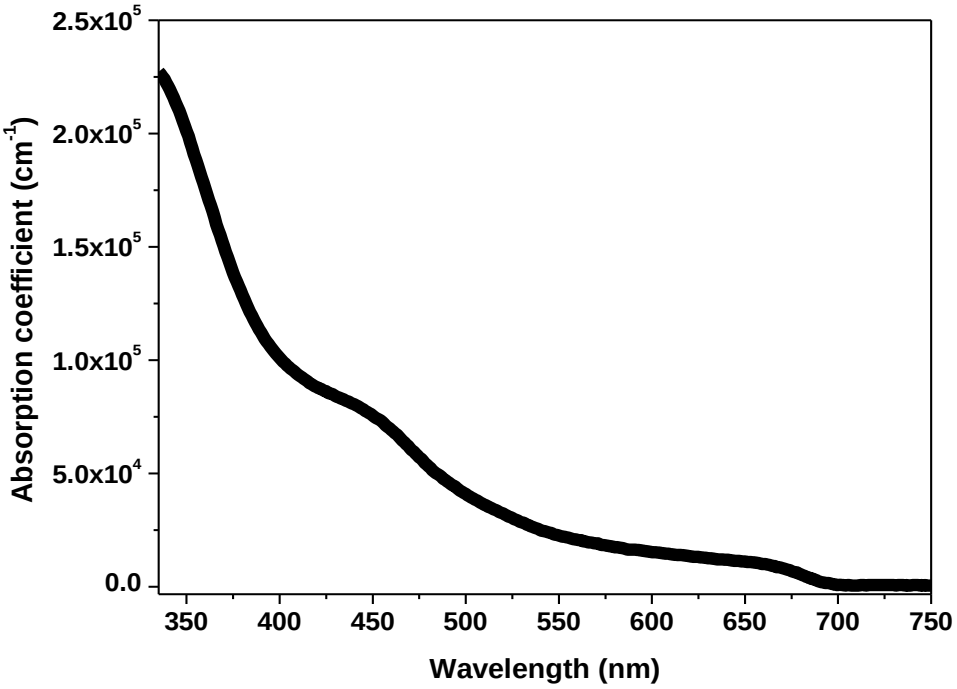

Figure 4.19: Absorption coefficient of α-$CsPbI_3$ NCs. Absorption coefficient value of α-$CsPbI_3$ NCs of size 12.5 nm at different wavelength.

Table 4.2: Cationic ratio (R = Pb^{2+}/Cs^{+}) and absorption coefficient, μ, of three different sized α-$CsPbI_3$ NCs.

Size (nm)	R = Pb^{2+}/Cs^{+} (from ICP-MS)	μ_{400} (cm^{-1})	μ_{335} (cm^{-1})
4.5	1.2	1.12×10^5	2.42×10^5
6.8	1.1	1.10×10^5	2.35×10^5
12.5	1.05	1.01×10^5	2.25×10^5

For further research works, to estimate the unknown concentrations of α-$CsPbI_3$ NCs from their UV-visible absorption spectra, the calculated value of ε (or μ) can be used. It will be easier to calculate the concentration of any sized NCs (and hence any size distribution) colloidal solution by using the ε value at higher energy.

4.4 Conclusions:

We synthesized colloidal α-$CsPbI_3$ NCs that are stable in ambient condition. Different sized NCs in the size range of 3.4 to 12.5 nm were prepared by varying the reaction temperature. The NCs were successfully purified without affecting the phase and colloidal stability. This stabilization of α-phase of $CsPbI_3$ NCs at room temperature is a major development, since for bulk $CsPbI_3$ δ-phase form at room temperature. Since α-phase is the optoelectronically active phase of $CsPbI_3$ for photovoltaic application, and is thermally stable one till ~500 ºC, α-$CsPbI_3$ NCs provides an opportunity for optoelectronic applications. Therefore, our synthesis of colloidal α-$CsPbI_3$ NC, a new material at room temperature, for which bulk counterpart is not stable. This newly developed α-$CsPbI_3$ is ready for use in photovoltaic cell, photodiode and LEDs. Some of the device fabrication and properties will be discussed in the subsequent chapter 5 of this thesis. In this regard, we first studied the photophysical properties understanding the effect of quantum confinement and surface defects on bandgap, excitonic transition properties and PL. All samples show excitonic (or bandgap) emission with PLQY in the range of 21 to 51 % maintaining a narrow FWHM (83 to 155 meV). PL decay show average radiative lifetime in the range of 10 ns for 4.5 nm sized NC to 15 ns for 12.5 nm sized NCs. These results suggest increase in transition probability for radiative excitonic recombination with decreasing size of the NCs. The high PLQY and near absence of significant non-radiative component in PL decay suggest defect tolerant behavior of these NCs and are encouraging for optoelectronic applications.

References:

1. Yakunin, S.; Protesescu, L.; Krieg, F.; Bodnarchuk, M. I.; Nedelcu, G.; Humer, M.; De Luca, G.; Fiebig, M.; Heiss, W.; Kovalenko, M. V., Low-threshold amplified spontaneous emission and lasing from colloidal nanocrystals of caesium lead halide perovskites. *Nat. Commun.* **2015,** *6*.

2. Wang, Y.; Li, X. M.; Song, J. Z.; Xiao, L.; Zeng, H. B.; Sun, H. D., All-Inorganic Colloidal Perovskite Quantum Dots: A New Class of Lasing Materials with Favorable Characteristics. *Adv. Mater.* **2015,** *27*, 7101.

3. Swarnkar, A.; Chulliyil, R.; Ravi, V. K.; Irfanullah, M.; Chowdhury, A.; Nag, A., Colloidal $CsPbBr_3$ Perovskite Nanocrystals: Luminescence beyond Traditional Quantum Dots. *Angew. Chem-Intern. Ed.* **2015,** *54*, 15424-15428.

4. Hu, F. R.; Zhang, H. C.; Sun, C.; Yin, C. Y.; Lv, B. H.; Zhang, C. F.; Yu, W. W.; Wang, X. Y.; Zhang, Y.; Xiao, M., Superior Optical Properties of Perovskite Nanocrystals as Single Photon Emitters. *Acs Nano* **2015,** *9*, 12410-12416.

5. Zhang, X.; Lin, H.; Huang, H.; Reckmeier, C.; Zhang, Y.; Choy, W. C. H.; Rogach, A. L., Enhancing the Brightness of Cesium Lead Halide Perovskite Nanocrystal Based Green Light-Emitting Devices through the Interface Engineering with Perfluorinated Ionomer. *Nano Lett.* **2016,** *16*, 1415-1420.

6. Song, J. Z.; Li, J. H.; Li, X. M.; Xu, L. M.; Dong, Y. H.; Zeng, H. B., Quantum Dot Light-Emitting Diodes Based on Inorganic Perovskite Cesium Lead Halides ($CsPbX_3$). *Adv. Mater.* **2015,** *27* , 7162.

7. Park, Y. S.; Guo, S. J.; Makarov, N. S.; Klimov, V. I., Room Temperature Single-Photon Emission from Individual Perovskite Quantum Dots. *Acs Nano* **2015,** *9*, 10386-10393.

8. Protesescu, L.; Yakunin, S.; Bodnarchuk, M. I.; Krieg, F.; Caputo, R.; Hendon, C. H.; Yang, R. X.; Walsh, A.; Kovalenko, M. V., Nanocrystals of Cesium Lead Halide Perovskites ($CsPbX_3$, X = Cl, Br, and I): Novel Optoelectronic Materials Showing Bright Emission with Wide Color Gamut. *Nano Lett.* **2015,** *15*, 3692-3696.

9. De Roo, J.; Ibáñez, M.; Geiregat, P.; Nedelcu, G.; Walravens, W.; Maes, J.; Martins, J. C.; Van Driessche, I.; Kovalenko, M. V.; Hens, Z., Highly Dynamic Ligand Binding and Light Absorption Coefficient of Cesium Lead Bromide Perovskite Nanocrystals. *ACS Nano* **2016,** *10*, 2071-2081.

10. Swarnkar, A.; Mir, W. J.; Nag, A., Can B-Site Doping or Alloying Improve Thermal- and Phase-Stability of All-Inorganic $CsPbX_3$ (X = Cl, Br, I) Perovskites? *ACS Energy Lett.* **2018,** *3*, 286-289.

11. Akkerman, Q. A.; D'Innocenzo, V.; Accornero, S.; Scarpellini, A.; Petrozza, A.; Prato, M.; Manna, L., Tuning the Optical Properties of Cesium Lead Halide Perovskite Nanocrystals by Anion Exchange Reactions. *J. Am. Chem. Soc.* **2015,** *137*, 10276-10281.

12. Nedelcu, G.; Protesescu, L.; Yakunin, S.; Bodnarchuk, M. I.; Grotevent, M. J.; Kovalenko, M. V., Fast Anion-Exchange in Highly Luminescent Nanocrystals of Cesium Lead Halide Perovskites ($CsPbX_3$, X = Cl, Br, I). *Nano Lett.* **2015,** *15*, 5635-5640.

13. Kulbak, M.; Gupta, S.; Kedem, N.; Levine, I.; Bendikov, T.; Hodes, G.; Cahen, D., Cesium Enhances Long-Term Stability of Lead Bromide Perovskite-Based Solar Cells. *J. Phys. Chem. Lett.* **2016,** *7*, 167-172.

14. Eperon, G. E.; Paterno, G. M.; Sutton, R. J.; Zampetti, A.; Haghighirad, A. A.; Cacialli, F.; Snaith, H. J., Inorganic caesium lead iodide perovskite solar cells. *J. Mater. Chem. A* **2015,** *3*, 19688-19695.

15. Murray, C. B.; Norris, D. J.; Bawendi, M. G., Synthesis and characterization of nearly monodisperse CdE (E = sulfur, selenium, tellurium) semiconductor nanocrystallites. *J Am. Chem. Soc.* **1993,** *115*, 8706-8715.

16. Lignos, I.; Stavrakis, S.; Nedelcu, G.; Protesescu, L.; deMello, A. J.; Kovalenko, M. V., Synthesis of Cesium Lead Halide Perovskite Nanocrystals in a Droplet-Based Microfluidic Platform: Fast Parametric Space Mapping. *Nano Lett.* **2016,** *16*, 1869-1877.

17. Lin, C. C.; Meijerink, A.; Liu, R.-S., Critical Red Components for Next-Generation White LEDs. *J.Phys. Chem. Lett.* **2016,** *7*, 495-503.

18. Trots, D. M.; Myagkota, S. V., High-temperature structural evolution of caesium and rubidium triiodoplumbates. *Journal of Phys. and Chem. of Solids* **2008,** *69*, 2520-2526.

19. Makarov, N. S.; Guo, S.; Isaienko, O.; Liu, W.; Robel, I.; Klimov, V. I., Spectral and Dynamical Properties of Single Excitons, Biexcitons, and Trions in Cesium–Lead-Halide Perovskite Quantum Dots. *Nano Lett.* **2016**.

20. Yu, W. W.; Qu, L.; Guo, W.; Peng, X., Experimental Determination of the Extinction Coefficient of CdTe, CdSe, and CdS Nanocrystals. *Chem. Mater.* **2003,** *15*, 2854-2860.

21. Leatherdale, C. A.; Woo, W. K.; Mikulec, F. V.; Bawendi, M. G., On the Absorption Cross Section of CdSe Nanocrystal Quantum Dots. *J. Phys. Chem. B* **2002,** *106*, 7619-7622.

22. Jasieniak, J.; Smith, L.; Embden, J. v.; Mulvaney, P.; Califano, M., Re-examination of the Size-Dependent Absorption Properties of CdSe Quantum Dots. *J. Phys.l Chem. C.* **2009,** *113*, 19468-19474.

23. Nirmal, M.; Brus, L., Luminescence Photophysics in Semiconductor Nanocrystals. *Acc. Chem. Res.* **1999,** *32*, 407-414.

24. Moreels, I.; Lambert, K.; Smeets, D.; De Muynck, D.; Nollet, T.; Martins, J. C.; Vanhaecke, F.; Vantomme, A.; Delerue, C.; Allan, G.; Hens, Z., Size-Dependent Optical Properties of Colloidal PbS Quantum Dots. *ACS Nano* **2009,** *3*, 3023-3030.

25. Cademartiri, L.; Montanari, E.; Calestani, G.; Migliori, A.; Guagliardi, A.; Ozin, G. A., Size-Dependent Extinction Coefficients of PbS Quantum Dots. *J. Am. Chem. Soc.* **2006,** *128*, 10337-10346.

26. Dai, Q.; Wang, Y.; Li, X.; Zhang, Y.; Pellegrino, D. J.; Zhao, M.; Zou, B.; Seo, J.; Wang, Y.; Yu, W. W., Size-Dependent Composition and Molar Extinction Coefficient of PbSe Semiconductor Nanocrystals. *ACS Nano* **2009,** *3*, 1518-1524.

27. Moreels, I.; Lambert, K.; De Muynck, D.; Vanhaecke, F.; Poelman, D.; Martins, J. C.; Allan, G.; Hens, Z., Composition and Size-Dependent Extinction Coefficient of Colloidal PbSe Quantum Dots. *Chem. Mater.* **2007,** *19*, 6101-6106.

28. Semonin, O. E.; Johnson, J. C.; Luther, J. M.; Midgett, A. G.; Nozik, A. J.; Beard, M. C., Absolute Photoluminescence Quantum Yields of IR-26 Dye, PbS, and PbSe Quantum Dots. *J. Phys. Chem. Lett.* **2010,** *1*, 2445-2450.

29. Cottingham, P.; Brutchey, R. L., On the Crystal Structure of Colloidally Prepared $CsPbBr_3$ Quantum Dots. *Chem. Commun.* **2016,** *52*, 5246-5249

30. Pearson, R. G., HARD AND SOFT ACIDS AND BASES. *J. Am. Chem. Soc.* **1963,** *85*, 3533-3539.

31. Akkerman, Q. A.; Motti, S. G.; Srimath Kandada, A. R.; Mosconi, E.; D'Innocenzo, V.; Bertoni, G.; Marras, S.; Kamino, B. A.; Miranda, L.; De Angelis, F.; Petrozza, A.; Prato, M.; Manna, L., Solution Synthesis Approach to Colloidal Cesium Lead Halide Perovskite Nanoplatelets with Monolayer-Level Thickness Control. *J. Am. Chem. Soc.* **2016,** *138*, 1010-1016.

32. Bekenstein, Y.; Koscher, B. A.; Eaton, S. W.; Yang, P.; Alivisatos, A. P., Highly Luminescent Colloidal Nanoplates of Perovskite Cesium Lead Halide and Their Oriented Assemblies. *J. Am. Chem. Soc.* **2015,** *137*, 16008-16011.

33. Swarnkar, A.; Shanker, G. S.; Nag, A., Organic-free colloidal semiconductor nanocrystals as luminescent sensors for metal ions and nitroaromatic explosives. *Chem. Commun.* **2014,** *50*, 4743-4746.

34. Yu, P.; Beard, M. C.; Ellingson, R. J.; Ferrere, S.; Curtis, C.; Drexler, J.; Luiszer, F.; Nozik, A. J., Absorption Cross-Section and Related Optical Properties of Colloidal InAs Quantum Dots. *J. Phys. Chem. B* **2005,** *109*, 7084-7087.

35. Maxwell Garnett, J. C., Colours in Metal Glasses and in Metallic Films. *Philosophical Transactions of the Royal Society of London. Series A* **1904,** *203*.

Chapter 5

Surface Ligand-Engineering of $CsPbX_3$ (X=Br, I) Nanocrystal Film for Optoelectronics

---

The following articles have been published based on the work presented in this chapter.

1. Swarnkar, A.; Marshall, A. R.; Sanehira, E. M.; Chernomordik, B. D.; Moore, D. T.; Christians, J. A.; Chakrabarti, T.; Luther, J. M. Quantum Dot–Induced Phase Stabilization of α-$CsPbI_3$ Perovskite for High-Efficiency Photovoltaics. *Science* **2016,** *354*, 92. Copyright permission has been taken from American Association for the Advancement of Science (AAAS) for the entire article.

2. Sim, K. M.; Swarnkar, A.; Nag, A.; Chung, D. S. Phase Stabilized α-$CsPbI_3$ Perovskite Nanocrystals for Photodiode Applications. *Laser Photonics Rev*.**2018,** *12*, 1700209. Copy right permission has been taken from Wiley-VCH Verlag GmbH & Co. for the entire article.

3. Kumawat, N. K.; Swarnkar, A.; Nag, A.; Kabra, D. Ligand Engineering to Improve the Luminance Efficiency of $CsPbBr_3$ Nanocrystal Based Light-Emitting Diodes. *J. Phys. Chem. C*, **2018,** *122*, 13767-13773. Copyright permission has been taken from American Chemical Society for the entire paper.

Summary

Organic capping ligands are the inherent part of the colloidal synthesis of nanocrystals (NCs). In a typical colloidal synthesis, ligands are required to dissolve the reaction precursors, to control the size and shape of the NCs, and to passivate dangling bonds on NC surface. Also, these ligands provide colloidal dispersity of NCs. Mostly, these ligands are long-chain hydrocarbon and are insulating in nature. Therefore, when the NCs are deposited as films to fabricate electronic or optoelectronic devices, these ligands hamper the charge transport properties. Often, high polar solvents are used to do ligand modification of covalent system like CdSe NCs for improving the charge transport properties. But $CsPbX_3$ (X=Br, I) NCs are ionic compound and disintegrate in presence of high polar solvents. This problem motivated us to develop a new strategy for surface modification of $CsPbX_3$ NCs. In this chapter, we present deposition of electronically coupled $CsPbX_3$ NC film, in which ligands are on the surface of NCs washed/modified using mildly polar methyl acetate solvent. Optical and structural properties show efficiency of this ligand engineering methodology in preparing device grade NC films. Eventually, efficient and stable optoelectronic devices like solar cell, photodiode and light emitting diodes were fabricated using these ligand treated $CsPbX_3$ NCs films.

Graphical abstract

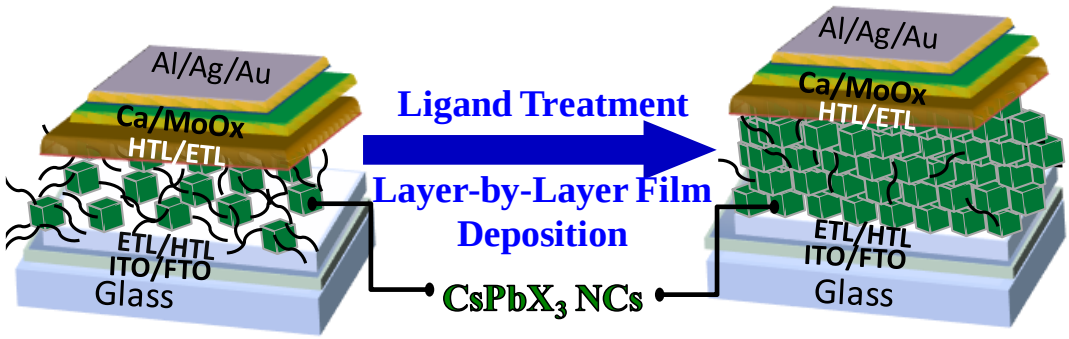

Deposition of Electronically Coupled NC Film for Optoelectronics

5.1 Introduction

Recently, all-inorganic lead halide perovskite ($CsPbX_3$; X= Cl, Br, I) materials are being employed for different optoelectronic devices because stability wise these have high melting temperature (~500 ^{0}C).[1] But thin film properties are not so great for device application due to coverage issue.[2] In this regard, colloidal nanocrystals (NCs) or quantum dots (QDs) could be an attractive approach for solar cell and light emitting diode (LED) applications as they combine both solution processibility and excellent photoluminescence (PL) quantum yield (QY).[3] In previous chapters it has already been discussed that defect tolerant $CsPbX_3$ NCs exhibit size as well as composition (varying halide) dependent emission color, narrow emission spectra, exceptionally high PLQY and high absorption coefficient.[3-4] Also, as discussed in chapter 4, red emitting α-$CsPbI_3$ NCs show optoelectronically active α-phase stability at room temperature unlike its bulk counterpart.[3] These unique properties of $CsPbX_3$ NCs open a new space in the research community for next-generation optoelectronic devices, such as, solar cells, photodiodes and LEDs.[5]

Long chain hydrocarbon ligands on the surface of colloidal NCs are integral part of the colloidal synthesis.[6] These ligands are required for dissolving reactants, controlling the size and shape of the NCs, passivating the NC surface and maintaining the long term colloidal stability of the NC solution. [3-4, 7] But in colloidal NCs based devices, poor charge injection (or extraction) into (or from) the NCs due to the presence of these insulating ligands on the surface of NCs, reduce the device performance.[8] Partial or complete removal of these ligands from the surface of NCs may improve both the charge transfer and charge transport efficiencies, improving the overall efficiencies of optoelectronic devices[9] such as photovoltaic cell, photodiode and LED. However, such surface modifications need to be carefully designed, such that the surface defects are reasonably well-passivated.

Here, we report the effect of surface treatment of $CsPbX_3$ NCs with methylacetate (MeOAc) on optical, photovoltaic, photodiode and electroluminescence (EL) properties after fabricating α-$CsPbI_3$ NC based photovoltaic cell, photodiode and $CsPbBr_3$ NC based LED. In this process, we first fabricate the electronically coupled α-$CsPbI_3$ NCs film as an active layer by doing ligand engineering and then produce air-stable, efficient photovoltaic cells with efficiency above 10%. Further, by following the same film fabrication method we made hysteresis-free photodiode of high detectivity of 1.8×10^{12} Jones. Also, the performance of electronically coupled $CsPbBr_3$ NCs film has been characterized by making $CsPbBr_3$ NC

based LED. We optimized reduced PL due to ligand washing versus charge-carrier balance and demonstrate current efficiency of 6 cd/A and EQE~2.2% in green emitting $CsPbBr_3$ NC LED.

5.2 Experimental section

5.2.1 Chemicals

All chemicals were purchased from Sigma Aldrich and used without purification, unless otherwise noted. Colloidal $CsPbBr_3$ and α-$CsPbI_3$ NCs are synthesized in the laboratory (details are provided in Chapter 3 and Chapter 4 respectively). In this chapter of deposition of electronically coupled $CsPbX_3$ NCs film for different optoelectronic devices, α-$CsPbI_3$ NC of size (edge length of cube shaped NCs) 9 ± 1 and 12.5 ± 2 nm have been used to make photovoltaic and photodiode devices respectively while $CsPbBr_3$ NCs of edge length 11 ± 0.7 nm are employed to make LED device. For NCs film characterization different sized α-$CsPbI_3$ NCs (of edge length 4.5 nm, 6.8 nm and 9 nm) were used. Toluene (anhydrous 99.8%), hexane (reagent grade ≥95%), octane (anhydrous, ≥99%), methyl acetate (MeOAc, anhydrous 99.5%), lead (II) acetate trihydrate ($Pb(OAc)_2 \cdot 3H_2O$, 99.999%), lead (II) nitrate ($Pb(NO_3)_2$, 99.999%), ethanol (EtOH, 200 proof, ≥99.5%), titanium ethoxide (≥97%), hydrochloric acid (HCl, 37% in water), 2,2′,7,7′-Tetrakis(N,N-di-p-methoxyphenylamine)-9,9′-spirobifluorene (spiro-OMeTAD, Lumtec, ≥99.5%), chlorobenzene (anhydrous, 99.8%), 4-tert-butylpyridine, bis(trifluoromethane) sulfonimide lithium salt (Li-TFSI), and acetonitrile (anhydrous, 99.8%).

5.2.2 NC Film Fabrication

The NCs dispersion (~50 mg/mL in octane) were spin-casted at 1000 RPM for 20 sec followed by 2000 RPM for 5 sec on the substrate (glass/FTO (F-doped SnO_2) or glass/ITO (Sn-doped InO_3) and swiftly dipped 2-3 times in the ligand solution (neat MeOAc, saturated lead acetate solution or saturated lead nitrate solution dissolved in MeOAc) for ligand treatment. Ligand solutions were made by sonicating 10 – 20 mg of powder ($Pb(OAc)_2$ or $Pb(NO_3)_2$) in 20 mL of anhydrous MeOAc for 10 min. The excess salt was removed by centrifugation at 4000 RPM for 5 min. The films were then rinsed using neat, anhydrous MeOAc, and then dried with streams of air. Films treated using only MeOAc were simply treated with a single rinsing step. This treatment was repeated multiple (3-6) times to build up 100 – 500 nm thick films.

5.2.3 $CsPbX_3$ NC Optoelectronic Device Fabrication

α-$CsPbI_3$ NC Photovoltaic Device Fabrication

A ~50 nm TiO_2 layer was deposited via a sol-gel method onto pre-patterned FTO on glass substrates (Thin Film Devices, Inc.). Sol-gel TiO_2 was prepared by mixing 5 mL EtOH, 2 drops HCl, 125 μL deionized water, and 375 μL of titanium ethoxide resulting in a clear solution. The headspace of the vial was filled with nitrogen and the solution was stirred for 48 hours, and then kept in the freezer until use. The sol-gel was spin-casted at 3000 RPM for 20 seconds, and then annealed at 115 ^oC and 450 ^oC for 30 minutes each. The α-$CsPbI_3$ NC photoactive layer was deposited using the procedure described in "NCs film fabrication" section, resulting in a total thickness of ~150 nm. The hole-transporting layer was spin-coated from a solution consisting of 72.3 mg of Spiro-OMeTAD in 1 mL of chlorobenzene, 28.8 μL of 4-TBP, and 17.5 μL of Li-TFSI solution (520 mg/mL in acetonitrile). All spin-coating processes were performed in ambient. MoO_3 was deposited at a rate of 0.2–1.0 Å/s at a base pressure lower than 2×10^{-7} Torr for a total thickness of 15 nm. Al electrodes were evaporated at a rate ranging from 0.5–2 Å/s for a total thickness of 200 nm.

α-$CsPbI_3$ NCs Photodiode Fabrication: The ITO-patterned glass substrates were cleaned with detergent, distilled water, acetone, isopropanol and distilled water by sequential sonication. Sol-gel based ZnO solution was prepared by adding 1 g of zinc acetate dihydrate and 0.28 g of ethanolamine in 2-methoxyethanol and stirred at 600 rpm for 6 hr. The sol-gel based ZnO solution was spin-coated onto the cleaned ITO substrate. The α-$CsPbI_3$ NCs layer was fabricated by layer-by-layer spin coating methods as mentioned above (NC film fabrication). Here, α-$CsPbI_3$ NCs solution of concentration ~20 mg mL^{-1} in hexane was used. The ligand solution (saturated lead nitrate solution in MeOAc) was spin-coated 4000 RPM for 30 sec. Then a P3HT (poly(3-hexylthiophene-2,5-diyl) solution of 10 mg mL^{-1} in xylene was spin-coated onto the substrates. To complete the photodiodes, MoO_3 and Ag were deposited through a shadow mask with a thermal evaporator at the deposition rate of 0.5–1 $Å s^{-1}$ and the vacuum pressure of ~10^{-6} Torr.

$CsPbBr_3$ NCs LED Fabrication: Glass/ITO substrates were cleaned with soap water, deionized (DI) water, acetone, and 2-isopropanol (IPA) using a sonicator. The samples were exposed to oxygen plasma to remove organic contaminants. PEDOT:PSS solution was spin

coated at 5000 RPM for 60 sec and annealed at 150 °C for 30 min in the nitrogen atmosphere. After that, $CsPbBr_3$ NC film was deposited following the film fabrication method as mentioned above. The electron transport layers TPBi (2,2′,2″-(1,3,5-benzinetriyl)-tris(1-phenyl-1-H-benzimidazole) (∼50 nm), Ca (∼20 nm), and Ag (∼100 nm)) were evaporated in 0.75×10^{-6} Torr vacuum pressure using a thermal evaporator. After that, the device was encapsulated using epoxy for measurement.

5.2.4 Characterization

Ultraviolet-visible (UV-vis) absorption spectra were recorded using a Shimadzu UV-3600 UV-vis-NIR spectrophotometer. Steady-state PL was measured using a Horiba Jobin Yvon fluoromax-4 spectrophotometer. UV-vis absorption and PL experiments were done in solution and on thin films (prepared as described above). Time-resolved PL measurements were taken from NCs film. The excitation source was a pulsed Fianium, SC-450-PP, laser with a wavelength of 500 nm and a repetition rate of 1 MHz. A 590 nm long pass filter was used to remove scatter from the excitation source. The emission was detected using a Hamamatsu streak camera model number c10910 with a wavelength range of 200-900 nm and response of <20 ps. The cross-sectional image of the optimized photodiode was analyzed by high-resolution transmission electron microscopy (TEM, HF-3300, Hitachi). Scanning Electron Microscopy (SEM) images were obtained using FEI Quanta 400 FEG instrument (FEI, Hillsboro, OR).

5.2.5 Device Characterization

Photovoltaic Device (Solar Cell) Characterization: Solar cell devices were tested in both a N_2-filled glovebox or in ambient lab air. The solar simulators used for both setups are Newport Oriel Sol3A solar simulators with xenon lamps. A calibrated reference solar cell (either GaAs or KG2 filtered Si to minimize the spectral mismatch) was used to set the intensity of the lamp to 100 mW/cm^2 AM 1.5 conditions. Current density-voltage (*JV*) scans were taken from forward bias to reverse bias with a scan rate of 225 mV/s (scan parameters: step size = 10 mV, delay time = 10 ms, number of power line cycles = 1) unless otherwise noted. Devices were illuminated for 5 sec prior to starting the *JV* sweep and the device area was 0.10 cm^2. Devices were measured with and without a metal aperture (0.06cm^2) and produced equivalent current densities. Stabilized power output (SPO) was measured by holding the device at a constant voltage corresponding to the voltage at the maximum power

point of the *JV* scan. External quantum efficiency (EQE) measurements were taken using a Newport Oriel IQE200.

Photodiode Characterization: Current density–voltage (*JV*) for space charge limited current and characteristics were measured using a Keithley 2400 source measure unit under monochromatic illumination from a 150-W Xenon arc lamp assembled with a 1/8-m monochromator. The photocurrent spectra were measured by synchronizing the monochromator with the source meter.

LED Characterization: Steady-state $J-V-L$ (current density−voltage−luminance) characteristics were measured using a Keithley 2400 source meter, 2000 multimeter, and the brightness obtained by placing the large-area calibrated Si photodiode (RS components) directly onto the surface of LEDs, thus avoiding corrections needed to account for non-Lambertian spatial emission patterns. A device area was 1.5 mm × 3 mm = 4.5 mm^2.

5.3 Results and Discussion

5.3.1 Ligand Engineering Using MeOAc for Electronically Coupled α-$CsPbI_3$ NC Film The characterizations of α-$CsPbI_3$ NCs used in this chapter have been thoroughly carried out in chapter-4. The surface ligand olylammonium is an 18-carbon long hydrocarbon which is insulating in nature (shown schematically in Figure 1), and are expected to inhibit charge injection (or extraction) into (or from) NCs. In order to use these promising colloidal $CsPbX_3$ NCs in optoelectronic devices, we need to remove such long-chain ligands improving charge transport in NC film. By taking the advantage of dynamic nature of olylammonium and also the stability of the NCs in MeOAc solvent, we developed a method to cast electronically coupled NC films. To remove these long-chain hydrocarbons from the surface of NCs without affecting the advantageous properties of $CsPbX_3$ NCs, such as α-phase stability of $CsPbI_3$ NCs and high PLQY, films of $CsPbX_3$ NCs were treated with MeOAc (schematic shown in Figure 5.1 and details are provided in Experimental Section).

Figure 5.2 shows comparison of FTIR spectra of α-$CsPbI_3$ NCs before (black line) and after (red line) MeOAc treatment. FTIR spectra show the removal of organic ligands from the film with exposure to neat MeOAc, given the near absence of C–H modes near ~2900 cm^{-1} or below ~2000 cm^{-1} belonging to oleylammonium, oleate, or octadecene. In this process of ligand treatment, the NCs were first spin- casted from octane or hexane then

dipped in neat MeOAc. Also, saturated MeOAc solution of either $Pb(OAc)_2$ or $Pb(NO_3)_2$ has been used as a ligand treatment solution in some cases (which will be discussed later).

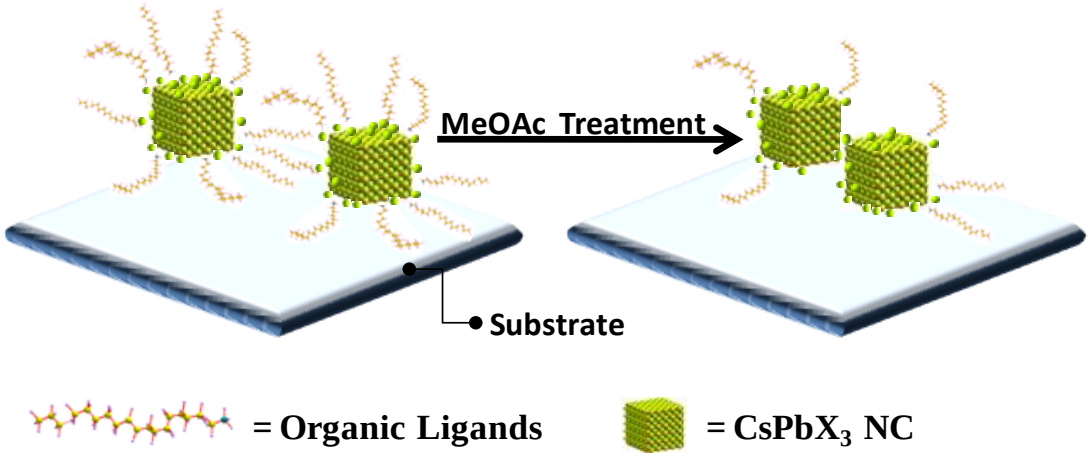

Figure 5.1: Deposition of electronically coupled $CsPbX_3$ nanocrystal film. Schematic showing steps before and after MeOAc treatment of $CsPbX_3$ nanocrystals.

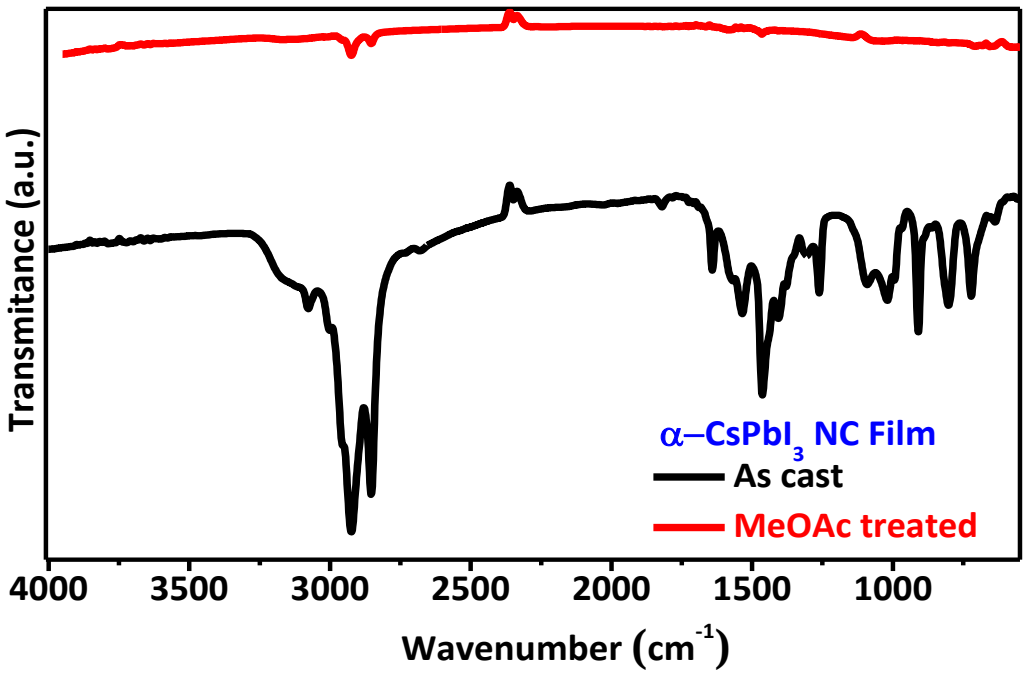

Figure 5.2: Removing organic ligands from α-$CsPbI_3$ nanocrystal surface. Change in FTIR spectra on MeOAc treatment of α-$CsPbI_3$ nanocrystal film.

Removal of organic ligands can result in significant weight loss from the film, generating cracks and pinholes in the films. To improve the film quality, and therefore improve the charge transport, multiple NC layers were deposited in a layer-by-layer fashion (see the Experimental Section). Repeating this process, typically, for three to six times, NC films with thicknesses between 100 and 500 nm (as shown in Figure 5.3c and d) were prepared. SEM image shown in Figure 5.3a and 5.3b show the uniformity of the ligand treated film with the absence of any pin holes.

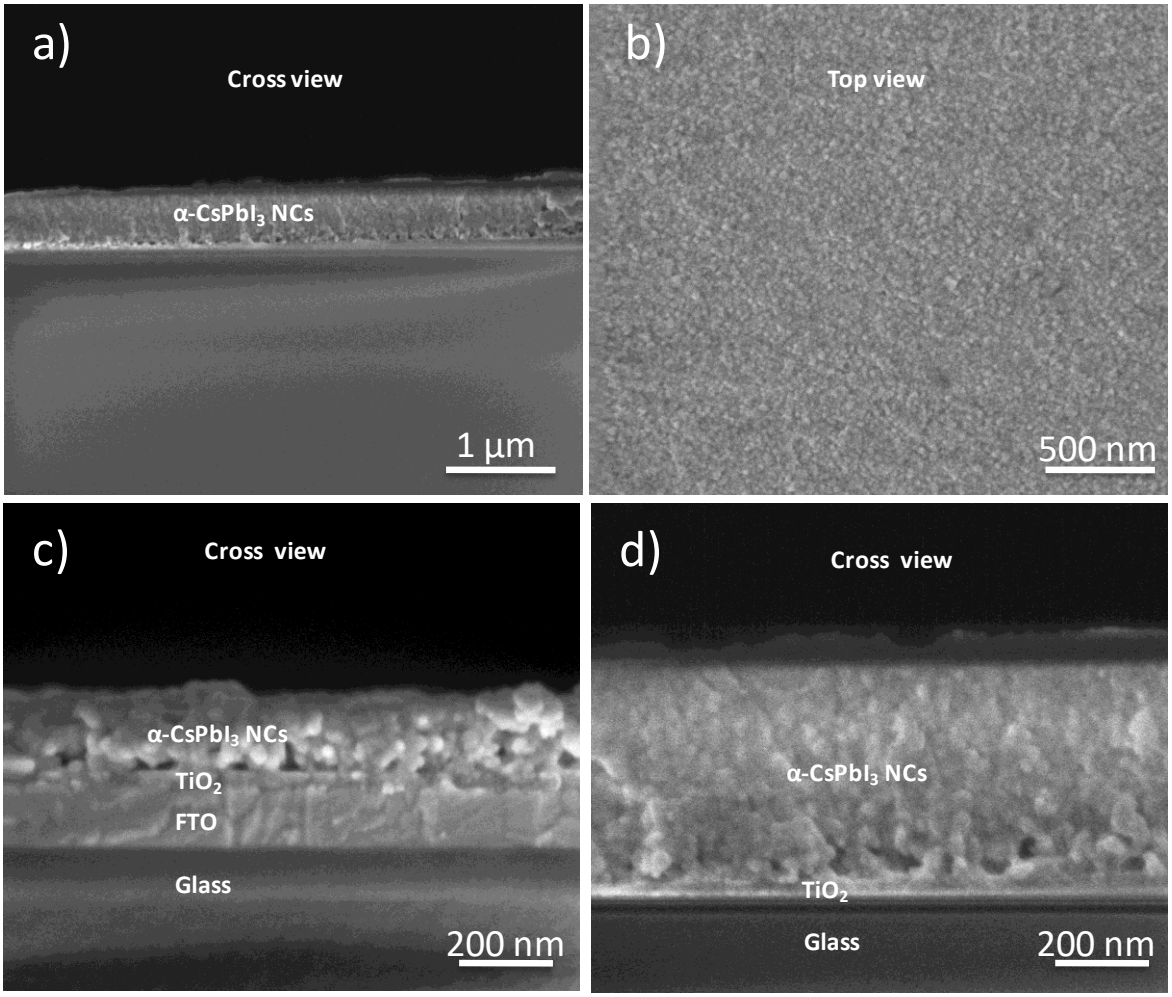

Figure 5.3: α-$CsPbI_3$ nanocrystal-film topology characterization. a) Cross-sectional SEM images under lower magnification, b) SEM top view and (c-d) cross-sectional SEM images under high magnification c) and d) of α-$CsPbI_3$ NCs film. In c) and d) α-$CsPbI_3$ NCs film of two different thickness, c) ~150 nm and d) ~450 nm are shown.

The optical absorption and PL spectra of α-$CsPbI_3$ NCs (Figure 5.4, for three different samples with indicated NC sizes) show that in each case, absorbance and PL of MeOAc treated film are red-shifted by ~20 nm from that of untreated film. This red shift of optical data on MeOAc treatment is most likely because of the increase of the NCs size in the quantum confinement regime which has been supported by PL decay dynamics. Figure 5.5 and Table 1 show the increase of PL lifetime of α-$CsPbI_3$ NCs on MeOAc treatment which is probably attributed to the increase of size. This tunable absorption and emission properties (Figure 5.4) of the α-$CsPbI_3$ NC films after MeOac treatment indicate that quantum confinement is preserved and the NCs are not increasing in size of bulk crystal, which is crucial for preserving the α-phase stability of $CsPbI_3$.

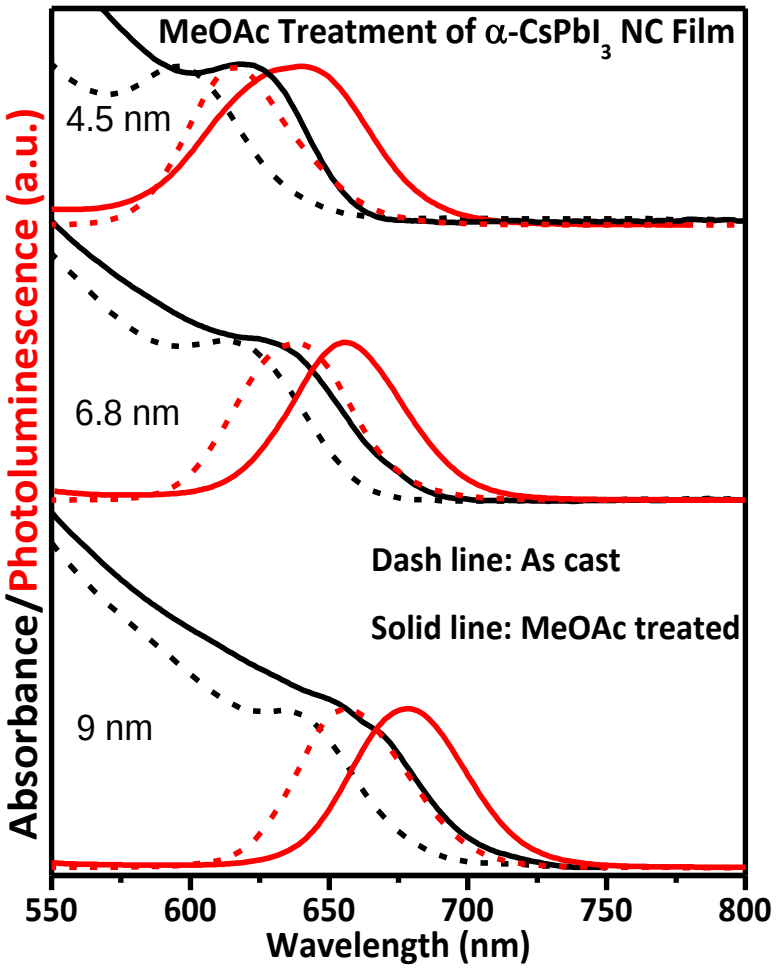

Figure 5.4: Phase stability of α-$CsPbI_3$ nanocrystals on MeOAc treatment. UV-visible absorption (black) and PL spectra (red) of $CsPbI_3$ nanocrystals before (dash line) and after (solid line) MeOAc treatment of nanocrystals of different sizes (edge length) of 4.5, 6.8 and 9 nm.

Interestingly, FTIR, UV-visible and PL data suggest that both the α-phase and size of $CsPbI_3$ NCs are preserved after the ligand treatment with MeOAc. There is a small red-shift in UV-visible absorption and PL peak position after the ligand exchange, but effect of quantum confinement is very much present after the ligand treatment. All these result suggest that the MeOAc treated α-$CsPbI_3$ NCs now can be tested for optoelectronic devices applications.

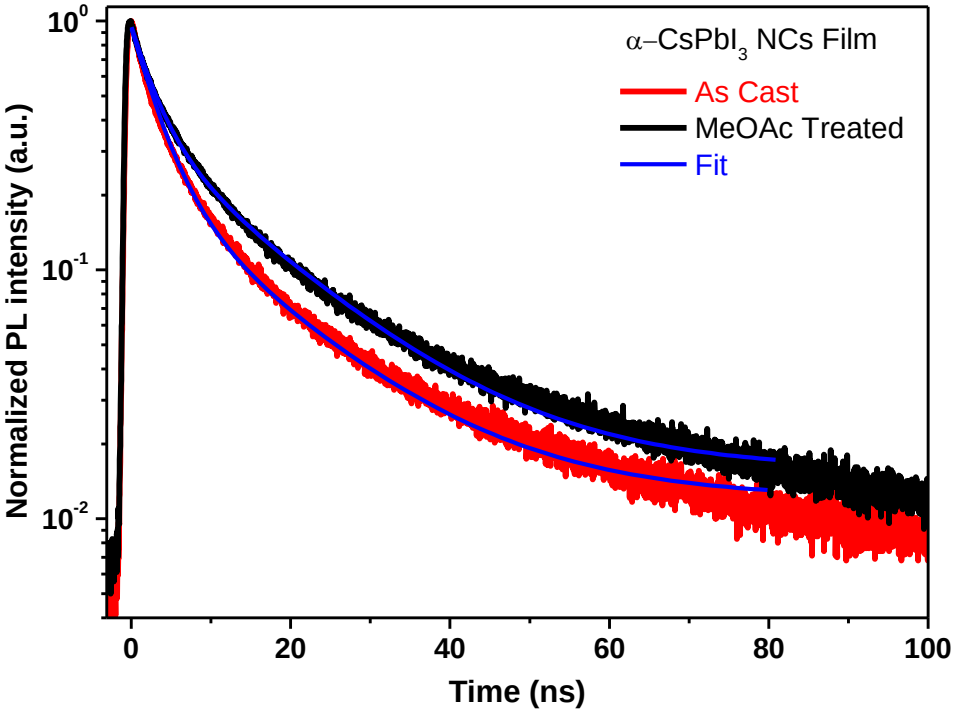

Figure 5.5: Change in PL decay dynamics on ligand removal from α-$CsPbI_3$ nanocrystal surface. PL decay dynamics of α-$CsPbI_3$ nanocrystal film before (red) and after (black) MeOAc treatment of nanocrystals. The excitation wavelength was kept at 550 nm.

Table 5.1. The best fit parameters (with 95% confidence limit) of photoluminescence decay profiles (shown in Figure 5.5) of 9 nm sized α-$CsPbI_3$ NCs film before and after MeOAc treatment (PL decays were measured at respective emission peak energies of the sample shown in Figure 5.4). Experimental data were fitted using bi-exponential decay: A_1 and A_2 are percent contributions from lifetimes τ_1 and τ_2 respectively. The average lifetimes (τ_{avg}) were calculated as $\tau_{avg} = \sum A_i\tau_i^2 / \sum A_i\tau_i$

α-$CsPbI_3$ NC Film	A_1 (%)	τ_1 (ns)	A_2 (%)	τ_2 (ns)	τ_{avg} (ns)
As Cast	26	14.6	74	3.2	10.2
MeOAc treated	39	14.7	61	3.0	11.9

5.3.2 Ligand Engineering using Lead Acetate ($Pb(OAc)_2$)

Typically, ligands passivate the surface traps in colloidal NC QDs. Hence, removal of ligands from the surface of the NCs can create trap states and its effect can be visible in PL properties. Figure 5.6a show the quenching of PL of α-$CsPbI_3$ NCs on drop wise addition of neat MeOAc to NC solution. We also probed the interaction of Pb^{2+} salts with NCs in solution and on films by monitoring the

PL (Figure 5.6b and 5.7).[10] Titration of a small amount of $Pb(OAc)_2$ dissolved in MeOAc to the NC solution showed an enhancement in PL, suggesting improved surface passivation. Similarly, dip-coating of the NC film in a saturated solution of $Pb(OAc)_2$ in MeOAc resulted in a PL enhancement of ~350% compared with dip-coating in MeOAc alone (Figure 5.7). The surface treatments increase the PL lifetime (Figure 5.8) over that of NC films treated with neat MeOAc, which highlights the importance of surface chemistry in this NC system.[10] It is to be noted that for device application, ligand treated NC films in neat MeOAc and MeOAc saturated with $Pb(OAc)_2$ or $Pb(NO_3)_2$ all work reasonably well in photovoltaic device (discussed in later part), without any significant difference, unlike the PL data discussed above.

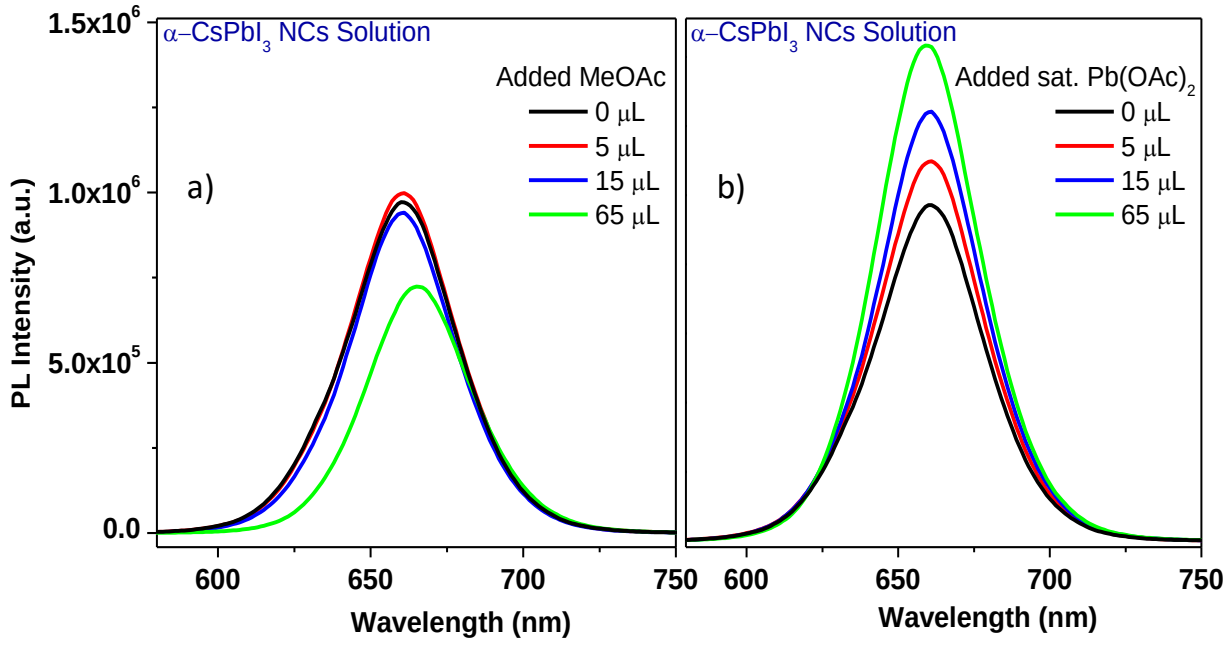

Figure 5.6: Effects of $Pb(OAc)_2$ treatment on PL of α-$CsPbI_3$ nanocrystal solution. PL of 3 mL (~3.6 μg/mL dispersion of 9 nm sized α-$CsPbI_3$ NC in hexane), upon the addition of (a) neat MeOAc and (b) a saturated solution of $Pb(OAc)_2$ in MeOAc.

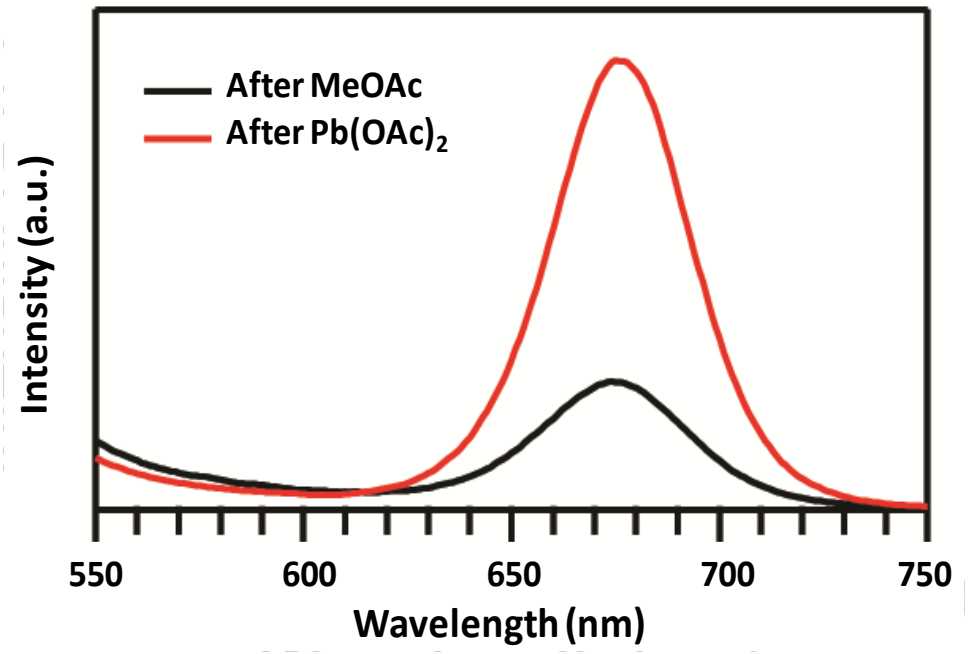

Figure 5.7: Effects of $Pb(OAc)_2$ treatment on PL of α-$CsPbI_3$ nanocrystal film. PL of a NC film treated with neat MeOAc (black) and MeOAc saturated with $Pb(OAc)_2$.

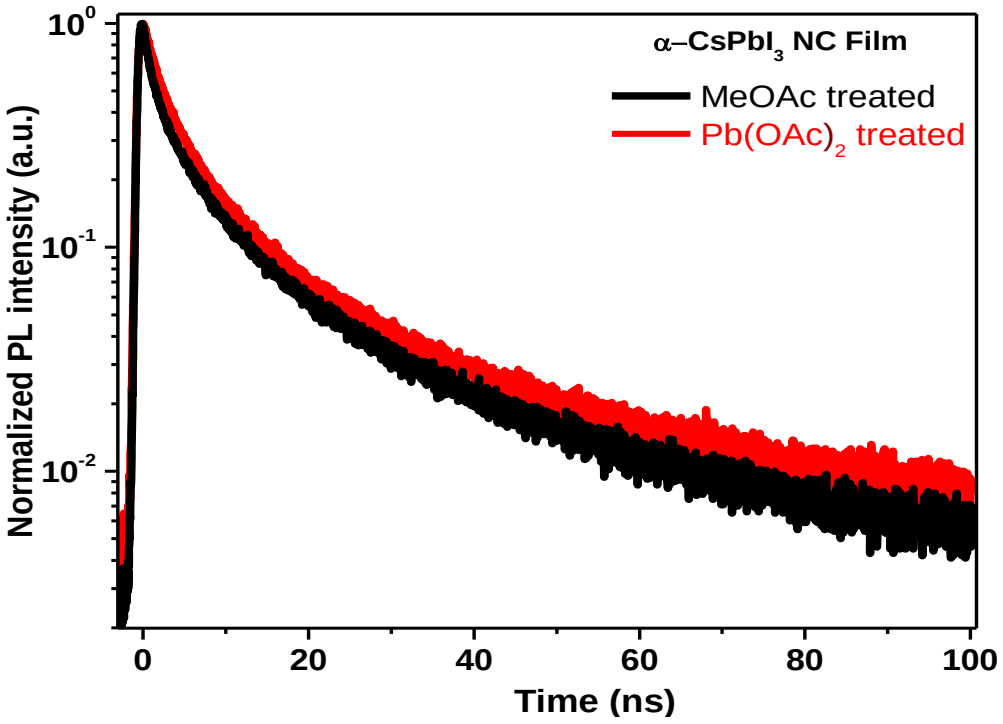

Figure 5.8: PL decay dynamics of α-$CsPbI_3$ nanocrystals surface passivation. PL decay dynamics of α-$CsPbI_3$ nanocrystal film after MeOAc (black) and $Pb(OAc)_2$ treatment.

5.3.3 Ligand Engineering for Electronically Coupled $CsPbBr_3$ NC Film

Similar to ligand treatment of α-$CsPbI_3$ NCs, green luminescent $CsPbBr_3$ NCs were also treated with MeOAc to get electronically coupled film to exploit its high PL efficiency in LED devices. Figure 5.9 shows comparison of FTIR spectra of $CsPbBr_3$ NC films before and after MeOAc treatment. A similar amount of NCs from both (before and after MeOAc treatment) the films were taken for FTIR measurements. Similar to MeOAc treatment of α-$CsPbI_3$ NCs, $CsPbBr_3$ NCs treatment with MeOAc shows a significant decrease in the transmittance at ~2900 cm^{-1} suggest removal of long hydrocarbon chain (olyleammonium, oleic acid, or any residual octadecene) from the NC film. However, the extent of decrease in transmittance is less for these $CsPbBr_3$ NCs compared to the case of α-$CsPbI_3$ NCs (as shown in Figure 5.2). This difference might arise from stronger hard acid−hard base interaction of oleylammonium ions bromide on the surface of $CsPbBr_3$ NCs, compared to the softer surface iodide ions in $CsPbI_3$ NCs (hard acid−soft base interaction).[11] In the case of MeOAc-treated film, the broad IR peak in the range of 3200−3600 cm^{-1} probably corresponds to O−H bond stretching due to the adsorption of moisture from the ambient surrounding (relative humidity (RH) = 40-55 % which is more than that of the condition for $CsPbI_3$ NCs treatment (RH = 15-25%), as $CsPbI_3$ NCs are highly sensitive to moisture), while the untreated film does not exhibit this peak due to the hydrophobic nature of OA, OAm, and residual ODE.

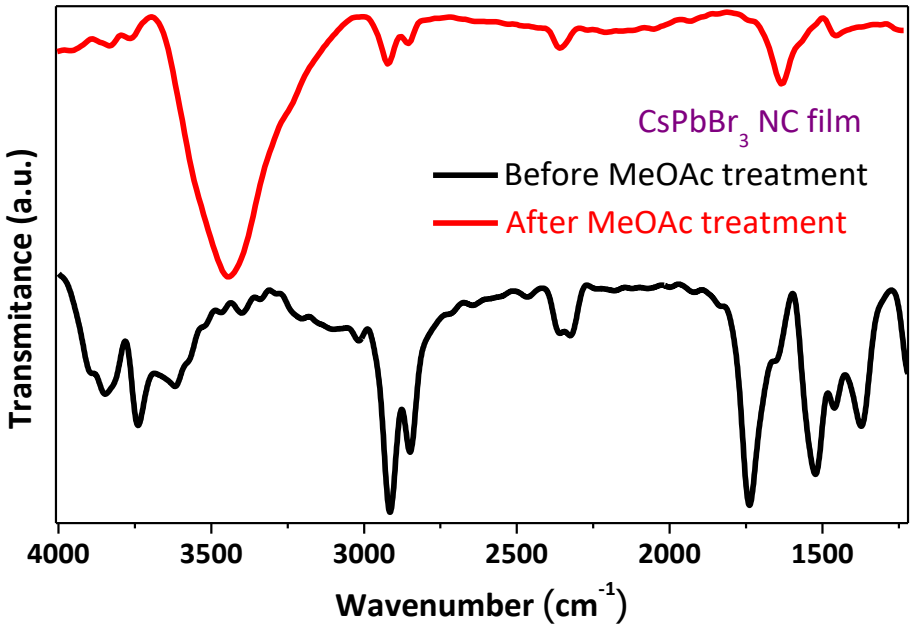

Figure 5.9: Removing organic ligands from $CsPbBr_3$ nanocrystal surface. Change in FTIR spectra on MeOAc treatment of $CsPbBr_3$ nanocrystal film.

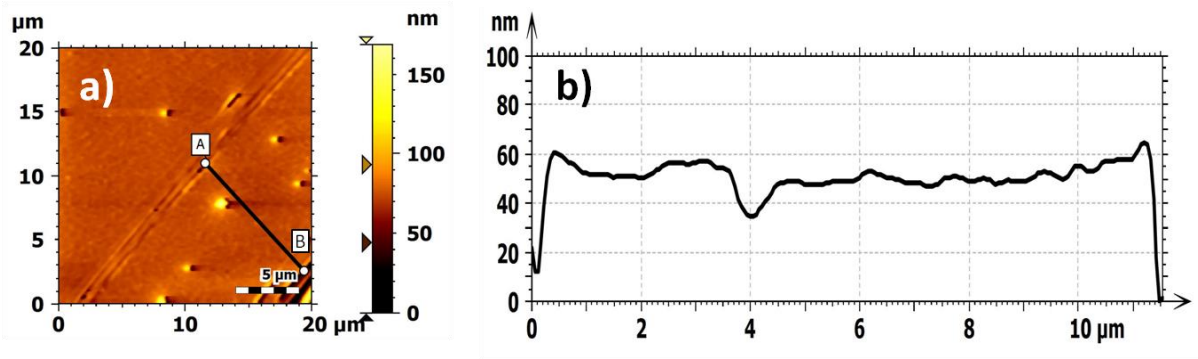

Figure 5.10: **Monolayer of $CsPbBr_3$ nanocrystal film.** Atomic force microscopy (AFM) image to show a) film morphology and b) height profilometry data to get thickness along the line A-B in image shown in a).

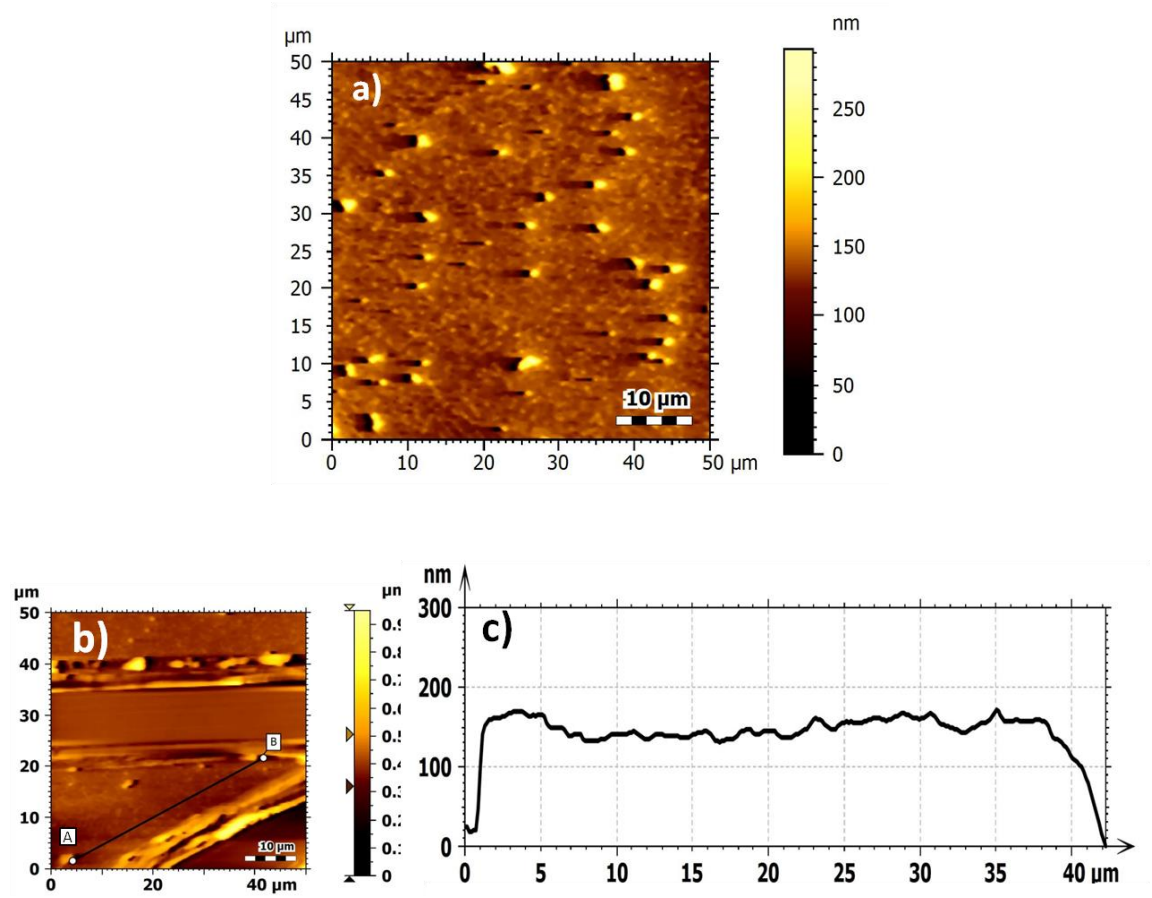

Figure 5.11: Four layer of $CsPbBr_3$ NC film deposited by layer-by-layer film deposition method. AFM images to show a) film morphology and (b-c) thickness determined from height profilometry c) along the line A-B shown in image b). Due to absence of pin holes in four layered NC film, scratch was made to find the thickness as shown b).

Here, again to improve the film quality, multiple NC layers were deposited by following layer-by-layer deposition method. Since there is a small fraction of organic ligands remain on the $CsPbBr_3$ NCs surface even after the film has been washed each time, there is a possibility of dissolving of NC film during the growth of subsequent layer. Hence, we are not able to grow much thicker films (Figure 5.10 and 5.11) unlike with different halide ion $CsPbI_3$ NCs in which ~400 nm thick $CsPbI_3$ NC film (Figure 5.3d) which was further made to fabricate photodiode (discussed later) by employing same film fabrication method. Owing to the presence of some amount of ligands in $CsPbBr_3$ NCs (unlike $CsPbI_3$ NCs), we are able to grow at most 140 ± 10 nm thick film by employing layer by layer deposition for four times, while ideally each layer should have added ~ 50 nm to the film thickness.

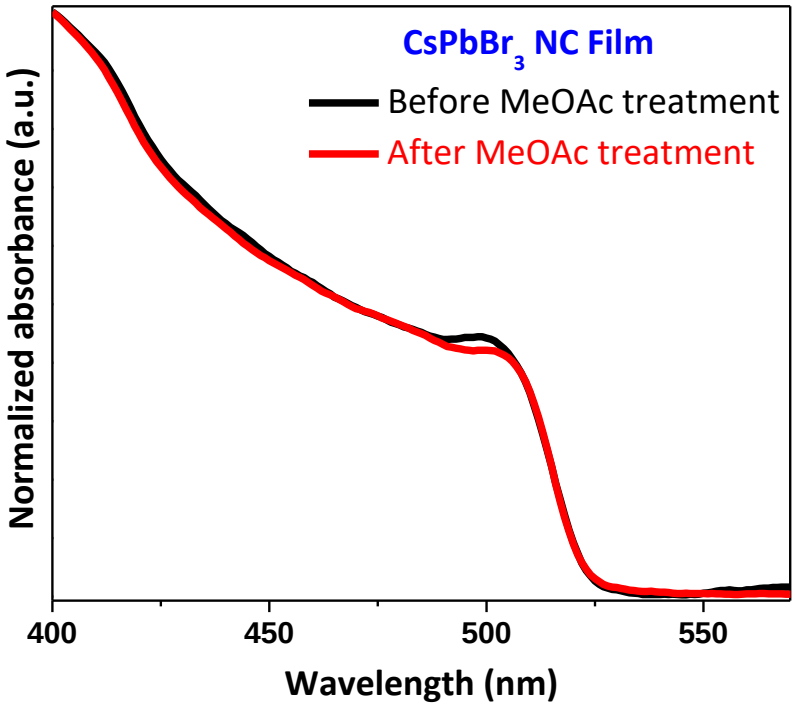

Figure 5.12: Material stability of $CsPbBr_3$ nanocrystals on MeOAc treatment. UV-visible absorption of $CsPbBr_3$ nanocrystals before (black) and after (red) MeOAc treatment of nanocrystals of sizes (edge length) 11 ± 0.7 nm.

Figure 5.12 and 5.13 shows the effect of MeOAc treatment (partial removal of oleylammonium) on UV−visible and PL properties of $CsPbBr_3$ NC film respectively. The absorption spectra in Figure 5.12 remain similar before and after the MeOAc treatment, suggesting that the $CsPbBr_3$ NCs remain unchanged during the MeOAc treatment. The sharpness of the first excitonic peak at ~500 nm decreases after the MeOAc treatment. This

change might arise due to the improved electronic coupling between adjacent NCs in the film after MeOAc treatment.

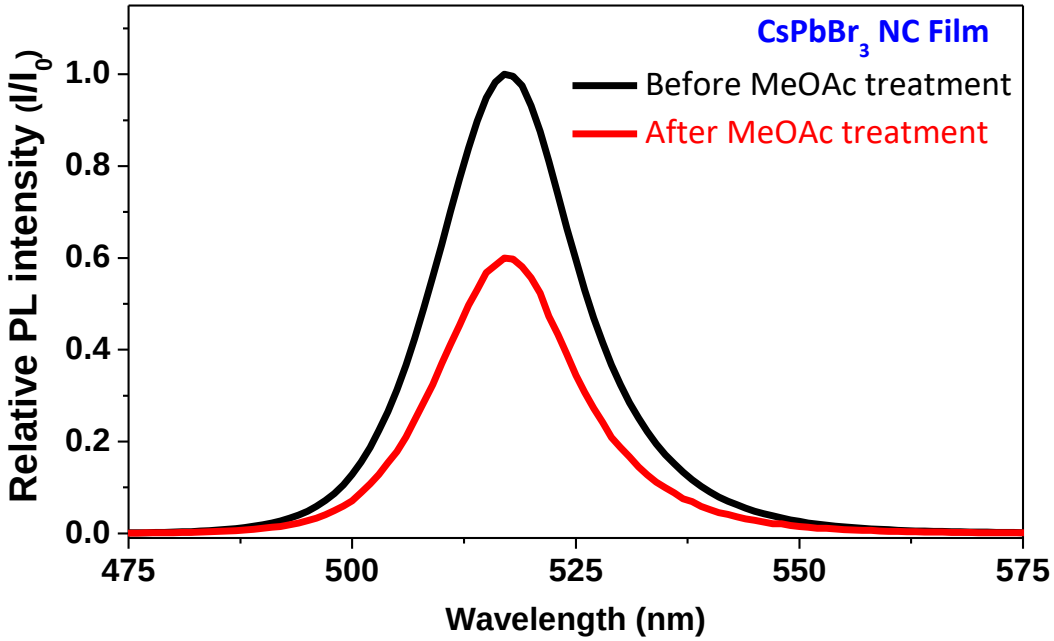

Figure 5.13: PL stability of $CsPbBr_3$ nanocrystals on MeOAc treatment. PL of $CsPbBr_3$ nanocrystals before (black) and after (red) MeOAc treatment of nanocrystals of sizes (edge length) 11 ± 0.7 nm. I and I_0 are PL intensities of the NCs after and before treatment of MeOAc.

PL spectra in Figure 5.13 show that the peak position remains unchanged; however, a decrease in PL intensity of $CsPbBr_3$ NCs is observed after MeOAc treatment. This decrease in PL intensity is expected, as the organic ligands passivate the dangling bonds on the surface of NCs, and partial removal of such ligands can give rise to nonradiative trap states. To probe it further, we used PL decay dynamics. Figure 5.14 shows a faster decay after the ligand treatment. While the PL decay without MeOAc treatment can be fitted with biexponential decay, a tri-exponential decay is required to fit the decay profile obtained after MeOAc treatment. The best fit parameters are shown in Table 2. The lifetimes, ~4 and 19 ns, observed in both with and without MeOAc-treated NCs are attributed to the radiative recombination of electron−hole pairs. However, the NCs after MeOAc treatment show an additional contribution from ~1 ns lifetime, which attribute nonradiative recombination of electron−hole pair. This faster decay, along with a decrease in PL intensity (Figure 5.13 and 5.14), suggests the formation of surface defects after the MeOAc treatment. This defect related decrease in PL lifetime was not visible in case of $CsPbI_3$ NCs when treated with

MeOAc probably because of the increase of the size of NCs which is antagonistic to the expected decrease of PL lifetime due to appearance of surface trap states. But further study is required for better understanding of how MeOAc treatment modify the non-radiative trap states. It is to be noted that here the size of $CsPbBr_3$ NCs (~11 nm) are larger than the Bohr excitonic diameter (7 nm) of $CsPbBr_3$, hence, quantum confinement effects should not be expected.

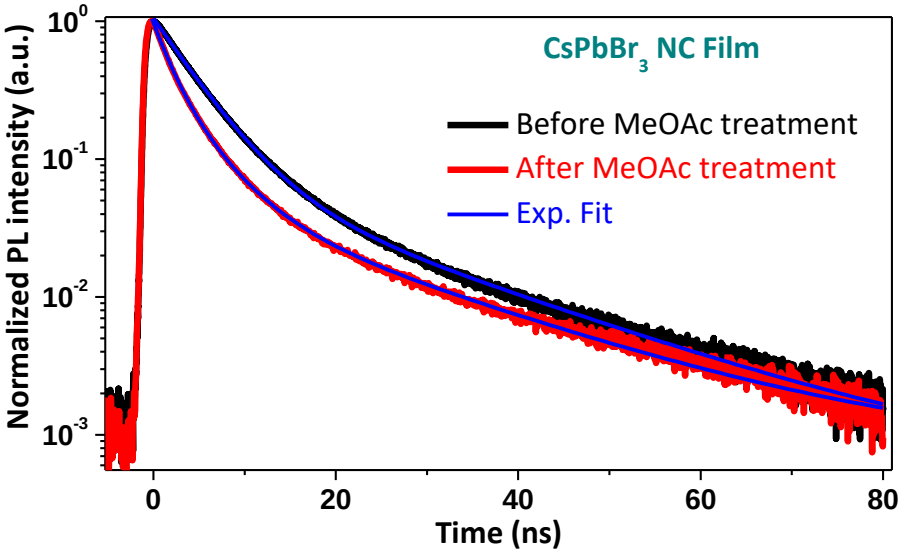

Figure 5.14: Change in PL decay dynamics on ligand removal from $CsPbBr_3$ nanocrystal surface. PL decay dynamics of $CsPbBr_3$ nanocrystal film before (red) and after (black) MeOAc treatment of nanocrystals. The excitation wavelength was kept at 400 nm and the PL decays were measured at respective emission peak energies of the sample shown in Figure 5.13. Experimental data were fitted using bi-exponential decay in case of before MeOAc treatment and tri-exponential decay in case of after MeOAc treatment.

Table 5.2: The best fit parameters (with 95% confidence limit) of PL decay profiles of $CsPbBr_3$ nanocrystals film measured at emission peak energies shown in Figure 5.14 using bi-exponential decay for as-cast and tri-exponential decay for MeOAc treated film respectively. A_1, A_2 and A_3 are percent contributions of lifetimes from τ_1, τ_2 and τ_3 respectively. The average life time ($\tau_{av.}$) was calculated as $\tau_{av} = \sum a_i \tau_i^2 / \sum a_i \tau_i$

$CsPbBr_3$ NC film	A_1 (%)	τ_1 (ns)	A_2 (%)	τ_2 (ns)	A_3 (%)	τ_3 (ns)
As Cast	06	18.56	94	4.26	-	-
MeOAc Treated	06	19.28	50	4.06	44	1.43

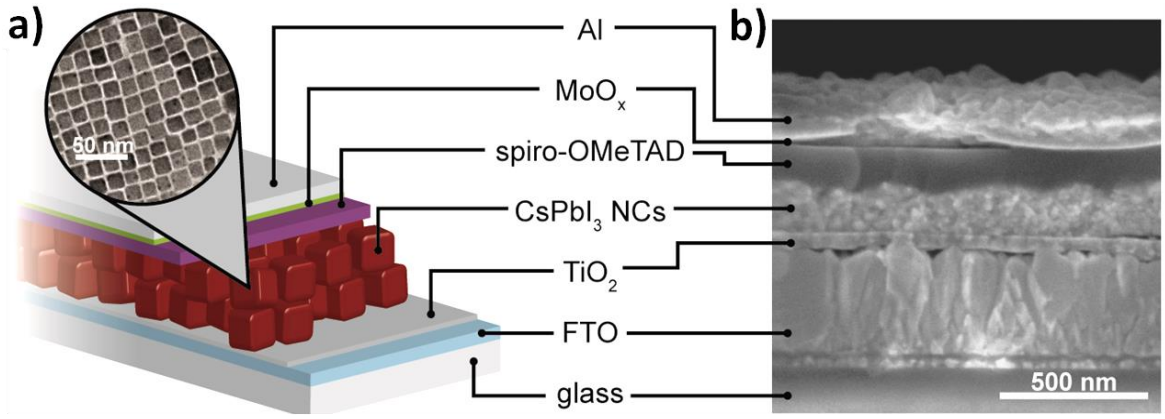

Figure 5.15: α-$CsPbI_3$ nanocrystal photovoltaic device. (a) Schematic (with transmission electron microscopy (TEM) image of α-$CsPbI_3$ nanocrystals) and (b) scanning electron microscopy (SEM) cross-section of the α-$CsPbI_3$ photovoltaic cell. These cells were fabricated and characterized in collaboration with Dr. Joseph M. Luther group at National Renewable Energy Laboratory (NREL), USA during my internship in this group.

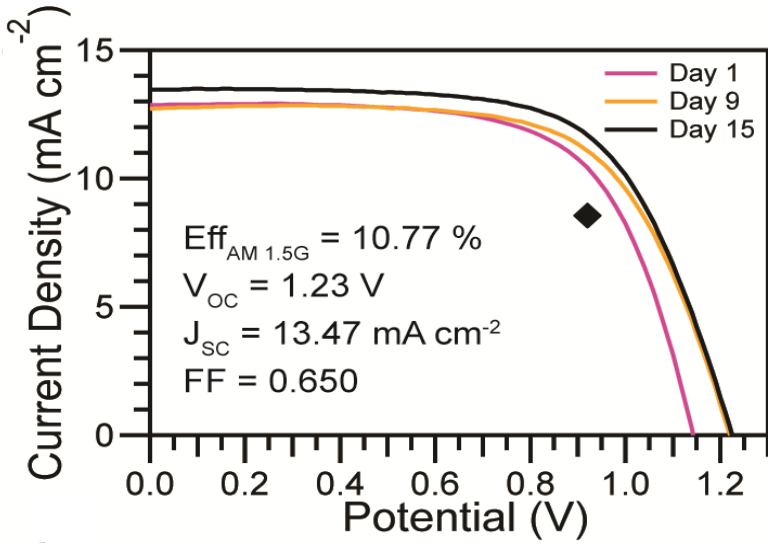

Figure 5.16: Photovoltaic device characterization. Current density–voltage (*J-V*) curves of α-$CsPbI_3$ nanocrystal based photovoltaic device measured in air over the course of 15 days. The black diamond represents the stabilized power output of the device at 0.92 V.

5.3.4 α-$CsPbI_3$ NCs Photovoltaic Cell

After achieving success in MeOAc treatment of αsPbI_3 NCs films, we employ these NCs for photovoltaic cells. These cells were fabricated and characterized in collaboration with Dr. Joseph M. Luther group at National Renewable Energy Laboratory (NREL), USA during my

internship in this group. A schematic of the device architecture is shown in Figure 5.15a and a scanning electron micrograph (SEM) cross-section image of the reported device with 9 nm NCs is shown in Figure 5.15b. The reverse-scan current density-voltage (*JV*) curves showed an open-circuit voltage (V_{OC}) of 1.23 V, and 10.77% power conversion efficiency (PCE) for a 0.10 cm^2 cell made and tested completely in ambient conditions (RH ~15 to 25%) (Figure 5.16).

Furthermore, the PCE improved from its initial value over the course of 60 days storage in dry but ambient conditions (inside desiccator). We compare NC devices to thin-film $CsPbX_3$ perovskite solar cells following literature reports, which have thus far reported at 9.8% PCE and stabilized power output (SPO) as high as 6.5%.[12-14] Our NC devices show improved *JV*-scan efficiency, operational stability, and tolerance to higher relative humidity levels. The V_{OC} is remarkably higher than that of other QD solar cells (typically <0.7 V) and among the highest V_{OC} in all perovskite photovoltaic cells for band gap values below 2 eV. We have not optimized the device architecture or the NC film-treatment scheme. We found that ligand treated NC films in neat MeOAc and MeOAc saturated with $Pb(OAc)_2$ or $Pb(NO_3)_2$ all work reasonably well (*JV*-scanned PCE > 9%) in PV devices. Large diffusion lengths and mobility values have been measured in $CsPbBr_3$ NCs by means of terahertz spectroscopy;[15] as discussed in chapter 3. However, a better understanding of the electronic coupling is critical to maximizing long-range transport in NC perovskite films.

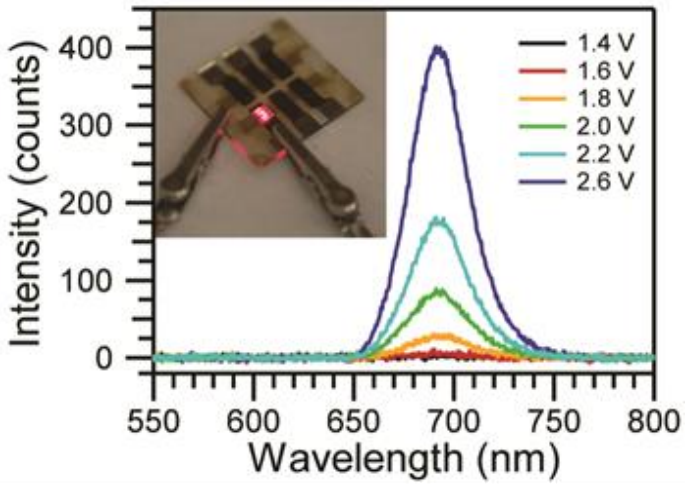

Figure 5.17: Electroluminescence (EL) from α-$CsPbI_3$ NC in photovoltaic cell. EL spectra of α-$CsPbI_3$ photovoltaic cell (α-$CsPbI_3$ nanocubes of edge length ~9 nm) under forward bias. (Inset) A photograph of the luminescent device.

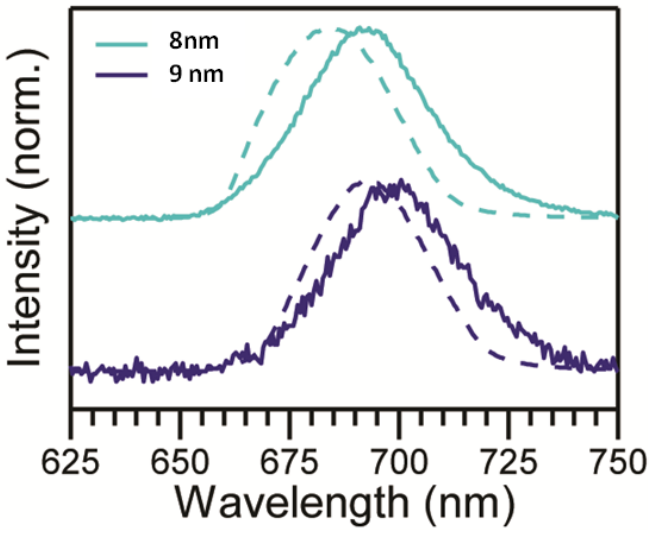

Figure 5.18: Electroluminescence (EL) from different sized α-$CsPbI_3$ NC in photovoltaic cell. PL (dashed lines) and EL (solid lines) spectra of completed devices fabricated by using $CsPbI_3$ NCs of size (edge length) ~8 and ~9 nm, demonstrating size quantization effects in the completed devices.

Given the PL properties of these perovskite NCs, we explored their use as LEDs. The photovoltaic devices produced bright visible EL when biased above V_{OC} (Figure 5.17, inset). The EL had a low turn-on voltage (1.4 V) near the band gap of the α-$CsPbI_3$ NCs, with increasing intensity at larger applied biases (Figure 5.17). These spectra provide direct evidence that quantum confinement is retained in the complete devices, which is critical to retaining the improved α-phase stability, as seen by the shift in both the EL and PL spectra of devices with different-size NCs (Figure 5.18).

5.3.5 α-$CsPbI_3$ NCs Photodiode

Motivated from the outstanding performance in photovoltaic device of α-$CsPbI_3$ NCs, we fabricated a high performing with high reliability photodiode by utilizing phase stabilized α-$CsPbI_3$ perovskite NCs. The photodiodes were fabricated and characterized in collaboration with Dr. Dae Sung Chumg's group in Daegu Gyeongbuk Institute of Science and Technology (DGIST), South Korea. In addition to high extinction coefficient and IR-blind characteristics of the perovskite material, the defect-tolerance nature of α-$CsPbI_3$ perovskite NCs are combined to realize hysteresis-free and high detectivity photodiodes. Here, α-$CsPbI_3$ NCs with ~12 nm edge-length were used.

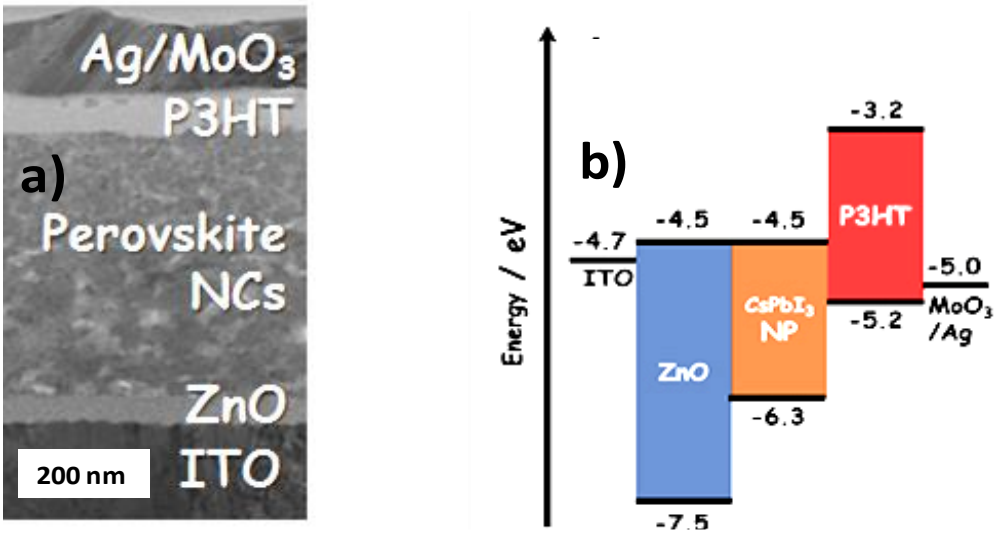

Figure 5.19: α-$CsPbI_3$ nanocrystal photodiode. a) The cross-section transmission electron microscope (TEM) image of the optimized photodiode. b) Energy level diagram of the optimized photodiode. The photodiodes were fabricated and characterized in collaboration with Dr. Dae Sung Chumg's group in Daegu Gyeongbuk Institute of Science and Technology (DGIST), South Korea.

The optimized photodiode with the structure of ITO (~200 nm)/ZnO (~30nm)/α-$CsPbI_3$ NCs (~420nm)/poly (3-hexylthiophene) (P3HT) (~50 nm)/MoO_3 (~30nm)/Ag (100 nm) are fabricated by following layer-by-layer spin coating methods. Figure 5.19 shows the device structure (cross sectional TEM image) and the energy level diagram of different components of the fabricated diode. In this work, to suppress undesirable charge injection and thus to minimize dark current density of the optimized photodiode, sol-gel synthesized ZnO hole blocking layer was introduced instead of porous TiO_2 layer. The extinction coefficient of α-$CsPbI_3$ NC films are 1.3×10^5 cm^{-1} at 400 nm and 6.4×10^4 cm^{-1} at 500 nm (as discussed in previous chapter), which are several times higher values compared to Si.[16] Furthermore, the absorption range covers the whole visible range without overlapping with IR region (Figure 5.4), showing the attractive optical properties of α-$CsPbI_3$ NCs for photodiode application. To further minimize interface defects coming from multi-layer photodiode construction, P3HT layer was strategically introduced as a passivation and electron blocking layer, resulting in a low diode ideality factor of 1.5. The passivation mechanism can be explained as the formation of Lewis adducts between unsaturated or under-coordinated Pb ions(Lewis acid) of $CsPbI_3$ NCs and P3HT with lone-pair electrons (Lewis base). The value of ideality factor

contains important information on the transport and recombination mechanisms in the photodiodes. For photodiodes without any charge carrier trapping or recombination, the ideality factor is expected to be unity. However, because of charge carrier trapping and recombination, most perovskite photodiodes have ideality factor near 2.0 or more.[17-19] Because of all the advantageous results, high detectivity of 1.8×10^{12} Jones at 640 nm (Figure 5.20) is demonstrated with near-zero hysteresis. This value is comparable to that of Si.[20] The obtained detectivity of our α-$CsPbI_3$ NC photodiode is orders of magnitude higher than the prior reports of any perovskite NC photodiode. Interestingly, detectivity spectra showed completely IR-blind characteristics, which means that the photodiode can avoid an unwanted IR photoresponse. This is particularly important because IR-sensitivity can be an additional noise source of photodiode. The responsivity R (Ampere (A)/Watt (W)), directly related with the EQE, gives indications on the intensity of the photocurrent that can be extracted per watt of the incident illumination at a given wavelength. As also shown in Figure 5.20, R at 640 nm is 0.035 A/W. Relatively low R of 0.035 A/W can be attributed to the thick active layer for suppressing noise current.

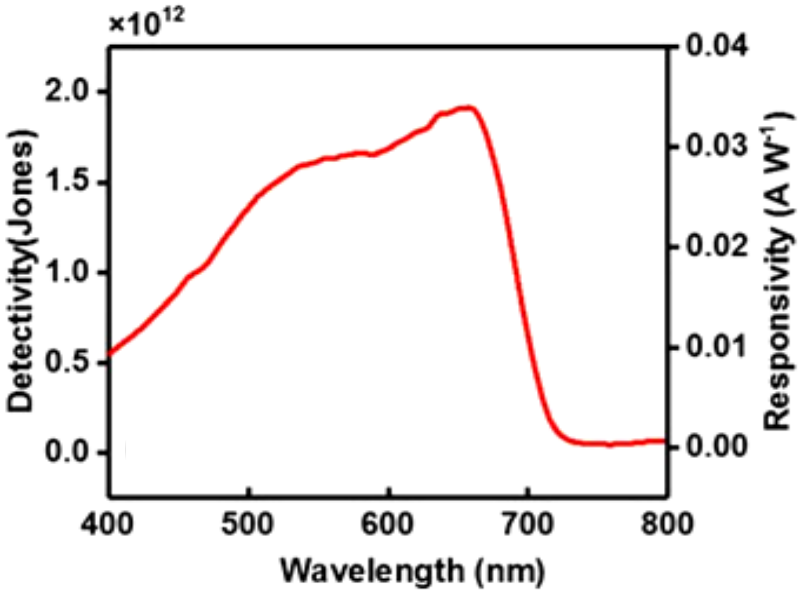

Figure 5.20: Figure-of-merits of the optimized photodiode. Detectivity and responsivity spectra. The measurements were conducted at reverse bias of −0.5 V and 520 nm of incident light for the specific wavelength.

Furthermore, the optimized photodiode exhibits excellent operational stability under high humidity conditions (transient measurement under the continuous illumination of $0.35 mW/cm^2$ at 520 nm in humid condition (R.H. of 80%) without any encapsulation) due to

the intrinsic nature of the defect-tolerant α-$CsPbI_3$ NCs. In overall, the results of this work are similar compared to those of bulk perovskite and better than those of perovskite NCs.[20-22] Details of this work can be found in our published article (*Laser Photonics Rev*.**2018,** *12*, 1700209).

5.3.6 $CsPbBr_3$ NCs LED

In the previous section of ligand treatment of $CsPbBr_3$, it has been found that MeOAc treatment decreases the PL intensity of $CsPbBr_3$ NCs, though it is expected to improve the charge transport in NCs. To study the effect of these two opposing aspects on electroluminescence (EL), we prepared $CsPbBr_3$ NC LED in collaboration with Dr. Dinesh Kabra's group at Indian Institute of Technology (IIT) Bombay, India. Figure 5.21a shows the LED device structure of glass/ITO/PEDOT:PSS/$CsPbBr_3$−NCs/TPBi/Ca/Al; here TPBi and PEDOT:PSS are 2,2′,2″-(1,3,5-benzinetriyl)-tris(1-phenyl-1-H-benzimidazole) and poly(3,4ethylenedioxythiophene)- poly(styrenesulfonate), respectively, and PEDOT:PSS and TPBi/Ca are hole and electron injection layers.

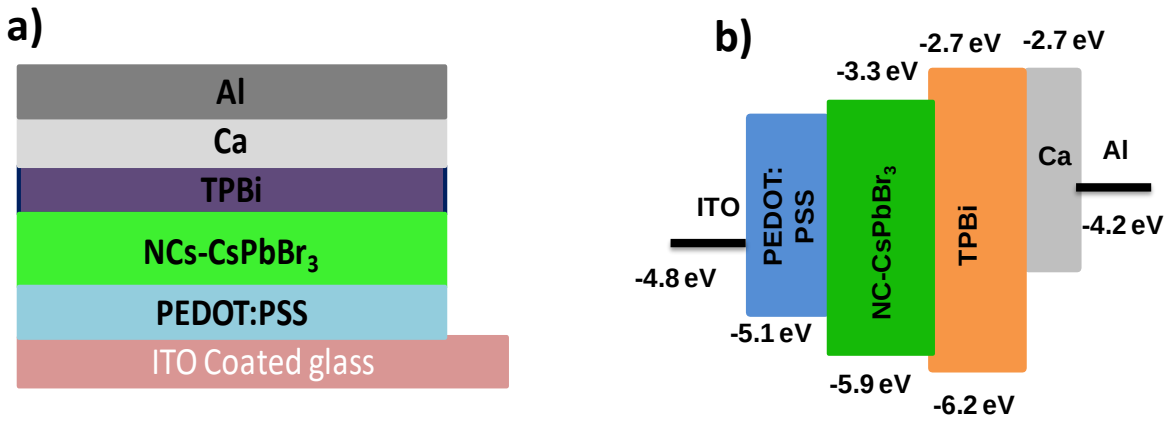

Figure 5.21: $CsPbBr_3$ nanocrystal light emitting device (LED). a) $CsPbBr_3$ nanocrystals light emitting device structure. b) Corresponding flat energy level diagram and energy levels of different components of the device. The values have been taken from the literature.[23] NC LEDs were fabricated and characterized in collaboration with Dr. Dinesh Kabra's group at Indian Institute of Technology (IIT) Bombay, India.

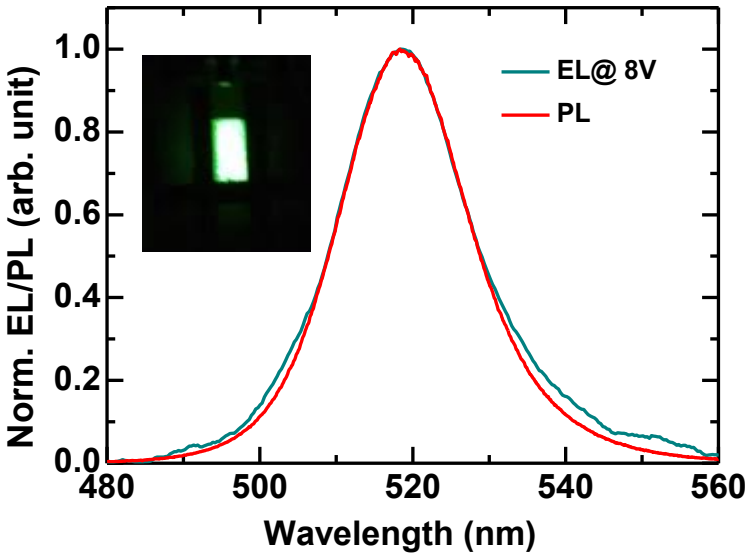

Figure 5.22: Electroluminescence (blue) and photoluminescence (red) spectra of $CsPbBr_3$-NC thin film. Inset shows a typical uniformly illuminated operational NCs based LED image.

Figure 5.21b shows the flat energy level diagram of the NC-LED with hole and electron injection layers. A multilayer (higher thickness) device showed higher current density and lower turn-on operating voltages compared to that of a single-layer device. Details of device characterization could be found in our published article (*J. Phys. Chem. C,* **2018,** *122,* 13767). Figure 5.22 shows the no change in PL and EL response in term of peak energy and line width suggesting the color purity is maintained in the device. Inset of Figure shows the optical image of the glowing device under applied voltage of 8 V. The multilayer device gets rid of pinholes and cracks in the NC film, improving the charge carrier-balance factor significantly to boost the efficiency number from ~1 cd/A (average efficiency of 0.54 cd/A over 6 devices) for single-layer to ~5.2 cd/A (average efficiency of 2.32 cd/A over 6 devices) for four-layer NC film. Our future work is focused on better charge injection by removing the residual ligand density for better performance and stability.

5.4 Conclusions:

We demonstrated layer-by-layer deposition of $CsPbX_3$ NC film for use in high performing optoelectronic devices such as solar cell, photodiode and LEDs. $CsPbX_3$ NCs exhibit promising optoelectronic properties. These NCs are capped with insulating OAm and OA ligands that inhibit charge transport. To overcome this problem, we treated the NC films with MeOAc that significantly removes these long-chain organic ligands from the NC surface.

This removal of ligands reduces the PL efficiency, but enhances the charge transport in NC films. Thickness of the NC films was increased by layer-by-layer method, where each layer corresponds to a thickness of 50-100 nm. $CsPbX_3$ NC based optoelectronic devices (solar cell, photodiode and LEDs) with multilayer (higher thickness) device showed outstanding performance with long term stability. The solar cell employing ~9 nm sized α-$CsPbI_3$ shows PCE of >10 % with V_{OC} = 1.23 V and the photodiode using the same material of larger size (~12 nm) exhibit remarkable detectivity value of 1.8 $\times 10^{12}$ Jones together with near-zero hysteresis. These results far exceed the prior studies of any perovskite NC solar cell and photodetectors NCs at the time of the publication of these work. In case of $CsPbBr_3$ NC based green LED, higher current density and lower turn-on operating voltages compared to that single-layer device was found. Multilayer device gets rid of pin-holes and cracks in the NC film, improving the charge-carrier-balance factor significantly to boost the efficiency number from ~1 cd/A for single-layer to ~5.2 cd/A four-layer NC film. This approach can be further utilized for waveguide lasers and optical-detectors using same class of materials.

References:

1. Kulbak, M.; Gupta, S.; Kedem, N.; Levine, I.; Bendikov, T.; Hodes, G.; Cahen, D., Cesium Enhances Long-Term Stability of Lead Bromide Perovskite-Based Solar Cells. *J. Phys. Chem. Lett.* **2016,** *7*, 167-172.

2. Yantara, N.; Bhaumik, S.; Yan, F.; Sabba, D.; Dewi, H. A.; Mathews, N.; Boix, P. P.; Demir, H. V.; Mhaisalkar, S., Inorganic Halide Perovskites for Efficient Light-Emitting Diodes. *J. Phys. Chem. Lett.* **2015,** *6*, 4360-4364.

3. Protesescu, L.; Yakunin, S.; Bodnarchuk, M. I.; Krieg, F.; Caputo, R.; Hendon, C. H.; Yang, R. X.; Walsh, A.; Kovalenko, M. V., Nanocrystals of Cesium Lead Halide Perovskites ($CsPbX_3$, X = Cl, Br, and I): Novel Optoelectronic Materials Showing Bright Emission with Wide Color Gamut. *Nano Lett.* **2015,** *15*, 3692-3696.

4. De Roo, J.; Ibáñez, M.; Geiregat, P.; Nedelcu, G.; Walravens, W.; Maes, J.; Martins, J. C.; Van Driessche, I.; Kovalenko, M. V.; Hens, Z., Highly Dynamic Ligand Binding and Light Absorption Coefficient of Cesium Lead Bromide Perovskite Nanocrystals. *ACS Nano* **2016,** *10*, 2071-2081.

5. Guangru, L.; Rocca, R. F. W.; K., D. N. J. L.; Sai, B.; C., J. T.; Francisco, d. l. P.; Shaocong, H.; Caterina, D.; Feng, G.; H., F. R.; C., G. N.; Zhi-Kuang, T., Highly Efficient Perovskite Nanocrystal Light-Emitting Diodes Enabled by a Universal Crosslinking Method. *Adv. Mater.* **2016,** *28*, 3528-3534.

6. Kovalenko, M. V.; Manna, L.; Cabot, A.; Hens, Z.; Talapin, D. V.; Kagan, C. R.; Klimov, V. I.; Rogach, A. L.; Reiss, P.; Milliron, D. J.; Guyot-Sionnnest, P.; Konstantatos, G.; Parak, W. J.; Hyeon, T.; Korgel, B. A.; Murray, C. B.; Heiss, W., Prospects of Nanoscience with Nanocrystals. *ACS Nano* **2015,** *9*, 1012-1057.

7. Sun, S.; Yuan, D.; Xu, Y.; Wang, A.; Deng, Z., Ligand-Mediated Synthesis of Shape-Controlled Cesium Lead Halide Perovskite Nanocrystals via Reprecipitation Process at Room Temperature. *ACS Nano* **2016,** *10*, 3648-3657.

8. Talapin, D. V.; Lee, J.-S.; Kovalenko, M. V.; Shevchenko, E. V., Prospects of Colloidal Nanocrystals for Electronic and Optoelectronic Applications. *Chem. Rev.* **2010,** *110*, 389-458.

9. Jianhai, L.; Leimeng, X.; Tao, W.; Jizhong, S.; Jiawei, C.; Jie, X.; Yuhui, D.; Bo, C.; Qingsong, S.; Boning, H.; Haibo, Z., 50-Fold EQE Improvement up to 6.27% of Solution-Processed All-Inorganic Perovskite $CsPbBr_3$ QLEDs via Surface Ligand Density Control. *Adv. Mater.* **2017,** *29*, 1603885.

10. Swarnkar, A.; Shanker, G. S.; Nag, A., Organic-free colloidal semiconductor nanocrystals as luminescent sensors for metal ions and nitroaromatic explosives. *Chem. Commun.* **2014,** *50*, 4743-4746.

11. Pearson, R. G., Hard and Soft Acids and Bases. *J. Am. Chem. Soc.* **1963,** *85*, 3533-3539.

12. Beal, R. E.; Slotcavage, D. J.; Leijtens, T.; Bowring, A. R.; Belisle, R. A.; Nguyen, W. H.; Burkhard, G. F.; Hoke, E. T.; McGehee, M. D., Cesium Lead Halide Perovskites with Improved Stability for Tandem Solar Cells. *J. Phys. Chem. Lett.* **2016,** *7*, 746-751.

13. Eperon, G. E.; Paterno, G. M.; Sutton, R. J.; Zampetti, A.; Haghighirad, A. A.; Cacialli, F.; Snaith, H. J., Inorganic caesium lead iodide perovskite solar cells. *J. Mater. Chem. A* **2015,** *3*, 19688-19695.

14. J., S. R.; E., E. G.; Laura, M.; S., P. E.; A., K. B.; B., P. J.; T., H. M.; B., J. M.; Abbas, H. A.; T., M. D.; J., S. H., Bandgap-Tunable Cesium Lead Halide Perovskites with High Thermal Stability for Efficient Solar Cells. *Adv. Energy Mater.* **2016,** *6*, 1502458.

15. Yettapu, G. R.; Talukdar, D.; Sarkar, S.; Swarnkar, A.; Nag, A.; Ghosh, P.; Mandal, P., Terahertz Conductivity within Colloidal $CsPbBr_3$ Perovskite Nanocrystals: Remarkably High Carrier Mobilities and Large Diffusion Lengths. *Nano Lett.* **2016,** *16*, 4838-4848.

16. A., G. M.; J., K. M., Optical properties of intrinsic silicon at 300 K. *Progress in Photovoltaics: Res. and Applications.* **1995,** *3*, 189-192.

17. Agarwal, S.; Seetharaman, M.; Kumawat, N. K.; Subbiah, A. S.; Sarkar, S. K.; Kabra, D.; Namboothiry, M. A. G.; Nair, P. R., On the Uniqueness of Ideality Factor and Voltage Exponent of Perovskite-Based Solar Cells. *J. Phys. Chem. Lett.* **2014,** *5*, 4115-4121.

18. Marinova, N.; Tress, W.; Humphry-Baker, R.; Dar, M. I.; Bojinov, V.; Zakeeruddin, S. M.; Nazeeruddin, M. K.; Grätzel, M., Light Harvesting and Charge Recombination in $CH_3NH_3PbI_3$ Perovskite Solar Cells Studied by Hole Transport Layer Thickness Variation. *ACS Nano* **2015,** *9*, 4200-4209.

19. Cui, P.; Fu, P.; Wei, D.; Li, M.; Song, D.; Yue, X.; Li, Y.; Zhang, Z.; Li, Y.; Mbengue, J. M., Reduced surface defects of organometallic perovskite by thermal annealing for highly efficient perovskite solar cells. *RSC Adv.* **2015,** *5*, 75622-75629.

20. Seung, R. Y.; Sang-Hoon, B.; Huajun, C.; Nicholas, D. M.; Yang, Y., Recent Progress in Materials and Devices toward Printable and Flexible Sensors. *Adv. Mater.* **2016,** *28*, 4415-4440.

21. Kang-Jun, B.; Maddalena, B.; Dario, N.; Mario, C.; Yong-Young, N., Organic Light Detectors: Photodiodes and Phototransistors. *Adv. Mater.* **2013,** *25*, 4267-4295.

22. I., S. M.; Azimul, H. M.; Jawaher, A.; Smritakshi, S.; Xiao-He, M.; Raihana, B.; A., Z. A.; Ibrahim, D.; Namchul, C.; Banavoth, M.; F., M. O.; Tom, W.; M., B. O., Inorganic Lead Halide Perovskite Single Crystals: Phase-Selective Low-Temperature Growth, Carrier Transport Properties, and Self-Powered Photodetection. *Adv. Opt. Mater.* **2017,** *5*, 1600704.

23. Jizhong, S.; Jianhai, L.; Xiaoming, L.; Leimeng, X.; Yuhui, D.; Haibo, Z., Quantum Dot Light-Emitting Diodes Based on Inorganic Perovskite Cesium Lead Halides ($CsPbX_3$). *Adv. Mater.* **2015,** *27*, 7162-7167.

Appendix-I

Impedance Spectroscopy of Electronic Grade Nanocrysal Films of PbS and PbSe

---

The following article has been published based on the work presented in this chapter.

1. Shanker, G. S.; Swarnkar, A.; Chatterjee, A.; Chakraborty, S.; Phukan, M.; Parveen, N.; Biswas, K.; Nag, A. Electronic Grade and Flexible Semiconductor Film Employing Oriented Attachment of Colloidal Ligand-Free PbS and PbSe Nanocrystals at Room Temperature. *Nanoscale,* **2015**, *7,* 9204-9214. Copyright permission has been taken from Royal Society of Chemistry for the entire article.

Introduction

Electrochemical Impedance spectroscopy (EIS) is a simple technique having a great value for analysing different electrical processes happening on perturbing a system by applying a sinusoidal AC signal (voltage in mV range) across the materials in form of pellet/film.[1-3] This is a important technique to discriminate between the capacitance and the resistance attributed to the grain boundaries present in the material.

Typically, impedance can is measured as a function of the frequency corresponding to perturbation. In general, the response of a sinusoidal perturbation comprises both the real component, resistance (independent of frequency) and the imaginary component, reactance (dependent on frequency) and can be shown either by a complex plane (named as Cole-Cole or Nyquist plot) or by a plot where the absolute value of impedance is plotted against frequency (Bode plot).[3]

In a Nyquist plot, the imaginary component, Z'' is plotted along Y-axis with negative sign while the real component, Z' is plotted along X-axis.[1] A series of semi circular features of the Nyquist plot represent the contributions from different electrical properties owing to intragrain (bulk) processes, intergrain process (grain boundary effect) and also processes because of interfacial polarization phenomena.[1-2, 4-5] Generally, in a testing sample different regions are characterized by a resistance and capacitance connected in parallel arrangement.

The impedance, in vector form and as a function of angular frequency (ω) is given by

$$\hat{Z}(\omega) = Z' - iZ'' \qquad (1)$$

Z'= real part of the complex impedance

Z''= imaginary part of the complex impedance

i = $\sqrt{-1}$, imaginary unit

The angle,ϕ between $|Z|$and Z', equal to the phase angle between the applied sinusoidal voltage and the current response, can be calculated as follow:

$$\frac{Z'}{Z''} = tan\phi \qquad (2)$$

After substituting the circuit value of Z' and Z'', eq. 1 can be rewritten as follow:

$$\hat{Z}(\omega) = R - \frac{i}{\omega C} \qquad (3)$$

R = Resistance

C = Capacitance

The peak points of the deferent semicircles are characterized by their individual time constants according to the relation

$$\omega_{max}\tau = \omega_{max}RC = 1 \qquad (4)$$

ω_{max} is the angular frequency of maximum loss in an RC circuit.

Thus, the relaxation capacitance is given by

$$C = \frac{1}{2\pi R f_{max}} \qquad (5)$$

f_{max} is the ordinary frequency measured in Hz.

In this Appendix-II chapter, we have characterized nanocrystals (NCs) films of lead chalcogenide by studying the electrical properties (resistance and capacitance) in grain and grain boundaries by using two-probe ac impedance spectroscopy.

Experimental section

AC impedance was measured in ambient condition, by using PARSTAT 2273 potentiostat/galvanostat, along the film material on glass and PET flexible substrate by applying colloidal silver liquid (TED PELLA, INC.) on the film for contacts with gold electrodes following two probe analyses. The AC perturbing voltage was kept at 500 mV in the frequency range of 2 MHz to 100 Hz. The measurement result has been fitted in ZSimpWin 3.2 electrochemical impedance modelling software with a R(RC) electrical model, which is generally used to analyse polycrystalline semiconductors, and then plotted in Origin software. The NC synthesis and the film fabrication details are available in the published article [G. Shiva Shanker et al. *Nanoscale* **2015,** *7*, 9204].

Results and Discussion

The electrical properties of a polycrystalline film such as our ligand free PbS NC film (Figure 1) depends upon both inter- and intra-granular resistance. A typical DC measurement cannot differentiate between such inter- and intra-NC contributions to electrical conductivity. In order to get a better understanding about resistance and capacitance arising from both within NC (intra-granular) and grain boundaries (inter-granular), we carried out AC impedance measurements over a wide frequency range (2 MHz to 100 Hz). Figure 2 shows Nyquist plot

for a PbS NC film on glass substrate. The experimental data (symbols) could be fitted (red line) well using a simple $R_b(R_{gb}C_{gb})$ electrical model (inset to Figure 2),[2, 5] where R_b and R_{gb} correspond to resistances due to bulk and grain boundary, respectively, and C_{gb} is the capacitance across grain boundaries. The semicircular shape of the Nyquist plot is due to R_{gb} parallel to C_{gb}. The radius of the semicircle will be $R_{gb}/2$, and centred at $R_{gb}/2$ if $R_b = 0$. The addition of R_b in series just shifts the curve to a higher Z' value by the small quantity of R_b. The values of R_{gb} and C_{gb} obtained from the fitting for the PbS film on glass substrate and processed at room temperature are 3.84 MΩ and 14.2 pF (Table 1). The value of the capacitance matches well with the capacitance due to grain boundary present in a typical polycrystalline film.[3] When the film was annealed at a 150 °C, radius of the semicircle decreased significantly (Figure 2) suggesting the decrease in R_{gb} upon annealing the film without any considerable change in the R_b. The best fit parameter values of R_{gb} and C_{gb} for the PbS film on glass substrate annealed at 150 °C are 0.45 MΩ and 20.7 pF (Table 1).

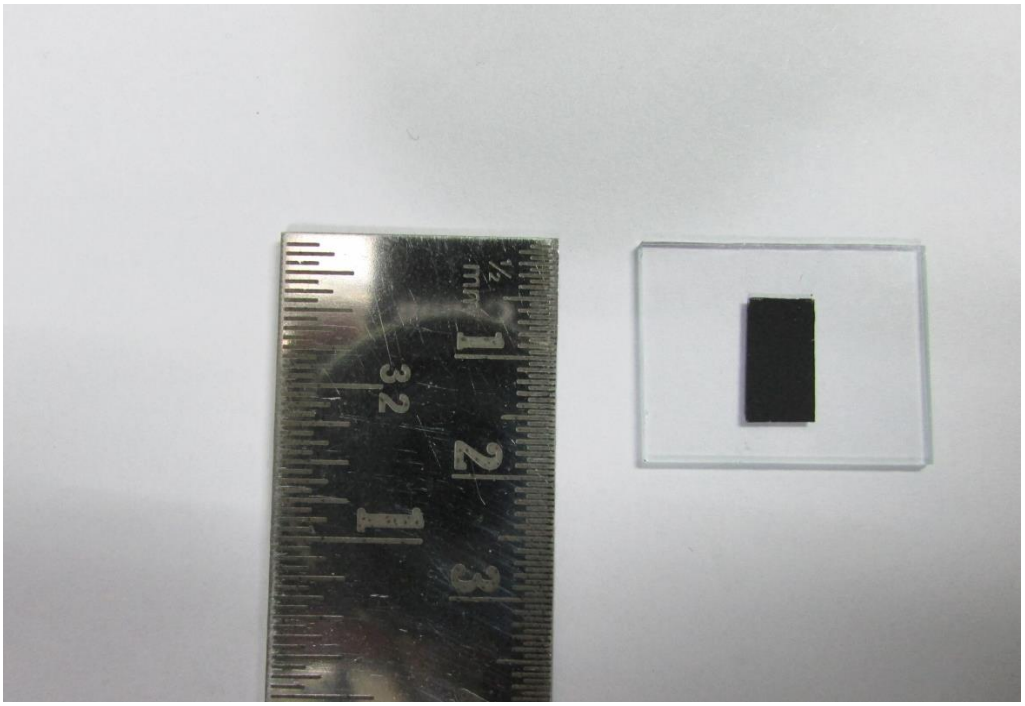

Figure 1: A typical PbS nanocrystal film on a glass substrate deposited by doctor blading technique and processed at room temperature.

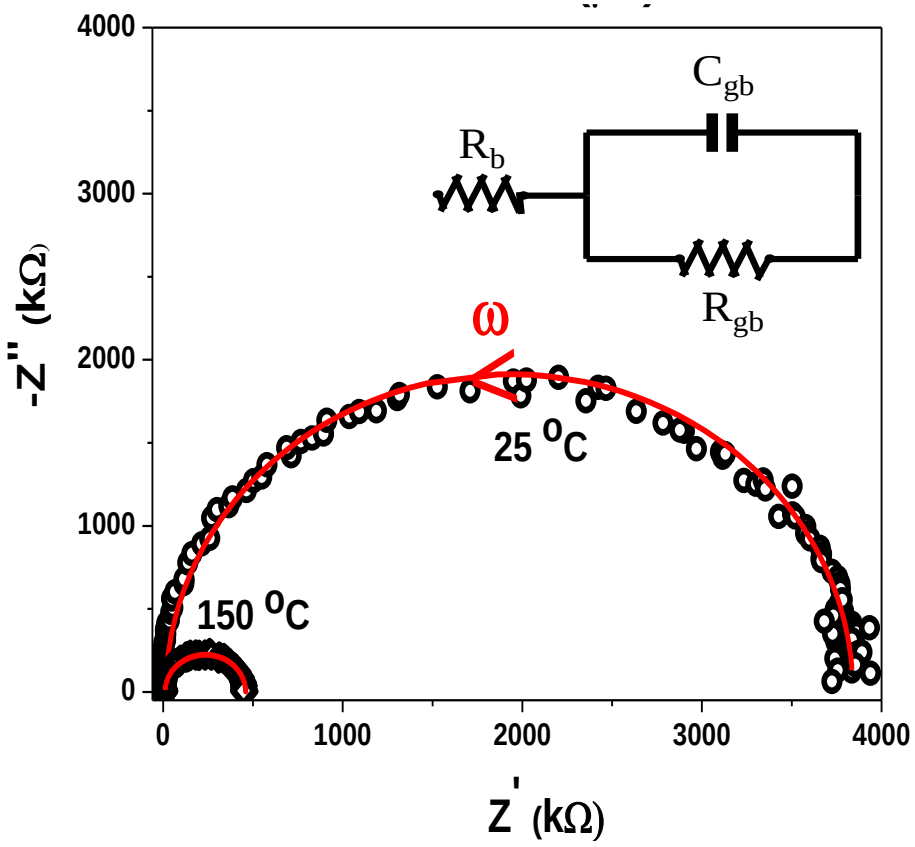

Figure 2: Nyquist plots of ligand-free PbS nanocrystals films obtained from two-probe AC impedance measurements. Films were annealed at 25 °C and 150 °C, but both the impedance measurements were performed at room temperature. The inset shows a schematic electric circuit of charge conduction in PbS nanocrystal film. Black symbols are experimental data and red solid lines show the fitting. All the electrical measurements shown in this figure were carried out under ambient air. The AC perturbing voltage was kept at 500 mV in the frequency range of 2 MHz to 100 Hz.

Table 1: The values of R_{gb} and C_{gb} obtained from the fitting of Nyquist plot for the PbS films on glass substrate measured at room temperature.

Samples	R_b (Ω)	R_{gb} (Ω)	C_{gb} (Fcm^{-1})
Preannealed PbS	1.143×10^4	3.836×10^6	2.091×10^{-11}
Annealed PbS	1.078×10^4	4.482×10^5	1.42×10^{-11}

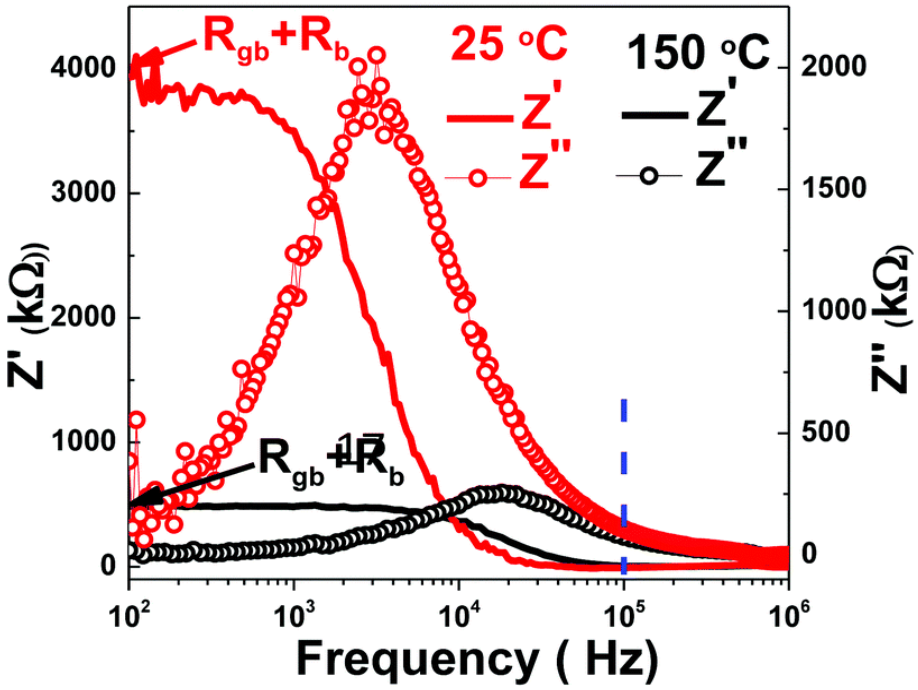

Figure 3: Spectroscopic plots of ligand-free PbS nanocrystals films obtained from two-probe AC impedance measurements. Films were processed at 25 °C and 150 °C, but both the impedance measurements were performed at room temperature and under ambient air. The AC perturbing voltage was kept at 500 mV in the frequency range of 2 MHz to 100 Hz.

The spectroscopic plot, presented in Figure 3, is another way of presenting impedance as a function of frequency, where we can separate the Z′ and Z″, and can analyze their dependency at different ranges of frequency. There is no considerable change in the value of Z′ and Z″ at high frequencies (>10^5 Hz), indicated by the vertical blue-dashed line, whereas at lower frequencies, (<105 Hz) Z′ and Z″ decrease significantly after annealing the film at 150 °C. The electrical responses in the high and low frequency regime typically correspond to grain and grain boundaries respectively.[4] Therefore, the observed change in charge conduction (Z′ and Z″) at low frequency is attributed to the change in the characteristics of grain boundaries upon annealing the film. On the other hand, the value of the capacitance

also increased after annealing the film (Table 1), suggesting that the inter-granular regions were narrowed upon annealing the film.[4] Moreover, the electrical relaxation time, τ, which is the product of R_{gb} and C_{gb} and equal to $(\omega_{max})^{-1}$, was also reduced to 5.7 times after annealing the film at 150 °C, where ω_{max} is the angular frequency of maximum loss in an RC circuit.[4] The decrease in R_{gb} and τ along with an increase in C_{gb} after annealing the film is because of the improved electrical connectivity between adjacent NCs (grains) via the removal of defects from the interface of connected NCs ensuring better fusion of NCs.

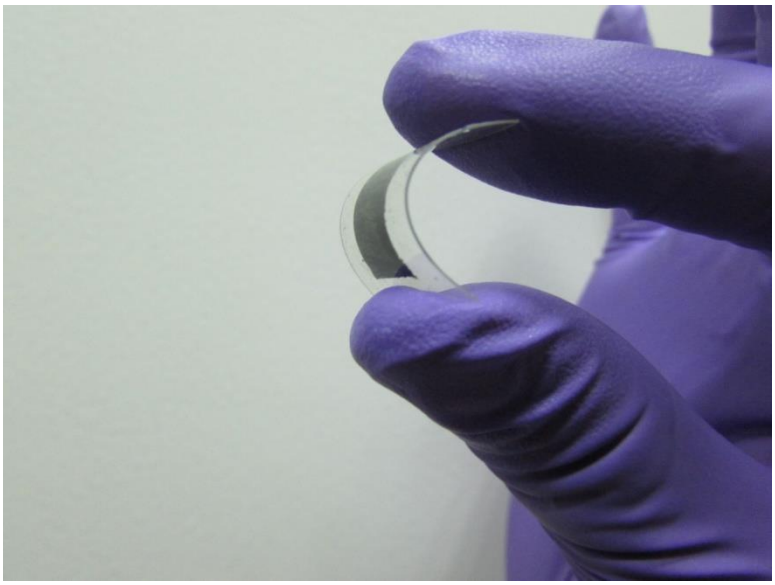

Figure 4: Ligand-free PbS nanocrystal films on a flexible polyethylene terephthalate (PET) substrate.

We also casted similar films of PbS NCs on flexible polyethylene terephthalate (PET) substrates. The film processing was done at room temperature. The film on the PET substrate can be bent, as shown in the Figure 4. The film was repeatedly bent 50 times and the electrical measurements were repeated. AC impedance data, as shown in Figure 5, for the PbS NC film on PET show a semicircular Nyquist plots similar to those in Figure 1. The radius of the semicircle increased after bending the film repeatedly for 50 times (Table 2).

Both the plots, before and after bending the film, can be fitted with the $R_b(R_{gb}C_{gb})$ electrical model. The best fit values of R_{gb} are 5.42 MΩ and 10.72 MΩ before and after bending the film, respectively, keeping C_{gb} largely unaltered at ~21 pF. Importantly, the film still exhibits a high electrical conductivity even after repeated bending experiments, suggesting the suitability of our PbS NC film for integration into flexible electronic devices. It should be noted that often the films made from traditional semiconductors generate cracks upon bending, resulting into a drastic (over many orders of magnitude) decrease in electrical conductivity.[6] The sustained electrical conductivity of the NC film after bending the film is because of the smaller size of our NC compared to the bending curvature of the film, and therefore the bending related strain is not strongly felt by NC grains and grain boundaries.

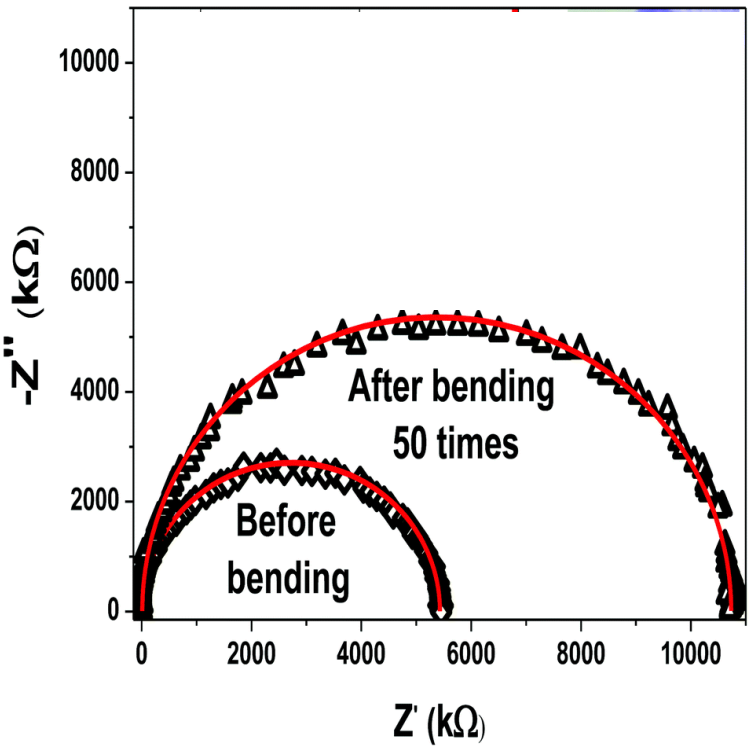

Figure 5: Comparison of Nyquist plots (two-probe AC impedance data) of ligand-free PbS nanocrystal films on a flexible PET substrate before and after bending the film 50 times. Black symbols are experimental data and red solid lines show the fitting. All the electrical measurements shown were carried out at room temperature and under ambient air. The AC perturbing voltage was kept at 500 mV in the frequency range of 2 MHz to 100 Hz.

Table 3: The values of R_{gb} and C_{gb} obtained from the fitting of Nyquist plot for the PbS films on PET substrate (before and after bending 50 times) measured at room temperature.

Samples (on PET flexible substrate)	No. of bending	R_b (Ω)	R_{gb} (Ω)	C_{gb} (Fcm^{-1})
PbS	0	1.139×10^4	5.42×10^6	2.017×10^{-11}
PbS	50	1.147×10^4	10.72×10^6	2.122×10^{-11}

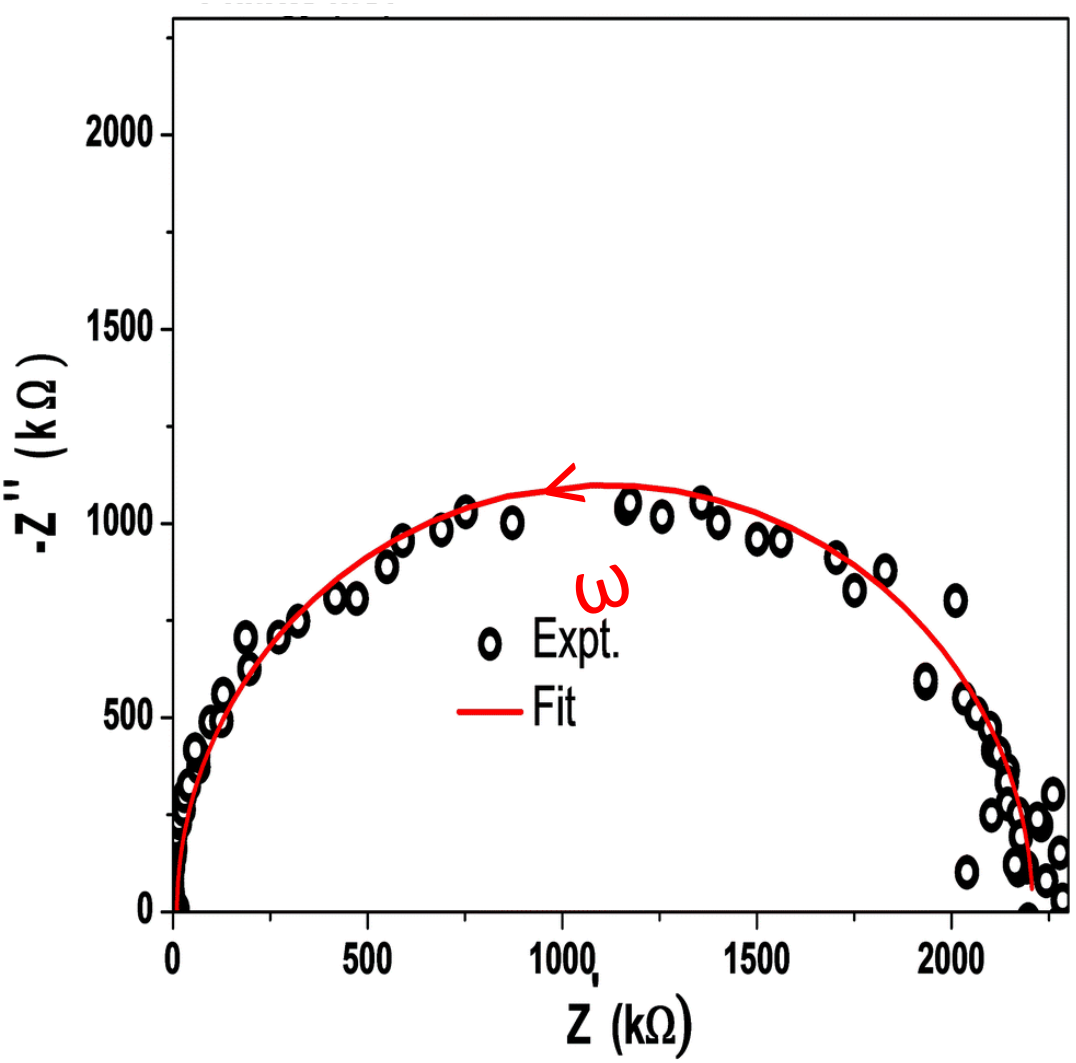

Figure 6: Nyquist plots of ligand-free PbSe nanocrystals film obtained from two-probe ac impedance measurements. The impedance measurements were performed at room temperature and under ambient air. Black symbols are experimental data and red solid lines show the fitting. The AC perturbing voltage was kept at 500 mV in the frequency range of 2 MHz to 100 Hz.

PbSe NCs:

Colloidal ligand-free PbSe NCs were also prepared in a manner similar to the synthesis of ligand-free PbS NCs and the details are available in the published article [G. Shiva Shanker et al. Nanoscale, 2015, 7, 9204]. All the observations for PbSe NCs are qualitatively similar to those of PbS NCs discussed above. Thin films of PbSe NC precipitates can be prepared on both glass and flexible PET substrates with a thickness in the range of 1–15 μm, using the doctor blading technique. Two-probe AC impedance data for PbSe NC film, shown in the form of a Nyquist plot (Figure 6), shows a single semicircular shape with R_{gb} = 2.20 MΩ and C_{gb} = 20.4 pF (Table 3) A comparison of electrical data shows that PbSe NC films are electronically more conducting compared to PbS NC films, similar to their bulk counterparts. The electrical conductivity of our PbSe NC films are comparable to the PbSe films prepared at higher temperatures using expensive methodologies.[7]

Table 3. The values of R_{gb} and C_{gb} obtained from the fitting of Nyquist plot for the PbS films on glass substrate measured at room temperature.

Samples	R_b (Ω)	R_{gb} (Ω)	C_{gb}(Fcm^{-1})
Preannealed PbSe	1.035×10^4	2.198×10^6	2.04×10^{-11}

Conclusions:

In the published article by G. Shiva Shanker et al. [*Nanoscale*, **2015**, 7, 9204], we developed a strategy to prepare electronic grade semiconductor thin films using colloidal ligand-free PbS and PbSe NCs at room temperature. The processing at room temperature allows us to prepare films on a flexible substrate, and the charge transport properties (measured by using impedance and other techniques) do not deteriorate considerably with the repeated bending of the film. Therefore, the lowering of the film processing temperature allows us to obtain flexible SC films, and also it reduces the cost of film deposition. AC impedance data show the dominance of grain boundaries, exhibiting single semicircular Nyquist plots.

References:

1. SINCLAIR, D. C., Characterization of Electro-materials using ac Impedance Spectroscopy. *Bol. Soc, Esp. Cerám. Vidrio* **1995,** *34*, 55-65.

2. Ponce, M. A.; Parra, R.; Savu, R.; Joanni, E.; Bueno, P. R.; Cilense, M.; Varela, J. A.; Castro, M. S., Impedance spectroscopy analysis of TiO2 thin film gas sensors obtained from water-based anatase colloids. *Sensors and Actuators B: Chem.* **2009,** *139*, 447-452.

3. Irvine, J. T. S.; Sinclair, D. C.; West, A. R., Electroceramics: Characterization by Impedance Spectroscopy. *Adv. Mater.* **1990,** *2*, 132-138.

4. Sashchiuk, A.; Amirav, L.; Bashouti, M.; Krueger, M.; Sivan, U.; Lifshitz, E., PbSe Nanocrystal Assemblies: Synthesis and Structural, Optical, and Electrical Characterization. *Nano Lett.* **2004,** *4*, 159-165.

5. Ponce, M. A.; Castro, M. S.; Aldao, C. M., Influence of oxygen adsorption and diffusion on the overlapping of intergranular potential barriers in SnO2 thick films. *Mater. Sci. and Eng.: B* **2004,** *111*, 14-19.

6. Hu, L.; Kim, H. S.; Lee, J.-Y.; Peumans, P.; Cui, Y., Scalable Coating and Properties of Transparent, Flexible, Silver Nanowire Electrodes. *ACS Nano* **2010,** *4*, 2955-2963.

7. Fardy, M.; Hochbaum, A. I.; Goldberger, J.; Zhang, M. M.; Yang, P., Synthesis and Thermoelectrical Characterization of Lead Chalcogenide Nanowires. *Adv. Mater.* **2007,** *19*, 3047-3051.

Appendix-II

Quantum Dot Sensitized Solar Cell from Ag_2S, $AgInS_2$ and Ag_2S-$AgInS_2$Heterodimer Nanocrystals

---

The following articles have been published based on the work presented in this Appendix.

1. Mir,W. J.; Swarnkar, A.; Sharma, R.; Katti, A.; Adarsh, K. V.; Nag. A.Origin of Unusual Excitonic Absorption and Emission from Colloidal Ag_2S Nanocrystals:Ultrafast Photophysics and Solar Cell. *J. Phys. Chem. Letts.*,**2015**, *6*, 3915-3922.Copyright permission has been taken from American Chemical Society.

2.Rao, M. J.;Swarnkar, A.;Markad, G. B.; Nag, A..Defect-Mediated Electron-Hole Separation in Colloidal Ag_2S-$AgInS_2$ Hetero Dimer Nanocrystals Tailoring Luminescence and Solar Cell Properties.*J. Phys. Chem. C*,**2016,***120*, 19461-19469.Copyright permission has been taken from American Chemical Society.

Introduction

In a published work by Wasim Mir et al. [*J. Phys. Chem. Letts.*,**2015,** *6*, 3915] we optimized the synthesis conditions which lead to minimize the lattice defects, and thereby, achieving sharp excitonic absorption and emission from Ag_2S quantum dots (QDs) with high (~20%) quantum yield at near infrared (~850 nm)region. Utilizing these new high quality nanocrystals (NCs), QD sensitized solar cells (QDSSC) were fabricated for the first time. These QDSSC perhaps exhibit the best performance compared reported Ag_2S QDSSC obtained via chemical bath deposition.

On the other side, in the published work by Jagadeeswararao et al. [*J. Phys. Chem. C,* **2016,***120,* 1946] we published the synthesis of heterodimer of Ag_2S and $AgInS_2$in a single nanocrystal to bring better charge separation in the hetero junction which can lead to better solar cell efficiency. Here, the interfacial defects are involved in PL. Utilizing the defect mediated charge separation; we fabricated the Ag_2S-$AgInS_2$heterojunction NCs based QDSSC with improved efficiency than the Ag_2S QDSSC.

Experimental Sections

Chemicals

Silver Nitrate ($AgNO_3$, 99.8%), 3-Mercaptopropionic acid (3-mpa, ≥99%), sulfur powder,sodium sulfide hydrate, and potassium chloride were purchased from Sigma Aldrich. Methanol (99.5%), Acetonitrile (99.8%), Propan-2-ol were purchased from Rankem India Ltd, Ethanol (99.9% AR, S D Fine chem. Ltd. Titanium tetrachloride was obtained from Merck.F-doped SnO_2 (FTO) coated glass (~ 7 ohm/sq) was obtained from Aldrich.Transparent titania paste (DSL-18NR-T, diameter ~20 nm), scattering titania paste (WER2-O, diameter 150-250 nm) were obtained from Dyesol.

Preparation of TiO_2 Coated FTOElectrode Ag_2S Quantum Dot Sensitized Solar Cell (QDSSC):

Preparation of TiO_2 Coated FTO Electrode

FTO(F-doped SnO_2) coated glass (Aldrich, ~ 7 Ω/sq) was cleaned sequentially with soap solution (30 min), water (30 min) and ethanol (30 min) using an ultrasonication bath. Finally cleaned FTO coated glass was heated at 450 °C for 10 minutes in order to remove organic contaminants. The compact layer of TiO_2 was prepared on top of conducting surface of FTO glass. For that 0.04 M aqueous solution of $TiCl_4$ was poured on conducting surface so that the

glass would fully dip into the solution and then the glass was heated at 80 ^{0}C for 30 min in dipped state. Then the FTO glass was cleaned by water and finally with ethanol. The mesoporous TiO_2 active film was then prepared by doctor blading method using commercial TiO_2 paste (Dyesol DSL-18NR-T, diameter ~20 nm). Over the active TiO_2 layer, a scattering layer of TiO_2 (Dyesol WER2-O, diameter 150-250 nm) was doctor bladed. The film was sintered at 450 °C for 30 minutes for each layer. The heating and cooling process for the TiO_2 electrode preparation was gradual to prevent the crack formation on film. After all, the sintered TiO_2 film was treated with aqueous $TiCl_4$ (0.04 M) and finally sintered again at 450 °C for 30 min in order to remove pin holes and cracks from the TiO_2 film. The thicknesses of active and light scattering layers were optimized to ~10 μm and ~4 μm respectively.

QDs Sensitization

Hot TiO_2 electrode (at 60 °C) was dipped in different NC solutions (mercaptopropanoic acid (MPA) capped AgS_2 QDsdispersed in DMSO, oleylamine capped Ag_2S-$AgInS_2$ HDNCsdispersed in $CHCl_3$ or oleylamine capped $AgInS_2$ NCs dispersed in $CHCl_3$) and kept in dark for 60 hours at room temperature.

Ligand Exchange on Film

QDs or NCs sensitized TiO_2 electrode was allowed to stay in sulfide solution (0.8 M Na_2S in 1:1 methanol: water solution) for 48 hours at room temperature in dark. The final photoanode was cleaned using water and then ethanol and dried at 80 °C inside N_2 environment for 30 min.

Ag_2S Deposition on Photoande by Successive Ionic Layer Adsorption and Reaction (SILAR)

To grow a very thin barrier layer of Ag_2S on the bared surface of active TiO_2, the as prepared photoanode was sequentially dipped in solution of Ag^+ (0.1 M $AgNO_3$ in ethanol) and S^{2-} (0.1 M Na_2S in Methanol). In between the two dipping the electrode was rinsed with ethanol and finally with methanol. And then the resultant photoanode was dried.

QDSSC Fabrication

QDSSCs were prepared by assembling the photoanode and Pt counter electrode using parafilm as spacer (~80 μm) along with a 10 μL electrolyte solution in between. Two types of electrolyte solutions: A and Bwere used in our work. Electrolyte solution A was prepared by mixing Na_2S (0.5 M), sulfur (2 M), KCl (0.2 M) and NaOH (0.5 M) in methanol : water in 7 : 3 v/v following ref[1-2]. Methanol-free electrolyte solution B was prepared by mixing Na_2S (2 M), and sulfur (2 M) in water following ref[3], however, power conversion efficiency decreases with electrolyte B, compared to electrolyte A.

Characterization

Current–voltage (I–V) measurement was performed using a Keithley 2611 source meter. All the solar cells were illuminated using a Xe lamp of 150 W, fitted with AM 1.5 filter and adjusted at 1 Sun intensity (100 mW/cm^2) by using an NREL-calibrated silicon solar cell. The active areas for the measurement were kept in the range of 0.24 cm^2 to 0.28 cm^2.

Results and Discussion

Ag_2S QDSSC.

QDSSC are being investigated for flexible and solution processed solar panels. Colloidal Ag_2S NCs with a broad absorption spectrum and low-toxicity can be a useful QDSSC material. A recent ultrafast spectroscopic study also suggestedmultiple exciton generation via absorption of a single high-energy photon.[4] A survey of literature shows no report of QDSSC starting from colloidal Ag_2S NCs exhibiting excitonic feature. There are reports where Ag_2S sensitization layer was grown by SILAR, but broad bulk-like absorption spectra was observed for all such cases.[2, 5] Here, we demonstrate QDSSC using high quality colloidal Ag_2S QDs (schematic shown in Figure 1).

Figure 2 shows the current density (J) vs. voltage (V) plot for Ag_2S QDSSCs. The cell prepared with Ag_2S QDs shows an open circuit voltage (V_{OC}) = 0.25 V, short circuit current density (J_{SC}) = 4.7 mA.cm^{-2}, along with a fill factor (FF) of 0.37. The power conversion efficiency (η) calculated to be 0.43%. It was observed that the performance of QDSSC improves significantly by suppressing electron-hole recombination at both FTO/electrolyte and TiO_2/electrolyte interfaces.[6-7] We already used compact TiO_2 layer on FTO to suppress the recombination across FTO/electrolyte. In order to suppress recombination acrossTiO_2/electrolyte, we grow thin 1monolayer (ML) of Ag_2S using SILAR on top of

Ag_2S-sensitized TiO_2 photoanode. Such SILAR deposition is expected to remove any pinholes from sensitization layer and thereby inhibiting interaction between TiO_2 and electrolyte. Expectedly, J_{SC} and V_{OC} increased after depositing 1 ML Ag_2S by SILAR. Figure 2 shows that J_{SC} increases to 8.7 mA.cm^{-2} and V_{OC} increased to 0.30 V for Ag_2S QDSSC with 1 ML Ag_2S. The overall power conversion efficiency increased to 1.04%.

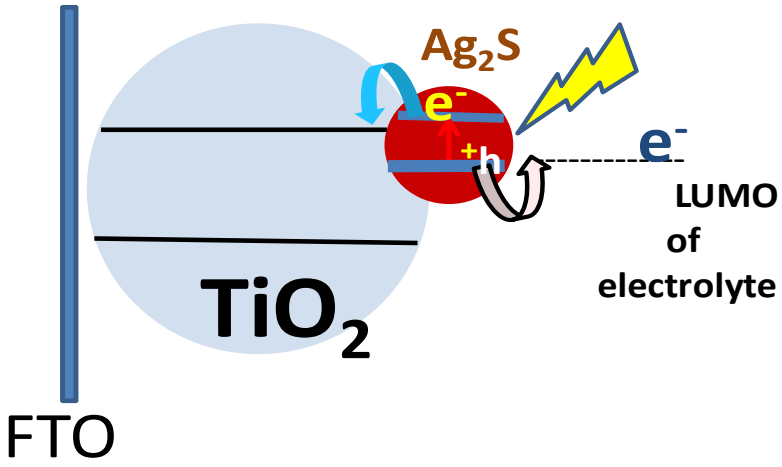

Figure 1: Schematic diagram explaining the mechanism of charge transfer in Ag_2S QDSSC.

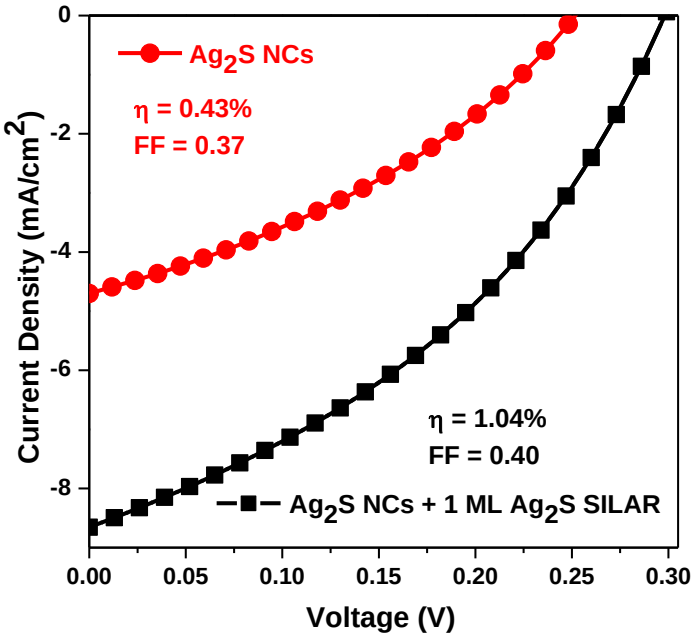

Figure 2: Current density (J) vs voltage (V) plot for Ag_2S QDSSCs. In one case, 1 monolayer (ML) Ag_2S was grown on the Ag_2S NC sensitized photoanode in order to fill up any pin-holes in the sensitization layer, which in turn reduce the loss due to interaction of electrolyte with TiO_2. Effective cell area was typically kept in the range of 0.24 to 0.28 cm^2 for all cells.

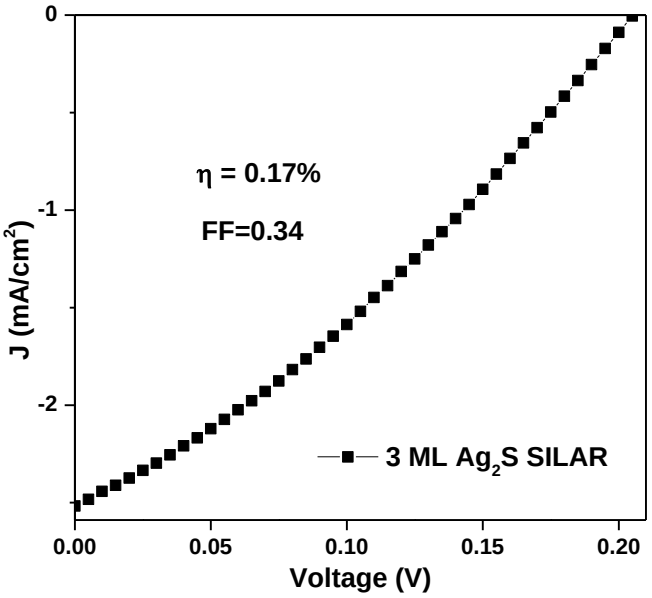

Figure3: Current density (*J*) vs voltage (*V*) plot for solar cell sensitized by 3 monolayer of Ag_2S by SILAR method.

Our control experiment with sensitization of mesoporous TiO_2 via depositing 1 ML Ag_2S using SILAR, in the absence of Ag_2S NCs did not yield any solar cell characteristic. However, we got a reasonable *J-V* plot for 3 ML Ag_2S in the absence of QDs. Figure 3shows V_{OC} = 0.2 V, J_{SC} = 2.5 mA.cm^{-2}, and FF = 0.34 for 3 ML Ag_2S solar cell. We note that the prior reports suggests similar V_{OC} (<0.25 V) for Ag_2S based solar cells obtained using chemical bath deposition (CBD)[8], sonochemical method,[2] or Ag_2S-polymer hybrid structure[9]. We found a report based on SILAR growth Ag_2S QDSSC showing V_{OC}> 0.3 V, but the obtained J_{SC} was less yielding η<1%.[5]

It is difficult to prepare small Ag_2S QDs with a control over size distribution employing above mentioned methodologies such as SILAR, CBD or sonochemistry, and therefore, colloidal synthesis of Ag_2S NCs is more desirable to achieve size-dependent properties and multiple exciton generation. Our QDSSC, fabricated using colloidal Ag_2S QDs exhibiting sharp excitonic feature, shows a combination of high V_{OC}= 0.3 V and high J_{SC} = 8.7 mA.cm^{-2} compared to prior reports and eventually resulting in to η = 1.04%. This enhanced V_{OC} and J_{SC} once again suggest the defect-free nature of our Ag_2S QDs.[10] To the best of our knowledge, the obtained η= 1.04% is the highest reported so far using Ag_2S QDSSC. In order to improve η of Ag_2S QDSSC, V_{OC} needs to be increased further. Search for better electrolyte or hole transport layer, and optimization of device fabrication minimizing electron-hole

recombinations, and enhancement of photo-absorption are required to improve performance of Ag_2S QDSSC.

$AgInS_2$ NCs and Ag_2S-$AgInS_2$HDNCs sensitized solar cell.

Further to improve the solar cell efficiency we introduced a high bandgap semiconductor $AgInS_2$ along with Ag_2S NCs. In this structure a single NCs has heterojuction of AgS_2 and $AgInS_2$ and we termed it as $AgInS_2$-Ag_2S heterodimerNC (HDNC). The detail of the synthesis and characterization of these NCs are available in the work byJagadeeswararao et al. [*J. Phys. Chem. C*, 2016,*120*, 1946]. It is well understood from this published work that electron-hole separation by type-II band alignment across the interface of two materials is beneficial for solar cell application. Our Ag_2S-$AgInS_2$ HDNC represents a unique situation, where defect-mediated spatial separation of electron and hole, in spite of having a type-I band alignment. Another important aspect of HDNCs is long (13 μS) PL lifetime, and it has been recently reported that the long lifetime of Mn^{2+} doped CdSe based NCs suppress charge recombination improvingsolar cell efficiencies.[11-13]We prepared QDSSCs using both $AgInS_2$ NCs and Ag_2S-$AgInS_2$ HDNCs. Figure 4 shows the corresponding current *J-V* plots.The obtained solar cell parameters, short circuit current density (J_{SC}), FF, and V_{OC},resulting into the overall η, are given in the Table 1. Interestingly, all these solar cell parameters are significantly superior for Ag_2S-$AgInS_2$ HDNC sensitized solar cells compared to $AgInS_2$ NC sensitized cells.

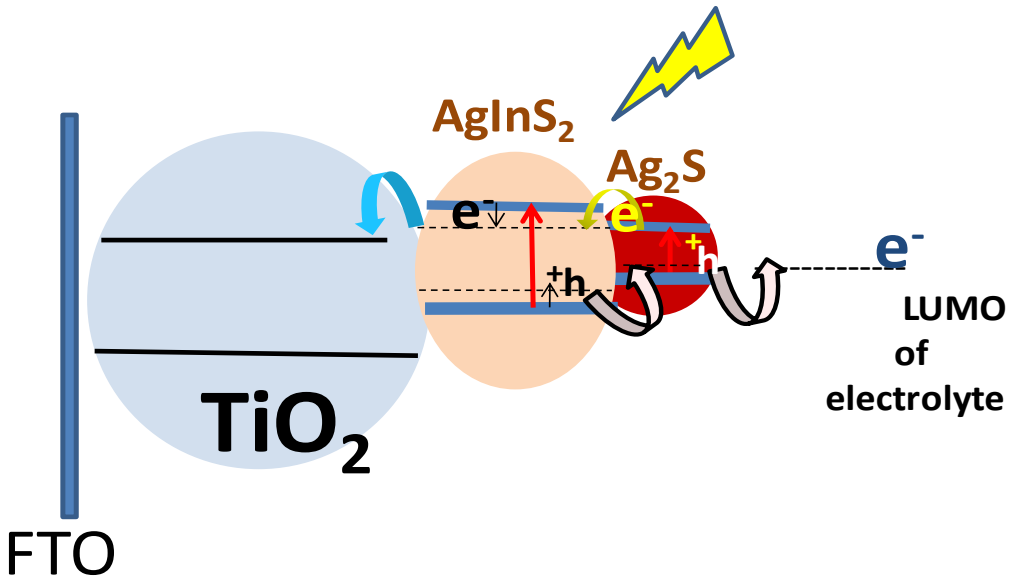

Figure 4: Schematic diagram explaining the mechanism of charge transfer in Ag_2S-$AgInS_2$ HDNC QDSSC. Black dotted lines on the NCs are representing the defect states.

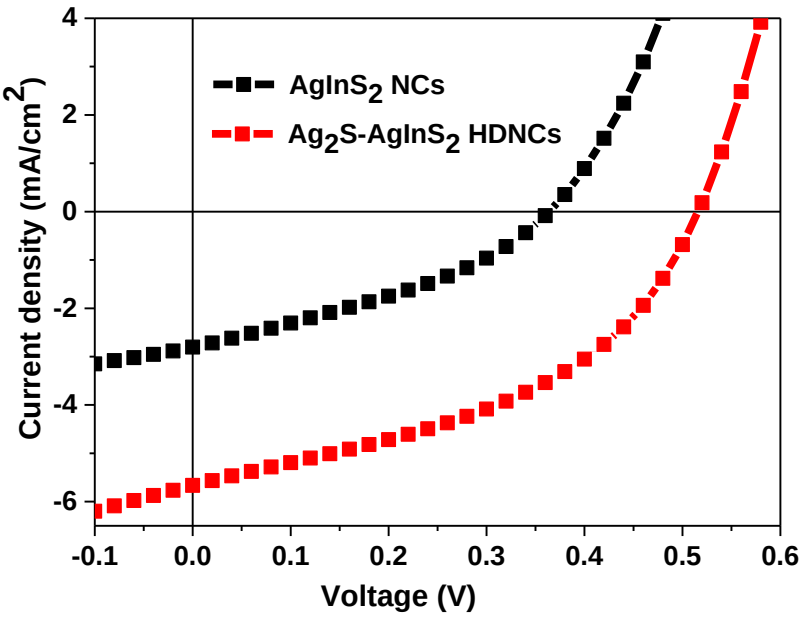

Figure 5: *J-V* characteristics of $AgInS_2$ NCs and Ag_2S-$AgInS_2$ HDNCs measured by Xe lamp at standard conditions AM 1.5 G. The active area of the solar cell measurement was 0.16 cm^2**.**

Table 1: Solar cell parameters obtained from I-V plots shown in Figure 5.

Sample	**J_{SC}(mA/cm^2)**	**Fill Factor**	**V_{OC} (V)**	**η (%)**
$AgInS_2$ NCs	2.8	0.35	0.37	0.4
Ag_2S-$AgInS_2$ HDNCs	5.7	0.43	0.52	1.3

Based on the investigation of the reported article of Jagadeeswararao et al. [*J. Phys. Chem. C,* **2016,***120,* 1946], the excited electrons mainly located in the trap states of $AgInS_2$ transfers to TiO_2 electrode, whereas, the hole residing in valence band maximum (VBM) or a shallow defect state of Ag_2S part transfers to the redox couple S^{2-}/S_n^{2-}(schematics shown in Figure 4) This spatial separation of electron and hole, yielding increased value ofJ_{SC}, which in turn increases V_{OC}, since V_{OC} is proportional to the logarithm of J_{SC}.Eventually, the power conversion efficiencie (PCE)for Ag_2S-$AgInS_2$ HDNCs is 1.3 %, which is 3 times higher compared tothat of $AgInS_2$ QDSSC and ~0.3 V higher than the previously discussed AgS_2 QDSSC.To the best of our knowledge, this 1.3% PCE is the highest reported value so far for QDSSC fabricated using both Ag_2S NCs, and $AgInS_2$ NCs.[14] Further optimization of device fabrication, with better selections of electrolytes and electrode is expected to improve the efficiency of Ag_2S-$AgInS_2$ HDNC based QDSSC.

Conclusions:

Based on reported work of Wasim Mir et al. [*J. Phys. Chem. Letts.*,**2015,** *6,* 3915], defect-free Ag_2S QDs exhibit sharp near infrared excitonic absorption at 800 nm and excitonic PL at858 nm.QDSSC were fabricated for the first time using these colloidal Ag_2S NCs. The defect-free nature of our Ag_2S NCs lead to an improvement of V_{OC} (0.3 V) and J_{SC} (8.7 $mA.cm^{-2}$) yielding η = 1.04%, which is highest compared to prior reports of Ag_2S QDSSC prepared via SILAR, CBD, or sonochemical methods. Further, as reported by Jagadeeswararao et al. [*J. Phys. Chem. C,* **2016,***120,* 1946], $AgInS_2$-AgS_2 HDNC defect-mediated charge separation across the interface of the HDNCs, where the photoexcited electron gets trapped by a defect state inside the $AgInS_2$ component, and the hole resides either in VBM or in shallow defect states of the Ag_2S component. The efficacy of such defect-mediated electron−hole separation was tested by fabricated QDSSC where the PCE (1.3%) of Ag_2S−$AgInS_2$ HDNCs is more than 3 times higher than that of $AgInS_2$ NCs (0.4%). The efficiency needs to be increased further for real life applications, however, it is a good starting point for these non-toxic colloidal Ag_2S based NCs.

References:

1. Tubtimtae, A.; Lee, M. W.; Wang, G. J., Ag2Se quantum-dot sensitized solar cells for full solar spectrum light harvesting. *J. Power Sources* **2011,***196*, 6603-6608.

2. Wu, J. J.; Chang, R. C.; Chen, D. W.; Wu, C. T., Visible to near-infrared light harvesting in Ag2S nanoparticles/ZnO nanowire array photoanodes. *Nanoscale* **2012,***4*, 1368-1372.

3. Santra, P. K.; Kamat, P. V., Tandem-Layered Quantum Dot Solar Cells: Tuning the Photovoltaic Response with Luminescent Ternary Cadmium Chalcogenides. *J. Am. Chem. Soc.* **2013,***135*, 877-885.

4. Sun, J. Y.; Yu, W. L.; Usman, A.; Isimjan, T. T.; Dgobbo, S.; Alarousu, E.; Takanabe, K.; Mohammed, O. F., Generation of Multiple Excitons in Ag2S Quantum Dots: Single High-Energy versus Multiple-Photon Excitation. *J. Phys. Chem. Lett.* **2014,***5*, 659-665.

5. Tubtimtae, A.; Wu, K. L.; Tung, H. Y.; Lee, M. W.; Wang, G. J., Ag2S quantum dot-sensitized solar cells. *Electrochem. Commun.* **2010,***12*, 1158-1160.

6. Ruhle, S.; Yahav, S.; Greenwald, S.; Zaban, A., Importance of Recombination at the TCO/Electrolyte Interface for High Efficiency Quantum Dot Sensitized Solar Cells. *J. Phys. Chem. C* **2012,***116*, 17473-17478.

7. Santra, P. K.; Nair, P. V.; Thomas, K. G.; Kamat, P. V., CuInS2-Sensitized Quantum Dot Solar Cell. Electrophoretic Deposition, Excited-State Dynamics, and Photovoltaic Performance. *J. Phys. Chem. Lett.* **2013,***4*, 722-729.

8. Shen, H. P.; Jiao, X. J.; Oron, D.; Li, J. B.; Lin, H., Efficient electron injection in non-toxic silver sulfide (Ag2S) sensitized solar cells. *J. Power Sources* **2013,***240*, 8-13.

9. Lei, Y.; Jia, H. M.; He, W. W.; Zhang, Y. G.; Mi, L. W.; Hou, H. W.; Zhu, G. S.; Zheng, Z., Hybrid Solar Cells with Outstanding Short-Circuit Currents Based on a Room Temperature Soft-Chemical Strategy: The Case of P3HT:Ag2S. *J. Am. Chem. Soc.* **2012,***134*, 17392-17395.

10. Panthani, M. G.; Stolle, C. J.; Reid, D. K.; Rhee, D. J.; Harvey, T. B.; Akhavan, V. A.; Yu, Y. X.; Korgel, B. A., CuInSe2 Quantum Dot Solar Cells with High Open-Circuit Voltage. *J. Phys. Chem. Lett.* **2013,***4*, 2030-2034.

11. Santra, P. K.; Kamat, P. V., Mn-Doped Quantum Dot Sensitized Solar Cells: A Strategy to Boost Efficiency over 5%. *J. Am. Chem. Soc.***2012,***134*, 2508-2511.

12. Debnath, T.; Maity, P.; Maiti, S.; Ghosh, H. N., Electron Trap to Electron Storage Center in Specially Aligned Mn-Doped CdSe d-Dot: A Step Forward in the Design of Higher Efficient Quantum-Dot Solar Cell. *J. Phys. Chem. Lett.***2014,***5*, 2836-2842.

13. Wang, J.; Li, Y.; Shen, Q.; Izuishi, T.; Pan, Z.; Zhao, K.; Zhong, X., Mn doped quantum dot sensitized solar cells with power conversion efficiency exceeding 9%. *J. Mater. Chem. A* **2016,***4*, 877-886.

14. Kadlag, K. P.; Patil, P.; Jagadeeswara Rao, M.; Datta, S.; Nag, A., Luminescence and solar cell from ligand-free colloidal AgInS2 nanocrystals. *CrystEngComm* **2014,***16*, 3605-3612.

Thesis Summary and Future Outlook

Research Content

CdSe Quantum Dots vs Defect Tolerant $CsPbX_3$ (X= Cl, Br, I) Perovskite Nanocrystals

Traditional semiconductor nanocrystals (NCs), such as CdSe based quantum dots (QDs) are well established system for various optoelectronic applications. However, there are many challenges on using these materials in devices. One of the big challenges is the presence of detrimental defect states lying deep within the bandgap which trap the charge carriers and hampers the performance of an optoelectronic device.[1] Owing to the high surface to volume ration of these QDs, surface related defects are abundant and inherent which cannot be removed from the system. However, changing the energy level of these defect states can somewhat solve the problem. For example, if the energy level of defect states are pushed near to (shallow region) or inside the conduction band and/or valence band, then those defect states would be partially delocalized in nature and do not trap the charge carriers. In this scenario a semiconductor NCs will exhibit interesting optoelectronic properties with efficiency, in spite of having surface defects and such a semiconductor NC is termed as defect tolerant NC. $CsPbX_3$ (X= Cl, Br, I) NCs are one of these kind of semiconductor NCs and exhibit attractive optoelectronic properties.[2]

Optoelectronic Properties and Crystal Phase of $CsPbX_3$ Perovskite Nanocrystals

In early 2014, Schimidt et al. have first time reported the synthesis and light emitting diode (LED) application of green emitting colloidal $MAPbBr_3$ (MA= CH_3NH_3) NCs.[3] After one year, in 2015, Protesescu et al. published a detailed work on colloidal $CsPbX_3$ (X= Cl, Br, I) perovskite NCs, in which synthesis, material characterizations and basic photophysical properties are discussed thoroughly.[2] Looking at the higher thermal stability of $CsPbBr_3$ perovskite in compare to $MAPbBr_3$,[4] due to its all-inorganic nature we started to work on $CsPbX_3$ perovslite NCs in a motivation to employ these NCs in high efficiency optoelectronic devices. In the present thesis, most of the works are done on $CsPbBr_3$ and $CsPbI_3$ NCs. Colloidal $CsPbX_3$ NCs has great potentials for light emitting applications, and have many advantages over the traditional colloidal QDs based light emitters, such as high photoluminescence quantum yield (PL QY) of 50-90 %, narrow emission line width (12 nm-42 nm). Emissions from $CsPbX_3$ NCs with different halide compositions cover the full visible spectrum. Also, tuning of emission color can be done by employing quantum size effect.

$CsPbI_3$ is an all-inorganic analogue to $MAPbI_3$, a popular energy material for high efficiency solar cell. It absorbs the visible portion of the sunlight and can solve the issue of thermal instability related to using $MAPbI_3$ in solar cell.

Unlike the reports on bulk $CsPbI_3$,[5] $CsPbI_3$ NCs exhibit cubic phase of perovskite structure in which $[PbI_6]$ octahedra are corner shared.[2] This result is surprising and need to be investigated in detail. It is also report that cubic phase $CsPbI_3$ NCs transform to orthorhombic phase where $[PbI_6]$ octahedra are not corner-shared, when the NCs are kept for months.[2] Corner-shared $[PbX_6]$ octahedra in a perovskite structure are crucial for the material to be used in optoelectonic applications.[6]

Important Results

This thesis discuss about defect-tolerant colloidal $CsPbX_3$ (X= Br and I) NCs. Unlike defect-intolerant CdSe based QDs, without any surface modifications, these colloidal NCs of $CsPbX_3$ have high PLQY (55-90%) with narrow line width (83-153 meV). 11 nm sized $CsPbBr_3$ NCs exhibit intense light emission in the weak quantum confinement region, and hence do not affected by size-distribution issues. This fact has led to a remarkable observation that spectral width of the ensemble of NCs as narrow as that of single-NC spectrum. Other size-distribution related problems, such as Föster resonance energy transfer (FRET) and self-absorption also do not influence the PL. Suppression of blinking-off time is another interesting result.

Devices employing $CsPbX_3$ NCs (such as, solar cell, photodiode, LED) have been fabricated. $CsPbI_3$ is an all-inorganic analogue to the $CH_3NH_3PbI_3$. However, the cubic phase of bulk $CsPbI_3$ is only stable at high temperature, preventing its adoption within the community. In this thesis, we describe formation of cubic phase $CsPbI_3$ NC films, phase stability for months in ambient air, with long-range electronic transport, leading to the fabrication of the first colloidal perovskite NC solar cells with a *Voc* = 1.23 V and PEC = 10.77 %. These devices also exhibit electroluminescence with low turn-on voltage and tunable emission. We also have made stable and hysteresis-free photodiode of high detectivity (1.8×10^{12} Jones) and reliability using $CsPbI_3$ NCs as photoactive material. Eventually, following the same film fabrication method and to use high PLQY of $CsPbBr_3$, we have made LED exhibiting ~ 6 cd/A luminance efficiency and 2.25% external quantum efficiency (EQE) with a device structure of ITO/PEDOT:PSS/$CsPbBr_3$ -NCs/TPBi/Ca/Ag. The synthesis of normally non-luminescent and unstable material phases stabilized through

colloidal NC synthesis provides another mechanism for materials design for other applications. All these optoelectronic behaviors of $CsPbX_3$ perovskite NCs are advantageous, and therefore, $CsPbX_3$ NC can be a better candidate for optoelectronics.

Methodology Development

In order to stabilize the α-phase of $CsPbI_3$ which absorb at lower energy (bulk bandgap 1.73 eV), we have developed a purification method in which mildly polar solvent, such as methyl acetate has been used. Using required amount of anhydrous methyl acetate as a non-solvent to clean the NCs does not allow the dynamic surface ligands of the NCs to cleave out and hence do not allow the NCs to agglomerate or to grow in size. In this process the surface energy of the NCs remains intact which help in maintaining the α-phase stability of $CsPI_3$ NCs at room temperature. Details can be found in chapter 4.

Further, we developed a film deposition method to deposit electronically coupled $CsPbX_3$ NC film required to fabricate optoelectronic devices. Colloidal $CsPbX_3$ NCs are capped with organic hydrocarbon long chained ligands which are insulating in nature and do not allow the charge carriers to move from one NC to another. This causes decrease in efficiency of devices in which semiconductor NCs are used as active material. Typically, in case of traditional QDs, high polar solvent, such as formamide, dimethyl formamide are used to remove the insulating ligands.[7] Using these high polar solvent in case of $CsPbX_3$ NCs destroy the integrity of the NCs. Hence, there a need of a new solvent chemistry for these $CsPbX_3$ NCs by using that solution processable ligand engineering would be easier. Our developed method of film deposition in which methyl acetate plays major role solves the above challenge to a great extent. Using this method, high efficiency devices are successfully made, such as solar cell, photodetectors and light emitting diodes, in which $CsPbX_3$ NCs are active materials. Details are given in chapter 5.

We also removed the organic ligand in solution to make CdSe QDs a solution based sensor. This work introduces a novel probe based on ligands free quantum dots for sensing cadmium and nitroaromatic explosives. Typically, hydrophobic quantum dot is synthesized by known method and converted into S^{2-} capped QDs by ligand exchange method. This colloidal quantum dot shows enhanced fluorescence in presence of Cd^{2+} and quenching of fluorescence in presence of trinitrophenol. Due to organic ligand free nature of QDs it offers more sensitive detection platform. The details can be found in chapter 2 of the present thesis.

Future Direction

Growth of Metal Chalcogenide Shell Over Individual Perovskite Nanocrystals

Research on $CsPbX_3$ NCs has shown tremendous progress in just few years. Despite this success, the stability of these ionic NCs against the serious damage by water, air, and light is still a big challenge.[8-11] Another big problem is the fast anion exchange which degrades the optical properties of these NCs, for example when the $CsPbBr_3$ NCs are exposed to Cl (or I) environment the absorption and PL spectra blue (or red) shifts.[12-13] A simplest way to protect the NCs from these harsh environments is the NC surface modification with a material of better stability. In this direction there are many reports have been published.[14-23] Li et al. show the improved stability of $CsPbBr_3$ NCs by incorporating them into a silica/alumina monolith.[14] While to improve water stability, Fu et al. embedded $CsPbX_3$ NCs into a polymer matrix. Having same motivation of improving the stability, Loiudice et al. encapsulated the $CsPbX_3$ perovskite NCs film using an atomic layer deposited amorphous alumina matrix.[16] Rogach and his coworkers used polyhedral oligomeric silsesquioxane to make $CsPbX_3$ NCs water stable.[17] However, till today, all the reports are dealing with an ensemble of $CsPbX_3$ NCs and the size of the resultant particle is in macroscopic ranges which do not allow the material to be used in many applications where single particles are preferable. For example, bio-imaging, single NC are allowed to be taken by cells and also to be taken out; while in light emitting application, small sized NCs are desirable to fabricate NC films for improved uniformity. Therefore, it is highly desired to develop a method in which single particle can be encapsulated inside a thin shell of material of higher stability than the halide perovskite.

Metal chalcogenides and metal oxides are comparatively more stable than the lead halide perovskite system. Growing a shell of metal chalcogenide, such as Tin(IV) chalcogenide over $CsPbX_3$ perovskite NCs in single NC level can solve the stability issue. Typically, in colloidal synthesis, growing a crystalline shell over a NCs in which the crystal phases of NCs and shell material is highly mismatch (crystal mismatch of more than 5 %), is very challenging.[24] In this scenario, the precursors used to grow shell prefer to nucleate separately and make separate NCs instead of growing over the pre-existing NCs. But if the crystal phase of shell and the core material matches well (less than 5%), the growth of shell on pre-existing NCs would be easier.

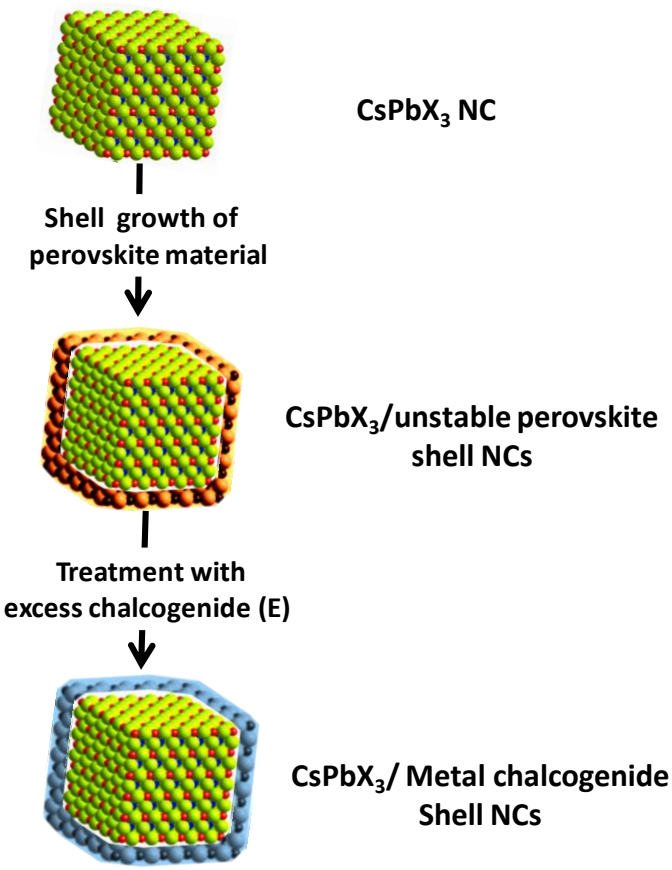

Figure 1: Surface modification of perovskite nanocrystals. In first step a shell of unstable metal halide perovskite other than lead halide is grown over $CsPbX_3$ nanocrystal. In step second, unstable metal halide perovskite shell is made to transform into stable metal chacogenide by treating the core/shell nanoparticle with excess of highly reactive chalcogenide source. The resultant core/shell nanocrystal would have improved stability in presence of water, air and light.

Based on the above argument, in our proposed hypothesis, tin(II) or germanium(II) based perovskite will be grown over pre-existing $CsPbX_3$ NCs in a colloidal solution. Further, tin(II) and germanium (II) being unstable transform to their tin(IV) and germanium(IV) states in presence of oxidizing environment, such as oxide or sulphide and convert to their corresponding metal chalcogenide composition (Tin(IV) chalcogenide and Ge(IV) chalcogenide). This kind of core/shell structure is supposed to be highly stable in presence of water, air and light. Also, different halide compositions of $CsPbX_3$ NCs would able to maintain their optical properties when mixed in different ratio to get white colour emission and in kept in tandem arrangement in fabricating solar cells.

References:

1. Brandt, R. E.; Poindexter, J. R.; Gorai, P.; Kurchin, R. C.; Hoye, R. L. Z.; Nienhaus, L.; Wilson, M. W. B.; Polizzotti, J. A.; Sereika, R.; Žaltauskas, R.; Lee, L. C.; MacManus-Driscoll, J. L.; Bawendi, M.; Stevanović, V.; Buonassisi, T., Searching for "Defect-Tolerant" Photovoltaic Materials: Combined Theoretical and Experimental Screening. *Chem. Mater.* **2017,** *29*, 4667-4674.

2. Protesescu, L.; Yakunin, S.; Bodnarchuk, M. I.; Krieg, F.; Caputo, R.; Hendon, C. H.; Yang, R. X.; Walsh, A.; Kovalenko, M. V., Nanocrystals of Cesium Lead Halide Perovskites ($CsPbX_3$, X = Cl, Br, and I): Novel Optoelectronic Materials Showing Bright Emission with Wide Color Gamut. *Nano Lett.* **2015,** *15*, 3692-3696.

3. Schmidt, L. C.; Pertegás, A.; González-Carrero, S.; Malinkiewicz, O.; Agouram, S.; Mínguez Espallargas, G.; Bolink, H. J.; Galian, R. E.; Pérez-Prieto, J., Nontemplate Synthesis of $CH_3NH_3PbBr_3$ Perovskite Nanoparticles. *J. Am. Chem. Soc.* **2014,** *136*, 850-853.

4. Kulbak, M.; Gupta, S.; Kedem, N.; Levine, I.; Bendikov, T.; Hodes, G.; Cahen, D., Cesium Enhances Long-Term Stability of Lead Bromide Perovskite-Based Solar Cells. *J. Phys. Chem. Lett.* **2016,** *7*, 167-172.

5. MØLler, C. K., Crystal Structure and Photoconductivity of Cæsium Plumbohalides. *Nature* **1958,** *182*, 1436.

6. Swarnkar, A.; Mir, W. J.; Nag, A., Can B-Site Doping or Alloying Improve Thermal- and Phase-Stability of All-Inorganic $CsPbX_3$ (X = Cl, Br, I) Perovskites? *ACS Energy Lett.* **2018,** *3*, 286-289.

7. Swarnkar, A.; Shanker, G. S.; Nag, A., Organic-free colloidal semiconductor nanocrystals as luminescent sensors for metal ions and nitroaromatic explosives. *Chem. Commun.* **2014,** *50*, 4743-4746.

8. Wang, Y.; Li, X.; Sreejith, S.; Cao, F.; Wang, Z.; Stuparu, M. C.; Zeng, H.; Sun, H., Photon Driven Transformation of Cesium Lead Halide Perovskites from Few-Monolayer Nanoplatelets to Bulk Phase. *Adv. Mater.* **2016,** *28*, 10637-10643.

9. De Roo, J.; Ibáñez, M.; Geiregat, P.; Nedelcu, G.; Walravens, W.; Maes, J.; Martins, J. C.; Van Driessche, I.; Kovalenko, M. V.; Hens, Z., Highly Dynamic Ligand Binding and Light Absorption Coefficient of Cesium Lead Bromide Perovskite Nanocrystals. *ACS Nano* **2016,** *10*, 2071-2081.

10. Dastidar, S.; Egger, D. A.; Tan, L. Z.; Cromer, S. B.; Dillon, A. D.; Liu, S.; Kronik, L.; Rappe, A. M.; Fafarman, A. T., High Chloride Doping Levels Stabilize the Perovskite Phase of Cesium Lead Iodide. *Nano Lett.* **2016,** *16*, 3563-3570.

11. Beal, R. E.; Slotcavage, D. J.; Leijtens, T.; Bowring, A. R.; Belisle, R. A.; Nguyen, W. H.; Burkhard, G. F.; Hoke, E. T.; McGehee, M. D., Cesium Lead Halide Perovskites with Improved Stability for Tandem Solar Cells. *J. Phys. Chem. Lett.* **2016,** *7*, 746-751.

12. Nedelcu, G.; Protesescu, L.; Yakunin, S.; Bodnarchuk, M. I.; Grotevent, M. J.; Kovalenko, M. V., Fast Anion-Exchange in Highly Luminescent Nanocrystals of Cesium Lead Halide Perovskites ($CsPbX_3$, X = Cl, Br, I). *Nano Lett.* **2015,** *15*, 5635-5640.

13. Akkerman, Q. A.; D'Innocenzo, V.; Accornero, S.; Scarpellini, A.; Petrozza, A.; Prato, M.; Manna, L., Tuning the Optical Properties of Cesium Lead Halide Perovskite Nanocrystals by Anion Exchange Reactions. *J. Am. Chem.l Soc.* **2015,** *137*, 10276-10281.

14. Li, Z.; Kong, L.; Huang, S.; Li, L., Highly Luminescent and Ultrastable $CsPbBr_3$ Perovskite Quantum Dots Incorporated into a Silica/Alumina Monolith. *Angew. Chem. In. Ed.* **2017,** *56*, 8134-8138.

15. Zhang, H.; Wang, X.; Liao, Q.; Xu, Z.; Li, H.; Zheng, L.; Fu, H., Embedding Perovskite Nanocrystals into a Polymer Matrix for Tunable Luminescence Probes in Cell Imaging. *Adv. Funct. Mater*. **2017,** *27*, 1604382.

16. Loiudice, A.; Saris, S.; Oveisi, E.; Alexander, D. T. L.; Buonsanti, R., $CsPbBr_3$ QD/AlO_x Inorganic Nanocomposites with Exceptional Stability in Water, Light, and Heat. *Angew. Chem. In. Ed.* **2017,** *56*, 10696-10701.

17. Huang, H.; Chen, B.; Wang, Z.; Hung, T. F.; Susha, A. S.; Zhong, H.; Rogach, A. L., Water resistant $CsPbX_3$ nanocrystals coated with polyhedral oligomeric silsesquioxane and their use as solid state luminophores in all-perovskite white light-emitting devices. *Chem. Sci.* **2016,** *7*, 5699-5703.

18. Wei, Y.; Deng, X.; Xie, Z.; Cai, X.; Liang, S.; Ma, P. a.; Hou, Z.; Cheng, Z.; Lin, J., Enhancing the Stability of Perovskite Quantum Dots by Encapsulation in Crosslinked Polystyrene Beads via a Swelling–Shrinking Strategy toward Superior Water Resistance. *Adv. Funct. Mater.* **2017,** *27*, 1703535.

19. Wang, H.-C.; Lin, S.-Y.; Tang, A.-C.; Singh, B. P.; Tong, H.-C.; Chen, C.-Y.; Lee, Y.-C.; Tsai, T.-L.; Liu, R.-S., Mesoporous Silica Particles Integrated with All-Inorganic $CsPbBr_3$ Perovskite Quantum-Dot Nanocomposites (MP-PQDs) with High Stability and Wide Color Gamut Used for Backlight Display. *Angew. Chem. In. Ed.* **2016,** *55*, 7924-7929.

20. Sun, C.; Zhang, Y.; Ruan, C.; Yin, C.; Wang, X.; Wang, Y.; Yu, W. W., Efficient and Stable White LEDs with Silica-Coated Inorganic Perovskite Quantum Dots. *Adv. Mater.* **2016,** *28*, 10088-10094.

21. Malgras, V.; Tominaka, S.; Ryan, J. W.; Henzie, J.; Takei, T.; Ohara, K.; Yamauchi, Y., Observation of Quantum Confinement in Monodisperse Methylammonium Lead Halide Perovskite Nanocrystals Embedded in Mesoporous Silica. *J. Am. Chem. Soc.* **2016,** *138*, 13874-13881.

22. Dirin, D. N.; Protesescu, L.; Trummer, D.; Kochetygov, I. V.; Yakunin, S.; Krumeich, F.; Stadie, N. P.; Kovalenko, M. V., Harnessing Defect-Tolerance at the Nanoscale: Highly Luminescent Lead Halide Perovskite Nanocrystals in Mesoporous Silica Matrixes. *Nano Lett.* **2016,** *16*, 5866-5874.

23. Raja, S. N.; Bekenstein, Y.; Koc, M. A.; Fischer, S.; Zhang, D.; Lin, L.; Ritchie, R. O.; Yang, P.; Alivisatos, A. P., Encapsulation of Perovskite Nanocrystals into Macroscale Polymer Matrices: Enhanced Stability and Polarization. *ACS Appl. Mater. & Interfaces* **2016,** *8*, 35523-35533.

24. Chen, O.; Zhao, J.; Chauhan, V. P.; Cui, J.; Wong, C.; Harris, D. K.; Wei, H.; Han, H.-S.; Fukumura, D.; Jain, R. K.; Bawendi, M. G., Compact high-quality CdSe–CdS core–shell nanocrystals with narrow emission linewidths and suppressed blinking. *Nature Mater.* **2013,** *12*, 445.

List of Publications

Part of Thesis

1. Swarnkar, **A.;** Shanker, G. S.; Nag, A. Organic-Free Colloidal Semiconductor Nanocrystals as Luminescent Sensors for Metal Ions and Nitroaromatic Explosives. *Chem. Commun.* **2014**, *50*, 4743

2. Shanker, G. S.; **Swarnkar, A.;** Chatterjee, A.; Chakraborty, S.; Phukan, M.; Parveen, N.; Biswas, K.; Nag, A. Electronic Grade and Flexible Semiconductor Film Employing Oriented Attachment of Colloidal Ligand-Free PbS and PbSe Nanocrystals at Room Temperature. *Nanoscale*, **2015**, *7*, 9204.

3. Mir, W. J.; **Swarnkar**, **A.;** Sharma, R.; Katti, A.; Adarsh, K. V.; Nag. A. Origin of Unusual Excitonic Absorption and Emission from Colloidal Ag_2S Nanocrystals: Ultrafast Photophysics and Solar Cell. *J. Phys. Chem. Letts.*, **2015**, *6*, 3915.

4. Swarnkar, A.; Chulliyil, R.; Ravi, V. K.; Irfanullah, M.; Chowdhury, A.; Nag. Colloidal $CsPbBr_3$ Perovskite Nanocrystals: Luminescence Beyond Traditional QuantumDots. A. *Angew. Chemie. Int. Edit.* **2015**, *54*, 15424

5. Ravi, V. K.;† **Swarnkar**, **A.;**† Chakraborty, R.; Nag, A. Excellent Green but Less Impressive Blue Luminescence from $CsPbBr_3$ Perovskite Nanocubes and Nanoplatelets. *Nanotechnology*, **2016**, 27, 325708

6. Rao, M. J.; **Swarnkar, A.;** Markad, G. B.; Nag, A..Defect-Mediated Electron-Hole Separation in Colloidal Ag_2S-$AgInS_2$ Hetero Dimer Nanocrystals Tailoring Luminescence and Solar Cell Properties. M. Jagadeeswararao, *J. Phys. Chem. C*, **2016,** *120*, 1946.

7. Swarnkar, A.; Marshall, A.R.; Sanehira, E. M.; Chernomordik, B. D.; Moore, D. T.; Christians, J. A.; Chakrabarti, T.; Luther**,** J. M. Quantum Dot-Induced Phase Stabilization of α-$CsPbI_3$ Perovskite for High-Efficiency Photovoltaics. *Science*, **2016**, *354*,92

8. Swarnkar, **A.;** Ravi, V. K.; Nag, A. Beyond Colloidal Cesium Lead Halide Perovskite Nanocrystals: Analogous Metal Halides and Doping. *ACS Energy Letts*, **2017**, *2*, 1089

9. Swarnkar, A.; Mir, W. J.; Nag, A. Can B-Site Doping or Alloying Improve Thermal- and Phase-Stability of All-Inorganic $CsPbX_3$ (X = Cl, Br, I) Perovskites? *ACS Energy Letts***., 2018,** *3*, 286**.**

10. Sim, K. M.;[†] **Swarnkar, A;**[†] Nag, A.; Chung, D. S. Phase Stabilized α-$CsPbI_3$ Perovskite Nanocrystals for Photodiode Applications. *Laser & Photonics Reviews,* **2118,** 1700209.

11. Kumawat, N. K.;[†] **Swarnkar, A.;**[†] Nag, A. Kabra, D. Ligand Engineering to Improve the Luminance Efficiency of $CsPbBr_3$ Nanocrystal Based Light Emitting Diodes. *J. Phys Chem. C.* **2018**, *122*, 13767

Others Publications

12. Pattanayak, S.; **Swarnkar, A.;** Priyam, A.; Bhalerao, G. M. Citrate–Hydrazine Hydrogen-Bonding Driven Single-Step Synthesis of Tunable Near-IR Plasmonic,Anisotropic Silver Nanocrystals: Implications for SERS Spectroscopy of Inorganic Oxoanions. *Dalton Transactions.* **2014,** ***43***, 11826

13. Yettapu, G. R.; Talukdar, D.; Sarkar, S.; **Swarnkar, A.;** Nag, A.; Ghosh, P.; Mandal P. Terahertz Conductivity within Colloidal $CsPbBr_3$ Perovskite Nanocrystals: Remarkably High Carrier Mobilities and Large Diffusion Lengths. *Nano Letters*, **2016**, *16*, 4838

14. Aneesh, J.; **Swarnkar, A.;** Ravi, V. K.; Sharma, R.; Nag, A.; Adarsh, K. V. Ultrafast Exciton Dynamics in Colloidal $CsPbBr_3$ Perovskite Nanocrystals: Bi-Exciton Effect and Quantized Auger Recombination. *J. Phys. Chem. C*, **2017,** *121*, 4734

15. 15. Pattanayak, S.;[†] **Swarnkar, A.;**[†] Paik, P.; Priyam, A. Seed Geometry and Hydrogen Bonding Dependent Plasmonic Tuning of Silver Nanocrystals in A Citrate–Hydrazine Matrix and SERS Spectroscopic Detection of Chromium. *RSC Adv.*, **2017**, *7*, 45911.

[†] Authors contributed equally.